# Plasma sprayed thermal barrier coatings : production, characterization and testing

# Plasma Sprayed Thermal Barrier Coatings: Production, Characterization and Testing

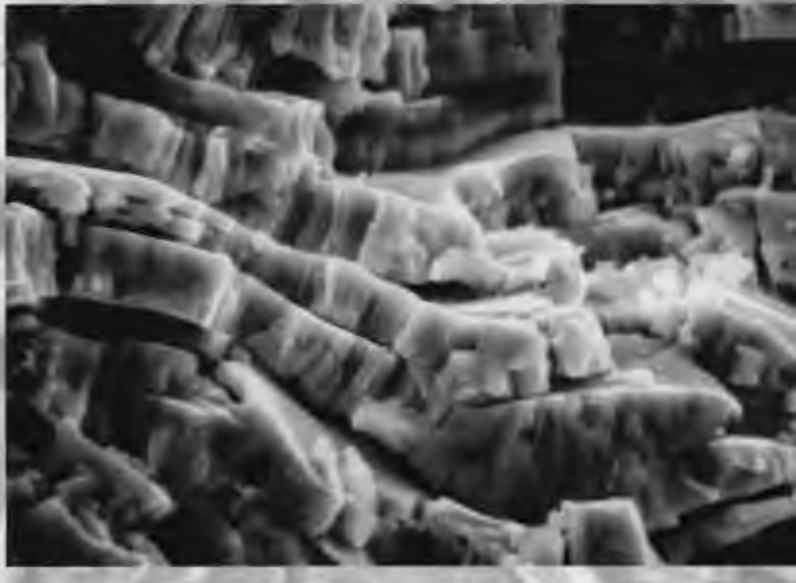

A.T.J. Verbeek

# Plasma Sprayed Thermal Barrier Coatings: Production, Characterization and Testing

PROEFSCHRIFT

ter verkrijging van de graad van doctor aan de
Technische Universiteit Eindhoven, op gezag van
de Rector Magnificus, prof. dr. J.H. van Lint, voor
een commissie aangewezen door het College
van Dekanen in het openbaar te verdedigen op
dinsdag 15 september 1992 om 16.00 uur

door

ADRIAAN THOMAS JACQUES VERBEEK

geboren te Heythuysen

Dit proefschrift is goedgekeurd
door de promotoren
prof.dr.ir. J.A. Klostermann
en
prof.dr. R. Metselaar
en de copromotor
dr.ir. J.M. Houben

# Plasma Sprayed Thermal Barrier Coatings: Production, Characterization and Testing

Dit onderzoek werd financieel gesteund door het
Innovatiegericht Onderzoeksprogramma Technische Keramiek (IOP TK)
onder projectnummer 86.B051

CIP-DATA, Koninklijke bibliotheek, Den Haag

Verbeek, Adriaan Thomas Jacques

Plasma Sprayed Thermal Barrier Coatings:
Production, Characterization and Testing
Adriaan Thomas Jacques Verbeek.-[S.l.:s.n]
Thesis Eindhoven.-With ref.
ISBN 90 3860082 8
Subject headings: thermal spraying, coatings

Ontwerp omslag: M. Vaessens
Druk: Drukkerij van Deursen bv, Nederweert

**SUMMARY**

The thermodynamical efficiency of heat engines such as gasturbines and diesel engines can be improved by the application of an increased combustion temperature. To protect the metallic parts of the heat engines to these increased temperatures, thermally insulating layers are applied: so called thermal barrier coatings. Thermal barrier coatings are applied in the hot sections of gas turbines such as combustion chambers, combustion liners and guide vanes, and on the pistons crowns and valves in diesel engines. Thermal barrier coatings generally consist of a metallic bondcoat of the MCrAlY type (M stands for Fe, Ni, Co or NiCo) and a ceramic topcoat of (partially) stabilized zirconia. Both the bondcoat and the topcoat are produced by powder plasma spraying. The thickness of the metallic bondcoat is generally 0.1 mm, whereas the thickness of the ceramic topcoat varies from 0.3 mm for an aero engine to several mm for a diesel engine. The thermal barrier coatings produced during this research programme consisted of a 0.1 mm FeCrAlY or NiCrAlY bondcoat and a 0.3 mm $ZrO_2$ 7.6 wt% $Y_2O_3$ topcoat.

The FeCrAlY bondcoats were sprayed by both the air plasma spraying (APS) process and the low pressure plasma spraying (LPPS) process.

The $ZrO_2$ topcoats were always produced by air plasma spraying.

Conventional ceramic topcoats have a high porosity to make them flexible and give them a high thermal shock resistance. This high porosity (10 to 25 results in a low resistance.

The goal of this research programme was to produce a thermal barrier coating having a ceramic topcoat with both a high thermal shock and a high erosion resistance.

To reach this aim, the factors involved with the production of the $ZrO_2$ topcoat were studied. First, the deposition behaviour of single $ZrO_2$ particles was studied. The influence of the plasma spray parameters and the use of several types of anode channels on the heat content, velocity and deposition morphology of single $ZrO_2$ particles was determined. New experimental techniques for the measurement of the particle velocity and the heat content of the particles were developed. The adhesion of $ZrO_2$ particles to several substrate materials was studied. The influence of the heat content and the particle velocity on the adhesion was determined.

The results of the investigations on single particles were used for the

production of the $ZrO_2$ topcoats. The development of residual stresses in the ceramic topcoat during the plasma spraying process was predicted, using a mathematical model. This model was verified experimentally.

The influence of substrate cooling on the characteristics of the topcoat was studied. Substrate cooling influenced both the microstructure and the residual stress state of the $ZrO_2$ coating. The cooled coatings displayed a dense micro crack network, giving the coatings a certain flexibility. The cooled coatings also contained residual tensile stresses.

The formation of cracks in the thermal barrier coatings, subjected to mechanical loading was investigated by combining the three point bending test with acoustic emission evaluation. It appeared that coatings, sprayed on cooled substrates, showed a distinct different fracture behaviour than coatings which were sprayed on non-cooled substrates.

The thermal shock behaviour and the erosion resistance of the new developed thermal barrier coatings were investigated in thermal shock and erosion tests. It appeared that the new developed coatings, sprayed with overheated particles on a cooled substrate had both a high thermal shock and a high erosion resistance. The results of these tests were compared to these of conventional thermal barrier coatings. It appeared that the erosion resistance of the new type of thermal barrier coatings improved three to four times, whereas the thermal shock resistance also improved.

The influence of the metallic bondcoat on the thermal shock behaviour was studied and it was found that both the LPPS FeCrAlY and the APS NiCrAlY coating formed a protective $Al_2O_3$ film on the interface bondcoat topcoat. The thermal barrier coatings with an APS FeCrAlY coating failed by severe oxidation of the bondcoat during thermal shock testing.

The influence of the plasma spray parameters, substrate cooling and the use of different anode channels on the tensile adhesion strength of the thermal barrier coatings was studied. It appeared that the failure modes, occurring during tensile adhesion testing, showed distinct differences. These differences could be explained by the experiences from the foregoing experiments.

The stability of the $ZrO_2$ 7.6 wt.% $Y_2O_3$ during annealing at high temperatures was studied by X-ray diffraction. It appeared that the $ZrO_2$ coating, which consisted mainly of the non-transformable tetragonal phase (T' phase), decomposed in a cubic phase and a tetragonal phase at temperatures above 1300 °C. On cooling down to room temperature, the tetragonal phase transformed to the monoclinic phase.

## CHAPTER I THERMAL BARRIER COATINGS

### 1 Introduction

The thermal efficiency $\eta_{th}$ of a gas turbine can be improved by the application of a higher operation temperature. The thermal or Carnot efficiency, as indicated by equation 1, shows that an increase of the process temperature $T_p$, with regard to the ambient temperature $T_a$, will result in a higher thermal efficiency.

$$\eta_{th} = 1 - \frac{T_a}{T_p} \qquad (1)$$

But the gas temperature of a turbine cannot be increased unlimited because the melting trajects of the super alloys, used in turbine construction give a limitation. These super alloys have melting trajects between 1230 and 1315 °C. To avoid failure of the components by creep, oxidation, thermal fatigue or even melting, the components are cooled with compressor discharge air. Too much cooling however, reduces the efficiency of a gas turbine. In order to increase the thermal efficiency of a gas turbine by raising the gas temperature or by a limitation of the amount of cooling air, turbine components are coated with thermally insulating layers, keeping the components at a lower temperature level. These thermally insulating layers are called Thermal Barrier Coatings (TBC's). In general, TBC's consist of a ceramic top coating with a low thermal conductivity, less than 2 W/mK, and a metallic bondcoat.

TBC's in gas turbines, both stationary gas turbines and jet engines, have been used widely since 20 years [1]. Sections which are coated are the combustion chambers and combustion liners and vanes. A new application of TBC's can be found in rocket engines, where certain parts are coated with thermally insulating layers.

Miller [2] reports about the temperature reduction of an air cooled blade of a jet engine which is coated with a 0.127 mm TBC. The decrease in component temperature, due to the TBC is 189 °C. When the cooling air flow is lowered to 50 % of its original value, the drop in component temperature still is 133 °C. Reardon and Dorfmann [4] report about savings of fuel of 6-12 % and Meier, Gupta and Sheffler [1] mention an annual fuel saving of 38 million litres for a 250 aircraft fleet.

Apart from the increase of thermal efficiency and the decrease of cooling there are two other benefits on applying TBC's. Thermal loading and thermal fatigue of the turbine materials is lowered, which may result in longer life times or the application of less expensive materials. Furthermore, the TBC protects the super alloy against corrosion and oxidation. So a wide range of fuels can be used when a TBC is applied. This is particularly important for stationary gas turbines where instead of jet fuel, heavy fuels may be used, which may produce several corrosive combustion products.

Apart from the successful use in gas turbines, TBC's are also applied in diesel engines, where piston crowns and valves are coated. So the temperature can be raised and the cooling rate can be lowered, resulting in a higher efficiency. Kvernes [3] estimates that the thermal efficiency of diesel engines, supplied with thermal barrier coatings can raise up to 48 %. Nevertheless, the application of thermal barriers in diesel engines is still in an experimental stage.
The emission of $NO_x$, which increases with increasing combustion temperature, gives an extra limitation for the development of thermal barrier coatings for diesel engines [5].
Although TBC's are already successfully applied for over 20 years, development and research still go on. New materials and coating techniques have to improve the quality and life time of the TBC's and the gas turbine as a whole.

**2.1 Composition of Thermal Barrier Coatings**

In general TBC's consist of a thermally insulating ceramic layer and a metallic bond layer, often called the topcoat and the bondcoat respectively. The typical thickness of the ceramic coatings is 0.3 mm in aircraft gas turbines and several mm in diesel engines. The thickness of the bondcoat is about 0.1 mm. Figure 1 shows the cross section of a TBC deposited on a Hastelloy Alloy X super alloy. The coating consists of a 0.3 mm zirconia/yttria 92/8 topcoat and a 0.1 mm FeCrAlY bondcoat.

A major problem in the production of metal-ceramic bonds is the difference in thermal expansion between metal and ceramic, causing high stresses which often lead to failure of the coating. In order to match with the difference in thermal expansion between substrate and coating it has been tried to

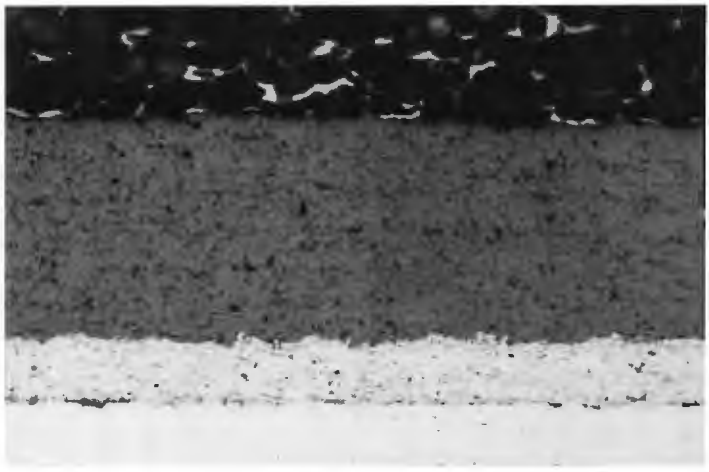


**Figure 1** Cross section of a thermal barrier coating, consisting of an air plasma sprayed FeCrAlY bondcoat and a $ZrO_2$ topcoat. The substrate material is Hastelloy X. The coating is sprayed at Eindhoven University of Technology.

produce TBC's with a graded zone between bondcoat and ceramic. The graded zone consisted of a mixture of ceramic and bondcoat material. The content of bondcoat material was high at the bondcoat side and low at the ceramic side. The idea looked promising but it has proven to be not very successful. Due to the oxidation of the metallic particles in the ceramic coating, high pressure stresses occurred, resulting in failure of the coating. This was found at Eindhoven University in 1981 by Bolleman [6], who sprayed and tested graded coatings, consisting of NiCrAlY and $ZrO_2$. Similar results were reported by Steffens and Fischer [7] and Strangmann [8].
Nowadays, a TBC consisting of a ceramic topcoat and a metallic bondcoat, is mainly used.

### 2.2. Production of Thermal Barrier Coatings

TBC's are mainly produced by means of thermal spraying, especially powder plasma spraying. As well the metallic bondcoat as the ceramic topcoat are deposited by plasma spraying.
Recently some new developments in coating deposition have been reported. Meier c.s.[9], Fancey c.s. [10] and Toriz [11] describe the successful use of TBC's applied by the Electron Beam Physical Vapour Deposition process.

This process will not be described here because it is beyond the scope of this chapter.

### 2.2.1 Powder plasma spraying.

During the powder plasma spraying, the coating powder is injected into a fastly streaming plasma. The individual powder particles are heated up to or beyond their melting points, accelerated and deposited on a substrate where they form a coating. During the impact on the substrate, the molten or partly molten particles spread out and form pancake-like deposits. The microstructure of a plasma sprayed coating shows a typical lamellar structure, caused by these individual splashed particles.

A powder plasma spray system consists of a plasma torch in which the plasma is generated, a power supply unit to produce and rectify the required high currents, a gas supply unit, a cooling unit, a powder injection system and a control unit for gas flow and current control. All these components are indicated schematically in figure 2.

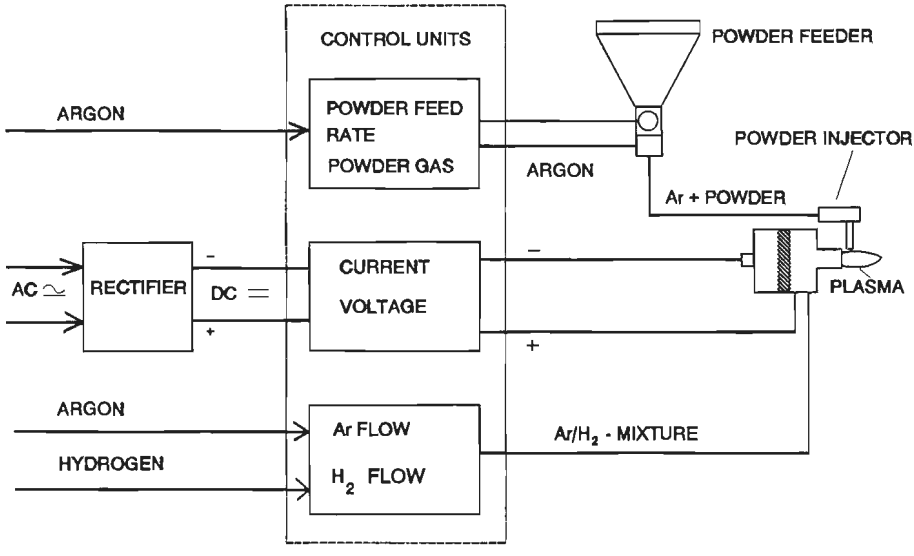


**Figure 2** Schematic view of an air plasma spray system. It has to be noted that the plasma torch, the powder injector and the high-current wires are water cooled.

The plasma is generated in the plasma torch. A gas mixture, of Ar and $H_2$, or He and $N_2$ flows between the anode and cathode where ionization of the gas takes place by an electrical arc discharge. The arc current varies between

300 and 1000 Amps at voltages from 50 to 100 Volts, mainly depending on the applied plasma gas. The input power of a plasma torch varies between 15 and 100 kW. Figure 3 shows the cross section of a plasma torch which was used for the production of the coatings, described in this thesis.

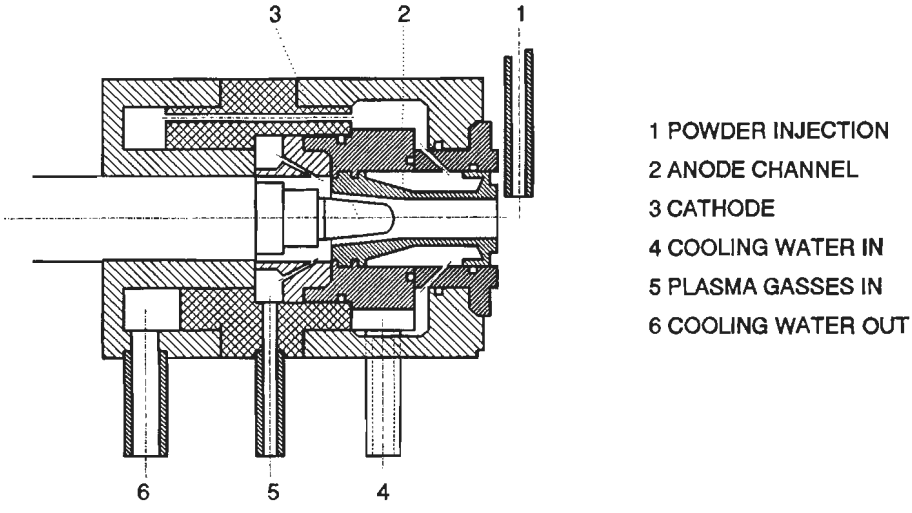


**Figure 3** Cross section of a plasma torch. This torch was developped at Eindhoven University of Technology and can be equipped with different types of anode channels. [12]

The maximum temperature of the plasma varies between 10,000 and 20,000 K and the gas velocity ranges from 100-800 m/s [13].
The powder is injected into the plasma flame by a carrier gas, usually Ar or $N_2$.
The grain sizes of the powders, manufactured for the plasma spray process, vary strongly. As well very fine powders, with grain sizes between 5 and 25 $\mu$m, as coarse powders (grain sizes between 100 and 200 $\mu$m) are available. Generally, the powders are delivered in certain grain size ranges. Common ranges are 22.5 to 45 $\mu$m and 45 to 90 $\mu$m. When the powder size range is narrow, the radial injection of the powder into the plasma flame is facilitated.
The velocity of the powder particles varies from 80-300 m/s, dependent on the particle size, the specific density, the plasma gas composition, the arc current and the nozzle geometry.
The deposition rate is about 40 grams coating material per minute, which is rather high compared to other deposition techniques. With special plasma

torches and anode channels it is possible to obtain a deposition rate exceeding 100 grams/minute.
The distance between the plasma torch and the object to be coated, the spraying distance, varies from 50 - 200 mm.
The great advantage of plasma spraying and thermal spraying in general is the fact that plasma spraying is a relatively cold process. Although the particle temperature is high, the sum of the thermal energies of all deposited particles, compared to the heat capacity of the substrate volume is generally low. So the substrate stays relatively cold during the spraying process and no unvoluntary heat treatment of the substrate will occur.
The cooling rate of the colliding particles is very high and varies, depending on the particle size, the coating material and the substrate material from 1E+5 to 1E+6 K/s [14]. This will be pointed out more extensively in chapter 2.

### 2.2.2. Vacuum or Low Pressure Plasma Spraying

Usually, the plasma spraying process takes place in air, so called Air Plasma Spraying (APS). As a consequence, metallic powders sprayed with the APS process may show severe oxidation caused by the oxygen from the air during the flight of the hot particles from the plasma torch to the substrate. The presence of these oxides embrittles the coating and causes an increase of the hardness. In the case of wear resistant plasma sprayed coatings, which are applied in situations where exist low contact pressures, this might be an advantage from a tribological point of view. However, the oxide films may affect the cohesive strength of the coating.
From experiments which are described in chapter 5 it appears that the oxidation resistance of especially MCrAlY coatings, which are used for oxidation protection of super alloys at high temperatures, decreases when a dense network of oxides is present in the coating. It appears that reactive elements as Cr and Al, which are needed to form a dense protective oxide film at the interface bondcoat-ceramic are already oxidized too heavily due to the APS process, thus preventing the formation of that protective scale.
To avoid the formation of oxides around the individual particles it is possible to spray under low partial oxygen pressure, using so called Low Pressure Plasma Spraying (LPPS) or Vacuum Plasma Spraying (VPS). The plasma torch and the components are placed in a vacuum vessel which is evacuated and thereupon filled with Ar at a pressure of 5-200 mbar.

The plasma gases which are blown into the vessel during the spraying process are exhausted by pumps, so that the argon pressure is kept at a constant, low level.
The use of a VPS installation results in coatings which are almost free of oxides. The experiments with bondcoats, sprayed under low pressure are described in chapter 5. The disadvantages of the LPPS or VPS process are the huge costs of the equipment and the fact that the dimensions of the work pieces to be coated are limited by the size of the vacuum vessel.
The behaviour of a plasma flame in a low pressure environment differs strongly from the behaviour of a plasma flame under atmospheric conditions. This requires extra efforts for the powder injection.

### 2.3 Thermal Barrier Materials

The material most used for TBC's is stabilized or partially stabilized $ZrO_2$, which has a very low thermal conductivity, in the order of 1 W/mK, and for ceramics a rather high thermal expansion coefficient of 10 E-6 $K^{-1}$. The thermal conductivity of $ZrO_2$ is almost constant over a wide temperature range.

#### 2.3.1 $ZrO_2$ and the stabilization of $ZrO_2$

Pure $ZrO_2$ has different phases, which are stable in different temperature ranges; the cubic phase (c), from the melting point at 2938 K to 2640 K, the tetragonal phase (t), from 2640 to 1220 K and finally the monoclinic phase (m) at temperatures below 1150 K. The phase transformation monoclinic-tetragonal shows hysteresis. The change from monoclinic to tetragonal occurs at 1440 K whereas the reverse transformation starts at 1220 K.

$$\textit{monoclinic} \quad \rightleftarrows^{1440}_{1220} \quad \textit{tetragonal} \quad \rightleftarrows^{2640}_{2640} \quad \textit{cubic}$$

The phase change tetragonal to monoclinic is accompanied by a volume increase of 4.6 percent (Calculated by the difference of the volume of the unity cells of tetragonal and monoclinic $ZrO_2$). This volume increase causes high compressive stresses, resulting in crack formation and destruction of the material. $ZrO_2$ in its pure state is not usable for thermal barrier coatings.
To avoid the change from the tetragonal phase to the monoclinic phase, ZrO2 is stabilized with oxides as MgO, CaO, $CeO_2$, $HfO_2$ or $Y_2O_3$. Depending on the amount of the stabilizing oxide, $ZrO_2$ maintains its tetragonal or cubic structure at room temperature. The stabilizer mostly used

at this time is $Y_2O_3$, which has proven to provide $ZrO_2$ with the highest thermal shock resistance. Several authors report about thermal shock experiments on $ZrO_2$ coatings stabilized with $Y_2O_3$. The highest thermal shock resistance was found at 7-8 wt% $Y_2O_3$ [2, 15, 16, 17,].

The use of $CeO_2$ stabilized $ZrO_2$ is the subject of many studies now, because of the high $K_{1c}$ value of this material.

Figure 4 shows the phase diagram of zirconia-yttria according to Scott.

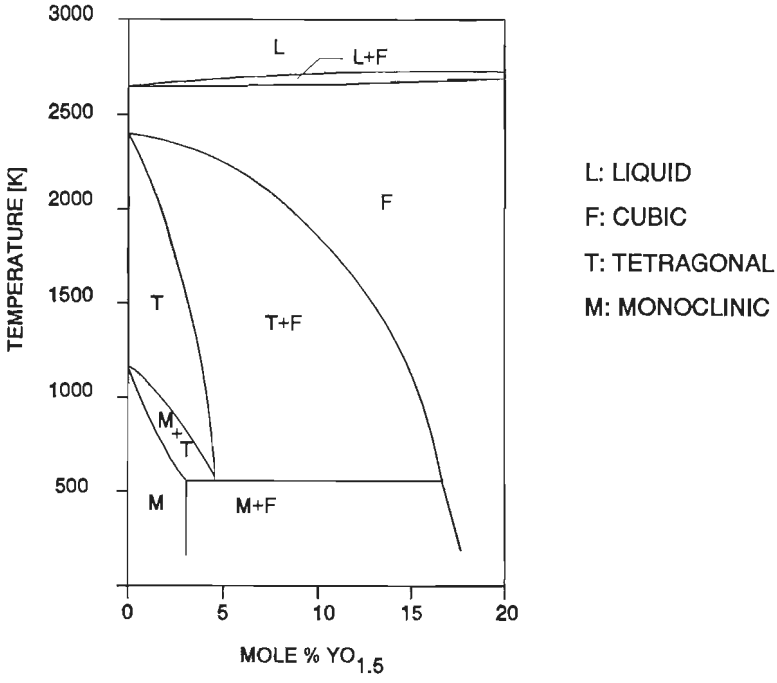


**Figure 4** The low yttria region of the phase diagram $ZrO_2$-$Y_2O_3$ according to Scott. The figure is redrawn from reference [18].

At a weight percent above 15-17 % $Y_2O_3$, $ZrO_2$ is fully stabilized and remains in the cubic structure at room temperature. Between 8 and 15 wt% $Y_2O_3$, $ZrO_2$ is tetragonal at room temperature, whereas between 6 and 8 wt% the material also may contain a little amount of monoclinic $ZrO_2$. It is called partially stabilized zirconia (PSZ) which has proven to have the highest thermal shock resistance. This may be due to the fact that Partially Stabilized Zirconia contains a metastable tetragonal phase which transforms to the monoclinic phase under the influence of stress fields. When for example a stress field, present at the tip of a crack, exceeds the transformation stress, the metastable tetragonal phase will change to the

monoclinic phase, causing local compressive stresses, which stop the propagation of the crack. This phenomenon is called transformation toughening. The presence of this phenomenon is the subject of discussion in literature. Miller [19] claims that plasma sprayed $ZrO_2$ with 6-9 mole% $Y_2O_3$ contains a quenched-in metastable tetragonal phase, which does not change to the monoclinic phase under the influence of a stress field. This quenched-in or t' phase will decompose in a low $Y_2O_3$ tetragonal phase and a high $Y_2O_3$ cubic phase when the material is annealed for long times at temperatures above 1300 °C. The low $Y_2O_3$ t phase will change to the m phase on cooling down to room temperature. From our own investigations, reported in chapter 5, it can be concluded that this phenomena happened to $ZrO_2/Y_2O_3$ 92/8 coatings, annealed for long periods of time at temperatures of 1400 C and higher.

### 2.3.2 Physical and mechanical properties of $ZrO_2$

Compared to other ceramics, the coefficient of thermal expansion of $ZrO_2$ is high and varies from 9-11.5 E-6 $K^{-1}$ [20, 21, 22, 23, 24]. Because the coefficient of thermal expansion of super alloys varies from 14-16 E-6 $K^{-1}$, there will be a mismatch of 25-70 % in thermal expansion, causing high stresses in the coating.
Figure 5 shows the thermal expansion of stabilized $ZrO_2$ as a function of temperature.

The thermal conductivity of $ZrO_2$ varies from 0.8-3 $Wm^{-1}K^{-1}$ [25]. The thermal conductivity of TBC's is dependent on the microstructure of the plasma sprayed coating and is mainly determined by the porosity of the coating. Coatings, deposited by the EB -PVD process have a thermal conductivity which is twice the thermal conductivity of plasma sprayed TBC's [9].
The thermal conductivity of $Y_2O_3/ZrO_2$ 15/85, with a relative density of 85 % varies between 1.5 and 1.67 $Wm^{-1}K^{-1}$ at 300 and 1500 K respectively. For a 100 % dense coating, these values range from 1.75 - 1.95 $Wm^{-1}K^{-1}$. Figure 6 shows the thermal conductivity of pure $ZrO_2$ in the temperature range from 300-2500 K. It can be seen that a porosity of 44 % decreases the thermal conductivity by 33 %.

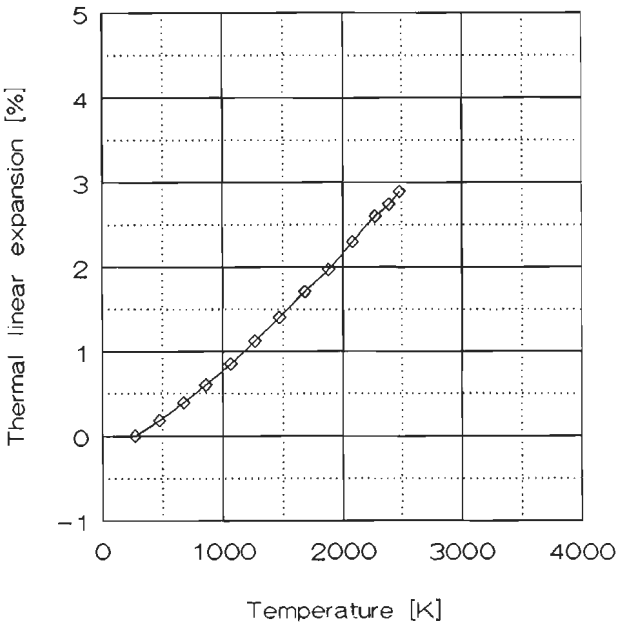


**Figure 5** The relationship between the thermal linear expansion and the temperature of ZrO2, stabilized with 15 wt% $Y_2O_3$. Redrawn from reference [25]

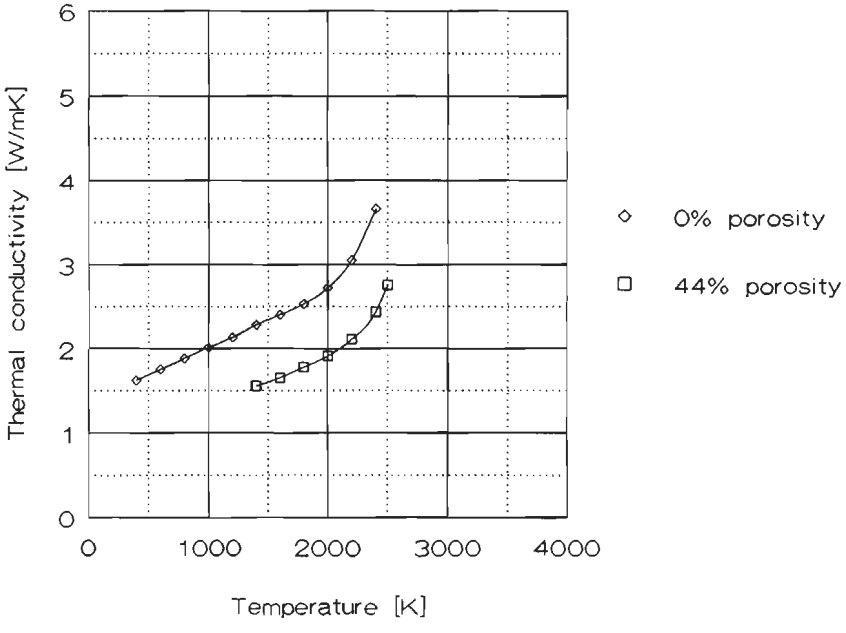


**Figure 6** The thermal conductivity of $ZrO_2$ as a function of the temperature and the porosity. Redrawn from reference [25]

The melting point of $ZrO_2$ is reported by several authors and ranges from 2473-3118 K. These values are reported by Schick and Gmelin [26, 27]. It has to be remarked that all these literature data are rather old. It is nowadays assumed that the melting point of pure zirconia is 2973 K. The melting points from stabilized $ZrO_2$ can be learned from the phase diagrams.
The boiling point of $ZrO_2$ is reported to be between 4300 and 5000 K [27]. This boiling point is of interest in the investigation of the vaporization behaviour of the $ZrO_2$ particles in the plasma flame, which will be discussed in chapter 2 of this thesis where the behaviour of single $ZrO_2$ particles in the plasma flame is reported.

The Young's modulus of pure $ZrO_2$ is reported between 170 and 200 GPa. For plasma sprayed coatings it is better to use the term stiffness instead of Young's modulus since the Young's modulus is an intrinsic material parameter, depending on the crystal structure. The stiffness of a plasma sprayed $ZrO_2$ coating varies strongly and is determined by the microstructure of the coating, e.g. the porosity or the presence of a microcrack network. The stiffnesses of the plasma sprayed zirconia coatings, as measured in this research programme, ranged from 14000 to 46000 MPa. This agrees with the values reported in literature. They range from 16000 to 50000 MPa for a plasma sprayed $ZrO_2$ coating [22, 24, 28, 29, 30, 31, 32, 33, 34, 35, 36].

### 2.4 Bondcoats

The bondcoat has a threefold function: improvement of the adhesion between substrate and ceramic topcoat, protection of the substrate against corrosion and oxidation and reduction of the stresses caused by the difference in thermal expansion between the topcoat and the substrate.

#### 2.4.1. Bondcoat materials

Bondcoats of earlier TBC's were made of NiAl, but because of the poor resistance against sulfidation, they were replaced by MCrALY coatings, where M is Fe, Co, Ni or NiCo. The choice of M depends on the atmosphere in which the coating operates. NiCrAlY coatings have a lower resistance against sulfidation than CoCrAlY coatings, but their mechanical strength is higher [37]. FeCrAlY shows a good resistance against sulfidation.
The protection against oxidation and corrosion is based on the formation of a dense oxide film of $Cr_2O_3$ or $Al_2O_3$ on the surface of the bondcoat. These

oxide films act as oxygen barriers and prohibit further oxidation or corrosion of the bondcoat and the substrate. Whether a $Cr_2O_3$ or an $Al_2O_3$ film will be formed depends on the concentration of both elements in the coating. The ease of formation of a protective $Al_2O_3$-scale is in the order of FeCrAl > NiCrAl > CoCrAl [38].

The adhesion and the formation of the protective oxide film are improved by the presence of a little amount of Y, between 0.3 and 1 wt%. The mechanism which is the cause of this improvement is not well understood.
If the Al content of the bondcoat is less than 5 wt%, the formation of a dense $Al_2O_3$ film is not likely to happen, and predominantly a $Cr_2O_3$ film will be formed [38].

### 2.5 Failure of Thermal Barrier Coatings.

Failure of TBC's can occur in several ways and is often a combination of several failure mechanisms. The main mechanisms will be discussed in the following paragraphs.

#### 2.5.1 Failure due to corrosion of stabilized $ZrO_2$

Although $ZrO_2$ is inert to the most corrosive products, it can be attacked by corrosion in two ways. Condensed corrosive products as $Na_2SO_4$ can penetrate into the coating and fill up the pores and microcracks, thus decreasing the ductility of the coating. This may lead to a decreased thermal shock resistance of the coating. Especially very porous coatings may fail in this way.
Secondly and more important is the deterioration due to the destabilization of the $ZrO_2$ coating caused by the reaction of the stabilizing oxide with corrosive products. Liquid vanadates, which may be formed on burning heavy fuels, react with $Y_2O_3$ and form $YVO_4$. $ZrO_2$ stabilized with $CeO_2$ shows the same degradation due to the formation of $CeVO_4$. The $ZrO_2$ will be destabilized and changes into the monoclinic phase [39].
The degradation of MgO stabilized $ZrO_2$ is described by Levy and MacAdam [40]. MgO reacts with $SO_3$ to $MgSO_4$, which leads to the destabilization of $ZrO_2$ and the formation of the monoclinic phase. Hancock [41] describes the degradation of CaO, MgO and $Y_2O_3$ stabilized $ZrO_2$ and reports that all the stabilizers react with $SO_3$, resulting in destabilization of the coatings.

### 2.5.2 Failure due to bondcoat oxidation and corrosion

As already mentioned in the foregoing paragraph, the protective behaviour of MCrAlY coatings is based on the formation of a dense thin oxide film of $Al_2O_3$ or $Cr_2O_3$. These protective films can be damaged by thermal cycling of the coated components. The damaged film can be restored by Al or Cr diffusion from the bulk of the bondcoat towards the interface bondcoat-ceramic. When the Al or Cr concentration becomes too low to restore the damaged film, less stable oxides will be formed, such as NiO or $Fe_2O_3$ in respectively NiCrAlY and FeCrAlY coatings. The failure of thermal barrier coatings due to the formation of a $Fe_2O_3$ film on a air plasma sprayed FeCrAlY bondcoat is described in chapter 5.

### 2.5.3 Thermal shock failure

Thermal shock failure occurs due to rapid changes of temperature in a gas turbine. When the turbine is started up, the coating is heated up from room temperature up to 1100 -1200 °C in a few minutes. On the other hand, the coating can be cooled down very fast in the case of a flame out, when cold air flows into the engine.

As a result of the low thermal conductivity of $ZrO_2$ and the difference in thermal expansion between substrate and coating, high stresses develop, causing cracks in the ceramic coating. After several cycles, the cracks may become so extended that parts of the coating delaminate. Improvement of the thermal shock resistance of the coatings can be reached by lowering the stiffness of the coating. This results in lower stresses and can be achieved by spraying a coating with a high porosity. A high porosity, however, may be disadvantageous in corrosive and erosive environments. Corrosive products may penetrate into the coating, affecting the bondcoat or filling up the pores and thus decrease the ductility of the coating. The erosion resistance of porous coatings is poor. (see chapter 5).

Another possibility of thermal shock failure is delamination at the interface bondcoat/ceramic. During service of the coating, a protective alumina or chromia scale is formed at this interface. Due to its brittle character, this film can be cracked during thermal cycling, leading to spallation of the coating. Cracking of the protective scale may also lead to severe local corrosion of the bondcoat, resulting in spallation of the topcoat.

To test the thermal shock resistance of thermal barrier coatings, several tests are used. The results of these tests cannot be compared to each other due to

the different parameters as heating time, temperature cycle etc.
The test rigs generally consist of a heater and a cooler. The heater is in most cases an acetylene-oxygen or propane-oxygen burner and sometimes a burner can of a gas turbine. The cooler is in most cases an air jet.
Typical test cycles are 300-900°C and 400-1100°C. The heating up and cooling down temperature take 30 seconds each.
The thermal shock test rig, which was used in our research programme, is described in chapter 5. The results of the thermal shocks tests, carried out on different types of coatings, can also be found in this chapter.
The failure of TBC's is often a combination of the mechanisms which were mentioned above. Especially bondcoat oxidation in combination with crack growth due to thermal cycling is regarded as one of the most important means of failure of TBC's. Many models, used to predict the lifetime of thermal barrier coatings [9, 42, 43] use crack growth in the ceramic topcoat and weight gain due to oxidation of the bondcoat in relationship to the number of cycles as the main parameters.

**2.6. The design of TBC systems**

The design of a TBC system is determined by the environment in which the coating has to operate.
To avoid the penetration of liquid corrosive products, the ceramic coating has to be dense. This results in a coating with a high stiffness, a low flexibility and a low thermal shock resistance.
A porous coating deforms easily under elastic stress, but does not show a high intrinsic strength, resulting in a low erosion resistance. This makes a porous coating less suitable for serving under erosive environments, such as may exist in deserts.
The presence of vanadates makes it impossible to use yttria or ceria stabilized zirconia, there the ceramic will be destabilized. The alternative, the application of a MgO stabilized zirconia coating, results in a TBC with a lower thermal shock resistance.
It can be seen that there are conflicting interests, and it is strongly dependent on the environment of operation, which type of coating has to be chosen to withstand the most important degradation mechanism for that situation.

## 3 Outline of this thesis

This thesis describes the research programme on thermal barrier coatings which covered the whole field of production, characterization and testing of plasma sprayed thermal barrier coatings, consisting of a metallic bondcoat and a ceramic topcoat.

The goal of this research programme was to produce a thermal barrier coating with both a high thermal shock strength and a high erosion resistance. To obtain this goal, all factors influencing the characteristics and the properties of the ceramic topcoat were investigated by experiments on the basis of theoretical models.

Chapter 2 describes the behaviour of single zirconia particles during the plasma spray process. The deposition behaviour as a function of the plasma spray parameters and the spraying techniques is reported. Furthermore a model for the adhesion between the ceramic particles and the metallic substrate is presented in this chapter.

Chapter 3 reports about the production of thermal barrier coatings. The spraying of metallic APS and LPPS bondcoats, and ceramic APS topcoats is described. A theoretical model, predicting the origin of residual stresses in the ceramic coating is given. This model is experimentally verified. The influence of substrate cooling during the coating process is investigated and the microstructure of the coatings as a function of the plasma spray parameters is determined.

In chapter 4, the formation of cracks in plasma sprayed thermal barrier coatings is reported, using acoustic emission evaluation, combined with the three point bending test. The influence of substrate cooling on the fracture behaviour was studied.

Thermal shock and erosion tests were carried out on the different types of coatings. The results of these tests, together with the results of long term, high temperature experiments on bondcoats and ceramic topcoats are described in chapter 5.

Conclusions and recommendations can be found in chapter 6.

The next figure shows the production scheme of thermal barrier coatings. All steps which were undertaken in order to come to a thermal barrier coating with the desired properties are depicted in this scheme.

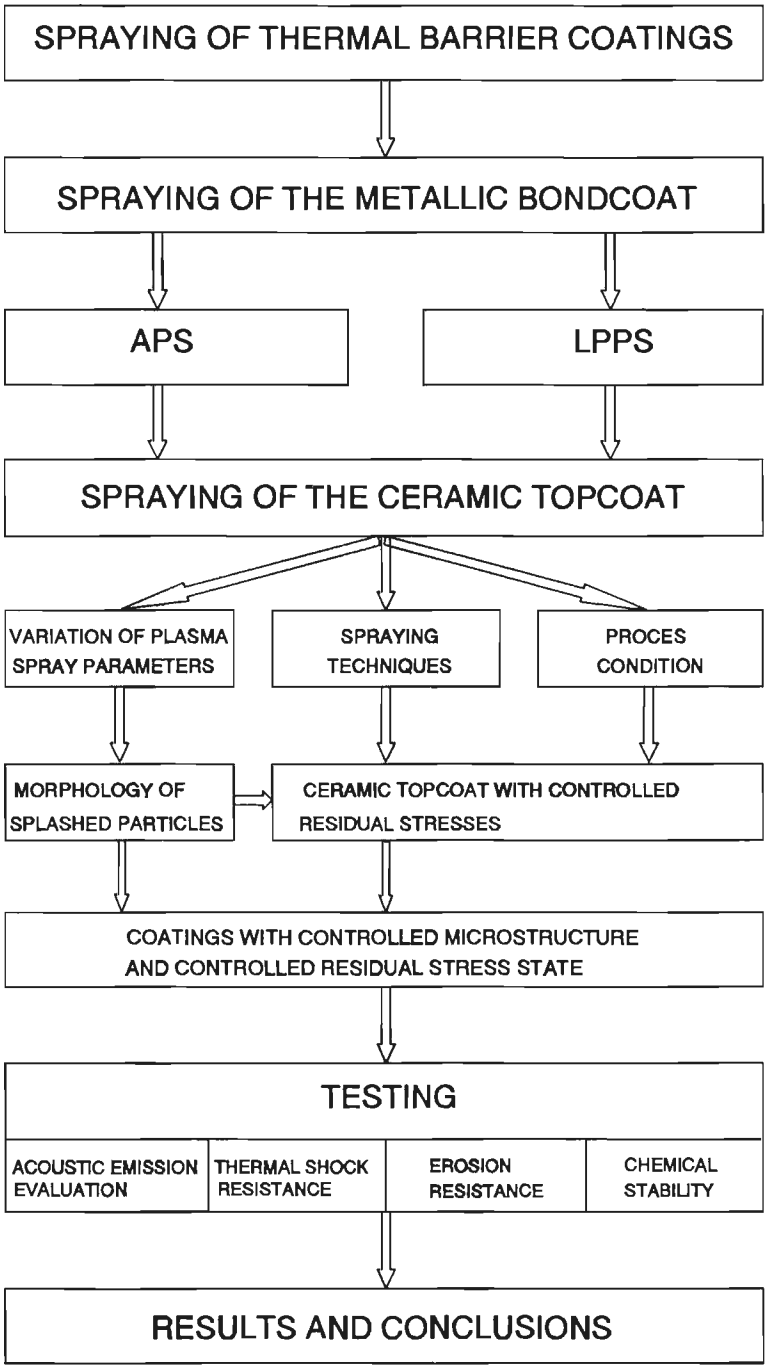
SPRAYING OF THERMAL BARRIER COATINGS
SPRAYING OF THE METALLIC BONDCOAT
APS
LPPS
SPRAYING OF THE CERAMIC TOPCOAT
VARIATION OF PLASMA SPRAY PARAMETERS
SPRAYING TECHNIQUES
PROCES CONDITION
MORPHOLOGY OF SPLASHED PARTICLES
CERAMIC TOPCOAT WITH CONTROLLED RESIDUAL STRESSES
COATINGS WITH CONTROLLED MICROSTRUCTURE AND CONTROLLED RESIDUAL STRESS STATE
TESTING
ACOUSTIC EMISSION EVALUATION
THERMAL SHOCK RESISTANCE
EROSION RESISTANCE
CHEMICAL STABILITY
RESULTS AND CONCLUSIONS

## 4 References of chapter 1


[1] Meier, S.M., Gupta D.K., Scheffler K.D.,Ceramic Thermal Barrier Coatings for Commercial Gas Turbines, J. Mater., 43(1991), No 3, pp. 50-53.

[2] Miller, R.A.,Current Status of Thermal Barrier Coatings, Surf. Coat. Techn. 30 (1987) 1-11

[3] Kvernes I., COST 501, Work Package W.P. 6. TBC for Diesel and other Internal Combustion Engines, EUCO/MCS/09/89, JRC, Petten, The Netherlands, 1989.

[4] Reardon J.K., Dorfmann M.R., Advanced Thermal Barrier Coating Systems, J. Mater. Energy Syst. 8(1987), No 4 pp. 414-419

[5] Murray R.G., Improved Engine Performance through Heat Transfer Control, Oklahoma State University, Stillwater, 1978

[6] Bolleman N.C.F., Materiaalkeuze voor de verbrandingskamer van een industriele gasturbine. Master's Thesis, Eindhoven University of Technology, 1981.

[7] Steffens H.D., Fischer U., Thermal Shock Testing of Thermal Barrier Coatings. In: Advanced Materials Research and Development for Transport: Ceramic Coatings for Heat Engines. Strasbourg, 1985, Editor I. Kvernes, Les Editions de Physique, Les Ulis, France, 1985

[8] Strangmann T.E., Thermal Strain Tolerant Abradable Thermal Barrier Coatings. ASME paper, 91-GT-39, 1991.

[9] Meier S.M., Nissley D.M., Sheffer K.D., Cruse T.A., Thermal Barrier Coating Life Prediction Model, ASME-paper 91-GT-40, 1991.

[10] James A.S., Fancey K.S. Matthews A., Thermo-ionically Assisted R.F. Plasma Assisted PVD of Stabilized Zirconia Thermal Barrier Coatings. Surf. Coat. Techn. 32 (1987) 377-387.

[11] Toriz F.C., Thakker A.B., Gupta S.K., Thermal Barrier Coatings for Jet Engines. ASME-paper 88-GT-279, 1988.

[12] Houben J.M.,Eindhoven University of Technology, Faculty of mechanical engineering, private communication

[13] Fauchais P., Bourdin E., Coudert J.F., McPherson R.
High Pressure Plasmas and Their Application to Ceramic Technology. In: Topics in Current Chemistry 107, Plasma Chemistry IV, editor F.L. Boschke, Springer Verlag, Berlin, Heidelberg, New York 1983.

[14] Houben J.M., Relation of the Adhesion of Plasma Sprayed Coatings to the Process Parameters Size, Velocity and Heat Content of the Spray Particles. Doctor's Thesis, Eindhoven University of Technology, 1988.

[15] Berndt C.C., Material Property Measurements on Thermal Barrier Coatings. ASME-paper 88-GT-277, 1988.

[16] Suhr D.S., Mitchell T.E., Keller R.J. Microstructure and Durability of Zirconia TBC's. In: Science and Technology of Zirconia II, Advances in Ceramics, vol. 12, editor N. Claussen. The American Ceramic Society, 1983.

[17] Johner G., Schweitzer K.K., Thermal Barrier Coatings for Jet Engine Improvement. Thin Sol. Fi., 119(1984) pp.301-315.

[18] Scott H.G., Phase Relationships in the Zirconia-Yttria System. J. Mater. Sci. 10(1975) 1527-1537

[19] Miller R.A., Smialek J.L., Garlic R.G., Phase Stability of Plasma Sprayed Partially Stabilized Zirconia-Yttria. In: Science and Technology of Zirconia III, Advances in Ceramics, vol 24, editor S. Somiya. The American Ceramic Society, 1988.

[20] Berndt C.C., Herman H.,Anisotropic Thermal Expansion Effects in Plasma Sprayed $ZrO_2$-8wt%$Y_2O_3$.Ceram. Eng. Sci. Proc. 4(1983), No 9/10 pp.792-801

[21] Bernard D., Gitzhofer F., Fauchais P. Thermal Diffusivity and Expansion Coefficients, In: Thermal Spray Technology, Editor D.L. Houck, ASM, Ohio, U.S.A. 1989.

[22] Boch P., Fauchais P., et-al, Plasma Sprayed Zirconia Coatings. In: Science and Technology of Zirconia II, Advances in Ceramics, vol 12, editor N. Claussen, The American Ceramic Society, 1983.

[23] Scott J,T., Restall J.E., Some Aspects of the Development and Performance of Ceramic Thermal Barrier Coatings for Gas Turbines. In: Thermal Spray Technology, Editor D.L. Houck, ASM, Ohio, USA, 1989.

[24] Chang G.C., Phucharoen W., Miller R.A., Thermal Mismatch and Plasticity in TBC's, NASA Report B89-17330/6/XAB 1987

[25] Touloukian Y.S.,Thermophysical Properties of High Temperature Solid Materials, vol IV, MacMillan Company, New York, 1967

[26] Schick H.L., Thermodynamics of Certain Refractory Compounds, Vol I. Academic Press, New York, London, 1966

[27] Gmelins Handbuch der Anorganischen Chemie. Verlag Chemie, Weinheim/Bergstrasse, 1958

[28] Mullen R.L., Hendricks R.C, McDonald G., Nasa Technical Memorandum 83418, 1983.

[29] Elsing R., Knotek O., Balting U. The influence of Physical Properties and Spraying Parameters on the Creation of Residual Stresses during the Spraying Process. Surf. Coat. Techn. 41(1990) pp. 147-156

[30] Hobbs N. The Structure and Properties of Plasma Sprayed 8% Yttria-Zirconia Thermal Barrier Coatings. Doctor's Thesis, University of Bath, U.K., 1989.

[31] Eckold G., Buckley-Golder J.M., Scott K.T., A theoretical Analysis of Residual Stresses in Flame Sprayed Brittle Materials. Harwell Laboratory, Didcot, Oxon, U.K., 1987.

[32] Noutoni A., Kodama M.,Inoue Y. Residual Stress Measurement on Plasma Sprayed Coatings. Weld. Int. 1 (1989) pp. 947-953

[33] Steffens H.D., Fischer U. Correlation between Microstructure and Physical Properties of Plasma Sprayed Zirconia Coatings. In: Thermal Spray Technology, Editor D.L. Houck, ASM, Ohio, USA, 1989.

[34] Muller R.L., Padovan J., Braun M.J., Thermomechanical Design Criteria of Ceramic and Coated Surfaces. In: High Tech Ceramics, Editor P. Vincenzini, Elseviers Science Publishers, Amsterdam 1987.

[35] Steffens H.D., Kaczmarek, Thermal Coatings for Heat Engines, IIW Document S.C. 25/89 University of Dortmund, Germany.

[36] Kaufmann A., Liebert C.H., Nachtigall A.J., Low Cycle Fatigue of TBC at 982 °C. Nasa Technical Paper 1322 (1978).

[37] Verstraaten A.J.M. De toepassing van TBC's op Verbrandingskamerwanden van Dieselmotoren. Master's Thesis, Eindhoven University of Technology, 1983.

[38] Kofstad P., High Temperature Corrosion
Elsevier Applied Science, London New York, 1988.

[39] Jones R.L., Williams C.E.,Hot Corrosion Studies of Zirconia Ceramics. Surf. Coat. Techn. 32 (1987) 349-358.

[40] Levy A., Macadam S. The Behaviour of Ceramic Thermal Barrier Coatings on Diesel Engine Combustion Zone Components. Surf. Coat. Techn. 30 (1987) 51-61.

[41] Hancock P. Degradation Processes for Ceramic Coatings
In:Advanced Materials Research and Development for Transport: Ceramic Coatings for Heat Engines. Strasbourg, 1985, Editor I. Kvernes, Les Editions de Physique, Les Ulis, France, 1985.

[42] Miller R.A., Agarwall P., Duderstadt E.C., Life Modelling of Atmospheric and Low Pressure Plasma Sprayed TBC's.
Ceramic Proceedings, 8th Annual Conference on Composites and Advanced Ceramic Materials, American Ceramic Society, Ohio, USA, 1984

[43] Pilsner B., Hillery R., McKnight R. Thermal Barrier Coating Life Prediction Model. General Electric Report 173332/2/XAB 1987.

## CHAPTER II THE BEHAVIOUR OF SINGLE $ZrO_2$ PARTICLES DURING THE PLASMA SPRAY PROCESS

### 1 Introduction

Each plasma sprayed coating is built up by millions of single particles. Each second, about two million powder particles are injected into the plasma flame, where they are heated up to, or beyond their melting points. They are simultaneously accelerated to velocities ranging from 80-300 m/s, depending on particle sizes, densities and the acceleration properties of the plasma. During the impact on the substrate, the particles spread out and solidify. All single particles together form the coating, and determine the final quality and characteristics of the coating.
For this reason, it is very important to get insight in the behaviour of single $ZrO_2$ particles during the plasma spray process.

The deposition morphology of a particle will largely be determined by its velocity and its temperature. Besides, the substrate, as the colliding partner, plays an important role. This chapter describes the theoretical considerations and experimental techniques for the measurement of the velocity, thermal energy content and collision behaviour of single $ZrO_2/Y_2O_3$ particles.
First a general introduction about the plasma spraying process, and the equipment used, is given. This will be followed by the applied experimental techniques, which were developed mainly by Houben [1], and the obtained results. The chapter is completed by a concluding paragraph, bringing together the results of the different experiments.

### 2.1 Plasma spraying, some definitions

When a particle is injected into the plasma flame, it is accelerated and heated up. Heating up occurs by thermal energy transfer from the hot plasma gasses to the particles, whereas acceleration is caused by momentum transfer from the fast moving ions and gas atoms to the particles.
The heat and momentum transfer can be characterized by three specific times; the heat absorption time $t_{ha}$, the heat supply time $t_{hs}$ and the dwell time $t_{dw}$.

The heat absorption time equals the time that a particle needs to obtain a uniform temperature distribution and is mainly determined by the thermal

diffusivity $a_p$ of the particle.
The heat absorption time for a well heated particle is derived by Houben [2] and can be defined by equation 1:

$$t_{ha}=0.3\frac{R_p^2}{a_p}, \quad where \quad a_p=\frac{\lambda_p}{\rho_p c_p} \tag{1}$$

$R_p$: Radius particle [m]
$\lambda_p$: Thermal conductivity particle [$Wm^{-1}K^{-1}$]
$\rho_p$: Density of the particle [$kgm^{-3}$]
$c_p$: Heat capacity of the particle [$Jkg^{-1}K^{-1}$]

The heat supply time equals the time needed to heat up a particle to a mean temperature $T_p$. The heat supply time is determined by the heat transfer from the plasma gasses to the particle and is governed by the next equation [2]:

$$t_{hs}=\frac{1}{3}\frac{R_p^2}{a_p}\frac{\lambda_p}{\lambda_g}\ln\left(\frac{T_g-T_{p,0}}{T_g-T_p}\right) \tag{2}$$

$\lambda_g$: Thermal conductivity of the plasma gas [$Wm^{-1}K^{-1}$]
$T_g$: Gas temperature [K]
$T_{p,0}$: Start temperature particle [K]
$T_p$: Required particle temperature [K]

The heat supplied by the plasma flame can not be absorbed fully by the particle if $t_{ha} > t_{hs}$. This phenomenon occurs preferably with materials with a low thermal conductivity, resulting in an overheated outer shell and a non-heated core. If $t_{ha} < t_{hs}$, the heat supplied by the plasma will be fully absorbed by the particle, and a well heated particle with a uniform temperature distribution will be the result.

To fulfil the conditions concerning $t_{ha}$ and $t_{hs}$, the time that a particle stays in the plasma flame, $t_{dw}$, must be sufficient.
The dwell time is determined by the velocity and viscosity of the plasma and the density and radius of the injected particles. In paragraph 3.1.3, the velocities and dwell times of zirconia particles, with varying diameters will be

calculated.
The velocity of a particle is proportional to $(R_p)^{-2}$, whereas the heat supply time is proportional to $(R_p)^2$. This implies that a coarse particle is heated up to the same extent as a fine particle due to the fact, that the dwell time of a coarse particle is greater.

According to Houben [2], the next conditions to obtain a well heated particle have to be fulfilled:

$$t_{dw} \geq t_{hs} \geq t_{ha}$$

The next table shows $t_{ha}$ and $t_{hs}$ of zirconia as a function of the particle radius.

Table 1
Heat absorption time and heat supply time for $ZrO_2$ particles with diameters between 22 and 45 $\mu$m.

| radius [$\mu$m] | $t_{ha}$ [s] | $t_{hs}$ [s] |
|---|---|---|
| 11 | 5.9E-5 | 3.7E-5 |
| 15 | 1.1E-4 | 6.98E-5 |
| 19 | 1.8E-4 | 1.12E-4 |
| 22.5 | 2.5E-4 | 1.57E-4 |

$a_p$=6.2E-7, $\lambda_p$=1.5, $\lambda_g$=0.8, $T_g$=10500, $T_{p,0}$=293, $T_p$=3000

This table shows that the condition $t_{ha} < t_{hs}$ for the above particle sizes is not fulfilled. This is caused by the fact that $ZrO_2$ has a very low thermal conductivity. For this reason, $ZrO_2$ is a difficult material to heat up thoroughly. If, however, the dwell time is sufficient, totally melting of the particles will occur. This will be pointed out more thoroughly in paragraph 3.1.3.

**2.2 Equipment**
The plasma torch, which has been used during the experiments for the characterisation of zirconia particles, was developed within the thermal

spraying group of Eindhoven University of Technology. It can be equipped with different types of anode channels or nozzles.[3]
During the research programme, the torch was equipped with three types of anode channels: a standard nozzle and two extended ones with extensions of 20 and 120 mm respectively. These nozzles are schematically shown in figure 2.1.

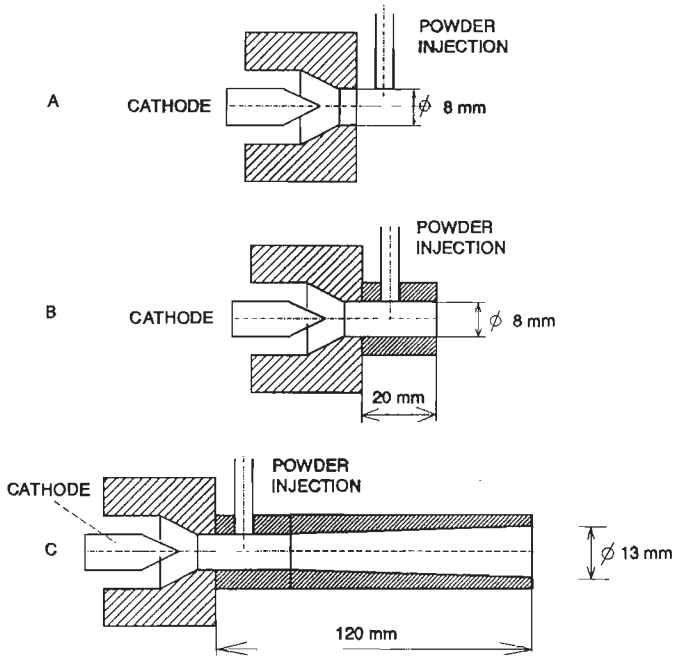


**Figure 2.1** Different types of anode channels, used during the research programme. Powder injection takes place into the nozzle at the extended anode channels.

The standard nozzle and the 20 mm one were used for both spraying of ceramic coatings and the production of single particle splashes.
The 120 mm extended nozzle was only used for the investigation of the interaction of single zirconia particles with the plasma and the substrate. A narrow duct with a length of 120 mm is not suitable for a long lasting block free transport of heated spray particles.

The use of an extended nozzle resulted in an increase of the length of the plasma, produced by the plasma torch. When the 20 mm extension was used, the length of the plasma increased by 22 mm and ranged from 67-72 mm,

depending on the $H_2$ content of the plasma. The length of the plasma, using a standard nozzle was 45-50 mm. The application of the 120 mm extended nozzle resulted in a plasma with an overall length of 145 mm.

When the standard nozzle is used, the injection of powder into the plasma, takes place at the nozzle exit, as can be seen in figure 2.1. When extended anode channels are used, powder injection takes place through a hole in the anode channel. (See figure 2.1). In this way, the extra length of the plasma, caused by the application of an extended nozzle, is used to increase the dwell time of the particles.

The spraying distance d is defined as the distance between the powder injection location and the substrate.
The particle jet of the 20 mm extended nozzle is very narrow and shows almost no divergency at the spraying distance of 100 mm.
The influence of the extended nozzles on the velocities, heat contents and morphologies of the $ZrO_2$ particles will be described in paragraphs 3.2.3, 4.3.3 and 5.4.2.

## 3 Particle velocity

When a particle is injected into the plasma flame, it will be accelerated and heated up. The velocity of an impacting particle has a strong influence on the morphology of the deposit [1]. This paragraph contains a theoretical part in which the velocity of a particle is calculated. The second part describes the experimental set up and results of the velocity measurements.

### 3.1 Calculation of particle velocities

The next paragraphs describe a mathematical model, concerning the velocity of particles, accelerated by a gas flow.

#### 3.1.1. Theory

The velocity of a particle with an initial velocity $V_p$ in a gas flow with velocity $V_g$ may be described by equation (3), which is given by Das and Savikumar [4]

$$\frac{dV_p}{dt} = \frac{3}{4}\frac{C_d}{D_p}\frac{\rho_g}{\rho_p}(V_g - V_p)|V_g - V_p| \qquad (3)$$

$V_{p:}$ Velocity particle [m/s]
$V_g$: Velocity gas [m/s]
$C_d$: Drag coefficient particle [-]
$\rho_g$: Density of the gas [kg/m$^3$]
$\rho_p$: Density of the particle [kg/m$^3$]
$D_p$: Diameter particle [m]

The Drag coefficient of a spherical body in a gas flow is given by Vaessen [5]:

$$C_d = \frac{24}{Re}(1+0.1315Re^{(0.82-0.05w)}), \quad w = {}^{10}logRe \qquad (4)$$

$$Re = \frac{\rho_g |V_g - V_p| D_p}{\mu_g} \qquad (5)$$

$\mu_g$: viscosity of the plasma gas [Nsm$^{-2}$]

The velocity of a plasma flame $V_g$ decreases with increasing distance. At the nozzle exit, the maximum velocity is about 500-800 m/s[5,6,7], decreasing to 100-200 m/s at 100 mm distance.
The viscosity $\mu_g$ of the plasma strongly depends on the temperature and the composition of the plasma flame [6].

When $V_g$ and the physical properties of the plasma are known, it is possible to calculate the particle velocity $V_g$ by numerically solving equation 3.

### 3.1.2 Gas velocities

The gas velocities to be used in the next calculations are based on literature values concerning $Ar/H_2$ plasmas [5,6,7]. Because of the fact that these literature values generally concern lower gas flows and input powers, the values used in the calculations must be corrected for the larger gas flows and input powers, used during our research programme.
The plasmas produced with the extended nozzles, don't mix up with the

surrounding air nor diverge, when the plasma is still inside the extended anode channel. The high initial velocity of the plasma flame is therefore maintained in the extended anode channel and starts to decrease when the plasma leaves the channel exit.
The 120 mm extended nozzle has an initial diameter of 8 mm, increasing conically to 13 mm. The gas velocity in this nozzle is simply calculated at he basis of the ratio of the surface areas of the nozzle exit and entrance.
The velocity profiles for the different anode channels are shown in figure 2.2. These values are used for the following calculations.

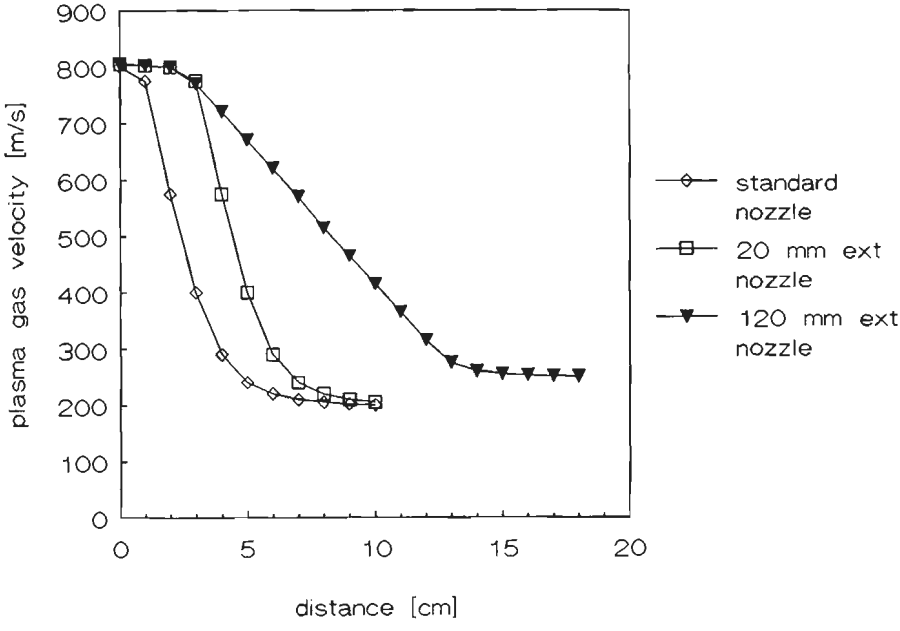


**Figure 2.2** Gas velocities of the plasma, using the standard, the 20 mm and the 120 mm extended anode channel.

### 3.1.3 Results of the calculations of the particle velocities.

The next calculations are based on the situation, schematically shown in figure 2.3. The calculations are valid for particles which are transported along the axis of symmetry of the plasma flame.
Further it is assumed that the particles don't evaporate and keep their original diameter during the transport.
The radial particle injection takes place at 5 mm of the nozzle exit with $V_p = 0$.

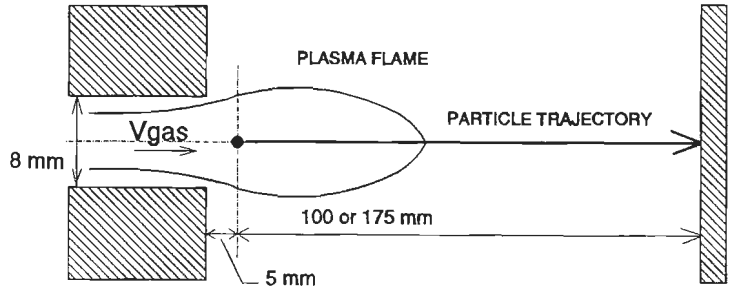


**Figure 2.3** Definitions of the assumptions used for the calculation of the particle velocity.

The viscosity of the plasma flame was taken from literature [6]. Figure 2.4 shows the viscosity of an Ar-$H_2$ plasma as a function of the temperature.In the visible part of the plasma flame (T=12600-9000 K) the viscosity was taken as a constant. (30E-5 $Nsm^{-2}$). The viscosity decrease at plasma temperatures below 9000 K is taken into account by a linear approximation. The visible lengths of the plasmas of the standard and extended anode channels were 48, 70 and 145 mm respectively.

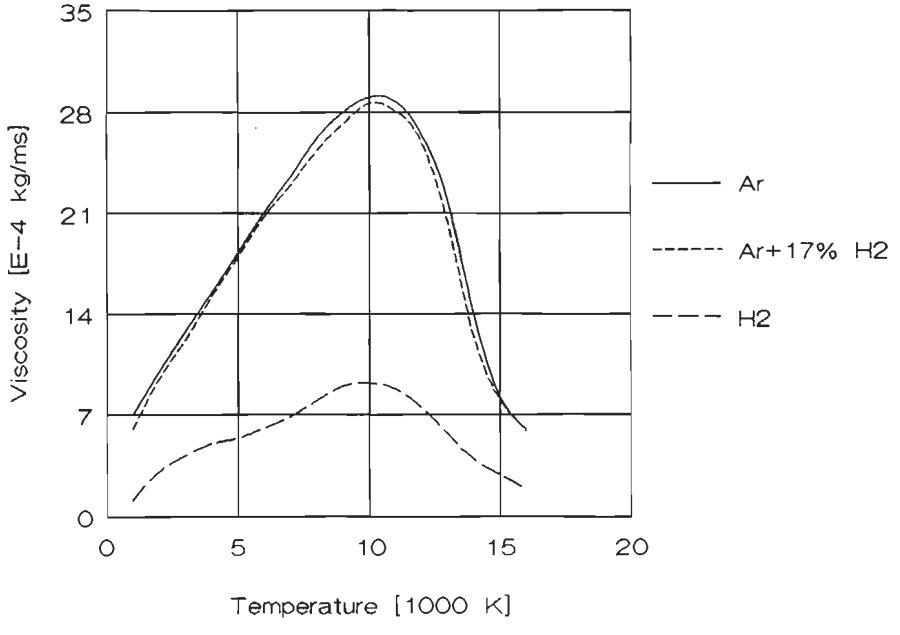


**Figure 2.4** Viscosity of an Ar-$H_2$ plasma as function of the temperature. Redrawn from Vardelle.[6]

The results for a 38 $\mu$m $ZrO_2$ particle, are plotted in figure 2.5.

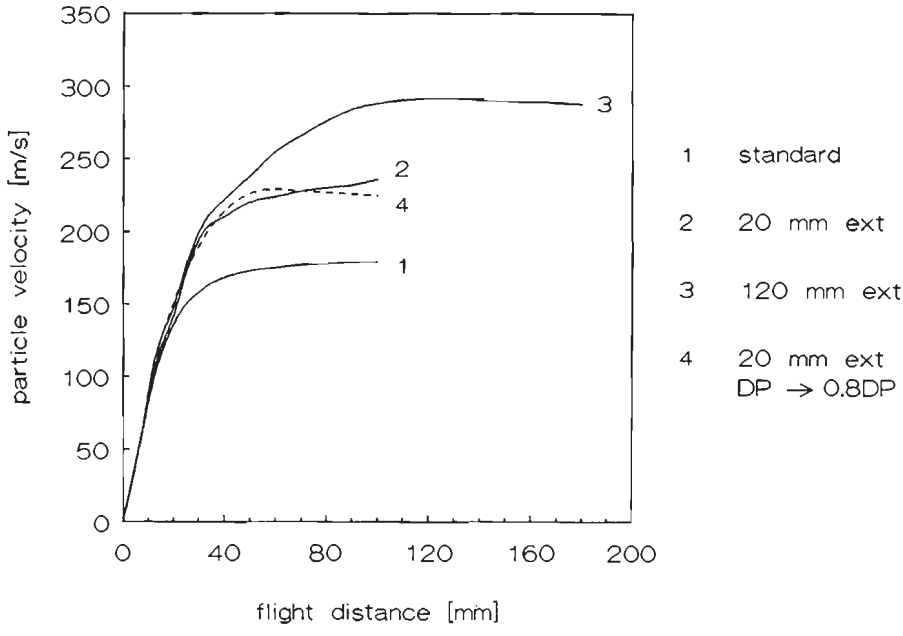


**Figure 2.5** Results of the velocity calculations for the standard (1), the 20 mm extended (2) and the 120 mm extended (3) nozzle. Curve 4 shows the velocity of a particle with an initial diameter of 38 µm. The diameter of this particle decreases due to evaporation to 30 µm.
(Weight loss of 50 %)

### 3.1.4 Discussion

Figure 2.5 shows that the particle velocity is mainly determined by the anode channel type. The ultimate velocity of a particle is mainly determined by the acceleration in the first part of the plasma flame. A high initial gas velocity results in a high particle velocity. The drag forces on the particles are at their maximum in this part of the flame. Because of the fact that the extended nozzles produce a plasma where the high initial gas velocity is maintained over a longer distance, very high particle velocities are the result. Diameter decrease of the particle due to particle evaporation has only a slight influence on the velocity of the particles. In the first part of the plasma, where the highest acceleration takes place, the diameter decrease is low. The dashed line in figure 2.5 represents a particle with an initial diameter of 38 $\mu$m, decreasing linearly to 30 $\mu$m. The volume, and hence the mass decrease amounts 50 %.

The dwell times of 38 $\mu$m particles are stated below. From this table it is clear that the use of an extended anode channel results in an increased dwell time and hence in a smooth temperature distribution throughout the particle. The dwell time is determined as the time a particle stays in the plasma flame.

Table 2.
Dwell times of $ZrO_2$ particles, sprayed with three types of anode channels. The dwell times are given in seconds.

| standard nozzle | 20 mm extended nozzle | 120 mm extended nozzle |
|---|---|---|
| 3.8E-4 | 4.2E-4 | 5.9E-4 |

The calculated dwell times are greater than $t_{hs}$ and $t_{ha}$ which were calculated in paragraph 2.1. The conditions as stated by Houben are thus fulfilled and fully molten particles are likely to be produced.

### 3.2 Particle velocity measurement

The measurements presented in this paragraph are based on a mechanical method for the determination of the velocity of $ZrO_2$ particles. These measurements do not intend to give an absolute value of the velocity of single particles as can be obtained by laser and photographic methods. They will give an indication of the maximum velocity of the particles. The most important goal was to determine the velocities in relationship with the type of anode channel.
The results of the measurements are compared to values, reported in literature, to the theoretical calculations and to measurements made by a photographic method.

#### 3.2.1 Experimental, principle.

The measurements are based on a conventional principle which is shown in figure 2.6.
Two parallel disks, connected to each other by a distance piece, rotate at the same speed. The front disk has two slits, located opposite to each other. When those slits pass the particle jet of the plasma torch, particles are deposited at the rear disk. The deposition takes place at a certain distance

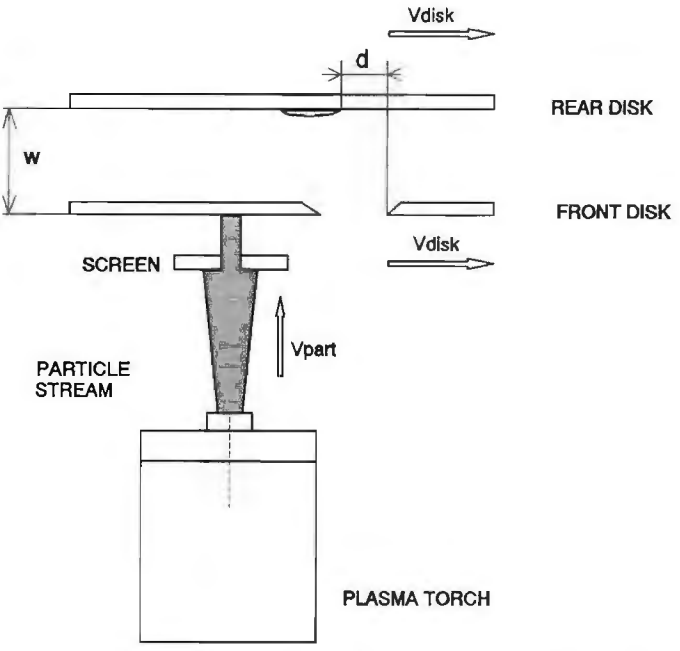


**Figure 2.6** Schematic setup for the determination of the velocity of $ZrO_2$ particles.

from the leading edge of the slit in the front disk, due to the fact that the disks are rotating at the same speed.

The velocity of the particles can now be calculated by the equation

$$V_p = \frac{w}{d} V_{disk}, \quad V_{disk} = \frac{2\pi nr}{60} \tag{6}$$

$V_p$: Particle velocity [m/s]
$V_{disk}$: Rotation velocity of the disk at radius r [m/s]
r: Radius [m]
n: Rotations per minute of the disk
d: Shift of the deposit [m]
w: Distance between the disks [m]

### 3.2.2 Experimental, set up

The disks are made of steel sheet and have diameters of 160 mm. The thicknesses of the rear and the front disk are 2 and 3 mm respectively, to avoid buckling of the front disk caused by the plasma flame and the particle stream. The slits in the front disk are edged (See figure 2.6) to avoid

collisions between the inside of the slit and the particles when they pass the slit. The disks are separated by a distance piece of 20 mm and are mounted on the axis of an AC frequency controlled motor with a maximum rotation speed of 25000 rpm.
The distance between the front disk and the plasma torch is 100 mm. In front of the front disk a masking screen with a 3 mm wide slit is placed. The screen can be moved axially and radially in front of the torch to give way to a certain part of the particle stream. The mobile screen makes it possible to measure velocity differences as a function of the radius of the plasma flame.
The powder size distribution used for the velocity measurement ranged from 38-45 $\mu$m. The plasma spray parameters are listed below.

| | |
|---|---|
| Ar: | 70 Sl/min |
| $H_2$: | 8 Sl/min |
| Current: | 600 Amps |
| Anode : | 8 mm, normal, extended 20 mm and extended 120 mm |
| Powder: | Amperit 825.1, 38-45 $\mu$m |
| Distance: | 100 mm, (175 mm for the 120 mm nozzle). |

Sl means standard litre. References T=293 K, p=1 bar.

### 3.2.3 Results

One half of the particle stream, at one side of the central axis of the plasma flame was divided in 3 and 4 sections respectively for the standard and the extended anode channel. After each cycle, the screen masking screen is shifted over 2 mm. The distance between the leading edge of the slit in the front disk and the first sticking particles on the rear disk are taken as the distance d. These are the fastest particles of that part of the particle jet.

The spraying particles passing the slit (figure 2.6), do not follow a horizontal line. This is caused by the fact that the centre of the particle jet does not coincide with the centre of the nozzle. Furthermore the particles in the outer regions of the particle jet show an additional deviation due to the fact that the particle jet diverges with increasing distance. Therefore the distance d, measured at the rear disk (figure 2.6) has to be corrected. This results in a larger value of d and hence a lower particle velocity.
The results of these measurements are plotted in figure 2.7.

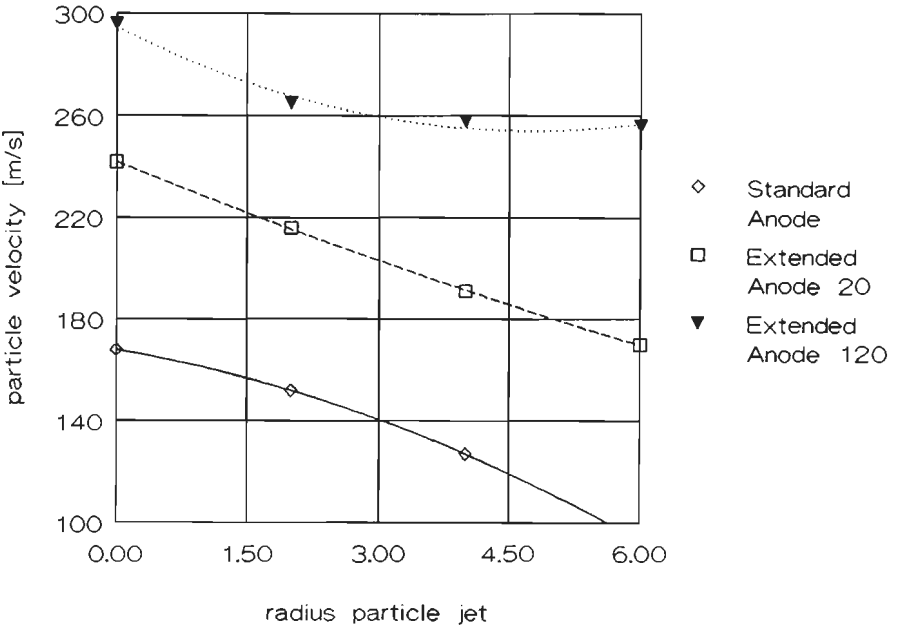


**Figure 2.7** Results of the velocity measurements, using the standard, 20 mm extended and 120 mm extended nozzle. Particle size 38-45 μm.

From this figure it can be learned that the maximum velocity of the particles sprayed with an extended anode channel is about 70 m/s higher than the particles sprayed with a standard anode. Secondly, the velocity difference between the particles in the centre of the jet and the particles in the outer part is less than with the standard anode. The particles sprayed with the 120 mm extended anode channel show a maximum velocity of 300 m/s.

### 3.2.4 Comparison of the measured values

The values measured with the disk method are compared to literature results, numerical calculations, a photographic method, and a laser based time-of-flight measurement method.

Roumilhac [8] reports about velocity measurements of $ZrO_2$ particles in the size range from 22.5-45 μm, sprayed with an anode of 8 mm and a plasma gas composition of 75 Sl/min Ar and 15 Sl/min $H_2$. The velocity of the particles at 100 mm from the nozzle is about 210 m/s . Although it is not evident from the text, it has to be assumed that these values concern the small particles.

Comparison of the disk method to a photographic method was carried out using molybdenum instead of $ZrO_2$. This because of the fact, that the velocity of Mo, measured with a photographic method, was well known and measured in our own laboratory [9]. The experiments could be repeated easily, using the disk instead of the photographic method. This resulted in almost the same values, 100 m/s with the photographical method and 105 m/s with the disk method.

The measured velocities agreed with the values calculated in paragraph 3.1.3. (Compare the calculated final velocities in figure 5 with the measured velocities in figure 2.7) The assumption that the gas velocity of the plasma in the extended nozzle keeps its high initial value has therefore proved to be correct.

The gas velocities of the plasma flames at the nozzle exit, which were reported on in literature and which were used for the calculations of the particle velocities, were measured on plasma torches which were not identical to the torch that was used during our research project. Since the characteristics of the different torches are not similar, the plasma gas velocities may differ even if the gas flows and input powers were equal.
A provisional test set up was used to determine the mean velocity of the plasma gasses.[15] The method was based on the measurement of the reaction force of the plasma torch, caused by the momentum transfer of the high-velocity plasma flame. The plasma torch was placed in a pendulum-like rig which was equipped with a sensitive force transducer (0 to 5 N). Due to its construction, friction forces in the rig could be neglected. The reaction force which is measured is given by the equation:

$$F=\dot{m}V_{gas}$$

F: reaction force [N]
$\dot{m}$: gas flow [kg/s]
$V_{gas}$: gas velocity [m/s]

Since the gas flows are exactly known, the mean gas velocity at the nozzle's exit can be calculated. The next table gives the results of the first, provisional measurements, carried out on a plasma torch equipped with a standard anode channel.

Table 3
Gas velocities at the nozzle exit, determined by the measurement of the reaction forces of the plasma torch

| reaction force [N] | gas flow [kg/s] | velocity [m/s] |
|---|---|---|
| 1.462-1.494 | 2.089E-3 | 700-715 |
| 1.595-1.606 | 2.099E-3 | 760-765 |

The table shows that the mean gas velocities range from 700 to 765 m/s for gas flows of $Ar/H_2$ of 70/8 and 70/15 respectively. This agrees well with the velocities which were used for the calculation of the particle velocities.

The laser based time-of-flight method was developed by Houben and the central construction service of the Eindhoven University of Technology [10] and is still in an experimental stage. Because of this, the method was used for only one measurement at the 20 mm extended anode channel.
The method is based on the following principle. When a particle crosses a

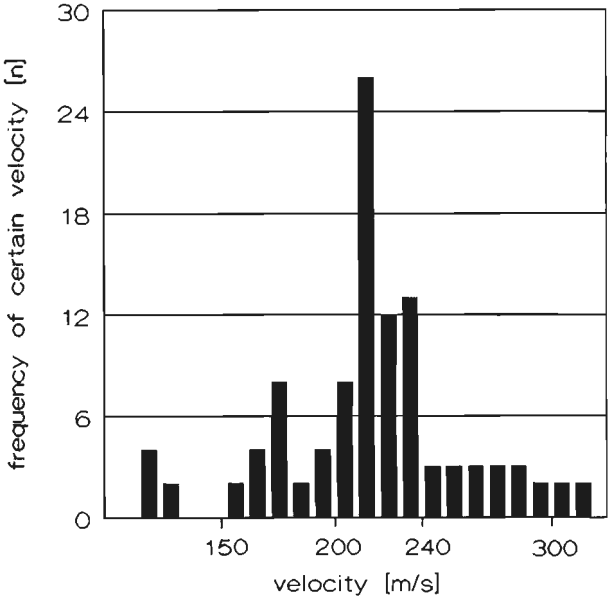


**Figure 2.8** Results of the velocity measurements using a laser based time of flight method. The particles were sprayed using a 20 mm extended nozzle.

laser beam, a counter is started. When this same particle crosses a second laser beam at little distance from the first one, the counter is stopped. From the number of counts the particle velocity can be calculated.
The time of flight measurement proved that the maximum velocity of the particles was about 240 m/s, and that the majority of the particles possessed velocities between 200 and 240 m/s. (See figure 2.8)

## 4 Measurement of the heat content of plasma sprayed zirconia-yttria particles

### 4.1 Introduction

After a powder particle is injected in the plasma flame, it is accelerated and heated up. The time that a particle stays in the plasma flame, the so called dwell time, must be long enough to melt the whole particle. The particle will not be fully molten when this dwell time is too short. One will obtain a particle with a molten outer shell and a solid core. When this particle impacts on the substrate, the unmolten core may be reflected by the substrate resulting in a very low deposition efficiency. For this reason it is necessary that the whole particle has reached the melting temperature, before it collides with the substrate.
It is possible to determine the mean temperature of the particles by means of a heat content measurement. The principles of this measurement and the experimental results will be discussed in the next paragraphs.

### 4.2 Theory

The heat content of a material at a certain temperature, compared to a reference temperature, is defined by equation 7:

$$H(T=T_a)=\int_{T=273.15}^{T_m} C_p(T)dT+L+\int_{T_m}^{T_a} C_{pm}(T)dT \qquad (7)$$

H: Enthalpy [kJ/kg]
$T_m$: Melting temperature [K]
$C_p$: Specific heat at constant pressure [kJ/kg/K]
L: Latent Heat [kJ/kg]
$C_{pm}$: Specific heat of the liquid material at constant pressure [kJ/kg/K]

When the enthalpy of a material can be measured and all its physical properties as mentioned in equation 7 are known, it is possible to calculate the mean temperature of the material.

The calculation of the enthalpy-versus-Temperature curve of zirconia/yttria is based on $C_p$-values available in literature. Because the $C_p$ values of zirconia and yttria are almost equal, the values for $ZrO_2$ were taken as standard.

The enthalpy curve of zirconia had to be composed of several parts because the literature does not give Cp values, covering the whole temperature range from 298 K to 3500 K. The enthalpy curve is given in figure 2.9.

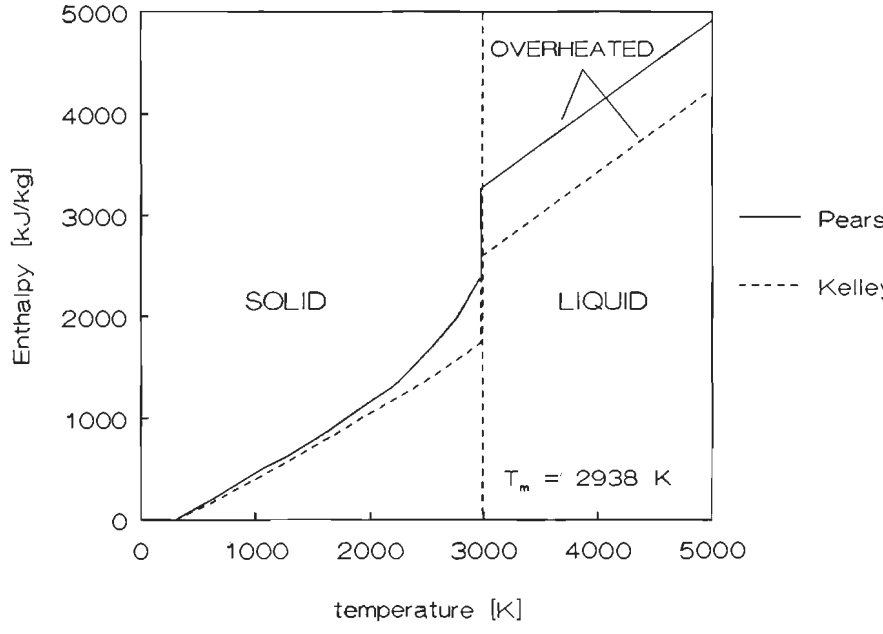


**Figure 2.9** Enthalpy curve of $ZrO_2$, based on values reported in literature.

For the temperature range up to 1700 K, two almost similar $C_p$ curves were available, reported by Kelley and Pears [11]. Above 1700 K the Pears data increased stronger than the Kelley data. According to Schick [11], the Kelley data have to be regarded as the most reliable, so these data are backing the calculations.

Kelley reports only values up to 1850 K. They can be extrapolated to 2000 K, without making great mistakes [11]. Above 2000 K the Cp can be described by the next equation [11]:

$$C_p = 0.006372 * T + 5.056 \qquad [cal\ mole^{-1}K^{-1}]$$

The heat of fusion (L) is 25 kcal/mole = 849.6 kJ/kg [11]
The $C_p$ value of liquid $ZrO_2$ is 815.6 J/kg/K [11]

### 4.3 Experimental

Two methods were used to determine the enthalpy of the plasma sprayed zirconia particles; the metal strip method as described by Houben for metals [1], and the water calorimetric method, specially suited for ceramics.

#### 4.3.1. The metal strip method

Figure 2.10 shows the experimental set up for the metal strip method.

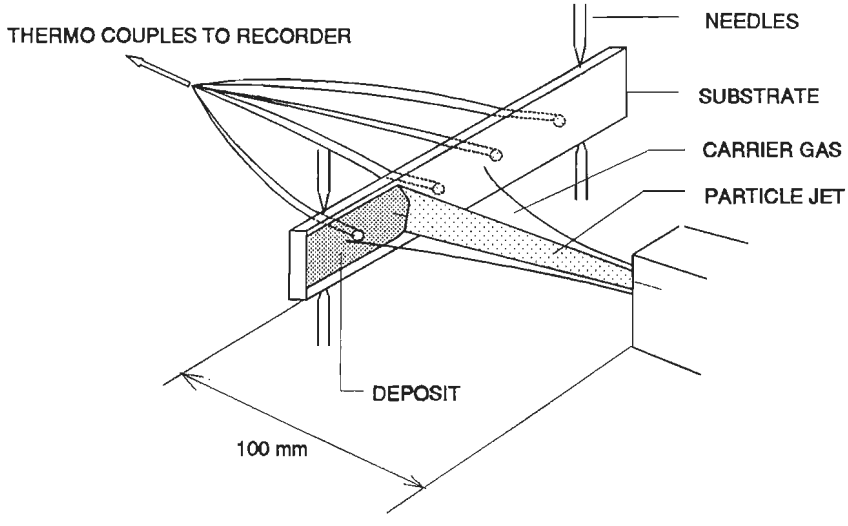


**Figure 2.10** Metal strip method for the determination of the heat content of plasma sprayed particles. The metal strip is clamped by needles to avoid heat transfer to the strip holder.

A thin metallic strip of pure iron (Armco) which has well known physical properties and a precisely determined weight is mounted in a holder. The strip is clamped by thin needles so that there exists almost no thermal contact between strip and holder. The temperature of the strip is measured by six thermocouples, which are spot welded to the backside of the strip. The measurement was carried out in the following way.
The strip was heated up by the plasma torch, without injecting powder. The

temperature increase due to the plasma gases was determined in this way. After cooling the strip down to room temperature it is heated up again, but now with powder injection. The temperature increase is measured again. After the spraying, the strip was weighed and the weight increase due to deposited coating material was determined. The enthalpy $H_d$ of the particles was then calculated by using the formula:

$$H_d = \frac{m_s C_s}{m_d} * (\Delta T_2 - \Delta T_1) + C_d * \Delta T_2 \qquad (8)$$

$H_{d:}$ Enthalpy of the particles [kJ/kg]
$m_{s:}$ Substrate mass [kg]
$C_{s:}$ Substrate heat capacity [J/kg/K]
$m_{d:}$ Deposited particles mass [kg]
$C_{d:}$ Particles heat capacity [J/kg/K]
$\Delta T_{1:}$ Temperature raise of strip due to plasma
$\Delta T_{2:}$ Temperature raise of strip due to particles and plasma

When using this method, the following assumptions have to be made:

1 All the thermal energy of the deposited particles is released by conduction to the substrate. Heat losses from the test piece due to radiation and convection are negligible.

2 The influence of the injected particles on the temperature of the plasma gases is negligible.

3 The $C_p$ values of the coating and the substrate material are constant in the temperature field used.

The experiments however, proved that this method was not suitable for the enthalpy determination of $ZrO_2$. Unmolten particles showed a higher enthalpy than fully melted particles. Reasons for this discrepancy are: particles which are not fully molten are reflected by the substrate, but during the collision there is a transfer of thermal energy from the particles to the substrate. Fused $ZrO_2$ particles have a temperature of about 3000 K, together with a very low thermal conductivity. So the thermal energy of the particles is not only released by conduction, but also by radiation and

convection. Although the strip method has proven to be successful for a lot of metallic spraying materials, it is less appropriate for a ceramic material as zirconia.

### 4.3.2 The water calorimetric method

To encounter the problems mentioned above, an other method to determine the enthalpy of zirconia particles was applied.
Instead of spraying on a metal strip, the particles were sprayed into water. The temperature rise of the water was measured and the enthalpy could be calculated. Figure 2.11 shows the schematic set up of this method.

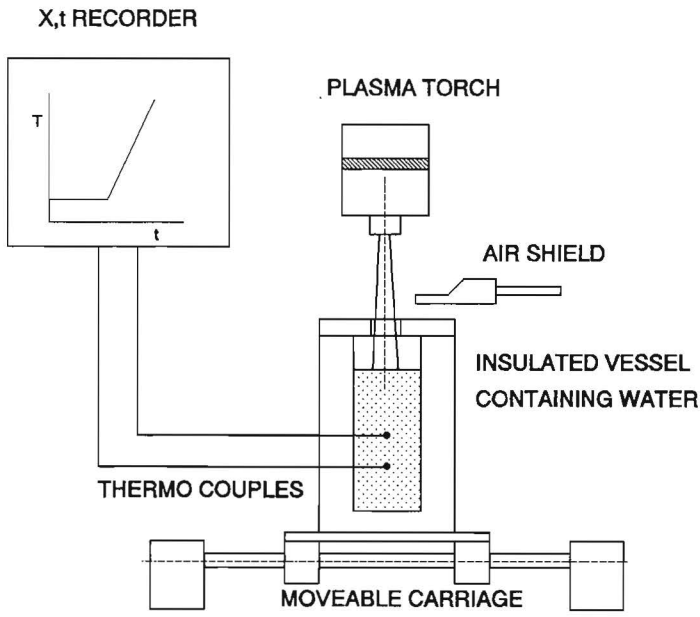


**Figure 2.11** Schematic setup of the water-calorimetric method for the determination of the enthalpy of $ZrO_2$ particles. The plasma gasses are blown away by an air shield.

The set up consists of a thermally insulated vessel with a heat resistant lid. This lid has a hole through which the particles can be sprayed into the water. The temperature of the water is measured by thermocouples.
To prevent the plasma from blowing the water out of the vessel, the gases are blown away side ways by an airshield, mounted just above the vessel.
The spraying distance, is kept at 110 mm for a standard anode channel and at 125 mm for an extended anode channel. These distances were for the two

types of anodes the shortest ones at which no water was blown out of the vessel.

The procedure of this measurement was carried out in the following way. The vessel was filled up with a precise amount of water.

To determine the influence of the plasma flame on the temperature raise of the water, the water was heated up for 3 minutes. After that the vessel is weighed and the water loss due to evaporation can be calculated. The temperature increase due to the plasma flame was only slight and varied from 1 to 5 K. The water loss due to evaporation varied between 0.7 en 4 grams in three minutes.

The enthalpy transfer from the plasma flame to the water containing vessel can now be calculated using the next equation:

$$E_{pl}=(m_w-m_{wpl})C_{p_w}(T_1-T_0)+m_{wpl}(T_b-T_0)C_{p_w}+m_{wpl}E_v+C_{vessel}(T_1-T_0) \qquad (9)$$

| | |
|---|---|
| $m_w$: | Water mass [kg] |
| $m_{wpl}$: | Water loss due to evaporation by plasma flame [kg] |
| $C_{pw}$: | Water specific heat 4180 [J/kg/K] |
| $T_1$, $T_0$: | Temperatures in [K], see figure 2.12. |
| $T_b$: | Water boiling point (393 K) |
| $E_v$: | Water heat of evaporation 22.6E5 [J/kg] |
| $C_{vessel}$: | Vessel heat capacity [J/K] |

The enthalpy transfer of the plasma flame plus the spray particles is given by equation 10:

$$E_{pl+p}=(m_w-m_{wpl}-m_{wpl+p})C_{pw}(T_2-T_1)+m_{wpl+p}C_{pw}(T_b-T_1)+m_{wpl+p}E_v+C_{vessel}(T_2-T_1) \qquad (10)$$

| | |
|---|---|
| $m_{wpl+p}$: | water loss due to the heat transfer of the plasma flame and the spray particles [kg] |
| $T_2$: | water temperature succeeding the powder spraying, see figure 2.12. |

The heat content of the particles can now be calculated using equation 11:

$$H_{particles} = \frac{E_{pl+p} - E_{pl}}{m_{part}} \qquad (11)$$

$H_{particles}$: Enthalpy of the spray particles [J/kg]
$m_{part}$: Mass of the spray particles [kg]

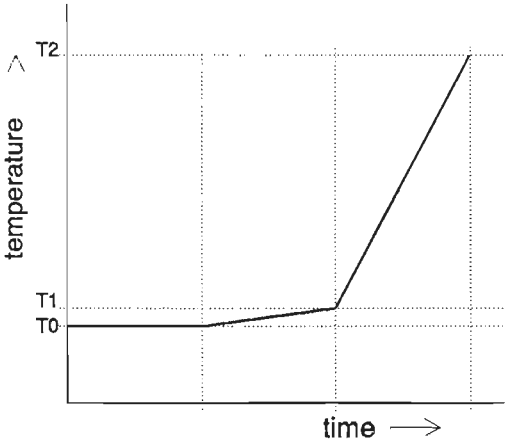


**Figure 2.12** Temperature development during the water-calorimetric method. From $T_0$ to $T_1$, the water is heated up only by the plasma gasses. From $T_1$ to $T_2$ it is heated up by the particles and plasma gasses.

### 4.3.3 Results of the measurements

The enthalpies of the $ZrO_2$ particles, sprayed with different plasma gas flows and the standard and the extended anode channel are listed in table 4.

From the heat transfer values, listed in this table it can be concluded that the particles sprayed with an extended anode channel but with the same gas flow as used with the standard nozzle, possess a higher enthalpy and hence a higher temperature. Figure 2.13 (page 44) shows the enthalpy curve of $ZrO_2$ once again. The results of the heat transfer measurements are indicated in this figure.

The particles, sprayed with a standard anode channel and a gas flow of $Ar/H_2$ of 70/8 [Sl/min], are just below the transition point from the melting line to the overheating line. When the powder, sprayed under the mentioned conditions, was investigated by electron microscopy, it was shown that especially the coarse particles, were not fully molten. When the plasma only contained Ar ($H_2$ = 0), the particles had a very low enthalpy, just on the transition point from the solid curve to the melting curve.

Table 4.
Heat transfers of the $ZrO_2$ particles sprayed with different gas flows and anode channels

| number | Anode channel | Argon [Sl/min] | Hydrogen [Sl/min] | Heat transfer of $ZrO_2$ to the water [kJ/kg] |
|---|---|---|---|---|
| 1 | standard | 70 | 8 | 2495 |
| 2 | | 70 | 15 | 2770 |
| 3 | | 70 | 20 | 3200 |
| 4 | extended 20 | 70 | 5 | 2914 |
| 5 | | 70 | 10 | 3174 |
| 6 | | 70 | 15 | 3300 |
| 7 | | 70 | 20 | 3780 |
| 8 | extend 120 | 70 | 0 | 1886 |
| 9 | | 70 | 15 | 3960 |

The powder particles sprayed with this setting, showed the same angular shape as the unsprayed material. From this it may be concluded that hardly any melting of the particles occurred. $H_2$ increases the thermal conductivity of the plasma [7]. This results in a reduction of the heat supply time $t_{hs}$. For this reason, the time a particle needs to be heated up to a certain mean temperature, is reduced. When the dwell time is constant, a higher thermal conductivity of the gas will result in a higher particle temperature.

The particles sprayed with the 120 mm extended anode channel showed a very high enthalpy, caused by the conjugated long plasma of 145 mm. The particles are strongly overheated and reach almost the boiling point of $ZrO_2$. This may lead to evaporation of the particles.
Due to the long dwell time, the momentum transfer (read particle velocity) and the heat transfer from the plasma to the particles (read particle

temperature) are more intensive than in the case of the 20 mm extended nozzle.

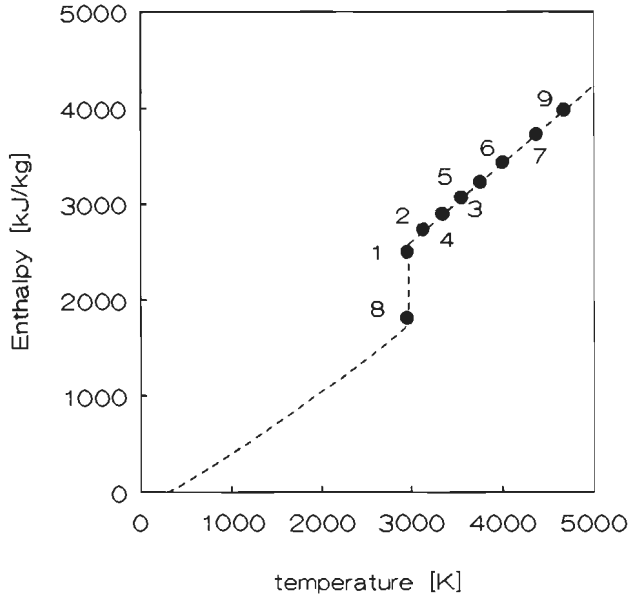


**Figure 2.13** Enthalpy curve based on Kelley data. The different measured enthalpy values of $ZrO_2$ particles are depicted in this curve. The numbers correspond with the numbers in table 4.

### 4.3.4. Conclusions

The water calorimetric method for the determination of the heat content of $ZrO_2$ particles has proven to be a very useful one. The obtained results using this method agreed with the enthalpies for the physical state of $ZrO_2$, as predicted by the enthalpy curve based on literature data.

The heat content and the corresponding physical state of the sprayed particles agreed well with the enthalpy curve based on the Kelley data. Because of this it may be concluded that the values reported by Kelley are the most accurate to describe the enthalpy of zirconia.

The $H_2$ content of the plasma gases has a great influence on the melting degree of the particles. The use of a standard anode channel with less than 8 Sl/min hydrogen does not produce completely molten particles.

The use of an extended anode channel results in particles with both a higher enthalpy and a higher velocity, compared to the particles sprayed with a

standard anode channel.

## 5 Single particle collisions

### 5.1 Introduction

The foregoing paragraphs gave insight into the velocity and heat content of $ZrO_2$ particles, which were determined as a function of the plasma-spray parameters and the type of anode channel. The collision behaviour of the single $ZrO_2$ particles will be described in the following paragraphs.

First a mathematical model describing the solidification of $ZrO_2$ particles on different substrate materials is given.
This will be followed by the results of collision experiments of $ZrO_2$ particles on different substrate materials. The adhesion mechanism of $ZrO_2$ on Fe will be described.
Furthermore, the influence of the plasma spray parameters on the morphology of the splashed $ZrO_2$ particles is described.

### 5.2 Solidification of $ZrO_2$ particles on different substrate materials

The thermal phenomena of the solidification of $ZrO_2$ particles on several substrate materials, with different physical properties, is described in this paragraph.
The mathematical model, used for the calculation of the solidification times and temperature profiles in the substrate and the deposit, are given by Carslaw and Jaeger [12], Kuypers and Zaat [13], Houben [1] and 't Hart [14]. The system to be considered is shown in figure 2.14.

A liquid deposit with initial temperature $T_m$ is in contact with a substrate with initial temperature $T_{so}$. At $t>o$, the solidification process starts and a solidification front with x-coordinate $x = X(t)$, is moving into the liquid deposit.

It is assumed that the velocity, at which the particle spreads out after the impact on the substrate, is an order of magnitude higher than the solidification velocity of the particles. Because of this it is allowed to consider the solidification of the particles after they spread out to disk

shaped deposits.

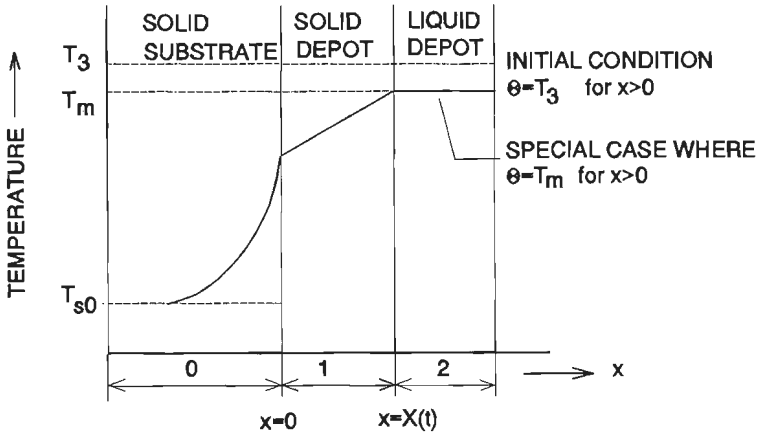


**Figure 2.14** Model for the solidification of particles with initial temperature $T_m$ on a substrate with temperature $T_0$. Redrawn from [1]

Furthermore, the next assumptions have to be made:

- The liquid deposit has a uniform temperature $T_m$;
- There exist no supercooling or pressure dependent effects in the contact area.
- Melting effects of the substrate materials have to be neglected.

The system shown in figure 2.14, now may be described by the next boundary conditions and equations.

We assume that the deposit has an initial temperature equalling the melting temperature $T_m$.

$$\text{for } t=0 \text{ and } x<0 \quad \theta_0 = T_{so}; \quad \text{for } t=0 \text{ and } x>0 \quad \theta_2 = T_m. \tag{12}$$

Equations for heat conduction

$$\frac{\delta^2\theta_0}{\delta x^2} - \frac{1}{a_0}\frac{\delta\theta_0}{\delta_t} = 0, \qquad x \leq 0 \tag{13}$$

$$\frac{\delta^2\theta_1}{\delta x^2}-\frac{1}{a_1}\frac{\delta\theta_1}{\delta t}=0, \qquad 0\le x\le X(t) \tag{14}$$

Boundary Conditions

$$\theta_0=T_{s0} \qquad as\ x\to-\infty \tag{15}$$

$$\theta_0=\theta_1 \qquad as\ x=0 \tag{16}$$

$$\lambda_0\frac{\delta\theta_0}{\delta x}=\lambda_1\frac{\delta\theta_1}{\delta x} \qquad as\ \ x=0 \tag{17}$$

$$\lambda_1\frac{\delta\theta_0}{\delta x}=L\rho\frac{\delta X}{\delta t} \qquad as\ x=X(t) \tag{18}$$

$$\theta_1=\theta_2=T_m \qquad as\ x\ge X(t) \tag{19}$$

The solutions for these equations are given below. The derivations of these equations can be found in appendix A.

The temperature profile in the substrate now becomes:

$$\frac{\theta_0-T_{s0}}{T_m-T_{s0}}=\frac{B}{B+erfp}\left(1+erf\frac{x}{\sqrt{4a_0t}}\right) \tag{20}$$

The temperature profiles in the deposit:

$$\frac{\theta_1-T_{s0}}{T_m-T_{s0}}=\frac{1}{B+erf\ p}\left(B+erf\frac{X}{\sqrt{4a_1t}}\right) \tag{21}$$

p: Neumann's constant, see appendix A

These two equations strictly hold for two semi-infinite bodies. But, they describe exactly the solidification of a liquid deposit on a solid substrate. Because of that the equations are valuable during the solidification time $t_{sol.}$

The solidification time $t_{sol}$ now can be calculated, using Neumann's assumption:

$$X=p\sqrt{4a_1 t} \tag{22}$$

$$t_{sol}=\frac{X^2}{4a_1 p^2} \tag{23}$$

### 5.2.1 Results of the calculations for $ZrO_2$ deposits on different substrate materials

The solidification times of $ZrO_2$ particles on different substrate materials were calculated using the equations described in the foregoing paragraph.

Table 5 shows the physical properties of the different substrate materials, together with the constants needed for the calculation of the temperature fields and the solidification times.

Table 5
Values needed for the calculation of the temperature fields and solidification times.

| substrate | λ | ρ | c | √(λρc) | B |
|---|---|---|---|---|---|
| Fe | 75 | 7880 | 460 | 16477.7 | 0.114787 |
| W | 147 | 19350 | 138 | 19812.5 | 0.095466 |
| Mo | 146 | 10200 | 255 | 19487.1 | 0.097061 |
| Hast X | 9.7 | 8220 | 486 | 6225 | 0.30384 |
| AISI 316 | 18 | 7670 | 489 | 8216.5 | 0.2303 |
| $ZrO_2$ | 1.5 | 5000 | 477 | 1891.4 | 1 |
| Al | 205 | 2700 | 900 | 22319.3 | 0.084744 |
| Cu | 385 | 8960 | 385 | 36443.1 | 0.0519 |

| Q | p | erf p | a | $\sqrt{(a_{1/a}0)}$ | $T_c$ [K] |
|---|---|---|---|---|---|
| 0.83783 | 0.679077 | 0.6631263 | 2.07171E-5 | 0.1742356 | 683 |
| 0.83783 | 0.685791 | 0.667882 | 5.50499E-5 | 0.1068866 | 623 |
| 0.83783 | 0.6852417 | 0.6674941 | 5.613226E-5 | 0.1058511 | 630 |
| 0.83783 | 0.6190796 | 0.6187043 | 2.42808E-6 | 0.508944 | 1164 |
| 0.83783 | 0.64136 | 0.6356 | 4.7992E-6 | 0.3620071 | 996 |
| 0.83783 | 0.4580689 | 0.4828908 | 6.28931E-7 | 1 | 2077 |
| 0.83783 | 0.6895752 | 0.6705428 | 8.43621E-5 | 0.08634313 | 589.8 |
| 0.83783 | 0.701294 | 0.6786956 | 1.11607E-4 | 0.075068 | 481 |

The solidification times on the different substrate materials are given in figure 2.15.

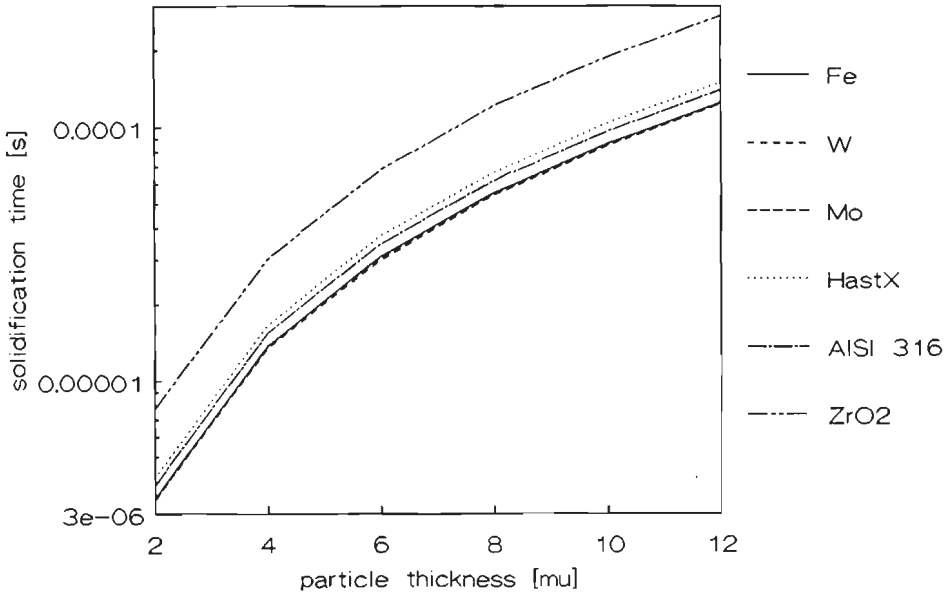


**Figure 2.15** Solidification times of $ZrO_2$ particles on different types of substrate materials. The thickness of the splashed particles ranges from 2 to 12 μm.

This figure shows that the solidification time of $ZrO_2$ on $ZrO_2$ is almost twice the solidification time on Fe.

The contact temperature of $ZrO_2$ particles on various substrate materials is

shown in figure 2.16. It can be seen that the contact-temperature between $ZrO_2$ and Fe, W and Mo is rather low, varying between 623 K and 683 K (350 - 410 °C). The contact temperatures between $ZrO_2$ and AISI 316 and Hastelloy X are respectively 996 K and 1164 K (723 and 891 °C). $ZrO_2$ on $ZrO_2$ shows a contact-temperature of 2077 K (1804° C).

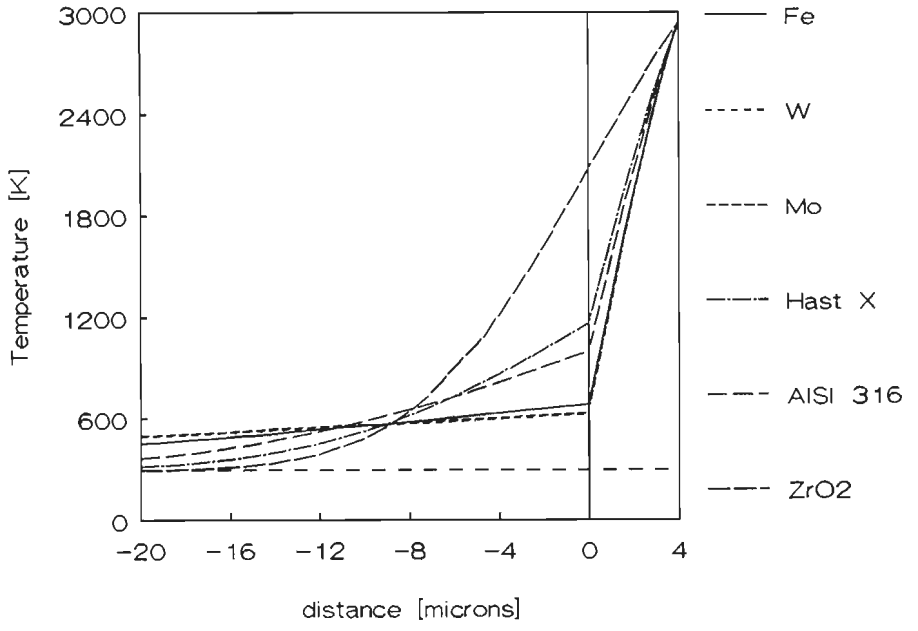


**Figure 2.16** Contact temperature of solidifying $ZrO_2$ particles on different substrate materials.

### 5.2.2. Results of the calculations for $ZrO_2$ deposits on a $ZrO_2$ substrate

During the coating process, the temperature of both the coating and the substrate will increase. Following particles will collide and solidify on a preheated surface. During the plasma spraying of $ZrO_2$ coatings, surface temperatures of the coating up to 600 °C were measured.
In this paragraph the results of the calculations of the solidification of $ZrO_2$ particles on a $ZrO_2$ substrate with temperatures, varying from 100 to 1000 °C, are presented.

The solidification times of $ZrO_2$ particles of thicknesses ranging from 2 - 12 $\mu$m on $ZrO_2$ substrates with temperatures ranging from 100° C to 1000° C are shown in table 6.

Table 6
Solidification times [s] of $ZrO_2$ particles on zirconia substrates with temperatures ranging from 20 to 1000 °C.
Particle thicknesses: 2 to 12 $\mu$m.

| | 293 [K] | 473 | 673 | 873 | 1073 | 1273 |
|---|---|---|---|---|---|---|
| | 20 [C] | 200 | 400 | 600 | 800 | 1000 |
| 2 | 7.58E-6 | 8.24E-6 | 9.13E-6 | 1.03E-5 | 1.17E-5 | 1.36E-5 |
| 4 | 3.03E-5 | 3.3E-5 | 3.65E-5 | 4.1E-5 | 4.68E-5 | 5.43E-5 |
| 6 | 6.82E-5 | 7.42E-5 | 8.22E-5 | 9.22E-5 | 1.05E-4 | 1.22E-4 |
| 8 | 1.21E-4 | 1.32E-4 | 1.46E-6 | 1.64E-4 | 1.87E-4 | 2.17E-4 |
| 10 | 1.89E-4 | 2.06E-4 | 2.28E-4 | 2.56E-4 | 2.92E-4 | 3.4E-4 |
| 12 | 2.73E-4 | 2.97E-4 | 3.29E-4 | 3.69E-4 | 4.21E-4 | 4.89E-4 |

The solidification time increases with 35% when the substrate temperature increases from 293 to 873 K.

Figure 2.17 shows the calculated contact temperature between the solidifying particles and the $ZrO_2$ substrate in relationship to the substrate temperature. The calculated contact temperature in conjugation with a substrate temperature of 873 K (600 °C) is 2325 K (2052 °C).

This makes clear that an increase of the substrate temperature also leads to a higher contact temperature. The increase of the contact temperature, however, is less than the increase in substrate temperature.

### 5.2.3 Conclusions

From the foregoing calculations it can be concluded that the solidification times are mainly determined by the physical properties of the substrate materials. The solidification time on Fe is almost twice as short as on a $ZrO_2$ substrate.

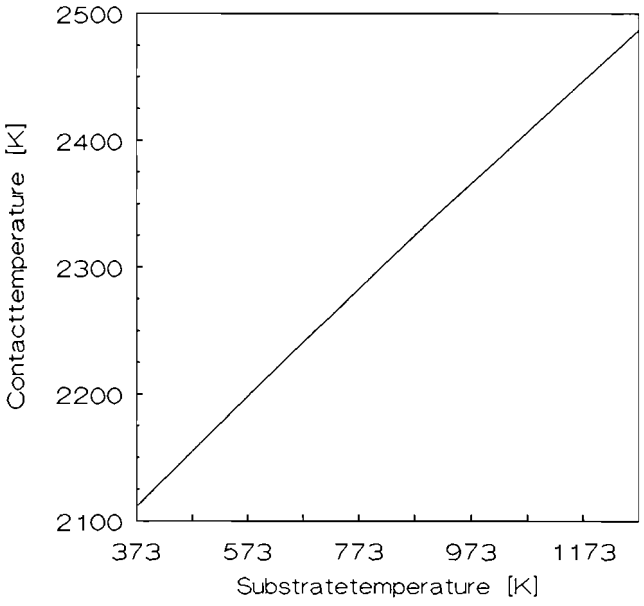


**Figure 2.17** Contact temperature of solidifying $ZrO_2$ particles on $ZrO_2$ substrates. The substrate temperature ranges from 20 to 1000 °C.

Although $ZrO_2$ has an elevated melting point, the contact temperature between $ZrO_2$ and the metallic substrates is low. This is mainly caused by the low thermal conductivity of $ZrO_2$.
The heat release per unit of time of the solidifying $ZrO_2$ is low and is immediately transported by the good conducting metal substrate, resulting in a low contact temperature.

The contact temperatures of the various substrate materials differ strongly. The metallic substrates with a high thermal conductivity, Fe, W and Mo, show a very low contact temperature, ranging from 623 - 680 K. The contact temperature between $ZrO_2$ and the substrate materials Hastelloy X and AISI 316 is higher, because of the fact that these materials posses a lower thermal conductivity. Figure 2.18 shows the contact temperature as a function of the thermal diffusivity $a=\lambda/(\rho c)$ of the various substrate materials.

An increase in substrate temperature of the $ZrO_2$ substrate leads to an increase in solidification time of the $ZrO_2$ particles.

The results of these calculations are used in the experiments which are

described in the following paragraph.

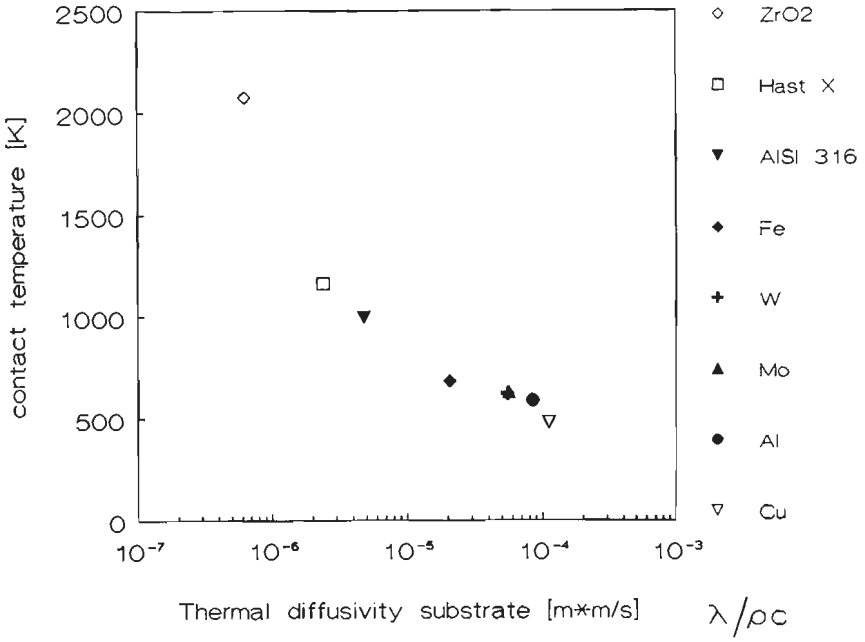


**Figure 2.18** Contact temperature of solidifying $ZrO_2$ particles versus the thermal diffusivity of different substrate materials.

### 5.3 Experimental

In this paragraph the experiments which were carried out to investigate the deposition behaviour of single $ZrO_2$ particles, are reported on.
The collision behaviour on different substrate materials, as well as the influence of different plasma spray parameters and the use of a special type of anode channel will be described.

#### 5.3.1 Single particle collisions, experimental set up

In order to determine the collision behaviour of single $ZrO_2$ particles, it is necessary to catch a few representative particles from the particle jet. This could be obtained by the use of the experimental equipment which is shown in figure 2.19. A pendulum, with a length of 60 cm, rotates on a stand which is mounted on a fixed position in front of the plasma torch. The pendulum is equipped with a substrate holder for pieces up to a maximum diameter of 20 mm, thus covering the whole cross section of the particle jet, which has a width close to 16 mm at 100 mm distance.
After the pendulum has traversed the particle jet it is stopped and the

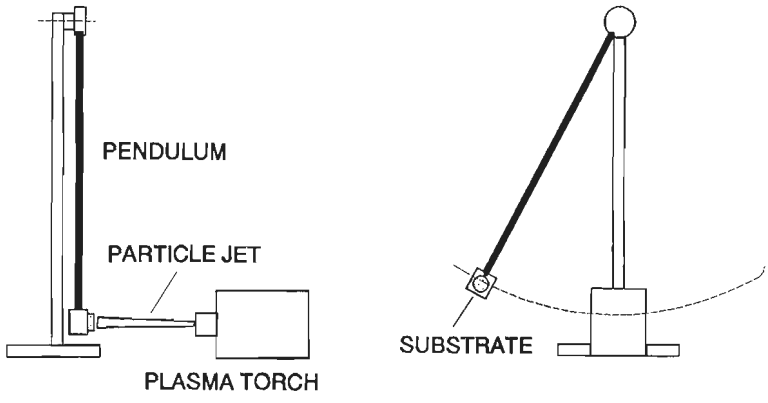


**Figure 2.19** Pendulum used for collision experiments with single particles.

substrate, which shows a track of splashed particles can be removed for microscopical examination. The velocity of the moving substrate, compared to the particle velocity is low. The particle velocity ranges from 100 - 300 m/s, whereas the substrate velocity is about 3,5 m/s and the influence of the cross movement on the collision morphology is insignificant.

A variation of the plasma spray control adjustments automatically includes a variation of both the heat content and the velocity of the particles. In order to investigate the influence of a change in velocity, at a certain heat content of the particles, the following experimental set up was used (figure 2.20).
A disk with four rectangular substrates is placed in front of the plasma torch. The disk has a diameter of 100 mm. The effective dimensions of the substrates are 10x10 mm. The disk is driven by an AC motor and the rotation velocity frequency controlled. The maximum velocity of the centre of the substrate is 110 m/s.
By changing the position of the plasma torch, it is possible either to increase the impact velocity or to lower it. This experimental set up was used for studying the adhesion mechanism of $ZrO_2$ to Fe.

## 5.4 Relationship between the plasma spray parameters and the morphology of the splashed particles

### 5.4.1. Experimental

In order to determine the influence of the plasma spray parameters and the

use of different anode channels on the morphology of splashed $ZrO_2$ particles, several experiments were carried out.

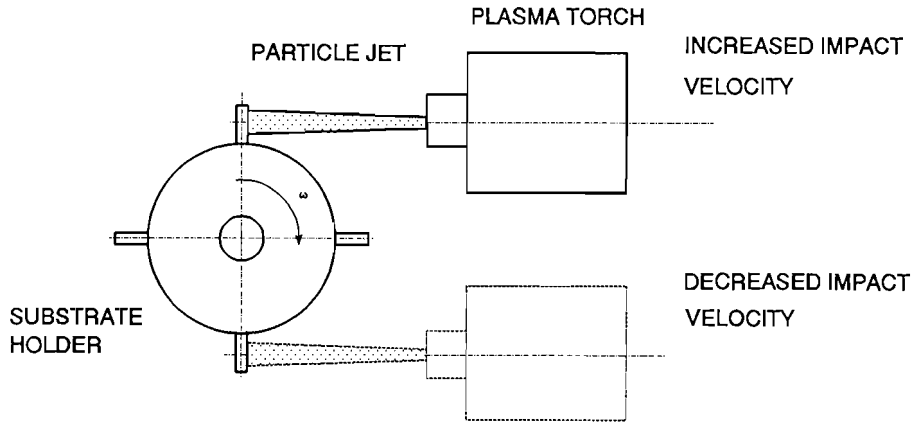


**Figure 2.20** Rotating substrate carrier for single particle experiments. The impact velocity of the particles can be lowered or increased by 110 m/s.[1]

The parameters to be varied were the plasma-gas flows of Ar and $H_2$ between 50 and 90 Sl/min and 3 and 30 sl/min. Besides, a standard and an extended anode channel were used.
The parameters of the experiments are listed below.

| | |
|---|---|
| I: | 600 A |
| Ar: | 50 .... 90 sl/min. |
| $H_2$: | 3 .... 30 sl/min. |
| Anode: | standard, 20 and 120 mm extended |
| spraying distance: 100 mm | |
| Powder feed rate: 40 gram/minute | |
| Substrate: | AISI 316 |
| Powder: | $ZrO_2$/7.6 wt% $Y_2O3$ |
| Powder size: | 38-45 $\mu$m |

The input power of the plasma torch varied with the amount of $H_2$ in the plasma gas. Figure 2.21 shows the input power of the plasma torch (equipped with a standard anode channel) as a function of the $H_2$ content. It can be observed that an increase of the argon flow from 50-90 Sl/min resulted in an increase of the input power of 2.4 kW. An increase of the $H_2$ content from 10 to 30 Sl/min, raised the input power by 11 kW.

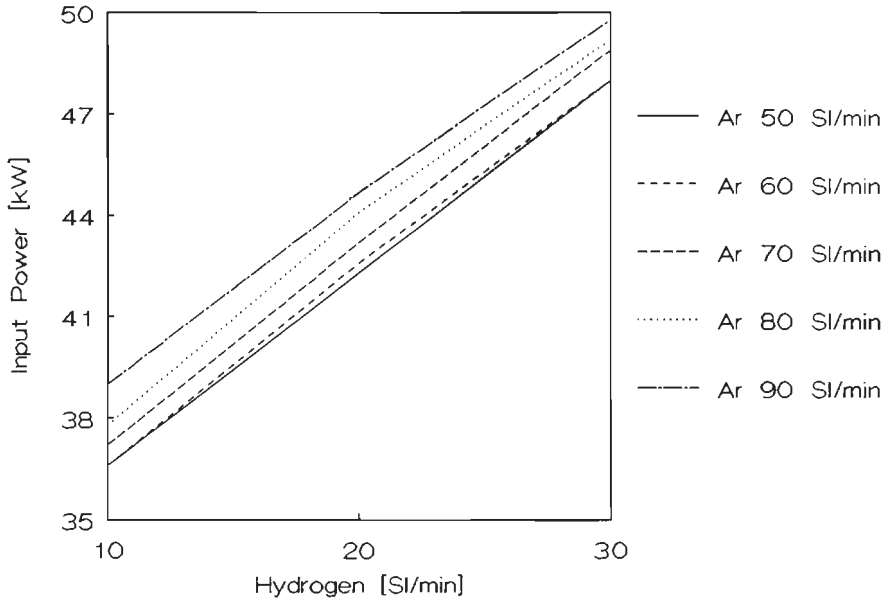


**Figure 2.21** Input power of the plasma torch (Arc current times voltage) of the plasma torch in relationship with the gas flows argon and $H_2$. The arc current is kept constant at 600 Amps.

The $H_2$ content had a great influence on the properties of the plasma flame. At low Argon flows (50-60 sl/min.) and $H_2$ flows of 20-30 Sl/min, the plasma became instable, resulting in a diverging particle jet.
When both the Ar and $H_2$ flows are kept relatively high (80-90 Sl/min Ar, 20-30 Sl/min $H_2$), severe erosion of the anode channel and cathode tip occurred. Because of this, these high gas flows are not appropriate for spraying during long periods of time.
The most stable and convergent plasma flame and particle jet was obtained at Argon flows from 60-70 sl/min. and $H_2$ ranging from 8 to 15 sl/min.

### 5.4.2.Results

The experiments were carried out using the pendulum, containing AISI 316 substrates with a diameter of Ø 20 mm.
After crossing the particle jet, the specimens were investigated microscopically. It was found that there exist three types of deposited particles which will be described below.

a) The flat star — A particle with an uniform thickness. The deposit is not circular but has a large number of radially directed rays.

b) The rough star — This is a splash with a morphology between the flat star and the pancake. It has rays but does not show the flat surface.

c) The pancake — An almost circular deposit, showing a very rough surface. The particle did not spread out well.

The diameter of the pancakes is less than the diameter of the flat stars. This is caused by the fact that the pancake exists of a "double splash". The origin of such a particle is shown in figure 2.22. Spreading out of the particles takes place in two stages. During the first stage, a part of the particle spreads out on the substrate's surface. Limited by mechanical factors (velocity, friction, viscosity) the particle does not spread out totally. Subsequently, the remaining part of the particle flows over the already flattened part.

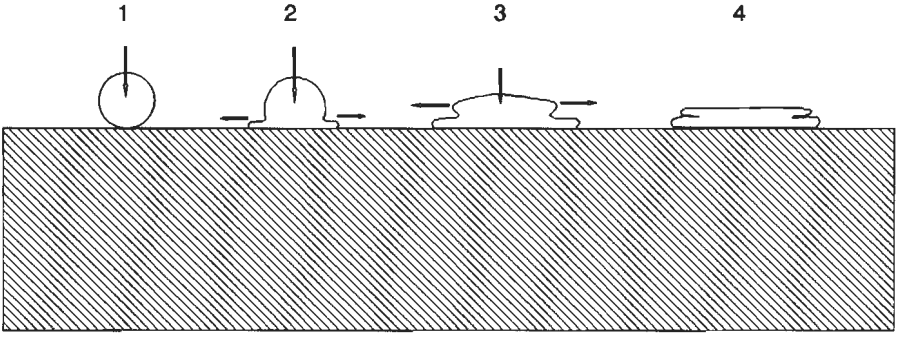


**Figure 2.22** Schematic view of the formation of a pancake. The first part of the particle spreads on the substrate. Subsequently, the remaining part of the particle flows over the flattened spread particle.

Figure 2.23 shows photographs of the different deposition morphologies, together with their cross sections.

The different morphologies of the splashed particles did not only depend on the plasma spray parameters, but also on the location of the particles in the particle jet. The particle track of a standard anode comprises three different zones. These are shown in figure 2.24.

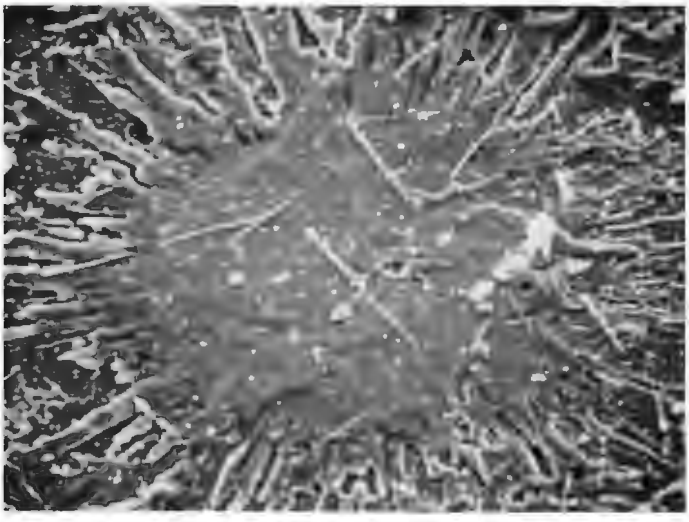


(A) Flat star


(B) Rough star

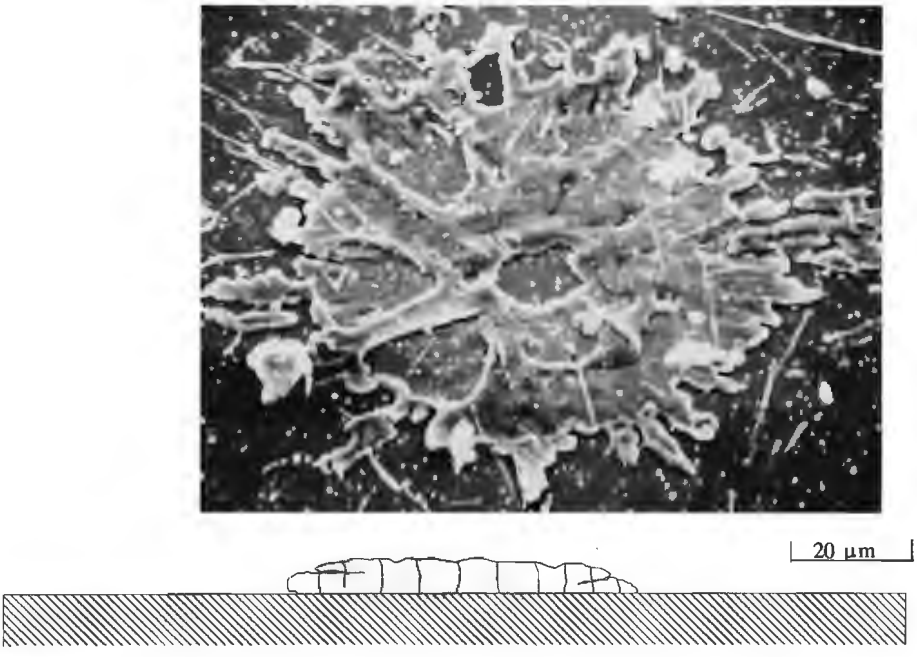


(C) Pancake

**Figure 2.23** Morphologies of the $ZrO_2$ particles. The flat star (A) shows radially directed rays and a smooth surface. The rough star (B) also shows some rays but has a rough surface. The pancake (C), has no rays and shows a very irregular surface.

Zone 1. This zone exists of very small splashes, created by very small particles. Due to their low mass, these particles have a very low impulse when they are injected into the plasma flame. As a result they are not able to penetrate to the centre of the flame, but they drift on the outer regions of the plasma flame, which has a low velocity and a low temperature, compared to the core of the plasma flame. Because of this, the particles are neither heated up nor accelerated well.

Zone 2. These are the particles which were transported through the central axis of the plasma flame and heated up well. These particles spread out well after impact on the substrate. The splashes in this zone show an uniform morphology and a uniform size. Mostly the splashes in this zone consist of flat and rough stars. The width of this zone is about 8 mm.

Zone 3. The deposits of this zone consists mainly of pancakes. Coarse particles fly through the centre of the plasma flame and leave the plasma flame at the underside. These particles are heated up well but possess a low velocity.

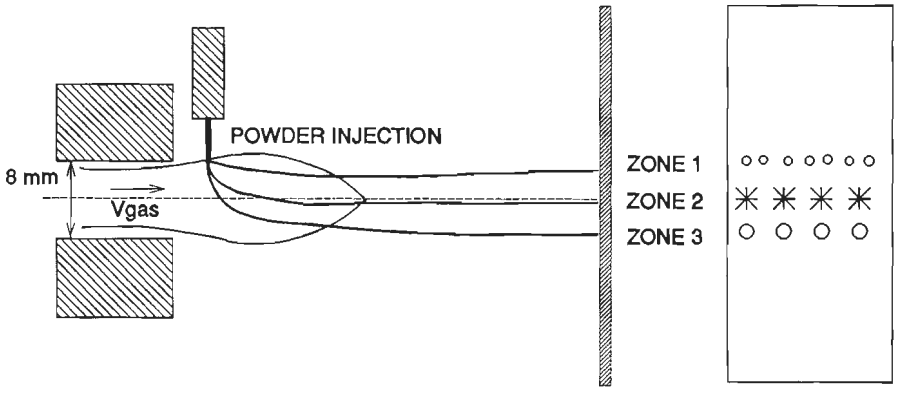


**Figure 2.24** Schematic drawing of the particle track of a standard anode channel.
Zone 1 shows small particles, which were not able to penetrate into the core of the plasma. These particles are poorly heated.
Zone 2 shows well heated particles. They spread out sufficiently on the substrate.
Zone 3 Coarse particles, which travelled through the core of the plasma but left it on the underside. The particles are well heated, bur possess a low velocity.

When an extended anode channel instead of a standard one is used, the differences between the three zones are not as distinct. The use of an extended anode channel results in a very uniform particle track. This is due to the fact that an extended anode channel produces a very narrow particle jet, which shows no divergency within a spraying distance of 100 mm.

In the next figures (2.25 and 2.26), the morphologies of the splashed particles are given as a function of the $Ar/H_2$ ratio and the total gas flow. The figures are related to zone 2, which is regarded to be representative for a certain gas flow and anode channel.

standard nozzle (figure 2.25)
At low argon flows and high $H_2$ contents ($Ar/H_2$ <2), the plasma becomes unstable. This results in a strongly diverging particle jet. Although the enthalpy of the particles increases with increasing $H_2$ content of the plasma, the deposited particles are mainly rough stars and pancakes.

At high $Ar/H_2$ ratios (>5) the splashes are mainly rough stars and pancakes. This is caused by the fact that the enthalpy of the particles in this area is just below the transition point from fusion to overheating. Because of this the particles do not spread out well during the impact on the substrate.

In the $Ar/H_2$ area between 2 and 5, the particles are mainly rough stars and in some cases also some flat stars. This is caused by the fact that the particles in this area are just overheated. The impact velocity, however, using a standard anode channel is not sufficient to obtain flat stars only.

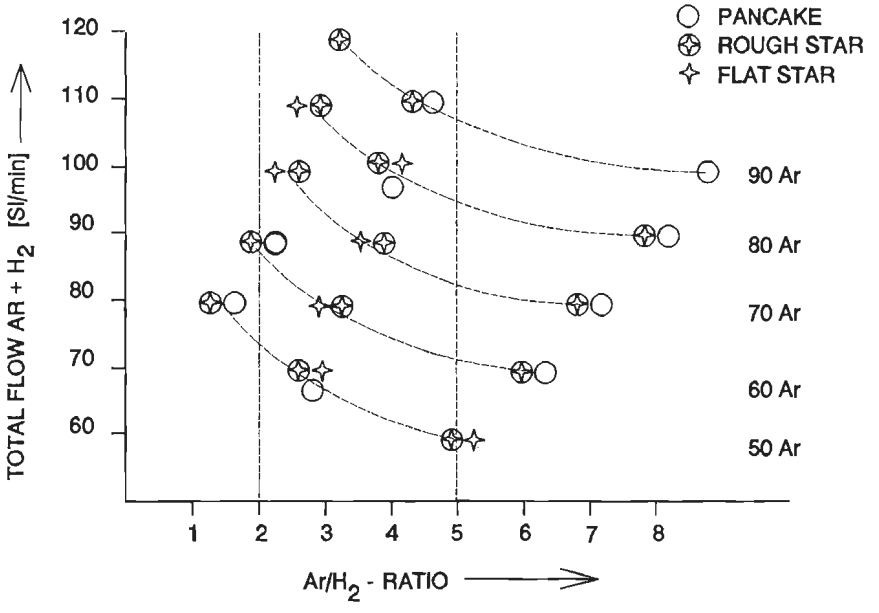


**Figure 2.25** Morphology of the splashed particles, sprayed with a standard nozzle, using different gas flows. The arc current was kept constant at 600 Amps.

20 mm extended channel (figure 2.26)

The $Ar/H_2$ ratio ranging from 2 to 7, produces mainly flat stars and a lower amount of rough stars. The particles are overheated and posses a higher velocity than the particles sprayed with a standard anode channel. During the impact on the substrate, they spread out well and form flat stars.

From these pictures it can be learned that the morphology of the splashed particles strongly depends on the plasma gas composition and the type of anode channel.

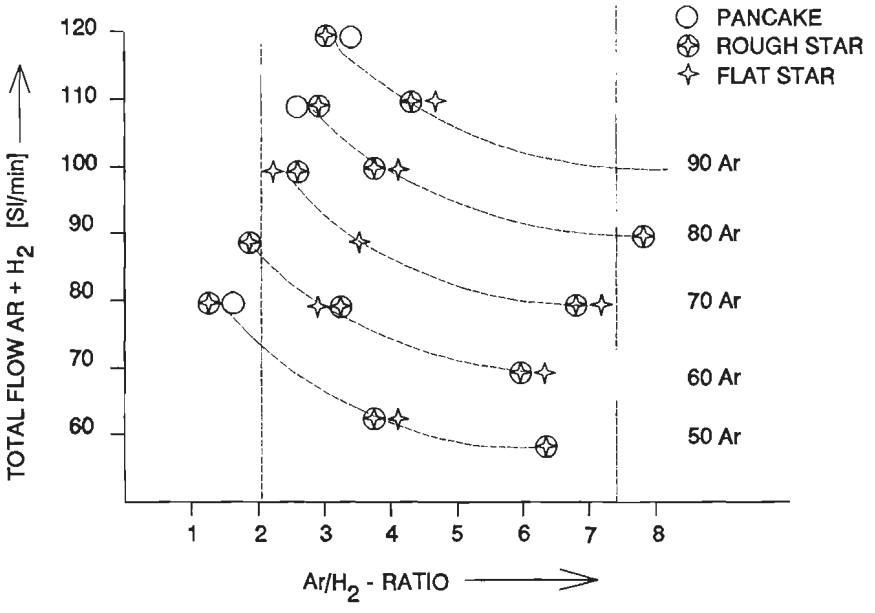


**Figure 2.26** Morphology of the splashed particles, sprayed with a 20 mm extended nozzle, using different gas flows. The arc current was kept constant at 600 Amps.

The particles sprayed with the standard anode channel show a lower amount of flat stars than the particles sprayed with an extended nozzle. When we observe for example the gas flow 70/20, both for the extended and normal anode, we see that the extended plasma produces almost only flat stars, whereas the standard anode produces rough stars.

When we compare particles having the same heat content and hence the same temperature, but sprayed with different anode channels, we can determine the influence of the particle velocity on the morphology of the splashed particles. The maximum velocity of the particles, sprayed with a standard anode channel was about 170 m/s, whereas the particles, sprayed with the extended nozzle possessed maximum velocities of 240 m/s. The enthalpy was 3200 kJ/kg for the standard nozzle ($Ar/H_2$ 70/20) and 3170 kJ/kg for the extended one ($Ar/H_2$ 70/10). At this enthalpy the particles were overheated.
The standard anode channel produced rough stars and pancakes, and the extended one flat stars and a little amount of rough stars and pancakes.

From the above results it may be concluded that the particle morphology is strongly influenced by the impact velocity of the particles. When the particles are overheated, and the particle velocity is sufficient, flat stars will occur. When the velocity is lower rough stars and pancakes will be formed.

The typical morphologies of flower type particles as reported by Houben [1] were not observed during the spraying of $ZrO_2$ particles.

To obtain both a high impact velocity and a high enthalpy the use of an extended anode channel is necessary.

### 5.4.3 Crack network of the splashed particles

A very remarkable characteristic of the single deposits was the very dense network of cracks which was observed in the well spread particles. The density of this network did depend on the physical properties of the substrate material. The splashed particles on the Fe substrates showed a dense network, with a mean distance between the cracks of 4 to 5 $\mu$m. The crack network on the $ZrO_2$ substrates in contrary showed a mean distance of 10 to 12 $\mu$m, and the mean distance between the cracks on an AISI 316 substrate was 4.7 to 5.5 $\mu$m.

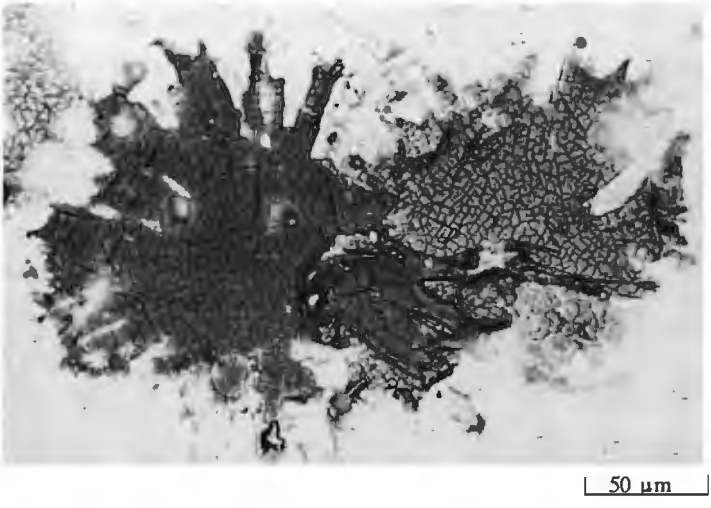


**Figure 2.27** Crack network in $ZrO_2$ particles sprayed on AISI 316. The particles partly overlap each other. The crack distance at the overlap is greater than the crack distance on the AISI 316.

Figure 2.27 shows two $ZrO_2$ particles on an AISI 316 substrate. These particles overlap each other partly. It can be seen that the particle, on top of the other particle shows a more coarse crack network than the rest of the particle which solidified on the AISI 316 substrate.

The dense crack network is caused by the high tensile stresses occurring in the $ZrO_2$ particles after solidification. Due to the great temperature difference between the particles and the substrate, these high tensile stresses, exceeding the strength of $ZrO_2$, occur. Stress relaxation now occurs by the formation of a crack network.
During the solidification of a particle, the temperature of the substrate surface is equal to the contact temperature $T_c$ as calculated in paragraph 5.2.1. The temperature difference which has to be taken into account for the calculation of the strains is therefore equal to $(T_m-T_c)$. The plot of the reciprocal value of the crack distance versus the strain $(T_m-T_c)*\alpha_c$, has a linear relationship. See figure 2.28.

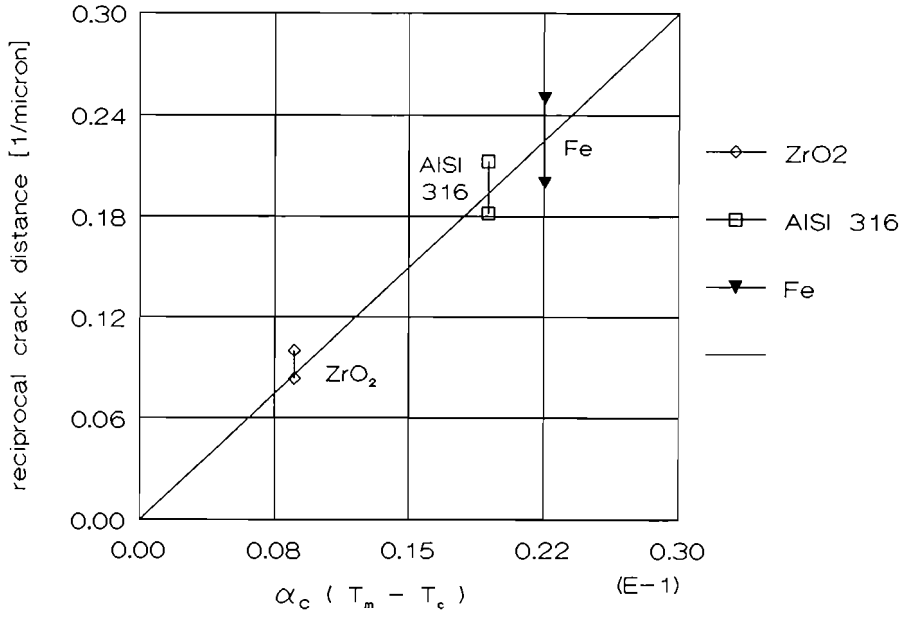


**Figure 2.28** Reciprocal value of the mean crack distance of $ZrO_2$ particles on Fe, AISI 316 and $ZrO_2$ substrates.

The relationship between the crack distance d and the strain (Tm-Tc)*$\alpha_c$ may now be described by the equation:

$$\frac{1}{d}=C(T_m-T_c)\alpha_c \qquad (24)$$

d: crack to crack distance [$\mu$m]
$T_m$: melting temperature [K]
$T_c$: contact temperature [K]
$\alpha_c$: coefficient of thermal expansion coating [-]

The crack to crack distance is not a function of the thermal expansion coefficient of the substrate or of the difference between the thermal expansion coefficients of the substrate and the deposit. If this were the case, the particles sprayed onto the AISI 316 substrate should show the most dense crack network due to the difference in thermal expansion coefficients. So, the stresses occurring during solidification of the particles, the so called primary cooling, are mainly determined by the contact temperature and $\alpha_c$ during solidification. In literature, the contact temperature is generally taken as the substrate temperature.

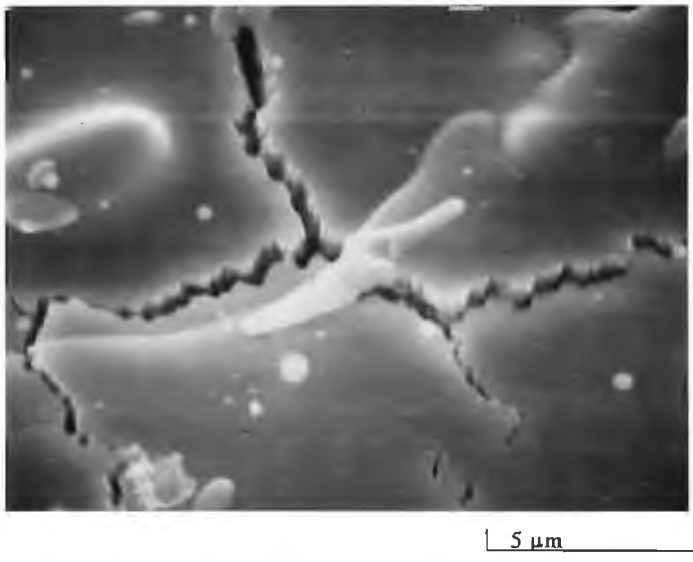


**Figure 2.29** Detail of the crack network in a $ZrO_2$ particle, sprayed onto a Fe substrate.

The stresses involved with the strains developing during solidification of the $ZrO_2$ particles will be calculated in chapter 3, where the origin of residual stresses in plasma sprayed $ZrO_2$ coatings will be reported.

Figure 2.29 shows a detail of a $ZrO_2$ particle on a Fe substrate. The detail of the dense network of microcracks can be seen very clearly in this photograph. This picture shows also that the cracks are very craggy and run along the columnar grains. This columnar grain structure developed due to the directed high cooling rate.

### 5.4.4 Collisions of $ZrO_2$ particles on different substrate materials

The collision behaviour of single $ZrO_2$ particles on various substrate materials is described in this paragraph. The various substrate materials, with their physical properties are shown in table 7.

Table 7
Physical properties of substrate materials

| substrate | $\lambda$ [$Wm^{-1}K^{-1}$] | $\rho$ [$kg\ m^{-3}$] | C [$Jkg^{-1}\ K^{-1}$] | $T_m$ [C] |
|---|---|---|---|---|
| Fe | 75 | 7880 | 460 | 1535 |
| W | 147 | 19350 | 138 | 3380 |
| Mo | 146 | 10200 | 255 | 2610 |
| AISI-316 | 18 | 7670 | 489 | 1375 |
| FeCrAlY * | 10 | 8000 | 450 | 1350 |
| $ZrO_2$ | 1,5 | 5000 | 477 | 2670 |

* These are estimated values, because values were not available in literature.

The $ZrO_2$ and FeCrAlY substrates were made by plasma spraying. Fe substrates were covered with a 0,4 mm $ZrO_2$ or FeCrAlY layer, which was thick enough to avoid the influence of the Fe substrate on the solidification of the impacting particles. All the substrates were ground and polished with

3 $\mu$m diamond to obtain a smooth surface. This made it possible for the impacting particles to spread out freely. Also the deformations which may be caused by the impacting particles could be observed well by microscopy.

The $ZrO_2$ particles, used for these experiments ranged in size from 38-45$\mu$m. These particles were obtained by sieving a batch of 22,5-45 $\mu$m powder.

All the experiments were carried out, using the same plasma spray parameters, which are listed below.

| | |
|---|---|
| I: | 600 Amps |
| Ar: | 70 Sl/min. |
| $H_2$: | 8 sl/min. |
| Anode: | Standard Ø 8 mm |
| Spraying distance : | 100 mm |

The maximum velocity of the particles using these parameters was about 170 m/s, whereas the heat content is just at the transition point from melting to overheating.
The different specimens were investigated microscopically after the spraying. It appeared that the substrate materials Mo and W showed no adhering particles; only some traces of particles were discovered. Fe, AISI 316 and FeCrAlY On the contrary showed a large number of splashed particles, with the shape of a rough star as described in the foregoing paragraphs. The particle morphology is rather determined by the plasma spray parameters and the type of anode channel than by the substrate material.

### 5.4.5 Adhesion of $ZrO_2$ on Fe, W and Mo

The fact that no adhesion occurred between the $ZrO_2$-particles and the Mo and W substrates cannot be explained only by the low contact temperature during the solidification of the particle. The contact temperatures between $ZrO_2$ and Mo and W were 630 and 623 K respectively. The contact temperature between $ZrO_2$ and Fe was 680 K, also only slightly higher. At this temperature, the particles adhere well on the Fe substrates.
The fact that only traces of $ZrO_2$ particles were found on the Mo and W substrates, suggested that the impacting particles were reflected by the substrates.

Cross sections of the Fe substrates with $ZrO_2$ particles did not show any visible diffusion zone between the two materials.
Interdiffusion of Fe, W and Mo and $ZrO_2$ is not likely to happen because of the low contact temperature and the short period of time the contact temperature is maintained (maximum 1E-5 s).
Because of this, another mechanism has to be responsible for the adhesion between $ZrO_2$ and the metallic substrates.
To investigate the relationship between the impact velocity of the $ZrO_2$ particles and the adhesion, the rotating substrate holder, as described in paragraph 5.3.1, was used. The substrate holder was equipped with Fe substrates and operated at velocities between -100 and + 100 m/s. Two types of anode channels were used; the standard nozzle and the 20 mm extended one. The following plasma spray parameters were used:

| | |
|---|---|
| I: | 600 Amps |
| Ar: | 70 Sl/min |
| $H_2$: | 8 Sl/min |
| d: | 100 mm. |
| powder size: | 38-45 $\mu$m |

The particles sprayed with the standard anode channel are just at the transition point from melting to overheating (rough stars and pancakes) and posses a maximum velocity of 170 m/s. The impact velocity will therefore vary between 70 and 270 m/s.
The extended anode channel delivers particles which are just overheated and form flat and rough stars. They possess a maximum velocity of 240 m/s. The impact velocities range from 140 to 240 m/s.
Cross sections of the specimens showed that an increased particle velocity resulted in an improved adherence of the particles. This phenomena is observed for both the standard and extended anode channel. Figure 2.30 shows the various cross sections of the specimens with the varying impact velocities for both the standard and extended anode channel.

At the high impact velocities, plastic deformation of the substrate occurred. This deformation, however, was not similar to the phenomena as described by Houben [1], who studied the adherence between metallic particles and metallic substrates. The typical wave patterns arising in the substrate

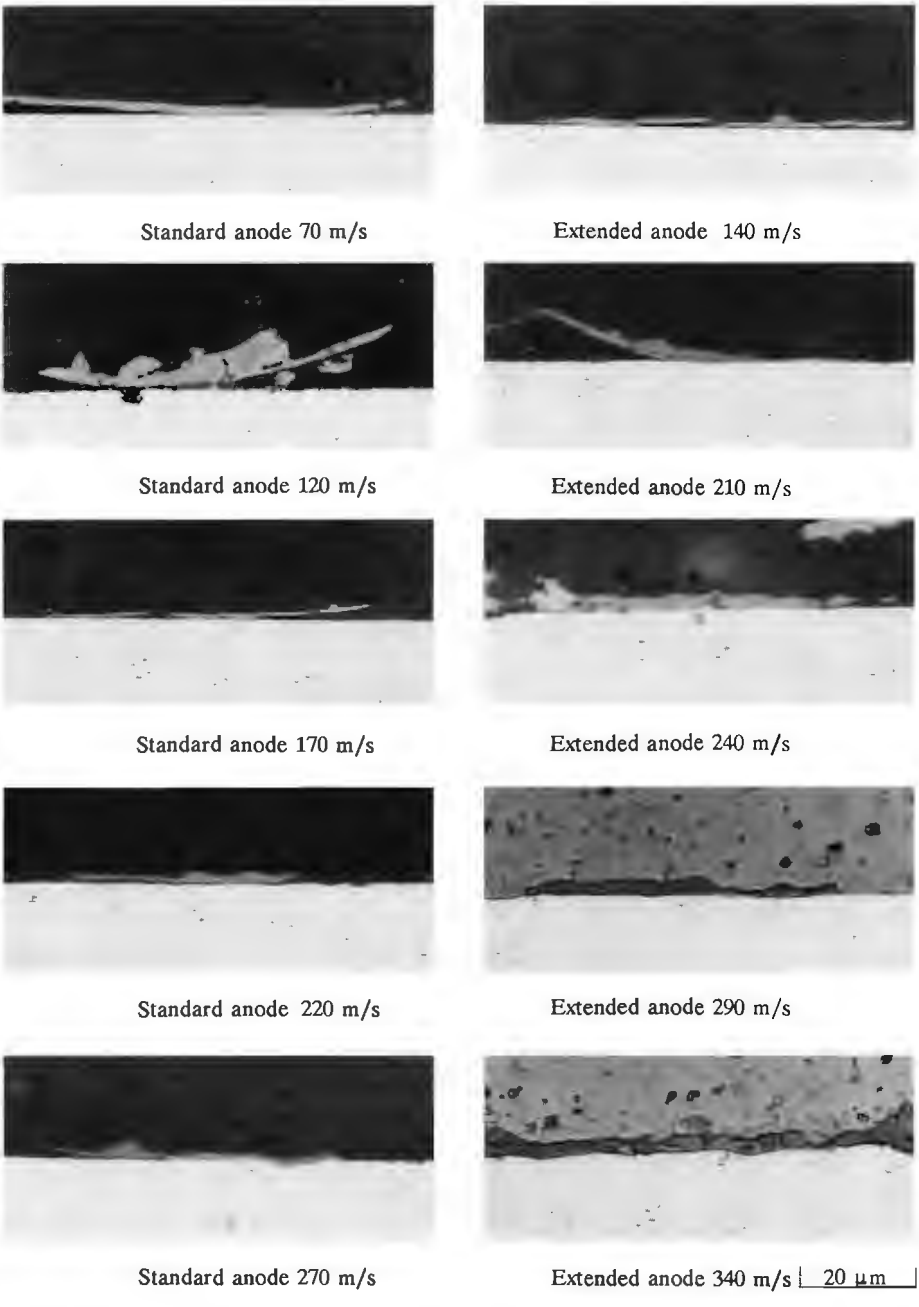


**Figure 2.30** Cross sections of $ZrO_2$ particles on Fe substrates, sprayed with a standard and a 20 mm extended nozzle. $Ar/H_2$ 70/15, 600 Amps, powder size 38-45 µm. The relative impact velocity was varied between -100 and +100 m/s. The captions state the absolute maximum impact velocity.

material, which occur in the case of explosion welding were not observed. Nevertheless it has to be assumed that mechanical processes play the most important role in the adhesion process. When the impact velocity of a particle increases, the friction forces between particle and substrate during spreading of the particle also increase. This may result in an extra temperature increase causing adhesion due to diffusion or mechanical mixing up of substrate and deposit. There may be also another mechanism which explains the improved adhesion when the impact velocity increased. During their impacts, the high velocity particles sweep away the oxide films and contaminations from the substrate's surface. At this clean surface, bonding may occur due to physical interaction between the metallic substrate and the $ZrO_2$ particle.
The assumptions given above are both supported by the fact that the adhesion improved when the impact velocity increased and lowered when the velocity decreased.

As already stated, no adhesion occurred between Mo and W when a standard anode channel in combination with the plasma spray parameters mentioned above were used.
Adhesion between $ZrO_2$ and Mo could be realized by the use of the 20 mm extended anode channel and a gas flow of $Ar/H_2$ of 70/15 Sl/min. The particles are overheated and form flat stars. Due to the impact velocity of 240 m/s slight plastic deformation of the substrate occurred.

When this set up was used still no adhesion between W and $ZrO_2$ occurred. The use of the 120 mm extended anode channel, however resulted in a good adhesion. The strongly overheated particles with a maximum velocity of 300 m/s formed flat stars and caused a slight deformation of the substrate as can be seen in figure 2.31.
From this it may be concluded that the impact velocity and heat content of the particles, play the most important role in the adhesion mechanism between $ZrO_2$ and the refractory metals Mo and W.

**6 Conclusions.**
The particle velocity of the $ZrO_2$ particles is strongly influenced by the type of anode channel used during the spraying process. The use of an extended anode channel results in a distinct velocity increase.


**Figure 2.31** Cross section of a $ZrO_2$ particle on W. The particle is sprayed using an 120 mm extended anode channel and a gas flow $Ar/H_2$ of 70/15. Arc current 600 Amps.

The enthalpy of the particles is also strongly influenced by the type of anode channel. When the plasma spray parameters are kept constant, particles sprayed with an extended nozzle possessed a higher enthalpy than particles sprayed with a standard nozzle. This is caused by the fact that powder injection takes place into the extended nozzle, resulting in a longer dwell time of the particles.

Three types of particle morphologies could be observed: the flat star, the rough star and the pancake. The flat star occurs when overheated particles with sufficient velocity impact on the substrate. Flat stars are mainly observed at overheated particles, sprayed with an extended nozzle.
The particle morphology is rather determined by the plasma spray parameters and type of anode channels, than by the substrate material.

The contact temperature between $ZrO_2$ particles and well conducting metallic substrate materials is low (600 to 700 K).
This is mainly caused by the low thermal conductivity of $ZrO_2$

The $ZrO_2$ particles show a dense micro-crack network. The distance between the cracks is determined by the contact temperature between substrate and particle during the solidification of the particle.

Adhesion of $ZrO_2$ to metallic substrates is strongly determined by the impact velocity and the heat content of the single particles. The experiments on W and Mo substrates showed this. Adhesion only took place at high heat contents and high velocities of the particles.

## 7 References Chapter II


[1] Houben J.M., Relationship between the Adhesion of Plasma Sprayed Coatings to the Process Parameters Size, Velocity and Heat Content of the Spray Particles. Doctor's Thesis, Eindhoven University of Technology, 1988

[3] Houben J.M., Remarks Concerning a Rational Plasma for Thermal Spraying. Proceedings 9th International Thermal Spraying Conference, 1980, The Hague, The Netherlands.

[3] Houben J.M., Eindhoven University of Technology, Faculty of Mechanical Engineering, private communication

[4] Das D.K., Savikumar R., Modelling of the Temperature and the Velocity of Ceramic Powder Particles in a Plasma Flame.
Acta Metallurgica en Materialia, 38(1990) 2187-2192

[5] Vaessen P.H.M. Heat and Momentum Transfer from an Atmospheric Argon Hydrogen Plasma Jet to Spherical Particles. Doctor's Thesis, Eindhoven University of Technology, 1984

[6] Vardelle M., Etude de la Structure des Depots d'Alumine Obtenus par Projection Plasma en Fonction des Temperatures et des Vitesses des Particules au Moment de leur Impact sur la Cible. Doctor's Thesis, Limoges University (F), 1980

[7] Fauchais P., Bourdin E., Coudert J.F., McPherson R.,High Pressure Plasmas and Their Application to Ceramic Technology. In: Topics in Current Chemistry 107, Plasma Chemistry IV, editor F.L. Boschke, Springer Verlag, Berlin, Heidelberg, New York 1983.

[8] Roumilhac Ph., Vardelle M., Vardelle A., Fauchais P., Comparison of Heat and Momentum Transfer to Ceramic Particles Sprayed in Ar-$H_2$ and Ar-He Plasma Jets at Atmospheric Pressure. In: Thermal Spray Technology, editor D.L. Houck, ASM, Ohio, USA, 1989.

[9] Heiden H.L.M. van der, Morfologie van Plasmagespoten Roestvast Staal en Molybdeen Deeltjes Afhankelijk van de Procesparameters Snelheid en Warmte-inhoud. Master's Thesis, Eindhoven University of Technology, 1989

[10] Houben J.M., Flesh T., Eindhoven University of Technology, Faculty of Mechanical Engineering and Central Construction Group, private communication

[11] Schick H.L., Thermodynamics of Certain Refractory Compounds, Academic Press, 1966

[12] Carslaw H.S. Jaeger J.C., Conduction of Heat in Solids, Clarendon Press, Oxford, 1986

[13] Kuijpers T.W., Zaat J.H., Influence of Oxygen and Cooling Rate on the Micro-structure and Microhardness of Plasma Sprayed Molydenum, Metals Technology, March 1974, 142-150

[14] Hart W.G.J. 't, Inleidend Onderzoek van Opgespoten Lagen met Betrekking tot de Mechanische Eigenschappen, Porositeit en Spanningen. Master's Thesis, Eindhoven University of Technology, 1972

[15] Members, thermal spraying group, Eindhoven University of Technology, private communication

## CHAPTER III SPRAYING OF THERMAL BARRIER COATINGS

### 1 Introduction

This chapter describes the production of thermal barrier coatings. The coatings were sprayed, bringing together the experiences from chapter 2, where the behaviour of single $ZrO_2$ particles was studied, and theoretical models on the origin of residual stresses, occurring during the spraying process.

As could be read in chapter 1, coatings with a high porosity possess a high thermal shock resistance. Dense coatings, on the other hand, have a high erosion resistance, but a poor thermal shock behaviour.

The aim of this research programme is to design a thermal barrier coating with both a high erosion and thermal shock resistance. To reach this goal, the intrinsic strength of the ceramic coating has to be high. Furthermore, the coating has to be flexible in order to avoid the building up of high thermal stresses during thermal shock loading.

The ceramic coating must possess a high cohesive strength to obtain a high erosion resistance. This means that the adherence between the individual $ZrO_2$ particles has to be optimized. This can be achieved by spraying well fused particles. These particles will spread out well over the already solidified particles and the formation of coarse pores is not likely to happen. Due to the fact that the contact temperature between $ZrO_2$ and $ZrO_2$ particles is high (Chapter 2) good adhesion is assured.
Overheated particles contain a high thermal energy. This energy is partly released by convection and radiation, but mainly by conduction to the substrate. This results in heating up and hence expansion of the substrate during the coating process. During cooling down to room temperature, the substrate may cause compressive stresses in the ceramic topcoat.
$ZrO_2$ has a low tensile strength and a high compressive strength [1]. Nevertheless, residual compressive stresses, added to the compressive stresses arising in the ceramic coating during heating up of the coating-substrate system, may lead to spallation of the ceramic coating by buckling. This is schematically shown in figure 3.1.

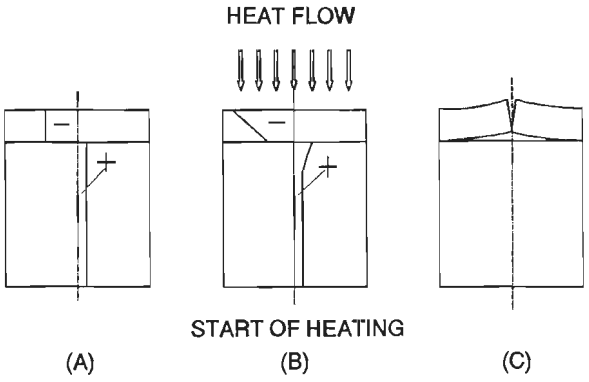


**Figure 3.1** Buckling of the coating, caused by compressive stresses at the initial state of heating up. a) residual stress at room temperature ,- compressive stress: + tensile stress b) stress distribution during initial state of heating up the coating c) buckling of the coating

To avoid the formation of compressive stresses, caused by the plasma spraying process, the substrate has to be kept at a low temperature. A possibility to obtain this goal is to spray the entire coating in a large number of thin layers, waiting between each pass until the coating-substrate system has cooled down. In practice this is not suitable because of the long production times, involved with this method.
A better option is cooling of the substrate by air, water or liquified gasses as $CO_2$ or Ar.
As a result of the low thermal conductivity of $ZrO_2$ (1-2 W/mK), the heat transport through the coating decreases, when the coating thickness increases. To keep the substrate and the already deposited coating at a low temperature, even at greater coating thicknesses, the coating has also to be cooled. Preferably, this has to be done by compressed air or gas cooling.

In this chapter a model will be presented, describing the origin of residual stresses in the $ZrO_2$ coating as a function of the substrate temperature and the primary cooling.
The second part of this chapter describes the production of thermal barrier coatings. The influence of substrate cooling on the residual stress state and on the microstructure of the coatings is reported. Also the influence of the use of extended anode channels (See chapter 2) on the characteristics of the

ceramic coating will be discussed.

**2 Models, presented in literature, for the calculation of residual stresses in plasma sprayed ceramic coatings.**

The formation of residual stresses in plasma sprayed ceramic and metallic coatings is a very complex process. Several factors, such as substrate material, substrate thickness, physical properties of both the substrate and the coating material, deposition rate, relative velocity of the plasma torch, etc, determine the final residual stress state of the coating at room temperature.

Several authors present models concerning the origin of residual stresses in plasma sprayed ceramic and metallic coatings. Many of the models are merely qualitative and predict only the sign of the stress in the coating, compressive or tensile.

Takeuchi c.s., Elsing c.s. and Buckley-Golder present quantitative models for the calculation of residual stresses. [2,3,5,6,7,8]

**2.1 Formation of stresses during the plasma spray process.**

The formation of stresses in a plasma sprayed coating can be divided in three stages.

The first stage concerns the solidification of single particles. Due to the great temperature difference between the substrate and the particles, tensile stresses will occur in these particles. In literature, this first stage is called primary cooling.

The second stage involves the heating up of the substrate during the coating process, caused by the heat transport from the coating to the substrate. This results in expansion of the substrate causing tensile stresses in the already deposited part of the coating. Next to this, the newly deposited layers solidify on an "extended" substrate.

The third stage describes the stresses caused by the cooling down of the substrate-coating system after the coating process has been completed. In literature this third stage is known as secondary cooling.

These three stages together determine the ultimate residual stress in the

coating and the substrate. Generally, primary cooling is not taken into account in the models presented in literature. Only Takeuchi considered primary cooling by introducing an additional strain term, representing stresses caused by primary cooling, in his equations describing the stress state of a substrate-coating system at room temperature. Takeuchi does not take into account the temperature-time history as described in stage two. He assumes that the substrate has a certain starting temperature and that the coating layer is deposited in one pass. Elsing on the contrary, takes this temperature-time history into account, calculating the instationary temperature fields, arising during spraying of the coatings. These temperature fields are used for the calculation of the residual stresses. Primary cooling however, is neglected in these calculations.

### 2.1.1 Stress due to primary cooling.

**Note:** In this chapter it is supposed that the coefficient of thermal expansion of the substrate is larger than the coefficient of thermal expansion of the coating.

In literature, strains due to primary cooling are mainly represented by the equation [5]:

$$\epsilon = \alpha_c (T_m - T_s) \qquad (1)$$

$\epsilon$: strain in the particle [-]
$\alpha_c$: coefficient of thermal expansion of the particle[$K^{-1}$]
$T_m$: melting point of the particle [K]
$T_s$: substrate temperature [K]

In the foregoing chapter however, it appeared that strains and hence stresses due to primary cooling may be related to the contact temperature $T_c$.
The contact temperature $T_c$ between a solidifying particle and a substrate stays at a constant level during the solidification process. (See paragraph 5.2, chapter 2). The maximum strain, occurring in the particle is therefore equal to:

$$\epsilon = \alpha_c (T_m - T_c) \qquad (2)$$

$T_c$: contact temperature between particle and substrate [K]
$\alpha_c$: splashed particle coefficient of thermal expansion

The tensile stress in the particle, caused by the strain is therefore equal to $\epsilon * E_c$, where $E_c$ is the Young's modulus of the particle.It has to be noted that both $\alpha_c$ and $E_c$ depend on the temperature T.

The contact temperature between $ZrO_2$ and the most metallic substrate materials is low. (See chapter 2). This indicates that the temperature on the solidifying particle, near the substrate is also low. Therefore, this part of the coating can not be deformed plastically during shrinking. When a certain strain is exceeded, crack formation occurs, resulting in the dense crack network in the single $ZrO_2$ particles. This mechanism is given schematically in figure 3.2. (See also chapter 2, paragraph 5.4.3)

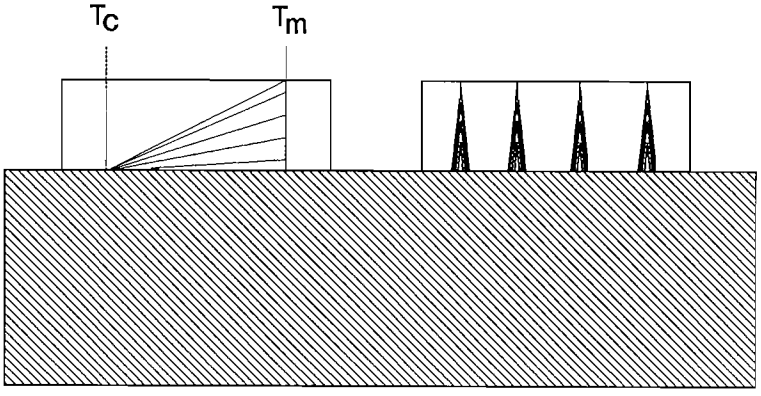


**Figure 3.2** A solidifying $ZrO_2$ particle on a substrate. Due to the low contact temperature, a steep temperature gradient exists over the particle thickness. Due to the shrinking of the already solidified part the particle, strains occur leading to crack formation in the particles.
($T_c$ = contact temperature, $T_m$ = melting temperature)

After solidification, the temperature in the particle rapidly drops to the substrate temperature $T_s$. The substrate below the solidified particle expanded due to the latent heat of the particle. The maximum strain caused by cooling down from the contact temperature to the substrate temperature

is equal to:

$$\epsilon_{T_c-T_s}=(\alpha_c-\alpha_s)*(T_c-T_s) \qquad (3)$$

$\alpha_s$: substrate coefficient of thermal expansion [$K^{-1}$]
$T_s$: substrate temperature [$K^{-1}$]

In the foregoing equation it is assumed that the substrate below the solidifying particle expands freely. This is not true. The part of the substrate under the particle is surrounded by solid material, so free expansion is not possible. For this reason, the strain introduced by cooling down to the substrate temperature is less than the strain stated by equation 3.

The strain in a particle at room temperature is equal to the tensile strain caused by cooling down from $T_m$ to $T_c$ minus the strain, caused by the shrinking metallic substrate. When the substrate and coating material are the same, e.g. $ZrO_2$ on $ZrO_2$, the strain will depend only on the contact temperature.

The maximum strain in a particle is limited by the maximum strain at which crack formation occurs in the particle. When this strain is exceeded, cracking occurs.

Ziegler [9] reports strengths at room temperature for partially stabilized zirconia which vary from 450 to 2000 MPa. When the Young's moduli of these materials are known, the maximum strains to failure can be calculated. The strengths at high temperatures however, are not available.

An estimation of the mean tensile strains in the $ZrO_2$ particles, sprayed onto a $ZrO_2$ substrate can be based on the X-ray diffraction stress measurements, carried out on thin $ZrO_2$ layers. These measurements are described in detail in paragraph 3.3.
The thickness of these $ZrO_2$ layers was 6-8 particles (mean particle thickness 3 $\mu$m). As a result, the influence of the substrate material on the solidification of the last deposited particles may be neglected. (See chapter 2, figure 2.16) It is also assumed that heating up of the substrate as a whole, during the coating process can be neglected. So, no compressive stresses are introduced in the particles.

At room temperature, the measured strains in these layers varied from 0.000479 to 0.000742. These strains resulted in a tensile stress at room temperature varying from 94 to 141 Mpa.(Young's modulus 190000 Mpa) Whether stress relaxation in the particles occurs, being caused by impinging particles is not known. It may however be supposed that a certain relaxation may take place when the high contact temperature between $ZrO_2$ and $ZrO_2$ is considered.

Crack formation in the splashed particles occured along the grain boundaries of the columnar grains. This can be seen in figure 2.29 in chapter 2. The fact that crack formation occured along these grain boundaries indicates that the stresses, causing these cracks are maximum at the grain boundaries. This may be caused by the fact that notches are present at the grain boundaries, as can be seen in figure 2.29. Due to these notches high stress concentrations may occur at the grain boundaries.

## 2.2 A model for the calculation of residual stresses in plasma sprayed coatings

In the following paragraphs, a model for the calculation of residual stresses will be presented. The three stages of stress formation: primary cooling, heating up and expanding of the substrate-coating system and cooling down to room temperature of the substrate and coating will be described. The equations describing the expansion and the shrinking of the substrate-coating system are given by Elsing, Knotek and Balting [6,7,8]. An extra strain term, representing the effect of primary cooling on the formation of stresses in the coating and substrate is introduced. Elsing c.s used instationary temperature fields for their calculations. In the following model, stationary temperature fields are used.

The results of the calculations of the residual stresses of $ZrO_2$ coatings on different substrate materials are presented and compared to the calculations which were made using the model of Takeuchi c.s.

### 2.2.1 Stress caused by heating up and cooling down of the substrate during the spraying process.

This paragraph describes the formation of stresses in the coating, introduced by the expanding and shrinking substrate: the so called secondary cooling. (See paragraph 2.1 of this chapter).

process, the substrate and already deposited coating layers expand. The newly deposited layers therefore, solidify on an expanded substrate. On cooling down to room temperature, the metallic substrate shrinks more than the ceramic coating and a compressive stress component will be acting on the coating.

Equations

Consider the situation which is shown in figure 3.3. A strip shaped substrate with a thickness $t_s$ and an initial length at room temperature of $l_{s0}$ is covered with a coating. The coating is deposited in $n_c$ elements of equal thickness. The ultimate thickness of the coating is $t_c$. The substrate is also divided in elements. The thickness of these elements is equal to the thickness of the coating elements.

Due to the heat release of the coating during solidification and cooling down, the substrate and the already deposited coating elements are heated up and expand. The substrate is not able to expand freely, but is partly restricted by the coating which possesses a lower thermal expansion. With increasing coating thickness, the stiffness of the coating increases and the expansion of the substrate is further restricted. The total length $l_{tot}$ of the substrate and coating after the spraying process is finished is described by equation 4 which is given by Elsing, Knotek and Balting [6,7,8]. This equation gives the length $l_{tot}$ when the substrate-coating combination is still at its final temperature after deposition of the last coating element

$$l_{tot}=\frac{n_s E_s+n_c E_c}{\sum_{i=1}^{n_s}\frac{1}{l_{0si}(1+\alpha_s \Delta T_i)}*E_s+\sum_{1=1}^{n_c}\frac{1}{l_{0ci}(1+\alpha_c \Delta T_i)}*E_c} \qquad (4)$$

$l_{tot}$: total length of substrate coating combination just after the spraying process is finished.
$n_s$: total number of substrate elements
$n_c$: total number of coating elements
$E_s$: Young's modulus of substrate [Pa]
$E_c$: Young's modulus of coating [Pa]
$l_{0si}$: length of substrate element at room temperature [m]
$l_{0ci}$: length of coating element [m]

$\alpha_s$: coefficient of thermal expansion substrate [$K^{-1}$]
$\alpha_c$: coefficient of thermal expansion coating [$K^{-1}$]
$\Delta T_{si}$: temperature of substrate element i [K]
$\Delta T_{ci}$: temperature of coating element i [K]

The length $l_{0ci}$ of a coating element is determined by the expansion of the substrate coating combination, caused by the previously deposited layers.

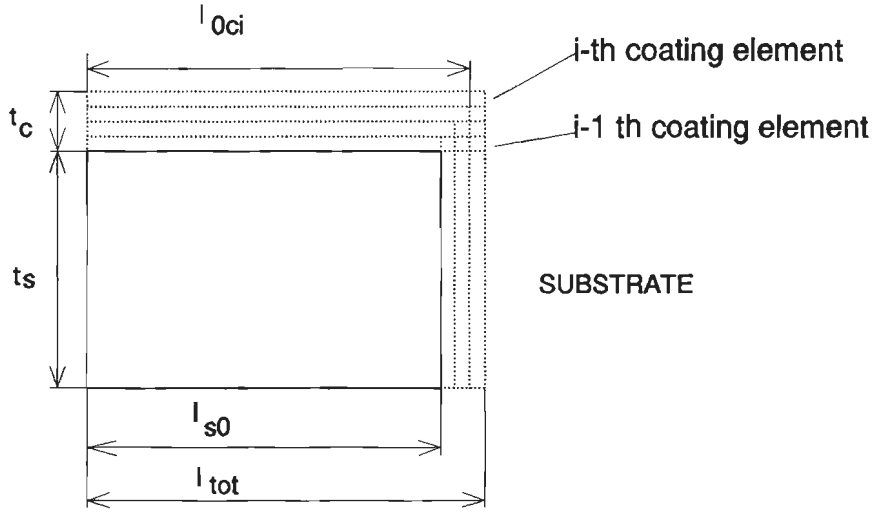


**Figure 3.3** System used for the calculation of stresses due to heating up of the substrate and coating during the coating process. Each deposited coating element causes heating up of the substrate and already deposited coating. This results in an expansion of the substrate coating combination. The coating elements will solidify on an expanded substrate. On cooling down to room temperature, the coating substrate combination shrinks. As a result, compressive stresses may occur in the $ZrO_2$ topcoat.

Due to the fact, that the substrate expands more than the coating, the coating is loaded by tensile stresses and the substrate by compressive stresses.

The stress in a coating element, after the last coating element is deposited and the coating and substrate are still at the final temperature may be described by equation 5.

$$\sigma_{c_{ni}} = \left(\frac{l_{tot}}{l_{0cn}(1+\alpha_c \Delta T_{cn})} - 1\right) * E_c \qquad (5)$$

$\sigma_{cni}$: stress in the i-th coating layer at temp. $T_i$ [Pa]
$l_{0cn}$: length of the deposited coating element [m]
$\Delta T_{cn}$: difference between the temperature at which the i-th coating element was deposited and the final temperature [K]

The stress in the substrate may now be described by:

$$\sigma_{s_{ni}} = \left(\frac{l_{tot}}{l_{0sn}(1+\alpha_s \Delta T_{sn})} - 1\right) * E_s \qquad (6)$$

$\sigma_{sni}$: stress in the i-th substrate element [Pa]
$l_{0sn}$: original length of the substrate element [m]
$\Delta T_{sn}$: absolute temperature substrate element [K]

After the coating substrate combination has cooled down to room temperature, the stress distribution has changed.
The stress in the coating and substrate elements at room temperature can now be described by the next equations:

Coating:

$$\sigma_{ci} = \left(\frac{l_0}{l_{tot}(1-\alpha_c \Delta T_{ci})} - 1\right) * E_c \qquad (7)$$

$\sigma_{ci}$: stress component in coating element due to shrinking process [Pa]
$l_0$: length of the coating substrate combination at room temperature [m]
$\Delta T_{ci}$: temperature of the i-th coating element [K]

Substrate:

$$\sigma_{si}=(\frac{l_0}{(l_{tot}(1-\alpha_s\Delta T_{si})}-1)*E_s$$ (8

$\sigma_{si}$: stress component in substrate element due to shrinking process [Pa]

$\Delta T_{si}$: Temperature of the i-th coating element [K]

**2.2.2 Introduction of primary cooling in this model**

Tensile stresses due to primary cooling as described in paragraph 2.1.1 can not be introduced directly in the above equations. This is caused by the fact that the tensile stress, caused by primary cooling is acting on a single particle, which has a stiffness, equal to the Young's modulus of $ZrO_2$. (190,000 MPa). The coating however, has a far lower stiffness due to porosity and microcracking. The stiffness of a plasma sprayed $ZrO_2$ coating varies between 16,000 and 46,000 MPa. (See paragraph 7.6 of this chapter). For the calculations, using the equations presented in the foregoing paragraphs, the stiffness of the coatings is used.

For that reason, primary cooling is introduced in the model by an extra elastic strain component $\epsilon_p$ in each coating element. $\epsilon_p$ is taken as a constant value for each coating element. This is allowed in the temperature range we consider. The stress, caused by primary cooling only varies slightly in this range.

To obtain force equilibrium in the coating substrate combination, the strain in each substrate element due to primary cooling is equal to :

$$\frac{E_c n_c}{E_s n_s}*\epsilon_p \qquad (9)$$

The stress in the coating and substrate after the coating process is finished (and the coating substrate combination is still at its final temperature) may now be described by:

$$\sigma_{c_{ni}}=(\frac{l_{tot}}{l_{0cn}(1+\alpha_c\Delta T_{cn})}-1+\epsilon_p)*E_c \qquad (10)$$

$$\sigma_{s_{ni}} = \left(\frac{l_{tot}}{l_{0sn}(1+\alpha_s \Delta T_{sn})} - 1 - \frac{E_c n_c}{E_s n_s} * \epsilon_p\right) * E_s \qquad (11)$$

The final stresses in the coating and substrate at room temperature can now be described by:

$$\sigma_{coating_i} = \sigma_{cni} + \sigma_{ci} \qquad (12)$$

$$\sigma_{substrate_i} = \sigma_{sni} + \sigma_{si} \qquad (13)$$

### 2.2.3 Materials

The following calculations concern $ZrO_2$ coatings, sprayed onto Fe, Hastelloy X and AISI 316. The thickness of the substrates was 1,2 and 3 mm. The table contains the relevant physical properties of the substrate and coating materials.

Table 1. Physical properties of substrate and coating materials to be used for the calculations of residual stress

| Material | Young's modulus [MPa] | Poisson modulus [-] | coefficient of thermal expansion [$K^{-1}$] |
|---|---|---|---|
| $ZrO_2$ | 40,000 | 0.3 | 10E-6 |
| Fe | 210,000 | 0.3 | 12E-6 |
| Hastelloy X | 195,000 | 0.3 | 14E-6 |
| AISI 316 | 200,000 | 0.3 | 16E-6 |

### 2.2.4 Temperature curves

On the contrary to the work of Elsing c.s., no time dependent temperature fields are taken into account. This implies that the next coating element will be deposited after the substrate and previously deposited layers have obtained the same temperature. In practice, this is not always true, especially when high deposition rates are applied and thick coatings are

deposited in one pass.
The coatings produced during this research programme however, were sprayed in many passes on rotating and translating substrates, as will be described in this chapter, paragraph 7. Therefore, it is assumed that the time elapse between the passes is sufficient to obtain a uniform temperature in the coating and the substrate [10]. This assumption will be used in the calculations for $ZrO_2$ coating on different substrate materials, which are given in the following paragraphs.

The temperature curves, used for the calculation of the stress in the coatings were based on temperatures, registered during plasma spraying. The temperatures at the end of the spraying process were 320, 250 and 200 C for the substrate thicknesses of 1,2 and 3 mm. It was presumed that the heat, released by the first coating elements is mainly released by conduction. When the coating thickness increases, heat release by conduction decreases, and heat transfer via convection and radiation takes place. This resulted in the temperature fields stated in figure 3.4. These temperature fields are used for the calculation of the residual stresses.

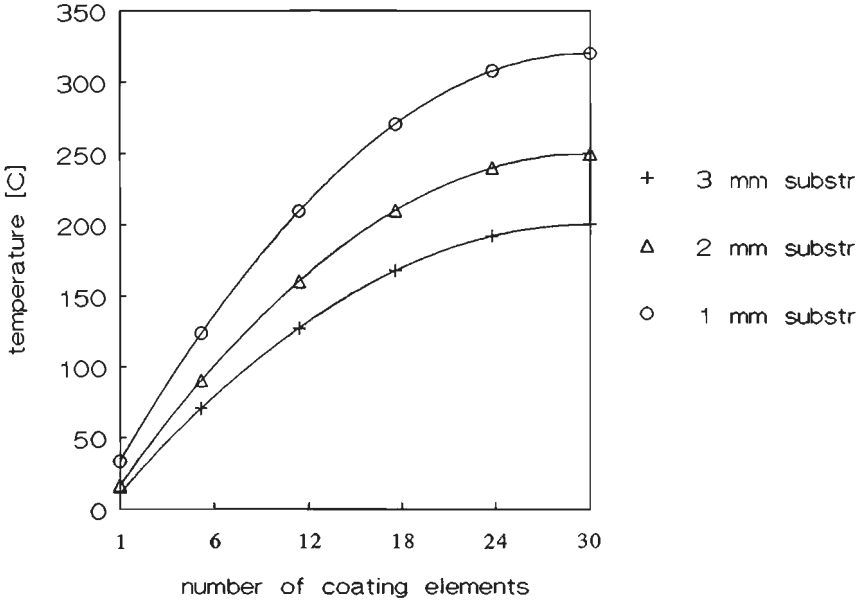


**Figure 3.4** Temperatures used for the calculation of residual stresses. The x-axis shows the number of elements. The temperature indicated for a certain i-th element is the temperature of substrate and coating after the i-th coating element is deposited.

### 2.2.5 Results of the calculations

This paragraph describes the results of the calculations for 0.3 mm $ZrO_2$ coatings sprayed on the substrate materials given above. The coatings were deposited in 30 elements with a thickness of 10 $\mu$m each.

The strains due to primary cooling were chosen as 0.0005, 0.001 and 0.002. These choices are based on the experiments which will be described in paragraph 4.3 of this chapter. Thin, water cooled substrates were coated with a 0.3 mm $ZrO_2$ layer. During spraying, the coating surfaces were cooled by an air jet. For that reason neither heating up of the coating nor of the substrate did exist. Therefore, the stress in the coating, resulting in deformation of the coating and substrate, is caused only by primary cooling effects.

From the deformation, the residual stresses due to primary cooling can be calculated. As a result, the strains can be determined.

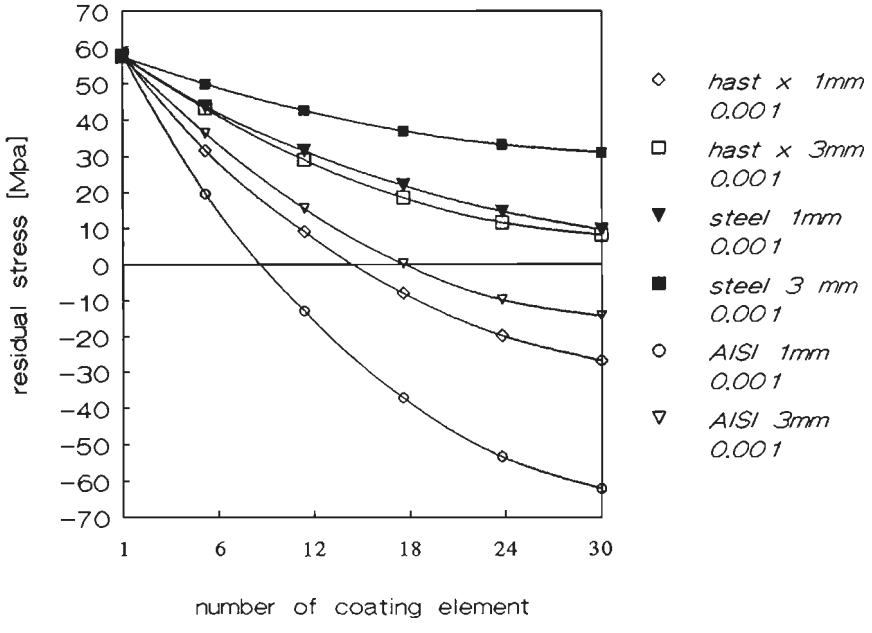


**Figure 3.5** Results of the calculations for 1 and 3 mm substrates of Fe, Hastelloy X and AISI 316. The strain due to primary cooling is 0.001. Residual stresses at room temperature

From the calculations it appeared that the compressive stresses, introduced by the substrate, were maximum at the AISI 316 substrate. This is caused by the great coefficient of thermal expansion of 16 E-6 [$K^{-1}$] of this material.
The stresses in the coatings, sprayed on steel substrates were moderate. The stress gradients over the coating thickness were limited.
Figure 3.5 shows the stress in the coatings on the three substrate materials, with thicknesses of 1 and 3 mm. The strain due to primary cooling was 0.001. It can be seen that the coatings sprayed on steel possess a tensile residual stress, whereas the coatings, sprayed on the AISI 316 substrate possess a stress, varying from tensile at the interface substrate-coating to compressive at the coating's surface.

The coatings sprayed on the Hastelloy X substrate were tensile at the 3 mm substrate and ranged from tensile to compressive at the 1 mm substrate.
The influence of the strain due to primary cooling is shown in figure 3.6.

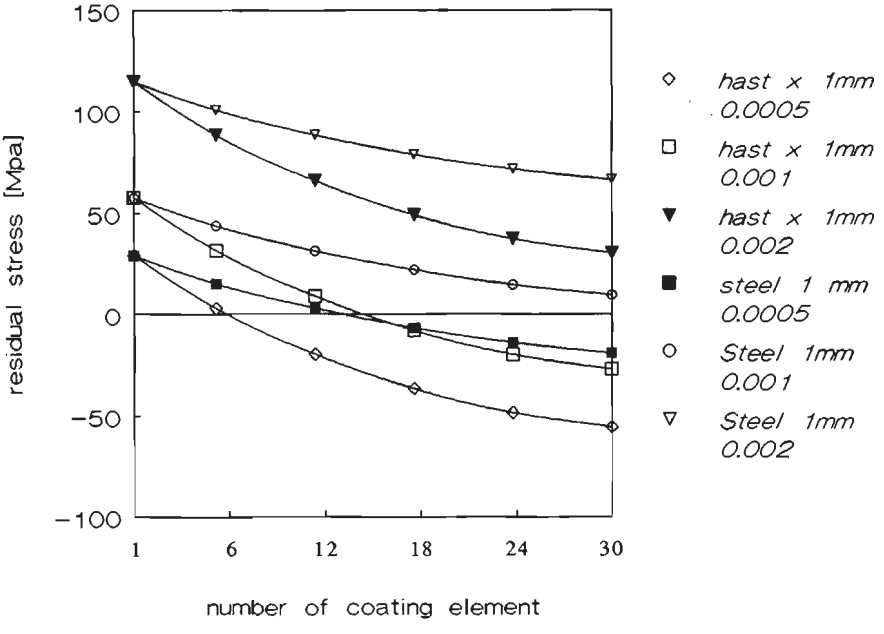


**Figure 3.6** Results of the calculations for 1 mm substrates of steel and Hastelloy X. The figure shows the influence of primary cooling on the residual stress at room temperature.

This figure shows the calculated stresses for 1 mm steel and Hastelloy X substrates: $\epsilon_p$ varies from 0.0005 to 0.002. It appeared that the coatings sprayed on the steel substrates possessed tensile stresses. Only in the case of a strain of 0.0005, the stress ranged from tensile to compressive.
The stress in the $ZrO_2$ layers on Hastelloy X ranged from tensile at the interface to compressive at the coating's surface.
The stress gradient is less in the coatings sprayed on a steel substrate.

From the above calculations it appeared that the coatings sprayed on AISI 316 substrates, possessed the highest compressive stresses. To avoid the formation of these stresses the substrate has to be cooled.

**2.3 The Model of Takeuchi**

The model of Takeuchi c.s. is described in reference [5]. This model takes primary cooling into account by introducing a strain term $\epsilon$, representing strains in the coating, caused by primary cooling. The Takeuchi model uses a uniform substrate temperature and assumes that the entire coating is deposited in one pass.
The stress in the coating at elevated substrate temperatures is described by the equation:

$$\sigma_c(t_c,x,T_s)=Ec\left[\left(\frac{E_c x+E_s t_s}{E_c t_c+E_s t_s}\right)^{\epsilon_e}(1+\epsilon_e)-1\right] \qquad (14)$$

x: position in coating [m]
$E_c$: Young's modulus coating [Pa]
$E_s$: Young's modulus substrate [Pa]
$t_s$: thickness of substrate [m]
$t_c$: thickness of coating [m]
$\epsilon_e$: strain in coating due to primary cooling [-]
$T_s$: substrate temperature [K]

According to Takeuchi, the strain $\epsilon_e$, caused by primary cooling equals:

$$\epsilon_e=\alpha_c(T_m-T_s) \qquad (15)$$

$\alpha_c$: coefficient of thermal expansion coating
$T_m$: melting point coating material

When the stress, caused by primary cooling, exceeds the yield or tensile strength of the coating material, $\epsilon_e$ has to be derived from the stress strain curve of that material.

After cooling down to room temperature, the stress in the coating is equal to:

$$\sigma_c(t_c,x,T_s)=E_c\left[\frac{(1+e_e)(\gamma+1)}{\beta+(\gamma+1)^{1+e_e}-1}\left(\frac{E_c x}{E_s t_s}+1\right)^{e_e}-1\right] \qquad (16)$$

$$\beta=\frac{1-\alpha_c(T_s-T_r)}{1-\alpha_s(T_s-T_r)} \qquad \gamma=\frac{E_c t_c}{E_s t_s} \qquad (17)$$

$T_s$: substrate temperature [K]
$T_r$: room temperature [K]
$\alpha_s$: coefficient of thermal expansion substrate [$K^{-1}$]

**2.3.1 Calculations and results of the calculations**

The equations stated above are used for the calculation of residual stresses in $ZrO_2$ coatings, sprayed onto Fe, Hastelloy X and AISI 316. The thicknesses of the substrates are 1,2 and 3 mm. The temperatures for these thicknesses were 320, 250 and 200 °C respectively.

Figure 3.7 gives the results of the calculations for 2 mm substrates of steel, Hastelloy X and AISI 316. The substrate temperature is 250 °C. It appears that the coatings sprayed on steel, possess tensile stresses whereas the coatings, sprayed on Hastelloy X and AISI 316 possess mainly compressive stresses.
The stress gradient over the coating thickness is negligible. This is caused the Takeuchi model which is based on the assumption that the substrate has a uniform temperature $T_s$ before the coating is deposited.

**2.4 Stresses in $ZrO_2$ sprayed on cooled substrates**

Figure 3.8 shows the results of calculations of $ZrO_2$ coatings sprayed on cooled substrates. It is presumed that the substrate temperature stays at room temperature during the coating process. The thickness of the Hastelloy X substrates is 3 mm. The strains due to primary cooling are 0.0005, 0.001

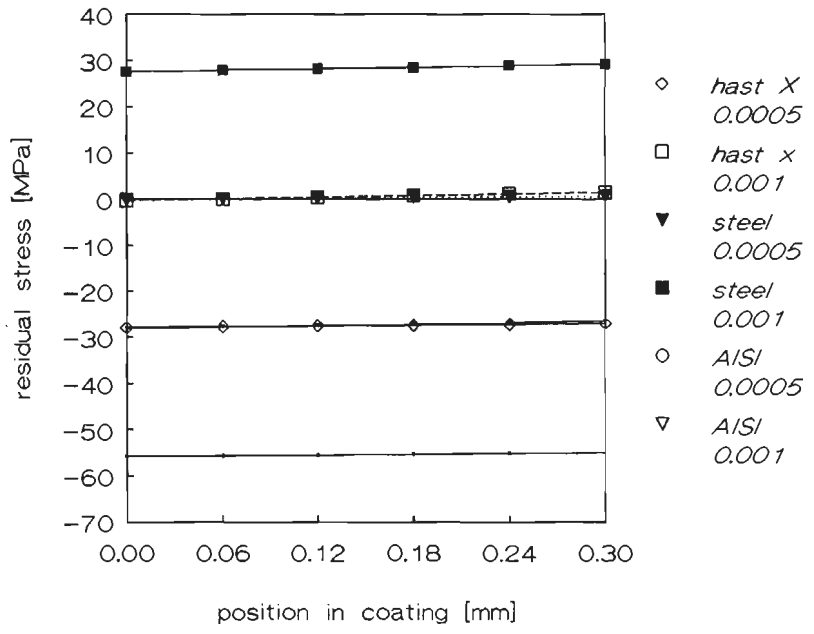


**Figure 3.7** Results of the calculations, using the Takeuchi model for 2 mm Fe, Hastelloy X and AISI 316 substrates. The strains due to primary cooling are 0.0005 and 0.001

and 0.002 mm. Both the modified model of Elsing and the Takeuchi model were used. It is shown that the values calculated by both models agree well. Furthermore it is shown that substrate cooling leads to a coating, possessing only tensile stresses. This may be positive when the coatings are subjected to severe thermal shock loading.

**2.5 Comparison of the Takeuchi model and the modified model of Elsing.**

Figure 3.9 shows the residual stresses in 0.3 mm $ZrO_2$ coatings on a 2 mm Hastelloy X substrate. The strains due to primary cooling were 0.0005, 0.001 and 0.002.

It can be seen that the stresses in the coating's surface almost agree, but that the stress on the interface substrate-coating differs distinctly.
The assumption of Takeuchi, not to take into account a temperature-time history leads to a prediction of an almost equal stress distribution throughout the whole coating.

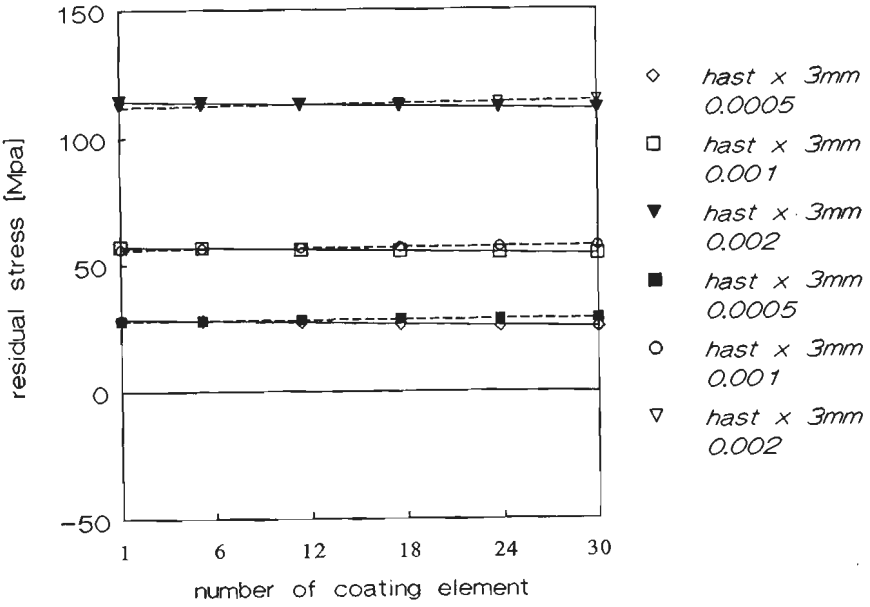


**Figure 3.8** Stresses in $ZrO_2$ coatings, sprayed on **cooled** 3 mm Hastelloy substrates. Strain due to primary cooling 0.0005, 0.001, 0.002. Results of the modified Elsing model and Takeuchi model (dashed lines)

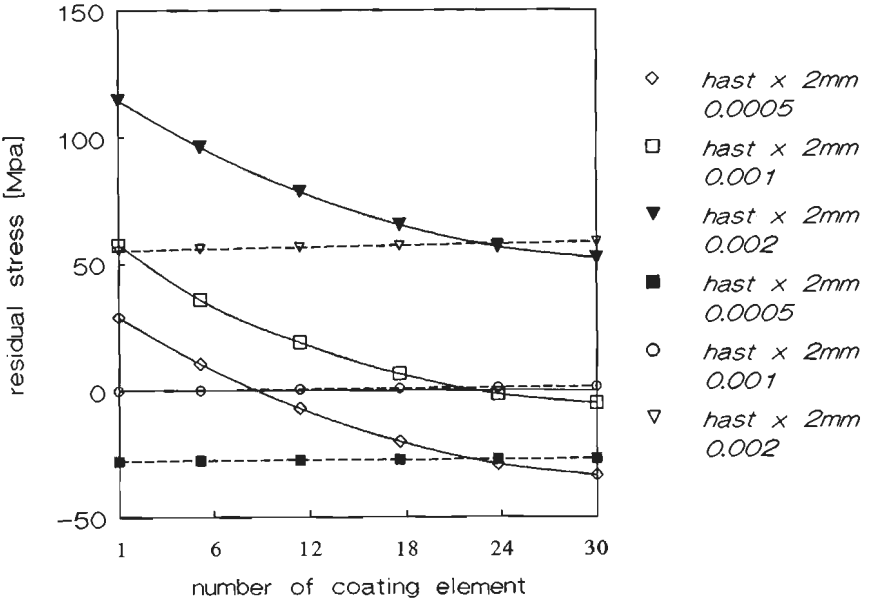


**Figure 3.9** Comparison of the stresses, calculated by the modified Elsing model and the Takeuchi model. 2 mm Hastelloy X substrate, strains 0.0005, 0.001, 0.002.

Although the modified model of Elsing uses a simplified assumption of the time-temperature history during the coating process, it has to be regarded as more accurate than the Takeuchi model.

**3 Stress measurements, using X-ray diffraction techniques.**

The next paragraphs describe the principles and results of stress measurements on plasma sprayed $ZrO_2$ coatings, using the $\sin^2 \psi$ method. This measurements were carried out at Delft University of Technology and at Karlsruhe University. The measured values are compared to values, reported in literature.

**3.1 Principle**

In each crystalline material, the atoms are arranged in periodic planes with a fixed distance "d" to each other.

This distance depends on the direction of the planes. For a material with a tetragonal crystal structure, d is given by the equation:

$$\frac{1}{d^2} = \frac{h^2 + k^2}{a^2} + \frac{l^2}{c^2} \qquad (18)$$

d: distance between the planes of atoms for a certain direction (h,k,l) of those planes

a, c: lattice parameters of a tetragonal unity cell [m]

h,k,l direction of the planes

When x-rays impinge on the atoms of a material, they will be scattered. When the scattered rays of the different planes of atoms meet each other, interference will occur. The waves may extinct or strengthen each other. Figure 3.10 shows this principle.

From this figure it can be derived that diffraction for a certain set of plains with the direction (h,k,l) will occur when the next condition is fulfilled:

$$n\lambda = 2d\sin\theta \qquad (19)$$

n: integral multiple of the radiation wave length.

$\lambda$: wave length of the radiation [m]

d: distance between the planes

$\theta$: angle at which diffraction occurs

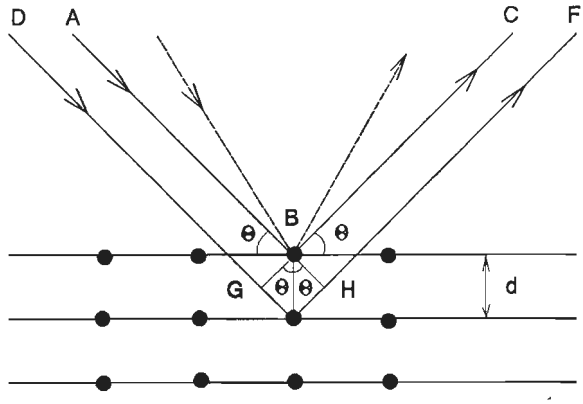


Figure 3.10 Schematic representation of the Bragg law.

Equation 19 is known as Bragg's law. It states that diffraction for a certain wave length of the X-rays and a certain direction of the planes of atoms will occur at a certain angle θ. The set of diffraction angles θ of the lattice planes of a certain material, is unique for that material.

The X-ray diffraction method for the determination of the residual stress is based on the following principle.
When an elastic body is subjected to a load, elastic deformation will occur. As a result, the distance between the lattice planes will change. This implies that the angle θ at which diffraction occurs, for that direction of planes also changes. By measuring the shift of the angle θ, the change of the distance d can be determined and the strain caused by the stress can be calculated.

Consider the situation which is given in figure 3.11. A specimen is subjected to a compressive stress as indicated in the figure. This implies that the distance d between the planes of atoms, parallel to this stress, increases. In the situation shown in part A, the diffraction angle for a set of planes, parallel to the surface of the sample is determined. Subsequently, the specimen is tilted over an angle ψ. Diffraction occurs now from other grains but than from planes with the same direction as in situation A. The distance between the planes however is different, since these planes are not parallel to the direction of the stress. As a result, a shift of the position of the diffraction peak takes place.
The distance d, for this value of θ can now be calculated.

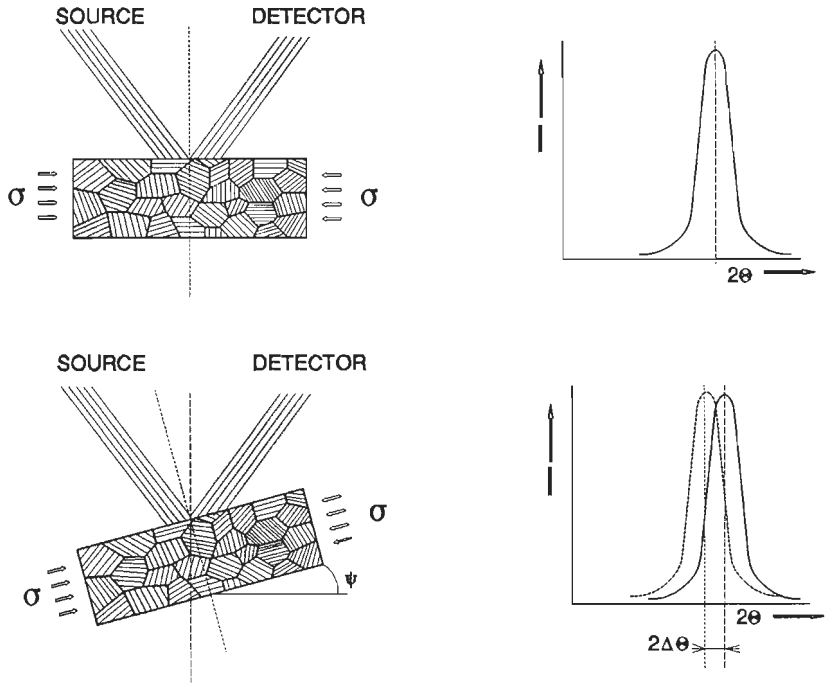


**Figure 3.11** Principle of the $\sin^2 \psi$ measurement. a) shows the diffraction peak of a certain set of planes {h,k,l}. b) shows the diffraction peak for the same planes, but now the specimen is tilted over an angle $\psi$. [11]

The procedure, described above is repeated for a number of values of $\psi$. The values of d versus $\sin^2 \psi$ are plotted in a figure, a so called $\sin^2 \psi$ plot. The coefficient of direction of the $\sin^2 \psi$ plot is an indication for the stress in the specimen. Figure 3.12 shows a $\sin^2\psi$ plot of a $ZrO_2$ coating under tensile stress. The different angles, involved with the stress measurement are indicated in fig 3.13.

The stresses can now be calculated using the equation:

$$\sigma_\varphi = \frac{E}{(1+\nu)\sin^2\psi} \cot\theta \Delta\theta \qquad \frac{\Delta d}{d} = -\cot\theta \Delta\theta \tag{20}$$

$\sigma_\phi$: stress in a plane in the direction $\phi$ [MPa]
E: Young's modulus [Mpa]
$\upsilon$: poisson modulus [-]
$\Delta\Theta$: shift of the diffraction peak.
$\Delta$d: decrease or increase of d.

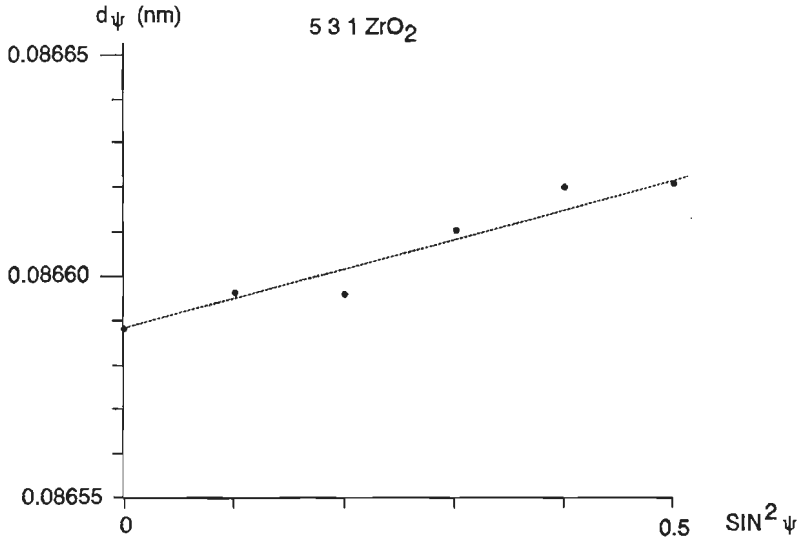


**Figure 3.12** $\sin^2\psi$ plot of a 20 μm $ZrO_2$ coating on a Hastelloy X substrate.

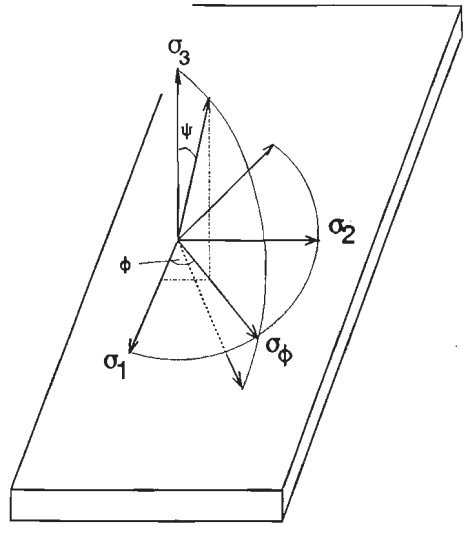


**Figure 3.13** Definition of the angles used for the $\sin^2\psi$ measurements [11]

Since the accuracy of this measurement technique increases with increasing value of 2θ, the measurements are preferably carried out using diffraction peaks with a great diffraction angle.

### 3.2 Specimens

The specimens for the stress measurements consisted of a Hastelloy X substrate with a 0.1 mm FeCrAlY bondcoat and a
$ZrO_2$ topcoat with variable thickness. Besides, some specimens without a bondcoat were measured.
The specimens were sprayed using the equipment, shown on figure 3.14. The Hastelloy X substrates, with a dimension of 1.6*20*18 mm, are clamped on brass substrate holder. This substrate holder translates and rotated. In this way it possible to produce $ZrO_2$ coatings with a thickness of 10 $\mu$m.
Due to the fact that the substrates are in contact with the brass substrate holder, the temperature of the substrates during the coating process stays low.

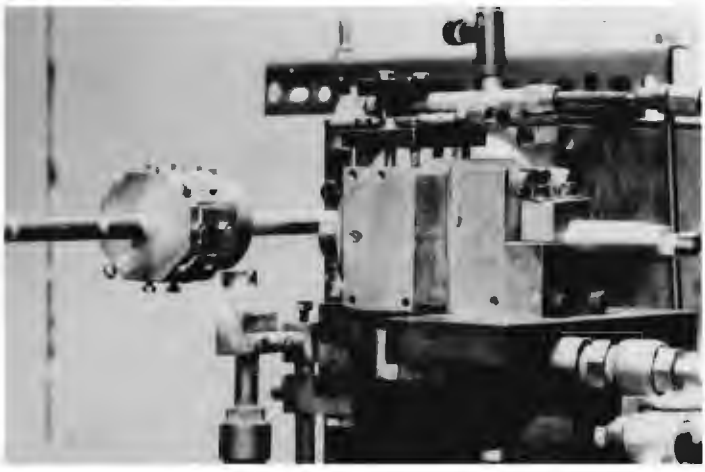

**Figure 3.14** Set up for the spraying of the specimens for the X-ray stress determination. The substrate holder is made of solid brass.

### 3.3 Results of the measurements

The measurements at Karlsruhe University were carried out, using the following parameters:

| | |
|---|---|
| Radiation: | $Cr_{k\alpha}$ |
| Mean depth of penetration: | 1.8 $\mu$m |
| Direction of planes: | {331/313} |
| $2\Theta_0$: | 153.500 ° |

| | |
|---|---|
| E: | 190,000 [MPa] |
| ν: | 0.3 [-] |

The measurements at Delft University were carried out using the following parameters:

| | |
|---|---|
| Radiation: | $Cu_{k\alpha}$ |
| Mean depth of penetration: | 6 $\mu$m |
| Direction of planes: | {531} |
| $2\Theta_0$: | 125.000 |
| E: | 190,000 [MPa] |
| ν: | 0.3 |

Table 2 shows the results of the measurements.

Table 2.
Results of the X-ray diffraction stress measurements at $ZrO_2$ coatings, sprayed on Hastelloy X substrates.

| bondcoat FeCrAlY | topcoat $ZrO_2$ | stress Karlsruhe [MPa] | stress Delft [MPa] |
|---|---|---|---|
| none | 10 $\mu$m | 94 +/- 17 | 141 |
| none | 20 $\mu$m | 104 +/- 7 | 153 |
| 100 $\mu$m | 10 $\mu$m | 92 +/- 6 | 87.7 |
| 100 $\mu$m | 60 $\mu$m | 32 +/- 7 | - |
| 100 $\mu$m | 300 $\mu$m | 40 +/- 7 | - |

This table indicates that there exists a difference between the measurements from Delft and Karlsruhe University. Only in the case of the 10 $\mu$m $ZrO_2$ layer on the FeCrAlY bondcoat, the measurements agree.

**3.4 Discussion**

There may be two reasons for the discrepancy of the measurements. First,

the depth of penetration of the Cr radiation is less than the penetration depth of the Cu radiation. This implies that the measurements made with Cr radiation mainly concern the upper 2 $\mu$m of the coating thickness. On the contrary, the measurements, using Cu radiation, concern a coating thickness of about 8 $\mu$m.

The $ZrO_2$ coatings have a very rough surface. This implies that the measurements made with a shallow depth of penetration concern the rough peaks at the surface which were able to relief their stresses.

When a greater depth of penetration is applied, the bulk stresses in the coating are measured. Because of the fact that the bulk material is fully surrounded by solid material it does not possess the ability for stress relief and hence maintains a higher level of residual stress. Figure 3.15 elucidates this principle.

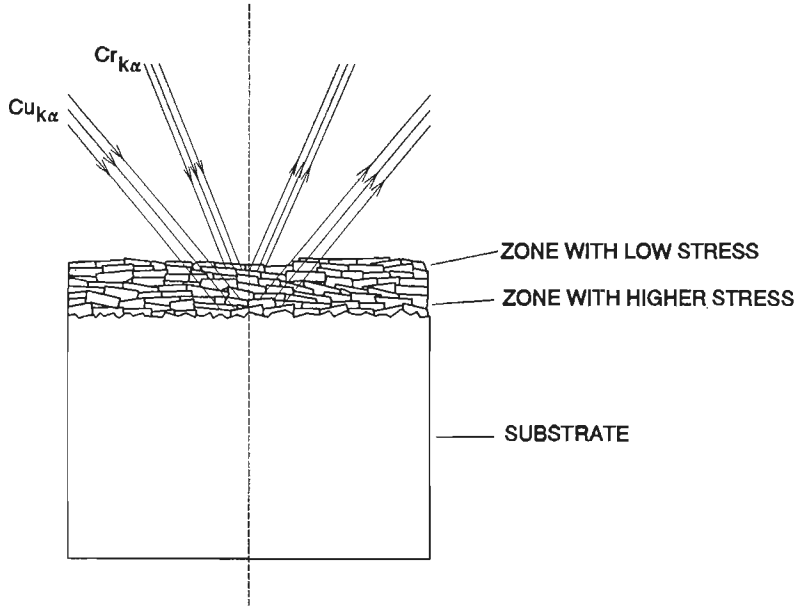


**Figure 3.15** Stress measurement at a plasma sprayed coating. The $Cr_{k\alpha}$ radiation had a low depth of penetration. So only the stresses in the surface particles were measured. These particles are not surrounded by other particles

Secondly, the measurements made with Cr radiation took place at a higher Bragg angle than the measurements with Cu radiation. The accuracy of measurements, increases with increasing values of $2\theta$. This, however, does

not explain the great differences between the two measurements.

### 3.5 Comparison with values reported in literature

Noutomi c.s. [12] report about the measurement of residual stresses in plasma sprayed $ZrO_2$ and NiCr coatings.
The measurements were carried out on the {331} planes using Cr radiation. The stresses measured in the $ZrO_2$ coatings, were almost negligible and were found to be independent of the coating thickness.
Zaouali [13] reports about measurements at 0.24 mm $ZrO_2$ coatings on Hastelloy X substrates. The stresses which were measured over the coating thickness, varied from 80 MPa at the interface to 40 MPa at the coating's surface. He used $Fe_{k\alpha}$ radiation. The coating was thinned by diamond polishing.
Richter [14] reports about measurements, carried out on 0.25 mm $ZrO_2$ coatings on Inconel 100. Before spraying, the substrates were preheated to 400 °C. The coatings, which were measured with both Cr and Cu radiation, showed low compressive stresses, -3 to -5 Mpa. The difference between the measurements made with Cr and Cu radiation was low. It has to be remarked that the coatings had a low roughness; about 1 $\mu$m.

From the values reported in literature, it can be remarked that the stresses in plasma sprayed $ZrO_2$ coatings are rather low. The order of magnitude of the stresses agrees well.

The Young's moduli used by the authors, differed strongly and were often related to the micro structure of the coatings, e.g. to porosity and to micro-cracking. The X-ray stress measurements however, concern the distance between the planes of atoms in the material. The change of the distance d between the planes of atoms is related to the stress by the bulk Young's modulus of the material and does not depend on its microstructure. For this reason, it is advisable to use the bulk modulus of elasticity for X-ray diffraction stress determination.

## 4 Experimental determination of the residual stress in plasma sprayed $ZrO_2$ coatings.

### 4.1 Introduction

The following paragraphs give a first introduction to a mechanical method for the determination of residual stresses in plasma sprayed $ZrO_2$ coatings. Some provisional results will be presented.

When an initially straight, thin metallic strip is covered with a plasma sprayed coating, the strip will deform due to the residual stresses, caused by the spraying process. From the curvature of the initially straight strip, the residual stresses in both the coating and the substrate can be calculated.

### 4.2 Experimental set up

When a strip shaped substrate is coated, it is possible that the heat front, caused by the solidifying and cooling particles not only moves in the direction perpendicular to the substrate, but also laterally. It is thus possible that the heat front travels ahead of the particle jet. This may result in a preheated substrate on which the first particle layer is deposited. To avoid this, the translation velocity of the plasma torch has at least to be equal to the lateral velocity of the heat front. Blok [15] states that heat transport will mainly take place in a direction perpendicular to the direction of movement of the heat source, when the Peclet number is greater than 10. The Peclet number is defined as:

$$Pe = \frac{R * V_t}{a} \tag{21}$$

Pe: peclet number [-]
R: radius of the heat source [m]
$V_t$: translation velocity of the source [$ms^{-1}$]
a: thermal diffusivity of substrate material [$m^2s^{-1}$]

From the above equation, the minimum required translation velocity of the plasma torch can be calculated. For the substrate materials: steel, Hastelloy X and AISI 316, these velocities are 25, 3 and 6 mm/s, respectively.

The statement of Blok, that the Peclet number has to be greater than 10, is valid for a semi-infinite body. In our case, we are dealing with thin strips. For this reason, the translation velocity of the plasma torch has to be higher than the calculated values.

In order to reach the high translation velocities, thin walled (1 or 2 mm) rings, with a diameter of 50 mm and a width of 15 mm, instead of straight metallic strip were used. These rings were mounted on a rotating substrate holder which could rotate at any speed. The rings were coated with a 0.3 mm $ZrO_2$ coating.
During the coating process, the inside of the substrate rings could be water cooled, whereas the coating's surface could be cooled by an air jet. When no cooling was applied, the temperatures as used in the calculations for non-cooled specimens were reached.

Apart form the problems with the lateral heat flow, there exist practical problems when spraying plates or strips.
The plasma torch or the substrate have to move in a plane, accelerating and decelerating again and again. Secondly, the crossection of the deposited track, which is shown in figure 3.16, makes it difficult to obtain a uniform layer thickness when the coating is deposited on a flat plate or strip. These problems can be encountered by spraying rotating and translating ring shaped substrates.

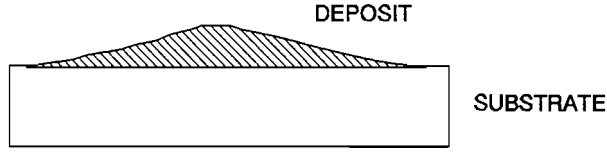


**Figure 3.16** Cross section of the deposition trace of splashed particles, produced by plasma spraying.

The rings were made of steel, Hastelloy X and AISI 316.
The steel rings were made of steel tube and had a wall thickness of 1 and 2 mm. The Hastelloy X and AISI 316 rings were made of 1 mm sheet, which was rolled to rings. The ends were joined together by welding. To improve the adherence of the plasma sprayed coating, the substrates were grit blasted.

Subsequently the rings were annealed to remove residual stresses, present in the tube and sheet material due to its fabrication and caused by grit blasting. After the rings had been annealed, some of them were sectioned as indicated in figure 3.17. Since the width of the slit was equal to the width of the disk saw, it was assumed that the rings were free of residual stresses.
Subsequently, the rings were coated with a 0.3 mm $ZrO_2$ coating. The adherence of the $ZrO_2$ coating to the Hastelloy X and AISI 316 rings was bad. Especially at the edges of the rings, spalling of the coating was observed. The coatings on the steel substrates, on the contrary, showed a good adherence.

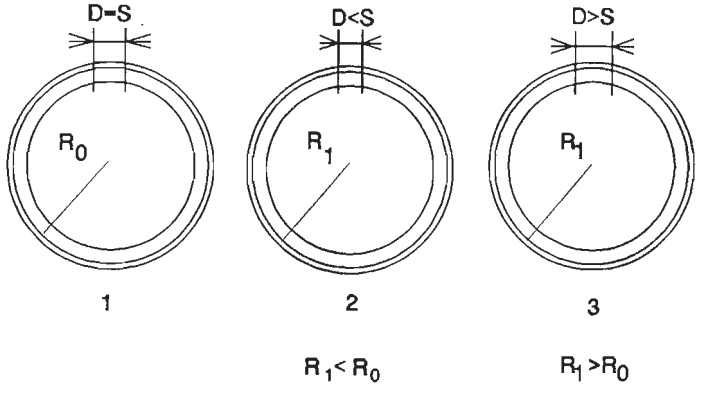


**Figure 3.17** Cross sections of thin metallic rings with a plasma sprayed coating. The rings are sectioned by a saw-cut with width "S". If the specimen is stress free, the opening "D" is equal to "S". If the coating possess residual tensile stresses than "D"<"S". In the case of residual tensile stress "D">"S"

From the above, it may be concluded that the adherence of the $ZrO_2$ coating to Hastelloy X or AISI 316 is bad when the substrates were annealed after they are grit blasted. This may be caused by two reasons: firstly, the substrates may be covered with a thin oxide layer, formed during annealing, despite the fact that they were annealed in vacuum, and secondly, as a result of the annealing process, the reactivity of the surface decreased. (See also paragraph 5.2 of this chapter).

To encounter the problem of the bad adherence, the Hastelloy X and AISI 316 substrates were covered with a plasma sprayed 20 to 30 $\mu$m FeCrAlY

layer. Subsequently, the substrates were annealed as described above. The application of this thin bondcoat resulted in a good adherence of the $ZrO_2$ topcoat. No spalling at the specimen's edges was observed.
Microscopical examination of cross sections showed that the adherence was good on both the Hastelloy X and AISI 316 substrates.

**4.3 Results**

It has to be remarked that the stress in the closed rings can not be calculated directly by the models which were presented in the foregoing paragraphs. For this reason, the stresses in the rings were estimated using models derived by 't Hart [16] and Kouyumdiyev [17]. These models are given in appendix B-I. These model was adapted to a closed ring. Although this model differs from the models previously used, it gives an indication of the residual stresses in the $ZrO_2$ coating.

After deposition of the coating, the rings were cut through as indicated in figure 3.17, and the width of the slit was measured by a measuring microscope.

Table 3 shows the decrease or increase of the width of the slit in the different substrates.

The table shows that the opening in the cooled rings is almost the same for all three 1 mm substrate materials. This indicates that the residual tensile stresses in the cooled coatings are almost equal. Since both the substrate and the coating's surface were cooled during spraying, the whole specimen was kept at room temperature during the spraying process. For this reason, it may be assumed that the tensile stresses in the cooled coatings are caused by primary cooling.

The non-cooled specimens showed another behaviour than the cooled ones. The 1 mm steel ring showed a closure, whereas the non-cooled Hastelloy X and AISI rings showed almost no closure.
The cooled, 2 mm steel specimen showed an increased saw cut width, indicating residual tensile stresses, whereas the width of the slit in the non-cooled 2 mm steel specimen was equal to the saw cut width, indicating that the residual stresses in the coating are very low.

Table 3.
Slit width minus saw-cut width in the specimens for stress determination. The saw-cut width was 0.78 mm

| No | Material | thickness [mm] | cooled | change of slit width [mm] |
|---|---|---|---|---|
| 1 | Steel | 1 | yes | 0.73 |
| 2 | Hastelloy X | 1 | yes | 0.76 |
| 3 | AISI 316 | 1 | yes | 0.8 |
| 4 | Steel | 2 | yes | 0.18 |
| 5 | Steel | 1 | no | -0.53 |
| 6 | Hastelloy X | 1 | no | -0.01 |
| 7 | AISI 316 | 1 | no | -0.03 |
| 8 | Steel | 2 | no | 0.01 |

The following table shows the results of the stress calculations. These calculations were made for the rings which showed a distinct change in curvature when they were cut.

Table 4
Stresses in the $ZrO_2$ coating on a ring shaped substrate
The specimen numbers correspond with the numbers of table 3.

| No | substrate | cooled | mean stress [MPa] |
|---|---|---|---|
| 1 | steel 1 mm | yes | 25.2 |
| 2 | Hast X 1mm | yes | 27.9 |
| 3 | AISI 316 1mm | yes | 28.8 |
| 4 | Steel 2 mm | yes | 31.5 |
| 5 | Steel 1 mm | no | -23.2 |

This table shows that the residual tensile stresses in the coatings, sprayed on cooled substrates, have the same order of magnitude.
The non-cooled 1 mm steel specimen shows compressive residual stresses. The residual stress in the coating on the non-cooled 2 mm steel substrate was negligible.
The stresses in the coatings on the cooled substrates are in accordance with the stresses which were calculated by the model presented in the foregoing paragraphs, using a strain due to primary cooling of 0.0005. The stresses in the non-cooled specimens with steel substrates are higher than predicted by the model.

**4.4 Discussion**

The fact that the tensile stresses in the $ZrO_2$ coatings, sprayed on several cooled substrate materials, were almost equal indicates that these stresses are caused by primary cooling.
The $ZrO_2$ coatings, sprayed on the non-cooled steel substrates showed higher compressive stresses than was expected. (-2 Mpa for the 1 mm substrate ). This may be caused by the presence of vertical cracks in these coatings. The cracks developed due to tensile stresses during the coating process. Due to the presence of these cracks, the influence of residual tensile stresses, caused by primary cooling, is reduced.

The fact that there occurred almost no closure of the slits in the non-cooled specimens with Hastelloy X and AISI 316 substrates indicated that residual compressive stresses are almost absent. This is in contradiction with the calculations made in the foregoing paragraphs. These calculations predicted the highest residual compressive stresses in the $ZrO_2$ coatings sprayed on Hastelloy X and AISI 316 substrates. This can be explained by the fact that the temperature in the specimens with the AISI 316 and Hastelloy substrate is not uniformly distributed before the next coating layer is deposited. Because of this, the coating has a higher temperature than the substrate and will shrink more than the substrate on cooling down to room temperature, resulting in a tensile stress in the coating, compensating the compressive stresses caused by the substrate. The fact that no uniform temperature distribution occurred, can be caused by the presence of the thin bondcoat. This bondcoat, which contains a lot of oxide films, act as a thermally insulating layer. Secondly, the Hastelloy X and AISI substrates have a far

lower thermal diffusivity than the steel substrates (steel 2.1 E-5, Hastelloy X 2.4 E-6, AISI 316 4.8 E-6).
Because of this, the model which was presented in the foregoing paragraphs has to be adapted to non-uniform temperature distributions, occurring during the plasma spray process. This makes it necessary to measure those temperature fields continuously during the coating process.

## 5 Spraying of the Thermal Barrier Coatings

The following paragraphs describe the production of the thermal barrier coatings. First an introduction of the used coating and substrate materials is given.

### 5.1 Materials

#### 5.1.1 Substrate materials

Thermal barrier coatings to be used in gas turbines are mainly sprayed on super alloys. In this research programme, Hastelloy Alloy X has been used. This nickel base super alloy is mainly applied for the construction of combustion chambers and combustion liners and is delivered as a sheet material.
Hastelloy X has as a super alloy a rather low thermal expansion coefficient of 14E-6 $K^{-1}$ and has the next nominal composition
Cr 22.0; Fe 19.0; Mo 9.0; Mn 1.0; W 0.6; Ni balance (wt%).

#### 5.1.2 Bondcoat materials

The bondcoat was made of FeCrAlY or NiCrAlY.
FeCrAlY is mentioned as the MCrAlY alloy with the best alumina forming properties [20]. Furthermore FeCrAlY performs well in sulfidizing environments.
The FeCrAlY (Amdry 970 F) has the nominal composition:
Cr 25; Al 9.5; Y 0.4, Fe balance (wt%).
The grain size ranged from 22.5 to 45 $\mu$m.
The NiCrAlY (Hermann Starck, Amperit 413.2) has almost the same

composition as the FeCrAlY with Ni instead of Fe.
Nominal composition NiCrAlY: Cr 22; Al 10, Y 1.0, Ni balance.
Grain size 45-90 $\mu$m. This NiCrAlY alloy is applied as a bondcoat material in many stationary and aircraft gas turbines.

### 5.1.3 $ZrO_2$ topcoat

All the ceramic topcoats were produced using partially stabilized $ZrO_2$; Starck Amperit 825.1. This pre-alloyd powder has the nominal composition: $Y_2O_3$ 7.6; $ZrO_2$ balance (wt%). The grain size is 22.5-45 $\mu$m.
$ZrO_2$, partially stabilized with 7-8 wt% $Y_2O_3$ is regarded as the thermal barrier material with the highest thermal shock resistance. ( See Chapter I, paragraph 2.3.1)

In this chapter always the term $ZrO_2$ is used for the $ZrO_2$ 7.6 wt% $Y_2O_3$ material.

## 6 General

The coatings described in the following paragraphs were all sprayed using the TUE plasma torch as described in chapter 2, paragraph 2.2. The used anode channels had a diameter of 8 mm. The spraying distance was kept at 100 mm. This distance is defined as the length between the injection point of the powder and the surface of the specimen to be coated.
In the case of the 120 mm extended anode channel the spraying distance was 175 mm.

### 6.1 The application of air shields.

An air shield is a flow of high velocity air with a thickness of 0.5-1 mm and a width of 30 mm. The air shield is placed between the plasma torch and parallel to the substrate at a small distance (5 mm) from the substrate surface. (See figure 3.18).
The air shield removes light oxides and metal or ceramic vapour from the particle jet and avoids them to be deposited on the substrate or previously deposited layers. Condensation or deposition of vapour or dust on the surface to be coated may result in bad adherence or separation between the coating layers.

Since the air shield blows away an important part of the plasma gasses,

heating up of the substrate and coating during the spraying process, caused by these gasses is reduced distinctively.

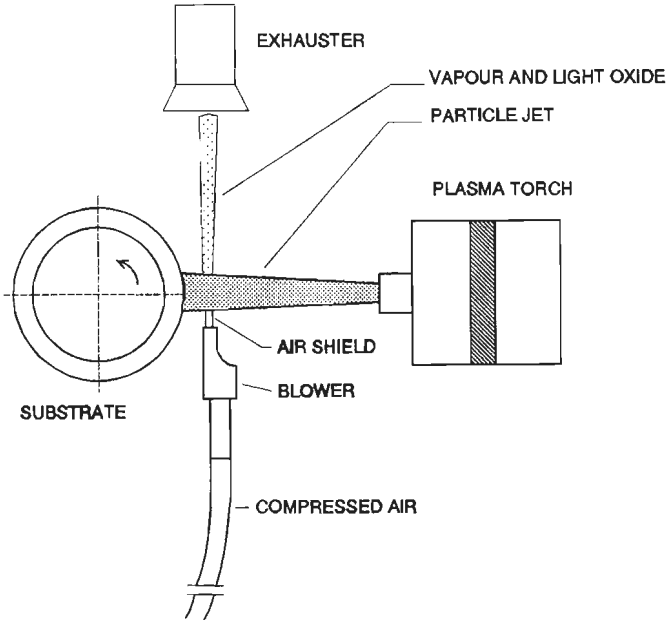


**Figure 3.18** Air shield, placed between the plasma torch and the substrate. The air shield removes vapour and light oxides out of the particle jet. (Air shield technique developed at TUE laboratory [22])

The application of an air shield has only a slight influence on the particle's trajectory and on its temperature. Due to the minor thickness of the air flow, deviation of the particles, caused by drag forces from the fast moving air may be neglected. The loss of heat of the particle caused by the air jet may also be neglected. The time the particle moves through the air jet (5 E-6 s for a particle possessing a velocity of 150 $ms^{-1}$) is much less than the heat absorption time and the heat supply time as described in chapter 2, paragraph 2.1.

### 6.2 Preparation of the substrates

The Hastelloy X substrates used in this research programme had dimensions of 125*30*1.6 mm for the bending specimens (See chapter IV) and 125*30*3.2 mm for the thermal shock specimens. The 3.2 mm substrates were cut out of the sheet material by laser machining. The substrates were

ultrasonically cleaned in acetone and thereupon grit blasted with alumina. This grit blasting has several reasons. First, the surface is roughened which improves the mechanical anchoring of the bondcoat particles. Secondly, the concentration of vacancies at the substrate's surface is increased by the plastic deformation due to the grit blasting process. This leads to an increased reactivity of the surface, which may result in an improved adherence of the impinging particles. Furthermore, the surface is cleaned from oxides, which were not removed during the ultrasonic cleaning.
Grit blasting has to be done just before the beginning of the spraying process.

**7 Production of the specimens for bending and thermal shock testing**

The Hastelloy X substrates were mounted on a cylindrical substrate holder. This holder rotated and translated. The rotating and translating speeds were controlled in such a way that the required coating thicknesses of both the bond coat and top coat were obtained in a prescribed number of passes of the plasma torch. The substrate holder could be cooled by the injection of a water flow. This water was in direct contact with the backside of the substrates to be coated. This resulted in an optimal cooling of the substrates during the coating process.

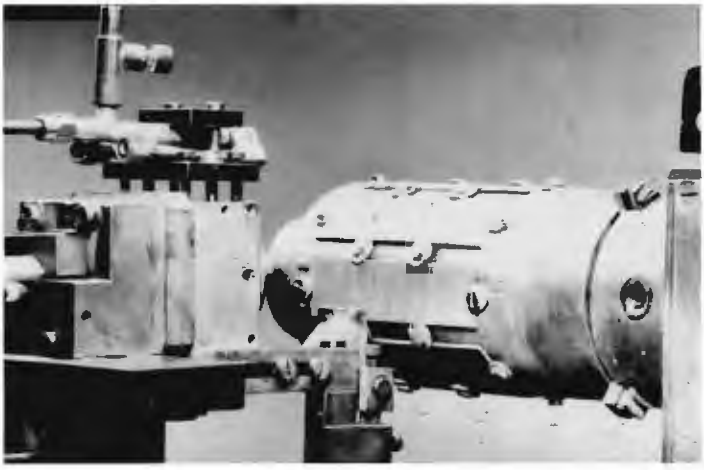

**Figure 3.19** Photograph of the set up used for the production of specimens for thermal shock and bend testing. The substrate holder can be cooled by water.

Apart from the water cooling, cooling of the coated surface took place by an air flow, directed radially to the coated surface. With both the air and substrate cooling, the temperature of the specimens could be kept at a level of 20-25 °C. Figure 3.19 shows the set up used for the spraying of the specimens.

### 7.1 Spraying of the bondcoats

The FeCrAlY bond coats were sprayed by air plasma spraying (APS) and low pressure plasma spraying (LPPS). The NiCrAlY bond coats were produced by air plasma spraying.

#### 7.1.1 Air plasma spraying of FeCrAlY and NiCrAlY.

The bondcoats were sprayed using the standard anode channel.
The 0.1 mm coatings were applied in one pass of the plasma torch. The application of an air shield was necessary to
avoid severe contamination of the coating's surface with condensed vapour and oxides.
The application of an extended anode channel for the spraying of the bondcoat materials was not successful. The particles were strongly overheated, resulting in a high concentration of vaporized metal.
The next plasma spray parameters for both the FeCrAlY and NiCrAlY were used:

| | |
|---|---|
| I: | 500 Amps |
| V: | 58 V |
| Ar | 50 Sl/min. |
| $H_2$: | 8 Sl/min |
| Powder feed rate: | 30 grams/min |
| Spraying distance: | 100 mm |

#### 7.1.2 Low pressure plasma spraying of FeCrAlY

LPPS was carried out at the "Institut für Werkstoff-Wissenschaften" at Aachen University of Technology.
After the substrates were mounted in the vacuum tank, this tank was evacuated. After evacuation, a constant argon pressure of 200 mbar was maintained. Before starting the spraying process, the substrates were cleaned by a transferred arc between the plasma torch and the substrates.
After cleaning the substrates were preheated to 800 °C (They became just

orange coloured) and the spraying process was started. The coating thickness of 0.1 mm was obtained in six passes of the plasma torch. After spraying, the specimen were cooled down to room temperature in an argon atmosphere. The following plasma spray parameters were used for the LPPS process:

| | |
|---|---|
| I: | 700 Amps |
| V: | 35 V |
| Ar: | 30 Sl/min |
| He: | 40 Sl/min |
| $H_2$: | 10 Sl/min |
| spraying distance: | 250 mm |
| anode diameter: | 6 mm |

**7.2 Spraying of the $ZrO_2$ topcoat**

The zirconia coatings were air plasma sprayed using a standard and a 20 mm extended anode channel and different $H_2$ flows. The arc current and Ar flow were kept constant at 600 Amps and 70 Sl/min respectively. These parameters were chosen as a result of the experiments with single $ZrO_2$ particles as described in chapter II.

An air shield, placed between the plasma torch and the substrate holder was used to remove the vaporized zirconia out of the particle jet and to blow away the hot plasma gasses.

This resulted in a temperature reduction of 150 °C for the non-cooled substrates.

The spraying with an 120 mm extended anode channel will be described in a separate paragraph because of the fact that this anode channel could not be used for the spraying of specimens used for the bending (chapter IV) and thermal shock (Chapter V) tests.

The total coating thickness of 0.3 mm was sprayed in 12 passes. This resulted in coatings showing neither separation between the passes nor large cracks, caused by strongly heating up of the coating substrate system.

From former experiments, which are not described in this thesis, it was known that deposition of $ZrO_2$ coatings in two or three passes, resulted in severe horizontal and vertical crack formation.

The following plasma spray parameters were used for the spraying of the $ZrO_2$ topcoats:

| | |
|---|---|
| I: | 600 Amps |
| V: | 63.5-71.4 V (depends on $H_2$ flow) |
| Ar: | 70 Sl/min |
| $H_2$: | 8 or 15 Sl/min |
| Anode channel: | standard or 20 mm extended. |
| spraying distance: | 100 mm |
| powder feed rate: | 38 grams/min. |

Together with the substrate cooling, eight different $ZrO_2$ topcoats were sprayed. Table 5 shows the codes which will be used further on in this thesis for the description of the different topcoats.

Table 5
Different types of $ZrO_2$ topcoats, sprayed for thermal shock and bending tests.

| Cooled C | Non-cooled NC | Ar | $H_2$ | Anode channel standard | Anode channel extended | code |
|---|---|---|---|---|---|---|
| | NC | 70 | 8 | SP | | NCSP70/8 |
| | NC | 70 | 15 | SP | | NCSP70/15 |
| | NC | 70 | 8 | | EP | NCEP70/8 |
| | NC | 70 | 15 | | EP | NCEP70/15 |
| C | | 70 | 8 | SP | | CSP70/8 |
| C | | 70 | 15 | SP | | CSP70/15 |
| C | | 70 | 8 | | EP | CEP70/8 |
| C | | 70 | 15 | | EP | CEP70/15 |

**8 Characteristics of the coatings**

The next paragraphs describe the characteristics of the bondcoats and topcoats which were sprayed using the techniques and the plasma spray

parameters as reported in the foregoing paragraphs.

### 8.1 Microstructure.

The microstructures of the bondcoats and the topcoats differ strongly and will be described separately.

**Note:** Vertical cracks are cracks which are directed perpendicular to the surface of the coating. Horizontal cracks are cracks which are parallel to the surface of the coating.

#### 8.1.1 Microstructure of the different bondcoats.

The APS bondcoats show the typical lamellar structure of plasma sprayed coatings. Especially the FeCrAlY coating has a dense network of oxide films. These films were formed during the spraying process. When the strongly heated particles fly from the plasma torch to the substrate, oxidation of the outer shell of the particles takes place, resulting in oxide films which can be observed throughout the whole coating. The NiCrAlY coatings showed a distinctly lower amount of oxide films. A possible explanation for this phenomenon can be found in the particle sizes of the two materials. The grain size of the NiCrAlY powder varied from 45-90 $\mu$m, whereas the grain size of the FeCrAlY powder ranged from 22.5-45 $\mu$m. As a result, the fine FeCrAly powder is more severely oxidized than the coarse NiCrAlY powder.

The FeCrAlY coating had a very low porosity and a very regular surface. All the particles spread out well after impacting on the substrate. The NiCrAlY coating on the contrary, presented a very irregular surface, caused by poorly molten coarse particles. Figure 3.20 gives cross sections of the APS NiCrAlY and FeCrAlY bondcoats.

Because the FeCrAlY powder was not available in the same grain size distribution as the NiCrAlY powder, it was not possible to compare the coatings exactly. Hence it was not possible to determine whether the formation of oxide films or poorly melting of the particles is caused by the particle size only, or is also influenced by the different chemical and physical material properties of NiCrAlY and FeCrAlY.

The low pressure plasma sprayed FeCrAlY coating exhibited no oxide films. Some porosity could be observed, caused by poorly molten particles. Powder

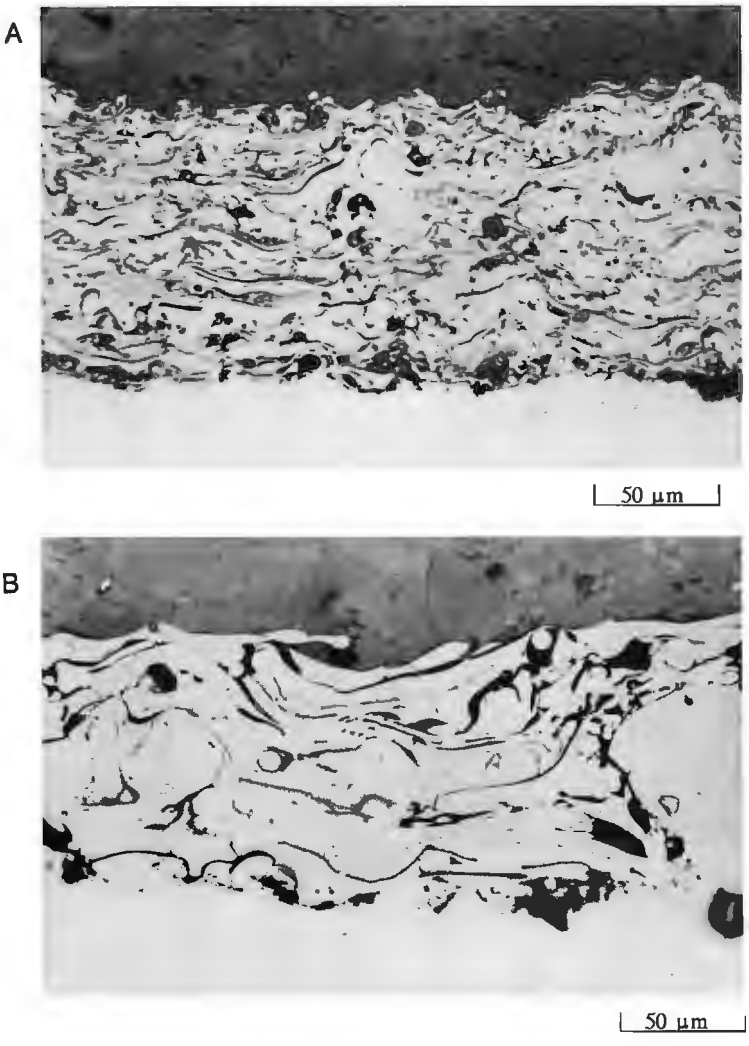


**Figure 3.20** Cross section of FeCrAlY (A) and NiCrAlY (B) bondcoats. It is shown that especially the FeCrAlY coating shows a dense network of oxyde films. The structure of the NiCrAlY coating is coarse due to the coarse particle size of the powder used.

injection into a plasma in a low pressure environment differs strongly from atmospherical conditions, implying the reason for a less than optimal particle heating. The next photograph gives a cross section of the LPPS FeCrAlY coating. (Figure 3.21)

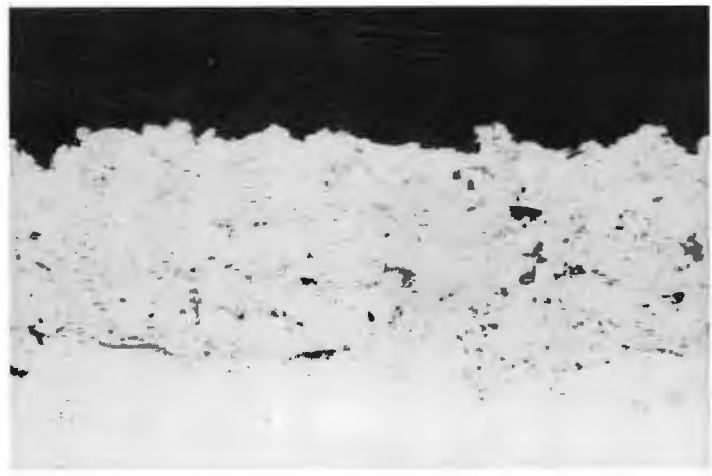


**Figure 3.21** Cross section of a LPPS FeCrAlY bondcoat. The coating shows some pores but no oxides.

### 8.1.2 Microstructure of the $ZrO_2$ topcoats

The microstructure of the ceramic topcoat which is observed under the light- or electron-microscope strongly depends on the way of preparation of the specimen. Appendix C-II gives the used procedure for the preparation of the specimens for microscopical investigation.

The solidified $ZrO_2$ particles have a typical columnar structure. This columnar structure is caused by the directional solidification of the particles. The structure can be seen in figure 3.22, where the fracture surface of a $ZrO_2$ coating is presented. When the cross section of the coating is only polished, this crystal structure can not be observed; it can be revealed by ion etching (See appendix C-II).

A texture measurement, carried out by X-ray diffraction at the faculty of chemistry of Eindhoven University of Technology proved, that there existed no texture in the coating.

The influence of substrate cooling during the spraying process can be observed in figures 3.23 a) and b). They show fracture surfaces of a cooled coating and a non-cooled coating, sprayed with a standard nozzle, (CSP70/15

and NCSP70/15) deposited onto an AISI 316 substrate.


**Figure 3.22** Plane of fracture of a $ZrO_2$ coating. The columnar grain structure, caused by the directed solidification of the particles, can be seen clearly.

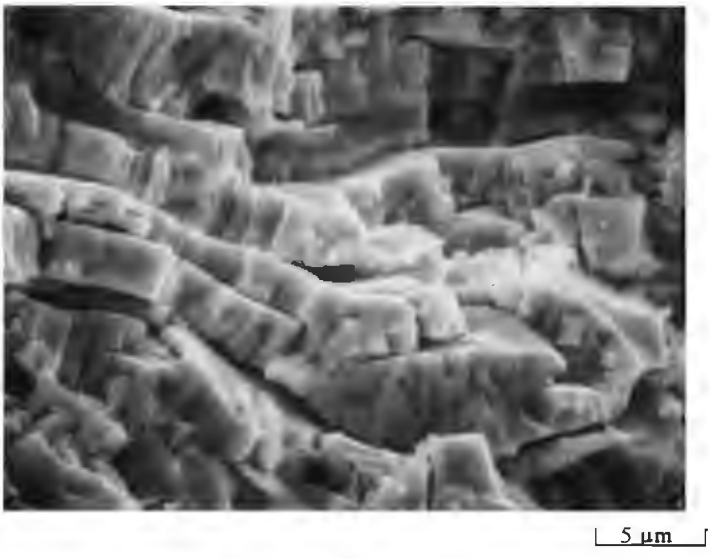


**Figure 3.23a** Plane of fracture of a cooled coating. The cooled coating shows distinct boundaries between the particles.

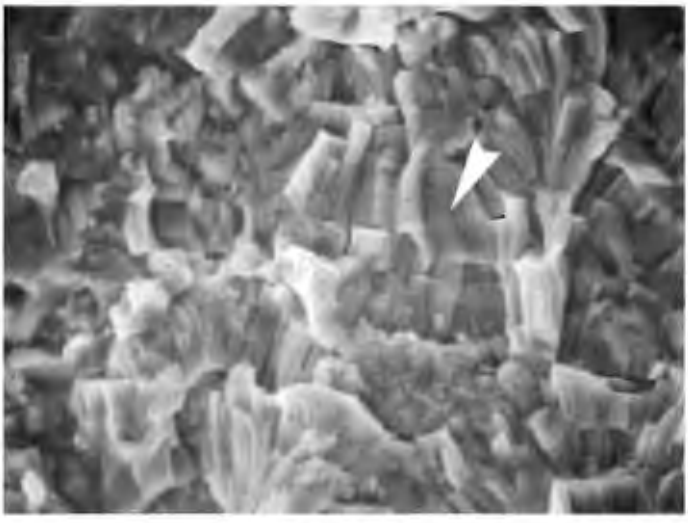


**Figure 3.23b** Plane of fracture of a non-cooled coating. The arrow in the non cooled coating shows two particles, on top of each other. The columnar grain structure proceeds through these particles.

The cooled coating has a lamellar structure with distinct boundaries between the individual particles. It can also been seen that the fracture surface has a very craggy appearance. This is caused by the event that the crack did not run in one plane, but partly followed the particle boundaries (See also chapter IV, paragraph 2.7)
The non-cooled coating also shows the lamellar structure but
the boundaries between the individual particles are not as distinct as in the case of the cooled coating. Furthermore it was observed that the vertical columnar structure continued throughout two particles, deposited on each other, thus indicating epitaxial growth. This is indicated by the arrow in figure 3.23 b). The fracture surface of the non-cooled coating is less craggy than that one of the cooled coating.

Observing polished cross sections of the thermal barrier coatings, it turns out that the cooled coatings have a dense network of microcracks, homogeneously spread over the whole coating. These microcracks are oriented as well horizontally as vertically.
Although the non-cooled coatings also show microcracks, their density and orientation differs strongly from the cracks observed in the cooled coatings.

The non-cooled coating exhibited a lower amount of vertical cracks. Horizontal cracks, which are in fact particle boundaries, are almost absent. Figures 24 a) and b) present cross sections of cooled and non-cooled coatings, prepared as indicated in appendix C-II. The difference between the crack networks can be observed clearly.

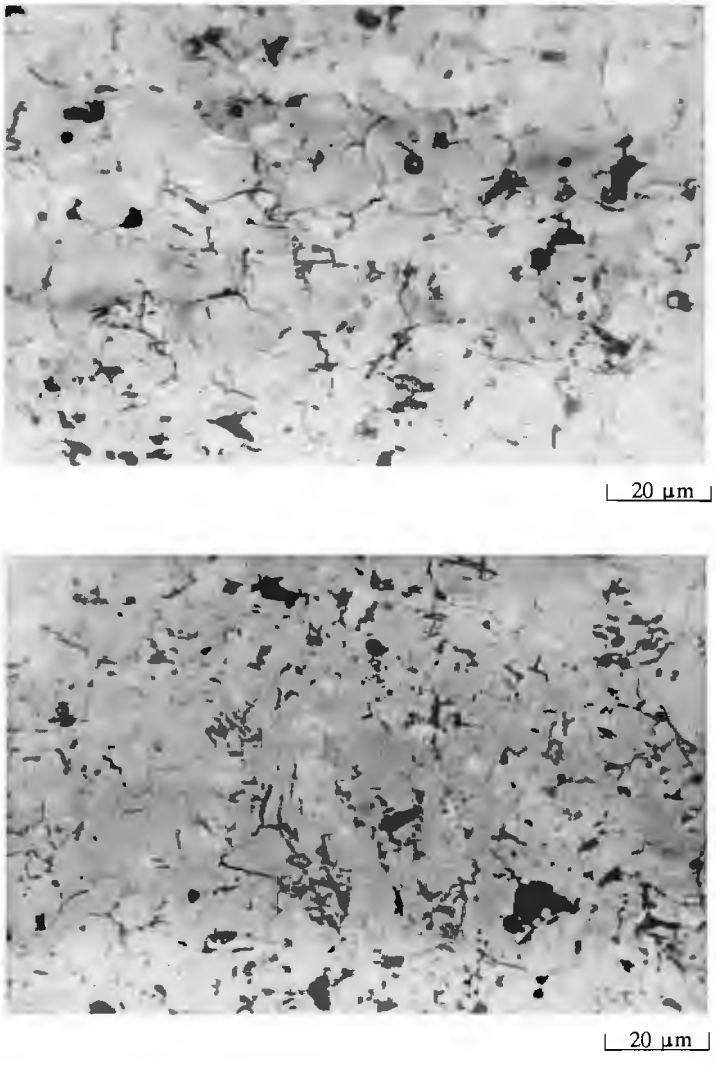


**Figure 3.24** Cross sections of a cooled (A) and a non-cooled coating (B). It is shown that the crack network in the cooled coating is much denser than in the non cooled coating.

The appearance of a dense crack network is also described by Sturlese [18], who investigated the effect of substrate cooling on the microstructure of plasma sprayed ceramic coatings of $Al_2O_3$ and $ZrO_2$.

Next to the micro cracks, the coatings sprayed with an extended nozzle also showed some larger vertical cracks, starting at the coating surface. These cracks have a length of 3 to 5 times the thickness of a splashed particle.

The porosity of the $ZrO_2$ coatings is low; 1 to 3 %. The coatings sprayed with an extended nozzle showed a lower porosity than the coatings sprayed with the standard anode, but the difference was only slight. The pores are distributed homogeneously throughout the coatings.

### 8.1.3 Comparison of the microstructure to conventional thermal barrier coatings

The $ZrO_2$ coatings, sprayed during this research project were dense and contained a low amount of pores. Since the heat content of the $ZrO_2$ particles was high, they spread out well.
The coatings sprayed with a standard nozzle and an $Ar/H_2$ flow of 70/8 Sl/min are just on the transition point from the melting to the overheating traject (See chapter II, paragraph 4.3.3), whereas all the other coatings were sprayed with particles which were more or less strongly overheated.

The conventional plasma sprayed $ZrO_2$ coatings which are applied in stationary and aircraft gas turbines have a porosity between 10 and 24 volume %. This porosity is prescribed by the turbine manufacturers in order to obtain coatings with a high thermal shock resistance.
To obtain these coatings, the heat content of the particles has to be low, just enough to melt the outer part of the particle. The collision with the substrate forces the particles to adhere but they do not spread out well. This results in a coating which contains mainly partly molten particles and hence a high amount of pores. Figure 3.25 shows the cross section of a conventional thermal barrier coating, applied in a stationary gas turbine. The coating material is $ZrO_2$ 7.6 wt% $Y_2O_3$ and equal to the material used at Eindhoven University.

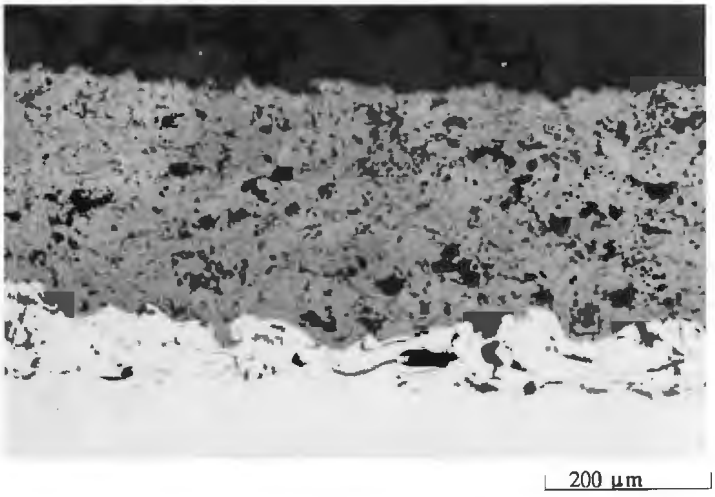


**Figure 3.25** Conventional Thermal Barrier Coating. The coating possesses a high porosity.

**8.2 The permeability of the $ZrO_2$ coatings.**

The coatings produced at Eindhoven University exhibited a low porosity. No interconnected pores were observed. Penetration of liquids via pores is therefore not likely to happen.

The cooled coatings however, show a dense microcrack network. The permeability of these coatings is investigated by impregnating them with a silver nitrate solution. Specimens of cooled and non-cooled coatings were soaked in a silver nitrate solution for several minutes. Subsequently the specimen were dried in a furnace at 485 °C. The specimen were cut through by a diamond wire saw and subsequently ground and polished and microscopically investigated.

The cooled coatings showed a homogeneous distribution of Ag throughout the whole coating thickness. As well vertical as horizontal microcracks were filled with Ag. This means that the cracks are interconnected and transport of liquids occurs along the cracks and particle boundaries.

The penetration in non-cooled coatings is less. Almost no horizontal traces of Ag were found. Penetration takes place by the vertical micro cracks in the single particles. Figure 3.26 a) and b) show Ag-traces in a cooled and a non-cooled coating. It can be observed that the cooled coating shows horizontal Ag-traces. These horizontal traces are almost absent in the case of the non-cooled coating.

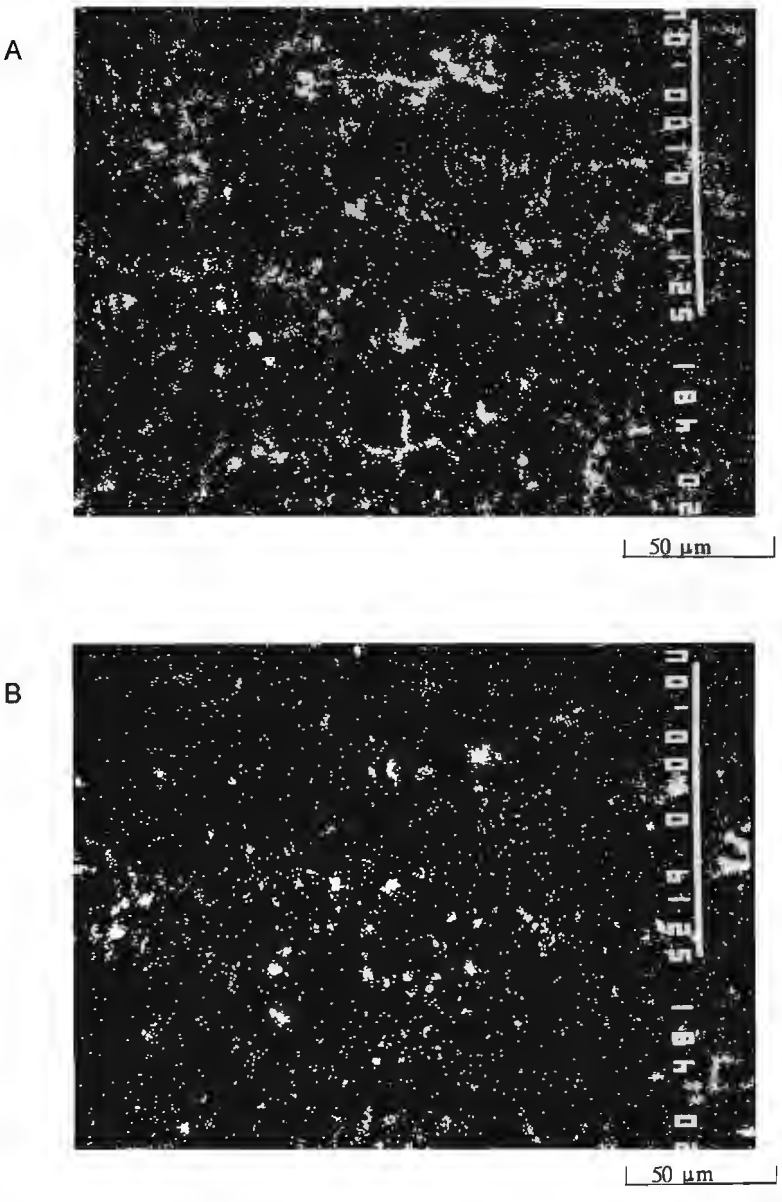


**Figure 3.26** Silver distribution in a cooled (A) and in a non-cooled $ZrO_2$ coating (B). The cooled coating shows horizontal Ag-traces, indicating that penetration of liquids may take place along the particle boundaries.

In practice, it depends on the viscosity and the wetting of the liquid contaminations or the corrosive products whether penetration into the ceramic coating will take place. This penetration may lead to a decreased

flexibility of the ceramic coating. Furthermore, corrosive products may affect the metallic bondcoat.

### 8.3 Roughness of the $ZrO_2$ coating surface

The roughness of the $ZrO_2$ coatings sprayed with the different plasma spray parameters and anode channels is given in figure 3.27. It appears that the coatings, sprayed with an extended anode channel show a lower roughness than the coatings sprayed with a standard nozzle.

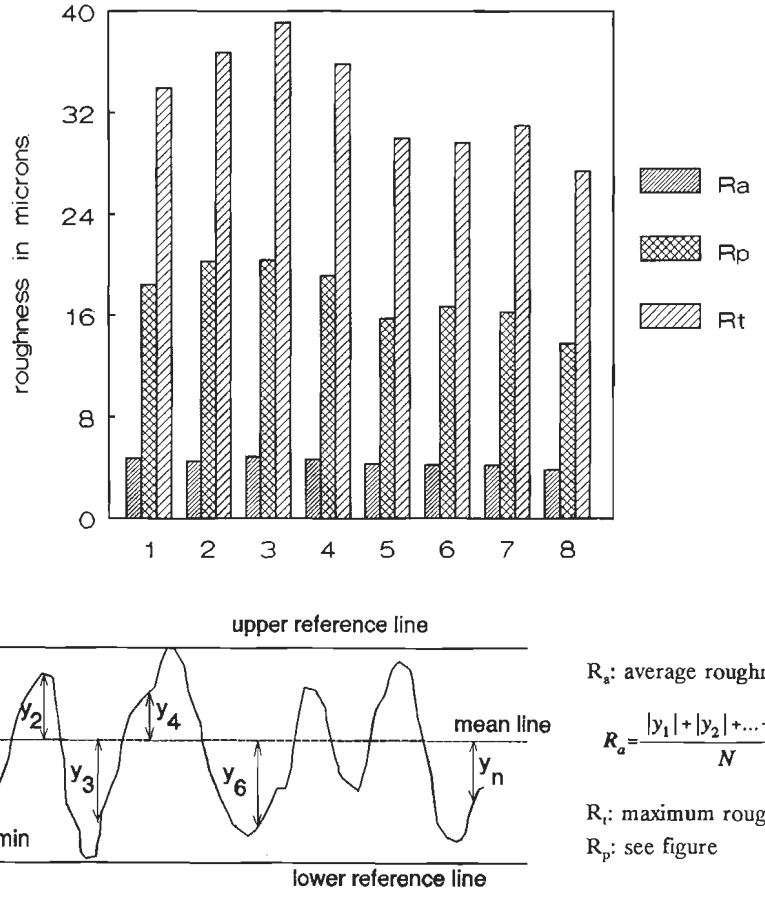


**Figure 3.27** Roughness of plasma sprayed $ZrO_2$ coatings. The coatings, sprayed with an extended anode channel possess a lower roughness.
1) NCSP 70.8 2) NCSP70.15 3) CSP 70.8 4) CSP 70.15
5) NCEP70.8 6) NCEP70.15 7) CEP70.8 8) CEP 70.15
B shows the definitions of the roughness parameters represented in the diagram. [21]

The $R_t$ values (maximum roughness: distance between the highest peak and the deepest valley) show the most distinct difference. This can be explained by the fact that the particles sprayed with an extended anode channel, possess a higher velocity and a higher heat content. As a result, they spread out well after impacting on the substrate or previously deposited layers. (See also chapter II, paragraph 5.4.2.).

**8.4 Colour of the $ZrO_2$ coatings**

The colour of the $ZrO_2$ 7.6 wt% $Y_2O_3$ coating material is yellow. After spraying, it shows a grey to white colour. This indicates that the composition of $ZrO_2$ has changed, due to the loss of oxygen. The coatings, cooled during spraying were grey, whereas the non-cooled coating were white.
When the coatings are heated up during service, they regain their yellow colour, indicating that the $ZrO_2$ absorbs the lacking oxygen.

**8.5 $ZrO_2$ coatings sprayed with the 120 mm extended anode channel.**

As is explained in paragraph 6.2, the 120 mm extended anode channel can not be used for the production of large coating areas. For that reason, small specimens were coated with one pass of the plasma torch. The microstructure of the coating obtained in this way, differed strongly from the coatings described in the foregoing paragraphs. The lamellar structure of the coating was not found back and the columnar crystal structure growed throughout the whole coating. This phenomena is caused by the high heat content of the $ZrO_2$ particles sprayed with this type of anode channel.(See chapter II, paragraph 4.3.3.). The particles reached almost their boiling points and melt fully together after impacting. The coating showed some large macro cracks, caused by the high thermal stress occurring at these high heat contents.
Figure 3.28 shows a cross section of this coating.

**8.6 Stiffness of the $ZrO_2$ topcoats**

The Young's moduli of the $ZrO_2$ coatings were measured using a three point bending test. Substrates of 1.6 mm Hastelloy X, were covered with 0.3 mm $ZrO_2$ coatings. The elastic deformation behaviour of the specimen was registered and the stiffness of the coatings could be calculated, using the equations, derived by Roark and Young [19] and applied to coatings by Verstraaten [19a]. It was assumed that the stiffness of the coatings was

constant over the coating thickness.

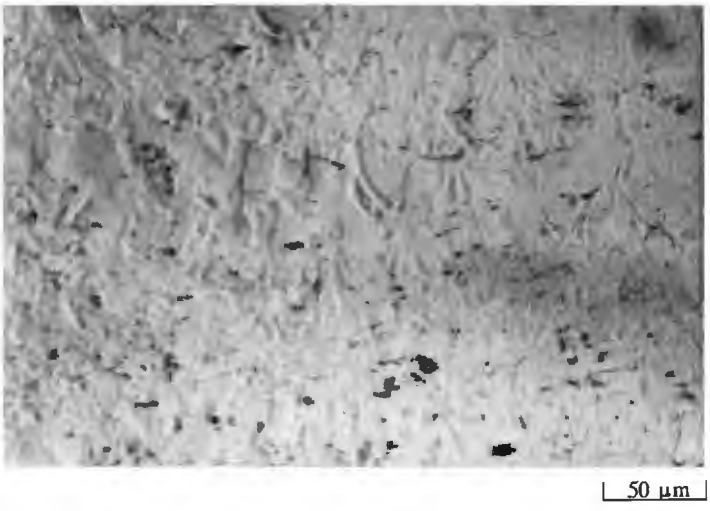


**Figure 3.28** Cross section of a $ZrO_2$ coating, sprayed with a 120 mm extended anode channel. The boundaries between the individual particles disappeared. A columnar grain structure can be observed.

Nearly all plasma sprayed ceramic coatings possess a stiffness depending on the direction of loading: tensile or compressive stresses. Therefore, the stiffnesses were determined for both compressive and tensile loading. Figure 3.29 gives the results of these measurements

It can be seen that the stiffness of the $ZrO_2$ coatings in tensile direction is lower than the stiffness in compressive direction. This is caused by the presence of the vertical cracks in the ceramic coatings. Furthermore, it can be seen that the cooled coatings possess a lower stiffness than the non-cooled coatings. This is caused by the dense microcrack networks in the cooled coatings.
The lower stiffness of the CEP70/15 coating may be explained by the presence of vertical cracks as described in paragraph 8.1.2. This is also the case for the non-cooled coatings. The coating sprayed with an extended plasma has a lower tensile stiffness than the one sprayed with a standard nozzle.

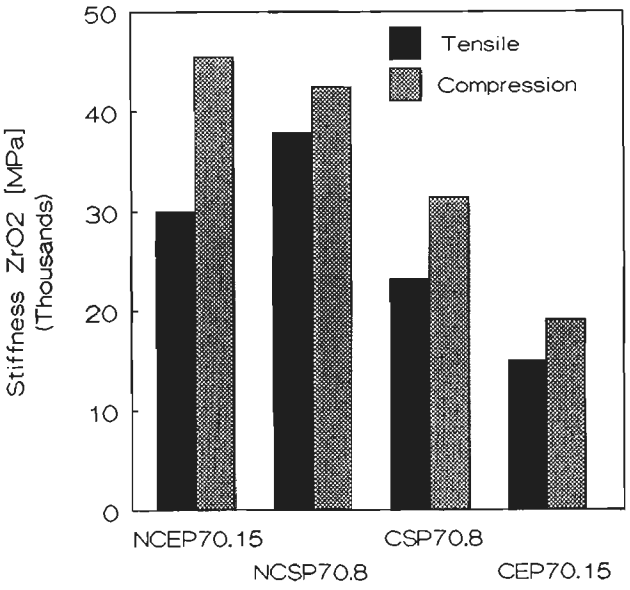


**Figure 3.29** Results of the measurements of the stiffness of plasma sprayed $ZrO_2$ coatings. It can be seen that the stiffness for compressive loading is higher than the stiffness for tensile loading.

## 9 Conclusions

The $ZrO_2$ topcoats, sprayed on water cooled substrates, possess residual tensile stresses. $ZrO_2$ topcoats, sprayed on non-cooled substrates, may possess residual tensile or compressive stresses. The residual tensile stresses in the non-cooled specimens are lower than the residual tensile stresses in the cooled coatings.

Generally, the residual stresses in plasma sprayed $ZrO_2$ coatings are low, they seldom exceed values of 100 Mpa.
X-ray stress measurements on thin (20 $\mu$m) $ZrO_2$ layers proved that these layers possessed residual tensile stresses. The stress decreased with increased coating thickness.

$ZrO_2$ coatings, sprayed on cooled substrates, showed a dense microcrack network. The microcracks were distributed homogeneously throughout the coating and directed as well vertically as horizontally. Although the non-cooled coatings also possessed microcracks, they were directed mainly

vertically, and their amount was less than in the cooled coatings.

The microcracks in the cooled $ZrO_2$ coatings were interconnected. Experiments proved that liquids, which penetrated through the coating's surface, reached the bondcoat via the horizontal and vertical microcracks.

$ZrO_2$ topcoats, sprayed with overheated particles (application of an extended anode channel), showed a lower surface roughness than the coatings sprayed with a standard anode channel.

The stiffness of the $ZrO_2$ coatings, sprayed on cooled substrates is lower than the stiffness of the coatings, sprayed on cooled substrates. Furthermore, the stiffness during tensile loading is lower than the stiffness during compressive loading. This appeared for both cooled and non-cooled coatings.

The use of an 120 mm extended anode channel for the spraying of $ZrO_2$ topcoats, resulted in coatings without the typical lamellar structure of a plasma sprayed coating. Further, these coatings showed a columnar grain structure, with columns, reaching from the substrate to the coating's surface.

## 10 References chapter III


[1] Steffens H.D., Fischer U., Correlation between Microstructure and Physical Properties of Plasma Sprayed Zirconia Coatings. Thermal Spray Technology, October 24-27, 1988, Cincinatti Ohio, Editor D.L. Houck, ASM, Ohio, USA, 1989

[2] Eckold G., Buckley-Golder I.M., Scott K.T. A Theoretical Analysis of Residual Stresses in Flame Sprayed Brittle Materials. Harwell Report, HAR 5123, Harwell Laboratory, Didcot, Oxon, Ox11, UK, 1987

[3] Rickerby D.S., Eckold G., Scott, K.T., Buckley-Golder I.M., The Interrelationship between Internal Stress, Processing Parameters and Microstructure of Physically Vapour Deposited and Thermally Sprayed Coatings. Thi. Sol. Fi., 154(1987), 125-141

[4] Hendricks R.C., McDonald G., Mullen R. Residual Stress in Plasma Sprayed Ceramic Turbine Tip and Gas-Path Seal Specimens. Ceram. Eng.Sci. Proc. 9-10(1983), 802-809

[5] Takeuchi S., Ito M., Takeda K., Modelling of Residual Stress in Plasma Sprayed Coatings: The Effect of Substrate Temperature. Surf. Coat. Techn., 43/44 (1990), 426-435

[6] Elsing R., Knotek O., Balting U., Calculation of Residual Thermal Stress in Plasma Sprayed Coatings. Surf. Coat. Techn. 43/44(1990), 416-425

[7] Elsing R., Knotek O., Balting U., The Influence of Physical Properties and Spraying Parameters on the Creation of Residual Thermal Stresses during the Spraying Process. Surf. and Coat. Techn. 41(1990), 147-156

[8] Knotek O., Elsing R., Balting U., On the Influence of Thermo Physical Data and Spraying Parameters on the Temperature Curves in Thermally Sprayed Coatings during Production.
Surf. Coat. Techn. 36(1988) 99-110.

[9] Ziegler G., Vorlesung "Keramiktechnologie" (In German) Eindhoven University of Technology, 1985

[10] Mathijsen S.P.M., Modellering van Thermische Spanningen in Plasmagespoten Keramische Coatings. Master's Thesis, Eindhoven University of Technology 1991

[11] Noyan J.C., Cohen J.B., Residual Stress: Measurement by Diffraction and Interpretation. Springer Verlag, New York, 1987

[12] Noutomi A., Kodama M., Inoue Y. Residual Stress Measurement on Plasma Sprayed Coatings., Weld. Int. 11(1989) 947-953

[13] Zaouali M., Lebrun J.L., Dias A., Pina J., Residual Stress in Ceramic Coatings. Joint Meeting of German, French and Dutch Residual Stress Groups, march 19-21, 1991, University of Twente, the Netherlands

[14] Richter H., Schneiderbanger S., X-ray Stress Measurements on Plasma Sprayed $ZrO_2$ Layers Joint Meeting of German, French and Dutch Residual Stress Groups, march 19-21, 1991, University of Twente, the Netherlands

[15] Blok H. Theoretical Study on Temperature Rise at Surfaces of Actual contact under Oiliness Lubrication Conditions, Appendix I, Inst. of Mech. Engs., London, october 1967.

[16] Hart, W.G.J. 't, Inleidend Onderzoek van Opgespoten Lagen met Betrekking tot de Mechanische Eigenschappen, Porositeit en Spanningen, Master's Thesis, Eindhoven University of Technology, 1972

[17] Kouyumdjiev C.N., A Calculation of Average Stress in Electro Depositsbased on the Bending of a Flat Plate Substrate. Surf. Techn. 26(1985), 35-43.

[18] Sturlese S., Bartuli C., Effect of Substrate Cooling on Properties of Ceramic Coatings. Document SC-30/88, Centro Sviluppo Materiali, Rome, Italy 1988.

[19] Roark R.J., Young W.C., Formulas for Stress and Strain, Mc Graw Hill, 1975.

[19a] Verstraaten A.J.M. De Toepassing van Thermal Barrier Coatings op verbrandingskamerwanden van Dieselmotoren. Master's Thesis, Eindhoven University of Technology, 1983

[20] Kofstad P., High Temperature Corrosion, Elseviers Science Publishers, London, New York, 1988

[21] Prakash A., Digital Techniques of Roughness Measurements applied to Surfaces, Representing some Manufacturing Processes. Doctor's Thesis, Eindhoven University of Technology, 1975

[22] Houben J.M., Eindhoven University of Technology, Faculty of Mechanical Engineering, Private communication.

# CHAPTER IV ACOUSTIC EMISSION EVALUATION OF CRACK FORMATION IN THERMAL BARRIER COATINGS SUBJECTED TO MECHANICAL STRESSES.

## 1 Introduction

This chapter describes the application of Acoustic Emission Evaluation of Thermal Barrier Coatings during a three point bending test. The experiments were carried out in order to investigate the formation of cracks in thermal barrier coatings subjected to tensile and compressive stresses

Thin, strip shaped substrates, were coated with TBC's and loaded in such way that the coating was under tensile or compressive stress. The AE signals, radiated by the different types of coatings were measured and analyzed and compared to the failure behaviour of the coatings.

The first sections of this chapter give a short overview of acoustic emission and acoustic emission theory. The other sections describe the experimental set up, the test results and the discussion of the obtained results.

## 2 Acoustic Emission

Acoustic emission is as well the name given to a physical phenomena as the technique used to observe and register this phenomena. In this section, a short overview of both items will be given.

### 2.1 What is Acoustic Emission ?

Acoustic Emission (AE) is the spontaneous release of transient elastic waves in a solid caused by a sudden change in the local stress state of that solid. Processes as crack initiation and crack growth or plastic deformation are examples of events that change the local stress state and thus radiate elastic waves to the surface of the body.

When the amplitudes of the waves are sufficient, they can be detected by AE transducers which are attached to the surface of the solid. These transducers make it possible to detect e.g. crack growth or crack initiation in a solid.

The first experiments with acoustic emission were reported by Kaiser in 1953 [1].

The advantage of AE, compared to other non destructive techniques, is that the defect source itself produces the signal which is detected and that no external source is required which emits waves into the material to detect defects.

Another advantage is the on-line monitoring of structures; crack initiation or crack growth is observed during service or during testing of an object and not by afterwards inspection with e.g. X-ray techniques.
A disadvantage is the fact that only growing defects can be monitored. Already existing cracks are not observed until they grow. Flaws, not growing during a load cycle remain undiscovered. Hence, AE is not suitable to inspect the initial state of a material, only the change of it.
An important phenomena in AE evaluation is the Kaiser effect. When a body undergoes a cycle of loading and unloading, acoustic emission only will occur when the new load exceeds the previous one.
Although AE evaluation generally is considered as a non destructive test (NDT) for materials evaluation, it is in fact a destructive test. A specimen which has been investigated once cannot be reused for AE evaluation.
According to Scruby [2], AE can never be regarded as a replacement for ultrasonics or radiography, but it should be viewed as an additional, complementary technique, providing new information about changes in flaw size and distribution. In our case this means that we have to combine AE evaluation with microscopical techniques.

**2.2 Applications of Acoustic Emission Evaluation**

Several authors report about the use of AE evaluation in various fields. Scruby [2,3], Wadley [4,5], Green [6] and Ohira and Pao [7] describe the fundamental research on AE, where source characterization, wave propagation and a mathematical approximation of AE are the main subjects.
Monitoring of pressure vessels, especially in the nuclear industry has been the item in many AE studies in the past, especially source localization in large structures.
A very important field of the application of AE is the research of the failure behaviour of fibre reinforced plastics [8].
Corrosion cracking, twinning and dislocation movement are typical applications of AE in the field of materials research.
AE is also applied as condition monitoring technique for cutting tools [9].
The application of AE in the field of plasma sprayed coatings and especially thermal barrier coatings is reported by several authors. Boehm c.s. report about the use of AE during the plasma spraying process in order to estimate the impact energy of single particles [10].
AE evaluation of TBC's during thermal cycling is reported by Berndt and

Miller [11], Berndt and Herman [12] and Pantucek [13].
The application of AE during bending tests of plasma coated specimens is reported by Verbeek, Houben and Klostermann [14,15], Crostack [16], Almond [17], Wen [18], Mora-Marquez [19] and Cohrt and Thuemmler [20].
The use of AE during tensile adhesion tests (TAT's) of several plasma sprayed coatings is reported by Shankar, Berndt and Herman [21].
Chulya [22] describes the use of AE evaluation during the failure process of fibre reinforced ceramics in order to estimate the time of failure of the fibres in the matrix material.

### 2.3 Theory of Acoustic Emission

Figure 4.1 shows a solid with an internal defect emitting acoustic emission. The waves propagate through the solid as transverse or longitudinal waves.

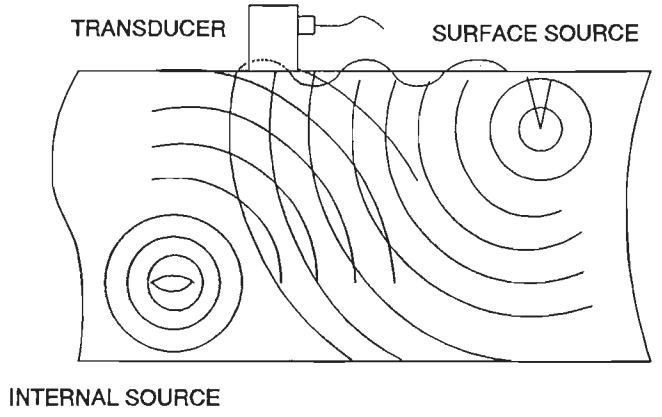


**Figure 4.1** Wave propagation in a solid, due to a surface source and an internal source. These sources cause both surface and bulk waves which are detected by the AE-transducer.[1]

The longitudinal waves are also called compressive waves and the transverse ones shear waves. The wave form which occurs during the AE tests depends on the type of acoustic emission source causing the acoustic emission. The different types of AE sources are described briefly in the next paragraph.

#### 2.3.1 Acoustic emission sources

An acoustic emission source produces elastic waves which propagate through a solid. In fact such a source has finite

dimensions and emits waves with different frequencies. But at a great distance from the source it seems that the waves are emitted from one point. Scruby [2] uses this so called far field approximation to define AE sources as point forces, acting within the material for very short periods, emitting elastic waves. Scruby assumes that every AE source is internal to the body, so that there is no net force or couple generated by the source, so every force must be part of a force dipole, and every couple part of a double couple.
The AE sources can now be represented as combinations of force dipoles, with a $\delta$-function (Dirac function) time dependence. The strength of an AE source, acting on a volume $D_v$ of a material is given by the so called seismic moment tensor $D_{ij}$.
This is a tensor, containing the stress components in the three main directions $x_1$, $x_2$, $x_3$. For a precise derivation of these seismic moment tensors, the reader is referred to references [2,3] and appendix C-I.

### 2.3.2 Wave propagation

The waves caused by the force dipoles described above propagate through the material as compression and shear waves.
The velocity of the compressive waves c1 is:

$$c_1 = \sqrt{\frac{(\lambda + 2\mu)}{\rho}} \tag{1}$$

and the velocity of the shear waves c2:

$$c_2 = \sqrt{\frac{\mu}{\rho}} \tag{2}$$

Where $\lambda$ and $\mu$ are the Lamé elastic constants.( See appendix C-I)
The propagation of waves, caused by the internal dipole forces can be described by Green's functions. Green's functions are special derivatives of the general formula of Newton. Appendix C-II contains the precise derivation of the Green's functions.
In general, a displacement u at a place x at a time t due to a point force source at time t' and place x' can be described by the following formula:

$$u_i(x,t) = G_{ij}(x,t,x',t')F_j \tag{3}$$

In the case of a force dipole this relationship turns into:

$$u_i(x,t) = -\frac{\partial}{\partial x_k'} G_{ij}(x,x',t,t') d_{jk}(t) \tag{4}$$

The radial displacement $u_r^c$ at a distance r from a micro crack source due to the compressive wave can be described by the equation:

$$u_r^c = \frac{\cos^2\theta}{4\pi(\lambda+2\mu)}\left[\frac{\dot{D}_{33}(t-\frac{r}{c_1})}{c_1 r} + \frac{D_{33}(t-\frac{r}{c_1})}{r^2}\right] \tag{5}$$

The displacement due to the shear wave has almost the same form:

$$u_\theta^s = \frac{\sin\theta\cos\theta}{4\pi\mu}\left[\frac{\dot{D}_{33}(t-\frac{r}{c_2})}{c_2 r} + \frac{D_{33}(t-\frac{r}{c_2})}{r^2}\right] \tag{6}$$

Figure 4.2 shows the displacements in an infinite body due to the shear and compressive waves, caused by the three types of AE sources, described in the foregoing paragraph.

In practice, we are never dealing with infinite bodies. For this reason, reflections of the waves to a boundary will happen. A shear wave will be reflected in a shear (S) wave and a compressive (P) wave, and a compressive wave in a P wave and a S wave. When the angle of incidence of a shear wave is greater than the critical angle $\theta_c$ (See appendix C-III) than an additional wave that propagates along the surface is generated. These waves are called Rayleigh waves. The wave velocity of a Rayleigh wave is generally slightly less than the transverse wave velocity. The amplitudes of Rayleigh waves attenuate with $R^{-0.5}$ whereas the bulk waves attenuate with $R^{-1}$, so at large distances of the source, Rayleigh waves tend to dominate over the bulk waves.

### 2.3.3. Source characterization

As stated in the foregoing sections, each type of force dipole produces its own type of compression or shear waves. It must also be possible to characterize the source of an internal defect by AE evaluation.

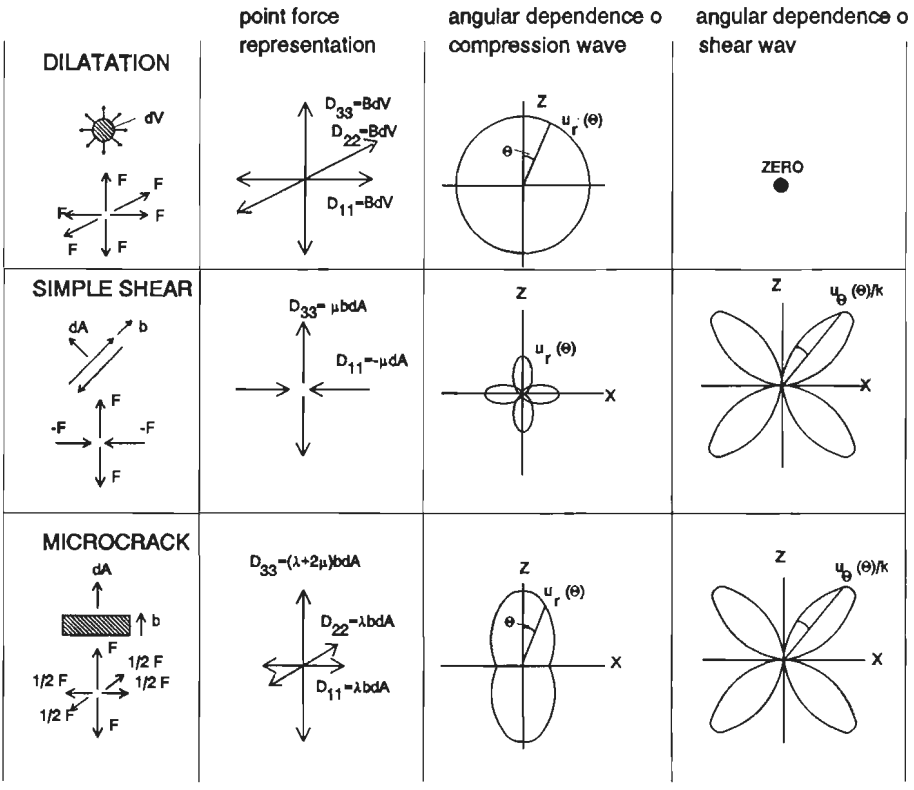


**Figure 4.2** Propagation of compression and shear waves in an infinite solid. The waves are caused by the three basic types of AE sources: The dilatation source, the shear source and the microcrack source. Redrawn from [2]

One tries to find the components of the seismic moment tensor by measuring the displacement of the surface at certain orientations with respect to the source. Scruby, Baldwin and Stacey [23] describe experiments on a $K_{1c}$ specimen, where they tried to characterize the AE sources with four transducers in order to find the values of the components of the seismic moment tensor. This method is only applicable at specimens with a simple shape, where the transducers can be placed in such way that the bulk waves will reach the transducers directly, without reflections.

In practice, this is not always possible, especially when the transducers have to be placed at large distances from the source. Furthermore it is not always possible to attach as many sensors as needed for a source characterization. For a three dimensional source characterization six transducers are needed.

Complex geometries can also influence the wave paths and reflections tremendously, so that it is almost impossible to reconstruct the AE source.

Frequency analysis of the AE signals in order to characterize the AE source is only possible in specimens with a simple shape and limited dimensions. High frequency signals attenuate strongly with increasing distance, and multiple reflections may strongly influence the frequency band of the signals.

Another technique to characterize the AE sources is the statistical or stochastical approach. Of a specimen with a well known defect one measures the AE signal. For various types of defects one tries to find typical AE signals and correlations between these signals and the defect sources. These correlations are used predictively in future tests.

The two techniques for source characterization are not to be seen as alternatives but as complimentary methods to describe the failure behaviour of a body.

### 2.4. AE Measurements

In this paragraph the measurement of acoustic emission in practice will be described. First an overview of available transducers is given, followed by a description of typical AE signals and their characteristics.

#### 2.4.1. AE transducers

The different types of internal sources, causing AE can be detected at the surface of a specimen. This happens with so called AE transducers which contain a piezo electric element that produces a slight voltage under load. This load results from acceleration of the surface due to the propagation of an elastic wave. The low voltage produced by the transducer is amplified by a preamplifier which is connected to the transducer as close as possible in order to amplify the very weak signal and make it possible to transfer it over larger distances. From the preamplifier, the signal is sent to an analyzer, where the characteristics of the signals are analyzed, and the data are stored on a hard-disk or magnetic tape. Mostly, the measuring process can be followed on-line on a computer screen. Figure 4.3 schematically shows the set up of an AE system.

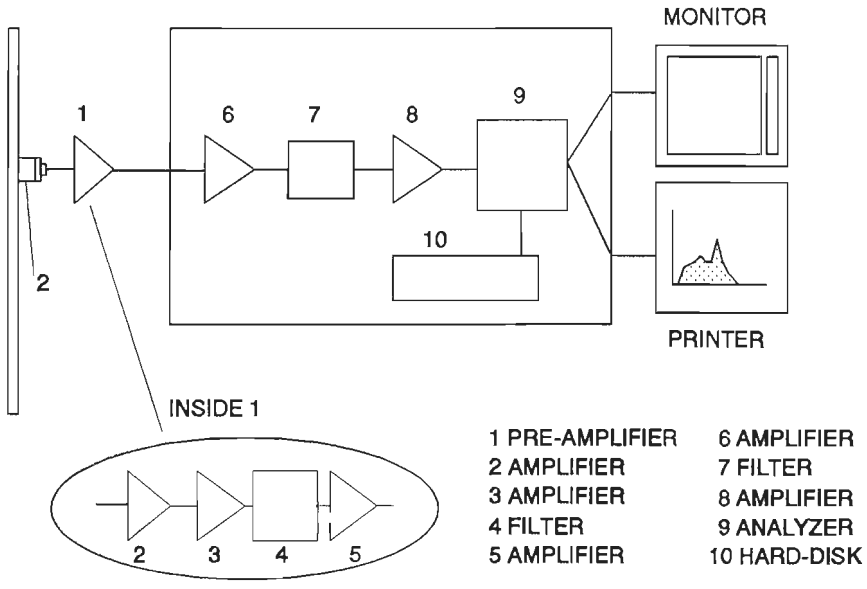


**Figure 4.3** The schematical set up of an Acoustic Emission system. The main components are depicted in this scheme.

In practice, two types of AE transducers are distinguished; wide band and resonant transducers. Wide band transducers have a sensitivity between 100 kHz and 1-5 MHz whereas resonant transducers have a resonant frequency somewhere between 100 kHz and 1 MHz. Characteristic frequencies of resonant transducers are 150 or 250 kHz.
Although the resonant transducers have a higher sensitivity [2,6,5], wide band transducers are required for source characterization. Acoustic emission events initially have a wide frequency band, but after travelling over a few centimetres only the frequencies of at maximum a few MHz are dominant. It is therefore advisable to measure AE with wide band transducers with a band width from 100 kHz to 2 Mhz or optimized transducers with a band width from 100 kHz to 1 Mhz.

Frequency analysis of AE signals with resonant transducers is not possible because these transducers produce signals with a frequency equal to the resonant frequency of the transducer and not of the AE source. Although it is possible to apply frequency analysis when wide band transducers are used, it has a limited use. Due to the attenuation of the higher frequencies only the lower ones are measured. And in complex geometries and thin plates,

the frequency is determined by the geometry of the construction rather than by the source [24]. Because of that the practical use of frequency analysis is very restricted.

### 2.4.2 AE signals

The signals measured by an AE transducer can be divided in two types, often called burst type and continuous type. The burst type has a high peak and damps out very soon. Continuous emission appears to consist of an overlapping sequence of individual bursts. Figure 4.4 shows the two types of AE signals.

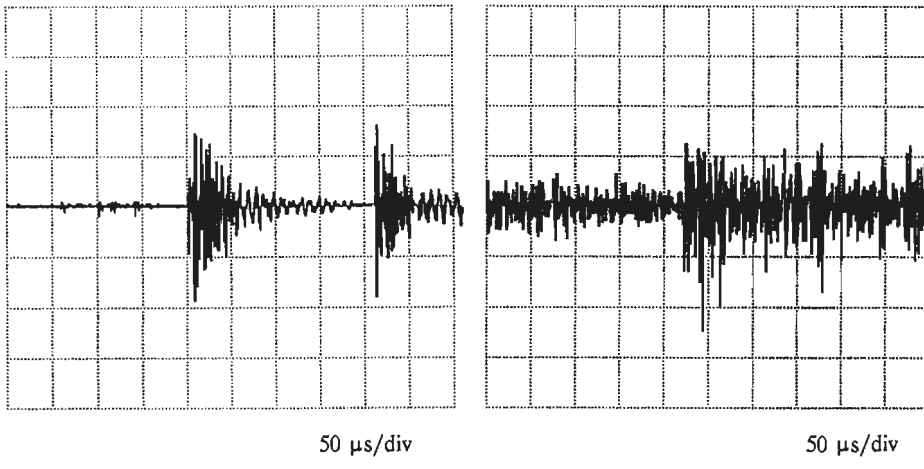


**Figure 4.4** Burst-type and continuous-type acoustic emission signals, measured during the AE evaluation of thermal barrier coatings.

Every individual burst is called a hit or an event. An event or hit can be described by certain characteristics which are shown in figure 4.5. A signal is recognized as a hit when its maximum amplitude exceeds a certain threshold value. This threshold, which can be varied acts as a filter to exclude disturbance signals.

- The counts are the number of peaks of an individual event which are greater than the threshold value.
- The risetime is the time a signal needs to reach its maximum amplitude after it exceeded the threshold value for the first time.
- The duration is the total time an AE signal lasts.

- The amplitude is the maximum value of the event.
- The energy of an AE event is defined as the surface under the envelope which encloses the AE event.

The duration, the amplitude and the energy are regarded as the most important characteristics of an AE hit. Together with the event rate, that is the number of hits, measured during a certain time or displacement interval, these characteristics are used to describe the failure behaviour of thermal barrier coatings during the three point bending test. The results of these tests are described in the following paragraphs.

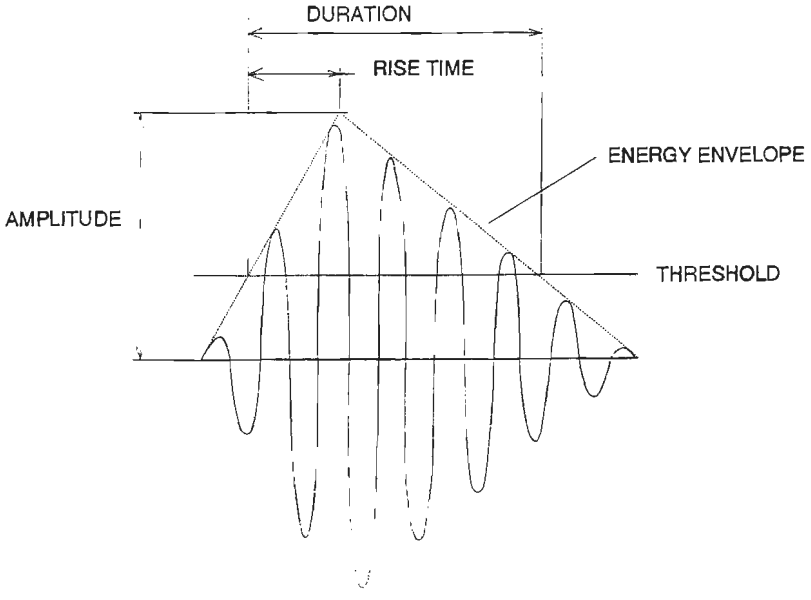


**Figure 4.5** Typical acoustic emission signal as produced by an AE transducer which was hit by an elastic wave.

## 2.5 Experimental

The experimental set up and the results of the acoustic emission tests will be described in the next paragraphs. These tests made it possible to determine the initiation and propagation of cracks in the coating, which could not be observed visibly. AE made it also possible to determine significant differences in the fracture behaviour of the different types of coatings.

### 2.5.1. The three point bending test

Several methods can be used to investigate the cohesive strength of coatings under mechanical load. Well known is the tensile adhesion test, where a coating is loaded perpendicular to its surface and the adhesion strength of the coating to the substrate or the cohesive strength of the coating material can be determined.

The loading of a coating parallel to its surface can be achieved by a tensile test on a coated bar, or alternatively by a three point or four point bending test, where a thin metallic strip, coated at one side, is subjected to a bending force.

The bending test has the advantage that the stress in the coating varies linearly from a maximum value at the outer surface of the coating to a lower value at the interface with the substrate, if is presumed that the stiffness of the coating is constant over the coating thickness. A bending test makes it possible to introduce cracks in a more gradual way than in the tensile test, where the stress distribution is constant throughout the coating. This is shown in figure 4.6.

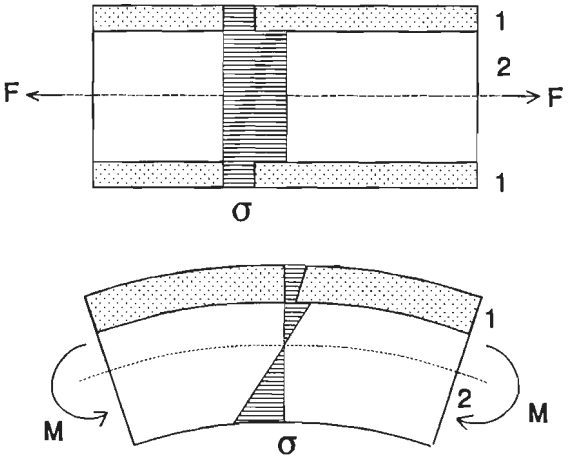


**Figure 4.6** Stress distribution in a coating subjected to tensile stresses in the case of a bending or a tensile test.

The choice between the three point and four point bending test was based on practical advantages. Between the points of application of the forces in the 4-point bending test, the bending moments and therefore also the

bending stress are constant. The formation of a crack will therefore take place somewhere in this area, whereas crack formation in the three point bending test will occur most probably in the middle of the specimen, just where the bending moment is maximum. This is advantageous in two ways. The distance between the AE transducer and the location of crack formation is constant, which benefits the evaluation of the AE signals as can be learned from the foregoing paragraphs. Secondly, the area that has to be prepared for microscopical observation of the coating after the bending test is limited.

### 2.5.2 Specimens

The specimens consisted of a Hastelloy X substrate, a FeCrAlY bondcoat and a $ZrO_2/Y_2O_3$ topcoat. The dimensions of the substrates were 124*30*1.65 mm. The thickness of the bondcoat and the topcoat were 0.1 and 0.3 mm respectively. They were sprayed using the spray parameters and spraying techniques as described in chapter 3. Both cooled and non-cooled substrates were used, together with a variation in plasma gas composition and type of anode channel. Besides these specimens, consisting of a bondcoat and a topcoat, also specimens with only a bondcoat were tested. Table 1 shows the different types of specimens.

Table 1.
The specimens used in the three point bending test. For identification of the topcoats the same codes as given in chapter III, were used.

| No | bondcoat | topcoat | remarks |
|---|---|---|---|
| 1 | cooled | CSP70/8 | |
| 2 | cooled | CSP70/15 | |
| 3 | cooled | CEP70/8 | |
| 4 | cooled | CEP70/15 | |
| 5 | cooled | NCSP70/8 | bondcoat cooled<br>topcoat non-cooled |
| 6 | non-cooled | NCSP70/8 | |
| 7 | non-cooled | NCSP70/15 | |

| No | bondcoat | topcoat | remarks |
|---|---|---|---|
| 8 | non-cooled | NCEP70/8 | |
| 9 | non-cooled | NCEP70/15 | |
| 10 | cooled | --- | bondcoat only |
| 11 | non-cooled | --- | bondcoat only |

* The bondcoats were always sprayed with a standard anode channel
C= substrate cooling, NC = no substrate cooling
SP= standard anode, EP = extended anode

**2.5.3 Microstructure of the coatings**

The various coatings showed different microstructures, due to the variations in the spraying process.(See chapter III, paragraph 8.1.2) All coatings contained a low porosity, which was uniformly distributed throughout the coating. The coatings, sprayed with an extended anode channel showed a slightly lower porosity, than those sprayed with a standard one. The coatings, sprayed onto a cooled substrate, showed a dense network of little cracks, both perpendicular and parallel to the surface. These parallel cracks were almost absent in the non-cooled coatings. The coatings sprayed with an extended anode channel on a cooled substrate showed next to the microcracks, also some little vertical macrocracks. These cracks started at the top of the $ZrO_2$ coating. The lengths of these cracks were about 50 to 100 $\mu$m.

The coatings sprayed with an extended anode channel and a plasma gas flow of 70/15 (NCEP70/15), on a non-cooled substrate showed also some macrocracks, perpendicular to the substrate. All the other types of coatings did not show these vertical macrocracks.

**2.5.4 Experimental set up**

The three point bending tests were carried out in a specially designed tool which was mounted in a 100 kN spindle driven tensile testing machine. The specimens were placed on two sharp edged beams, with an in-between distance of 100 mm, which were mounted on a sub-frame that was connected to a 1000 N force transducer. This force transducer was mounted to the fixed

crosshead of the tensile testing machine. The bending force was applied at the centre of the specimen by a sharp edged beam, which was connected to the moving crossheads of the tensile testing machine. This connection was realized by a thin, flexible steel cable avoiding the introduction of bending couples on the specimen. In this way, almost perfect bending was achieved. The displacement of the centre of the specimen was measured by an inductive displacement transducer. The testing machine was operating at a constant speed of 0.15 mm/min. The bending rig is schematically shown in figure 4.7.

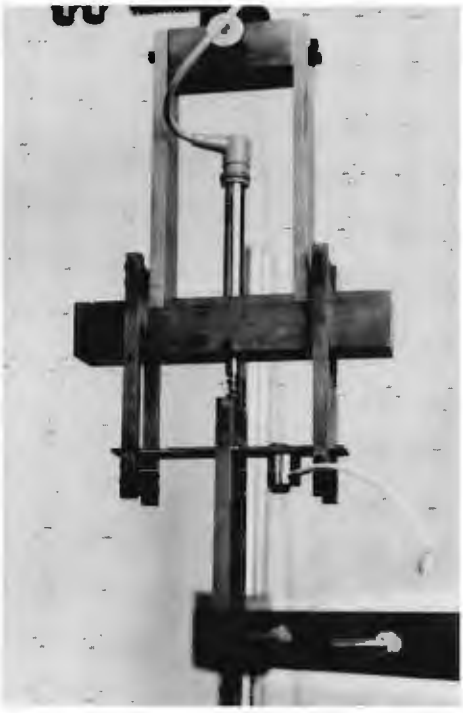

**Figure 4.7** Test rig for the bending tests in combination with acoustic emission evaluation.

The AE signals were taken up by an AE transducer which was attached to the coated side of the specimens. To optimize signal transfer from the coating to the transducer, a coupling agent was used, in this case high vacuum grease. (Dow Corning)
An additional clamp was used to assure a constant pressure between the transducer and the specimen.

The transducer was of the wide band type, with a frequency range from 100 kHz to 1 MHz. The transducer was connected to a preamplifier with a gain of 40 dB. The threshold value of the AE system was set on 30 dB and the gain on 40 dB. With this threshold value no disturbance signals either from the tensile testing machine or the bending tool were recorded.
The AE signals were stored on a hard-disk and could be observed on-line on a computer screen and a digital storage scope.
The bending force and the displacement of the centre of the specimen were also recorded by the AE equipment. Because of this it was possible to register the AE signals as a function of the displacement or the bending force.

### 2.6 Results

This paragraph describes the results of the AE tests. The two cases, coatings subjected to tensile stresses and coatings subjected to compressive stresses are discussed separately. The specimens, consisting of the substrate and only a bondcoat are also reported separately.

#### 2.6.1 Thermal Barrier Coatings subjected to tensile stresses

The coatings were tested in the equipment, described in paragraph 2.5.4.
Because of the fact that the tensile testing machine operated at a constant speed, the relationships of hits versus time or hits versus displacement could be compared directly.

The relationship between the number of hits and the displacement of the centre of the specimen was found to be a important characteristic. This relationship showed distinct differences between the coatings sprayed on a cooled substrate and the coatings sprayed on a non-cooled substrate. This is shown in figure 4.8, where a cooled specimen is compared to a non-cooled specimen. The diagrams show the hits versus displacement. It has to be noted that the number of hits is **not** cumulative; each bar represents the amount of hits that is produced during a certain time or displacement increment.
From this figure it can be learned that there exists a great difference in AE production between the cooled and the non-cooled specimens. The cooled coatings showed a gradually increasing amount of hits right from the start of the test. This level increased and then became almost constant.

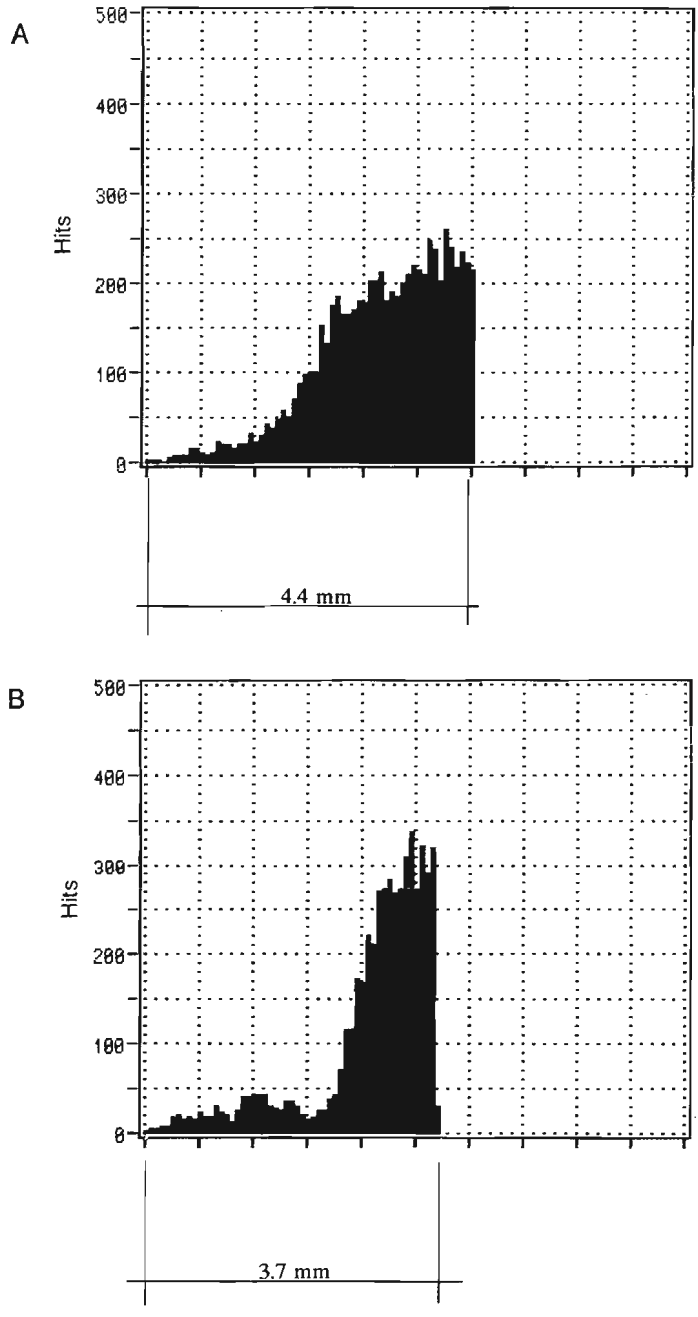


**Figure 4.8** Number-of-hits-versus displacement of the specimen center of a cooled (A) and a non-cooled (B) thermal barrier coating.

The coatings sprayed on a non-cooled substrate had a low level of AE after the start of the test. This level was constant or increased only slightly until a certain displacement was reached. At this point the amount of hits abruptly increased.
These typical AE patterns were measured for all cooled and non-cooled coatings, except for the coatings sprayed with an extended anode channel and an Ar/H2 flow of 70/15. The difference between the cooled coating and non-cooled coating here is not as distinct as determined by the coatings sprayed with other parameters.
The influence of a standard or an extended anode channel, on the AE production of a cooled or non-cooled specimen is only insubstantial.

To discover the reason for the abrupt increase of the amount of hits, produced by a non-cooled specimen after passing by a certain displacement, a test was carried out where the tensile testing machine was stopped just after the moment that the first high amount of hits appeared. This occurred at a displacement ranging from 1.8 to 2.2 mm, depending on the plasma spray parameters of the non-cooled coatings. A cooled specimen sprayed with the same spray parameters and the same anode channel was loaded until the same displacement was reached.
After this, the specimens were prepared for microscopical investigation. The non-cooled specimen showed one large crack in the ceramic coating, running from the top of the coating down to the bondcoat. Such a large crack was not observed in the cooled coating. These coating showed a number of vertical cracks. The cracks started at the top of the coating and ran down to the bondcoat. Figure 4.9 shows the photographs of the tested coatings, together with their AE diagrams.

**2.6.2 Characteristics of the AE hits.**

As described in paragraph 2.3.1 of this chapter, AE sources can be represented by force dipoles with a delta function time dependence. These sources produce waves which reach the surface and thus the AE transducer, where the waves are registered as hits. These hits have characteristics as duration, maximum amplitude, rise time, number of counts and energy. To get insight into the types of hits which were produced during the AE tests of the cooled and non-cooled coatings, the characteristics of the hits produced by these coatings were given in so called correlation plots.

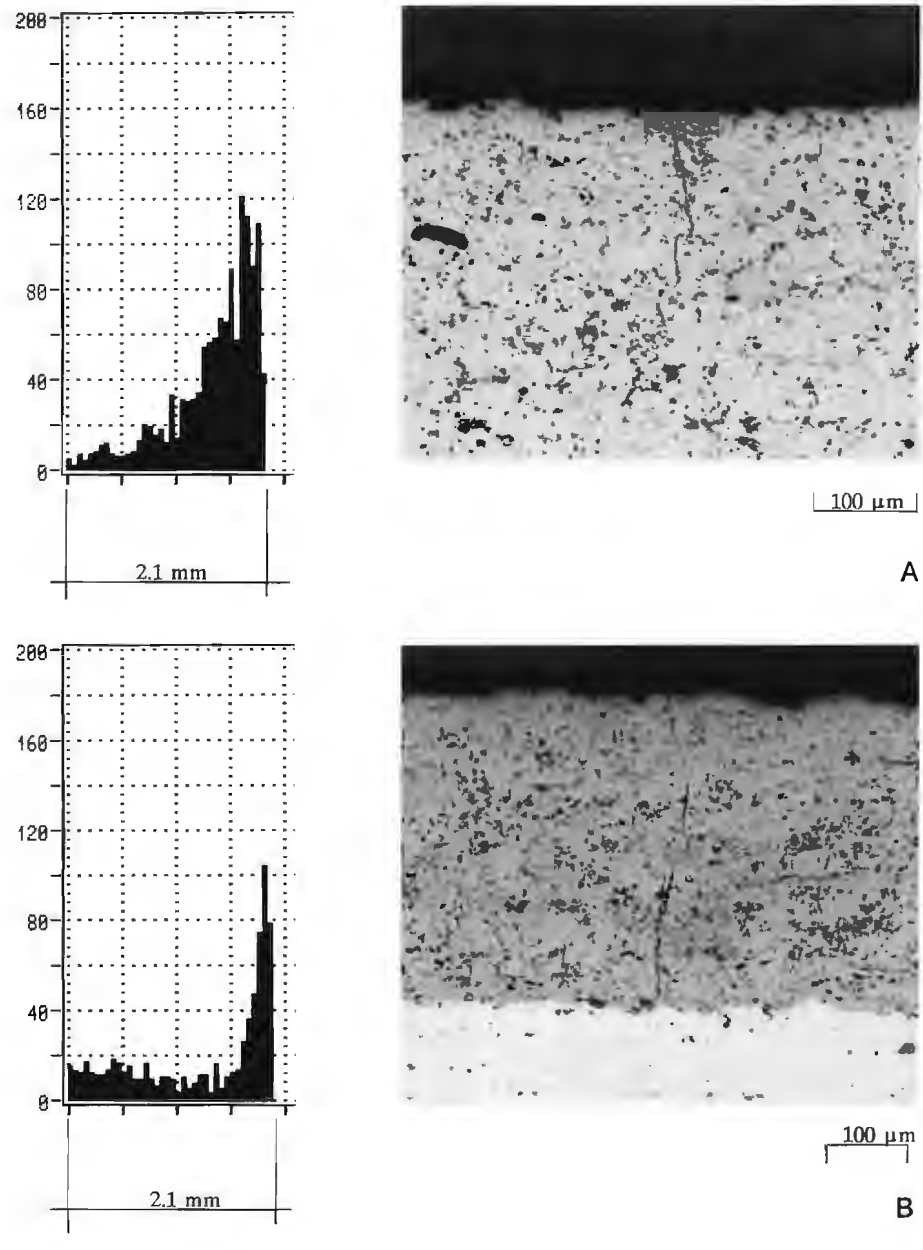


**Figure 4.9** Hits-versus-displacement for a cooled (A) and a non-cooled coating (B). (standard plasma, $Ar/H_2$ 70/15) Both coatings were bend to the same deflection of 2.1 mm. It can be seen that the non-cooled coating shows one coarse macrocrack, whereas the cooled coating shows several small macrocracks.

These plots show relationships between the different hit characteristics, for example energy- versus-duration or counts-versus-risetime. Figure 4.10 shows the correlation plots which were made during acoustic emission evaluation of the thermal barrier coatings. From this figure it is clear that this results in ten correlation plots.

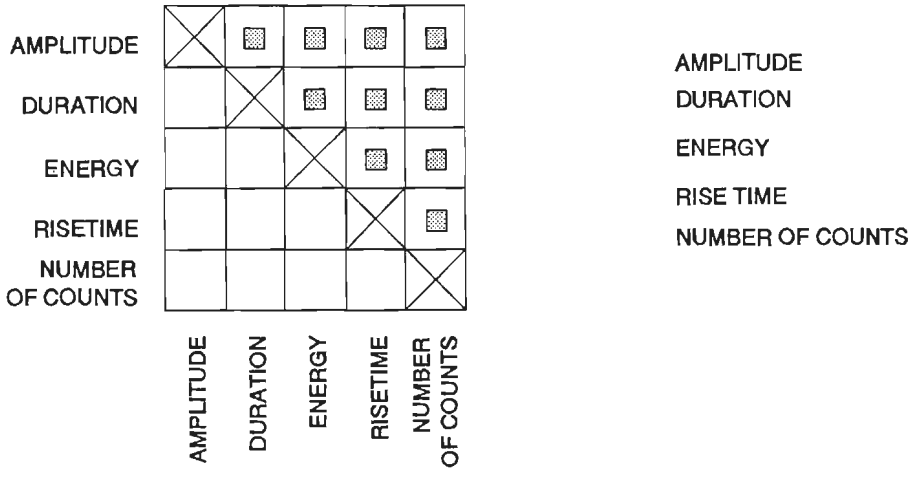


**Figure 4.10** Correlation plots of the various AE parameters, registrated during the bending tests.

The plots representing energy-versus-duration and energy-versus-counts, show almost straight lines. This indicates that hits with a long duration have also a high energy; and that the number of counts is proportional to the energy. The curves have almost the same slope in the case of a cooled or non-cooled specimen.

The non-cooled coatings, however, show more hits with a longer duration and thus a higher energy. Furthermore it can be observed that the coatings, sprayed onto a non-cooled specimen show hits with a short risetime but with a long duration.
Figures 4.11 a) and b) give the correlation plots of two coatings, sprayed with a standard anode channel and a gas flow of 70/15 at a cooled, respectively a non-cooled substrate.

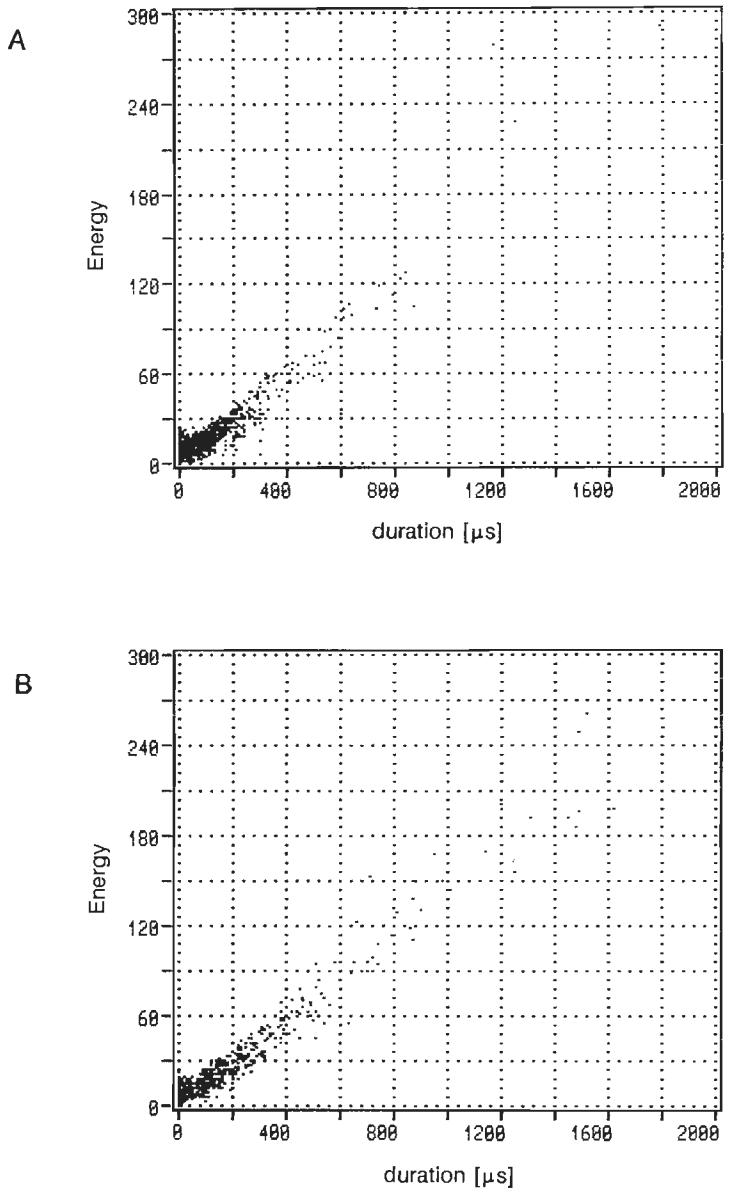


**Figure 4.11a** Correlation plots of duration-versus-energy of the AE signals of a cooled (A) and a non-cooled coating (B). The coatings were bend to the same deflection. It has to be remarked that the non-cooled coating produced hits with a higher duration and a higher energy.

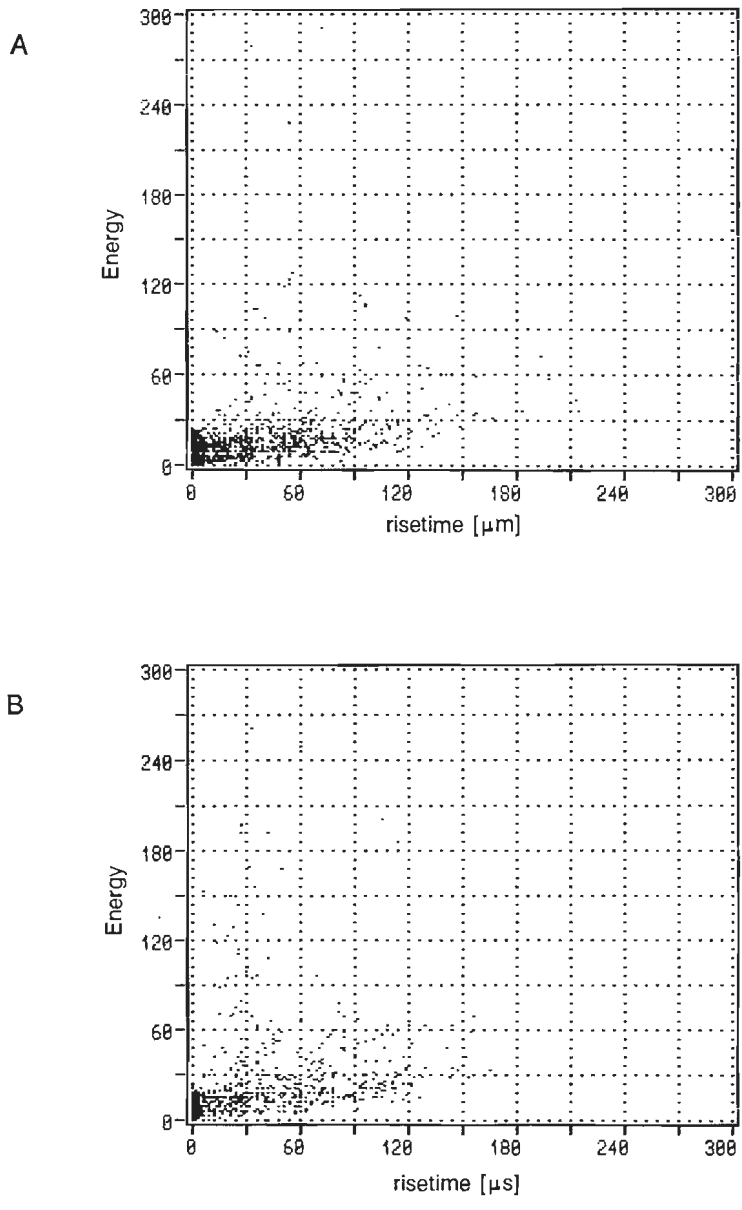


**Figure 4.11b** Correlation plots of risetime-versus-energy of the AE signals of a cooled (A) and a non-cooled coating (B). The non-cooled coating produced hits with a short risetime and a high energy.

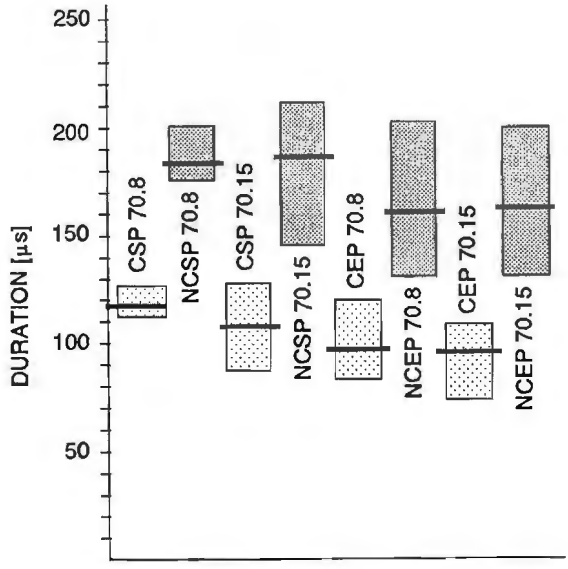


**Figure 4.12** Duration of the hits produced by the different types of thermal barrier coatings. The vertical bars indicate the maximum and minimum values, whereas the horizontal line indicates the mean value of the duration.

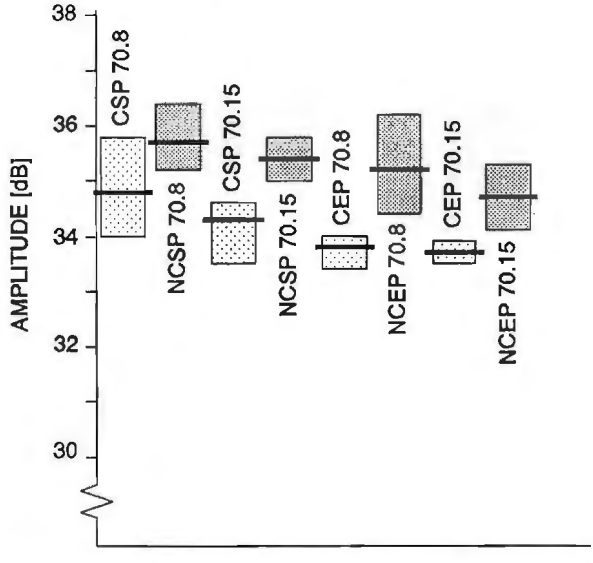


**Figure 4.13** Amplitude of the hits produced by the different types of thermal barrier coatings. The vertical bars indicate the maximum and minimum values, whereas the horizontal line indicates the mean value of the amplitude.

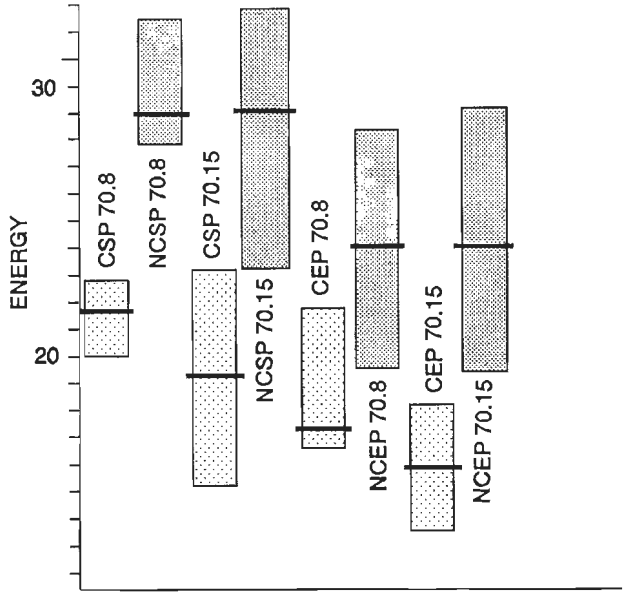


**Figure 4.14** Energy of the hits produced by the different types of thermal barrier coatings. The vertical bars indicate the maximum and minimum values, whereas the horizontal line indicates the mean value of the energy.

The phenomenon that non-cooled coatings produced AE hits with a higher energy, greater amplitude and longer duration, was observed for all types of non-cooled coatings. Next diagrams, which are given in figures 4.12, 4.13 and 4.14 show the mean duration, amplitude and energy of all tested coatings. All the characteristics presented in these diagrams concern hits which were produced in the displacement interval from 0 to 2,1 mm.

### 2.6.3 Coatings subjected to compressive stress.

Ceramics are known to have a low tensile strength, but in general they have a high compressive strength. Steffens [25] reports a compressive strength of plasma sprayed $ZrO_2$ of 300 - 600 MPa at a porosity of 5-3% respectively. The behaviour of the different coatings under compressive stress was investigated in the same bending apparatus as described in paragraph 2.5.4 but now with the specimen turned upside down. The distinct difference in AE diagrams which was measured in the tensile tests was not observed in this test mode. The amount of AE hits was much lower than in the foregoing tests. In the tensile mode, the amount of hits ranged from 2500 to 8000, whereas the number of hits in the compressive mode never exceeded 600.

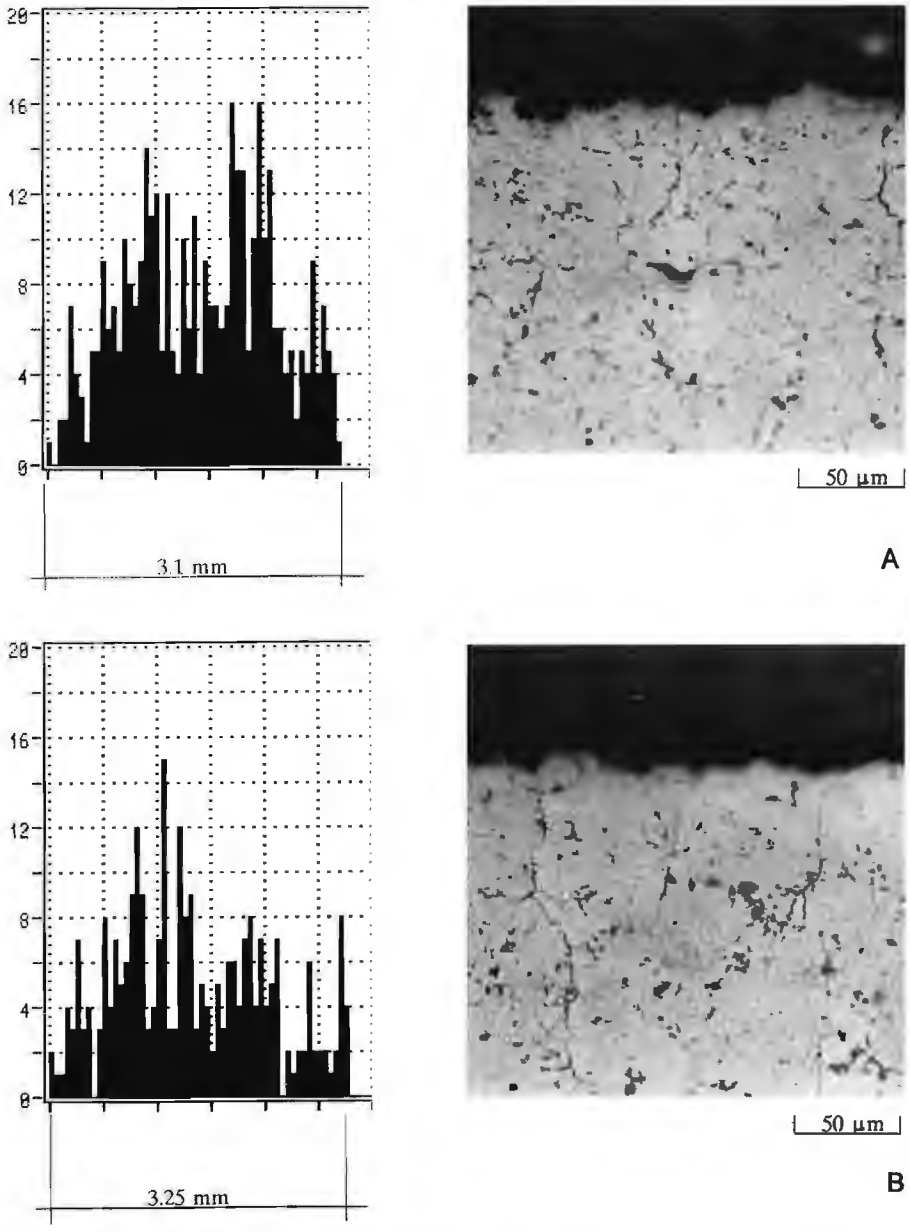


**Figure 4.15** Acoustic Emission graphs of the hits-versus-displacement of a cooled (A) and a non-cooled (B) thermal barrier coating, subjected to compressive stresses. The photographs show the cross sections of the coatings after they were loaded. It can be seen that vertical cracks were formed in both the cooled and non-cooled coatings. The vertical cracks in the cooled coating have horizontal branches.

The AE diagrams of hits versus displacement of a cooled and non-cooled coating subjected to compressive stress are shown in figure 4.15, together with their microstructures.
Severe crack formation in the ceramic coatings in the compression mode can hardly be observed. The cracks which developed existed mainly in the cooled extended plasma coatings. The cracks started at the top of the coating and had a maximum length of half the coating thickness. The cracks mainly propagate along the particle boundaries, which can be seen in figure 15.

The non-cooled extended plasma coating (gasflow Ar/H2 70/15) showed one large cross formed crack with vertical and horizontal branches but was further hardly damaged.

**2.6.4 Bondcoats subjected to tensile stress**
The two types of tested bondcoats, sprayed onto a cooled and onto a non-cooled substrate, showed great differences in AE patterns. The non-cooled coating showed a hits versus displacement relationship which was similar to the non-cooled specimens discussed in the foregoing paragraph. The cooled coating produced a very low amount of hits during the test. The results for both coating types are shown in figure 4.16.

**2.6.5. Calculation of the maximum strain at which macrocracking occurs in the non-cooled coatings.**
In the following calculations it is assumed that the stiffnesses of the bondcoat and the topcoat are constant over the coating thickness.

The deflection of a specimen, shown in figure 4.17, loaded by a central force F, and simply supported at two pivots at a distance l, can be described by equation 7.

$$u = \frac{Fl^3}{48(EI)'} \qquad (7)$$

| | |
|---|---|
| F: | bending force [N] |
| l: | distance [mm] |
| (EI)': | combined Young's modulus and moment of inertia for a layered beam. |

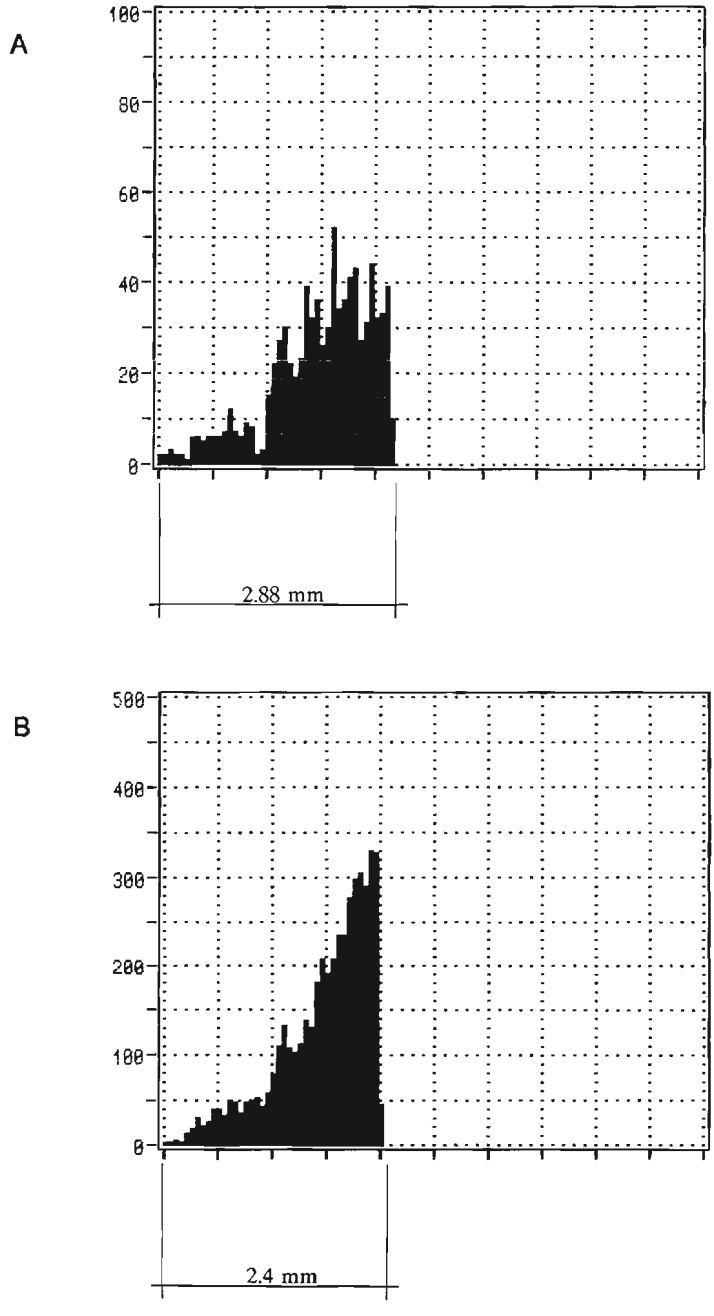


**Figure 4.16** Hits-versus-displacement of a cooled (A) and a non-cooled (B) air plasma sprayed FeCrAlY bondcoat, subjected to tensile stresses.

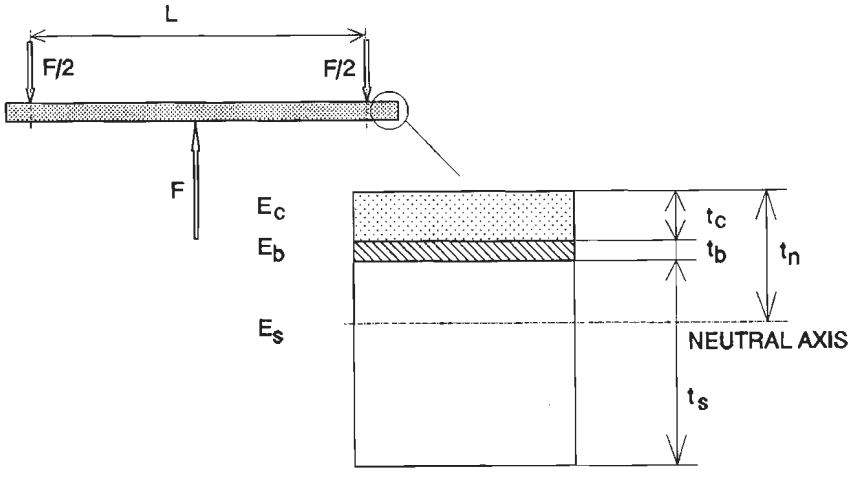


**Figure 4.17** A layered beam, bent by a central force F. The small figure shows a cross section of this beam which consists of a substrate, a metallic bondcoat and a $ZrO_2$ topcoat.

(EI)' can be calculated from the different Young's moduli and thicknesses of the substrate, bondcoat and topcoat [30]. The stiffnesses of $ZrO_2$ coatings are reported in chapter III, paragraph 7.6. The stiffness of a bondcoat, sprayed on a non-cooled substrate, and subjected to tensile stress had a mean stiffness of 147700 MPa.

To check the calculated values of (EI)', they can be compared to the (EI)' values which can be derived from the deflection versus force diagrams which were registered during the AE tests.

The maximum strain in the ceramic coating can be calculated by equation 8:

$$\epsilon_c = \frac{Flt_n}{4(EI)'} \tag{8}$$

$\epsilon_c$: Strain in the ultimate fibre of the ceramic coating

$t_n$: Distance from the ultimate fibre to the neutral axis of the layered beam.

The distance $t_n$ can be calculated by using equation 9 [29]

$$t_n = \frac{bt_{c0}.5t_c + \frac{E_b}{E_c}bt_b(t_c+0.5t_b) + \frac{E_s}{E_c}bt_s(t_c+t_b+0.5t_s)}{bt_c + \frac{E_b}{E_c}bt_b + \frac{E_s}{E_c}bt_s} \quad (9)$$

b: specimen width [mm]
$t_c$: $ZrO_2$ topcoat thickness [mm]
$t_b$: bondcoat thickness [mm]
$t_s$: substrate thickness [mm]
$E_c$: $ZrO_2$ topcoat stiffness [MPa]
$E_b$: bondcoat stiffness [MPa]
$E_s$: substrate stifness [MPa]

Figure 4.18 shows the deflection versus force diagram for a cooled and a non-cooled standard plasma coating. The point at which macrocracking in the non-cooled coating started is indicated by the arrow.

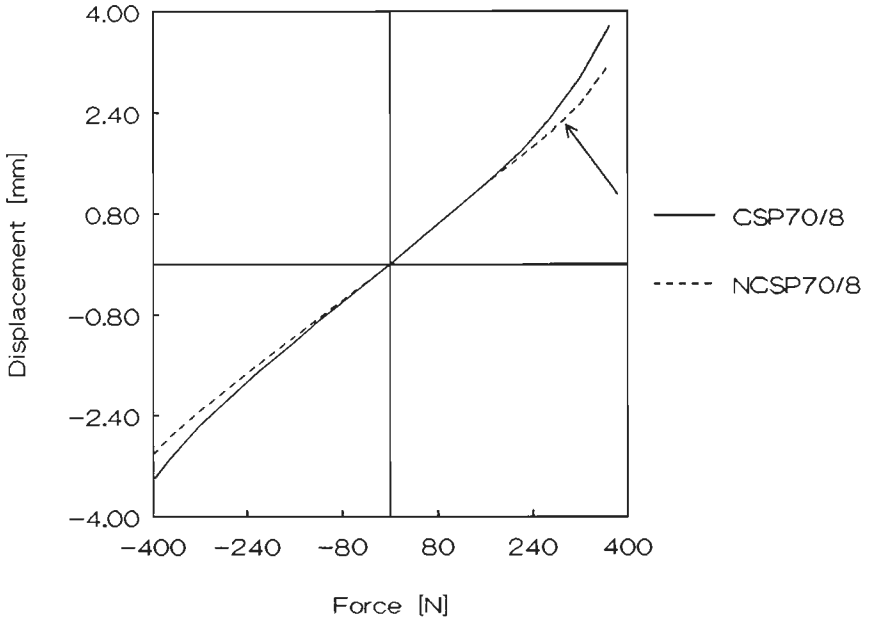


**Figure 4.18** Deflection versus force diagram of the specimens CSP 70.8 and NCSP 70.8 during the three point bending test. The arrow indicates the onset of macro cracking in the non-cooled coating.

The maximum strain can now be calculated by using the foregoing equations. This results in a strain at failure of 0.0025. This results in a tensile stress of 100 MPa, when the Young's modulus of the coating is about 40,000 MPa.
Table 2 shows the different strains at which macrocracking occurs in the non-cooled coatings. The coatings sprayed with an extended anode channel and a gas flow of 70/15 are not included in this table. These coatings showed already some macrocracks after spraying, so no abrupt growth of macrocracks could be determined during the AE tests.
The stresses causing macro crack formation in the non-cooled coatings, varied from 85 to 120 MPa. It has to be noted that the residual stresses which may be present in the $ZrO_2$ coatings are neglected.

Table 2
Maximum strain at which macro-cracking occurs in the non-cooled coatings. The residual stress state of the coatings is neglected.

| coating | $\epsilon_{min}$ | $\epsilon_{max}$ | $\sigma_{min}$ | $\sigma_{max}$ |
|---|---|---|---|---|
| NCNP708 | 0.00214 | 0.00296 | 85.6 | 118.4 |
| NCNP7015 | 0.00249 | 0.00297 | 99,6 | 118.8 |
| NCEP708 | 0.0025 | 0.00305 | 87.5 | 106.8 |

**2.7 Discussion**
The cooled and non-cooled coatings show distinct differences in the relationship between displacement and amount of hits. This difference may be explained as follows. The cooled coatings show a very dense network of microcracks, with an orientation in both vertical and horizontal direction, distributed homogeneously throughout the ceramic coating. These cracks give the cooled coating a certain flexibility. Especially the horizontal microcracks, which are in fact particle boundaries, allow the particles to slide over each other over small distances and make it possible for the coatings to undergo a certain strain before macrocrack formation occurs. This phenomena is also described by Berndt [26].
This in contrary to the non-cooled coating, were this dense microcrack network is almost absent, and macrocrack formation in the coating starts after a certain strain has been exceeded.
The amount of AE produced by the cooled coatings is caused by the gradual

growth of cracks during the loading of the specimens. The amount of hits is therefore also increasing gradually.
This in contrary to the non-cooled coatings where the macrocrack formation, occurring after exceeding a certain strain, caused an avalanche of hits. The macrocrack ran from the top of the ceramic coating down to the bondcoat.
A cooled specimen which was bent to the same deflection at which in a non-cooled specimen (sprayed, using the same plasma spray parameters) macrocrack formation occurred, showed a number of short vertical cracks. These cracks started at the top of the ceramic coating and went down in the direction of the bondcoat. These cracks, however, seldom reached the bondcoat and their lengths varied from 50 to 200 $\mu$m. This in contrary to the non-cooled coatings where one large crack ran from the top of the coating down to the top of the bondcoat.

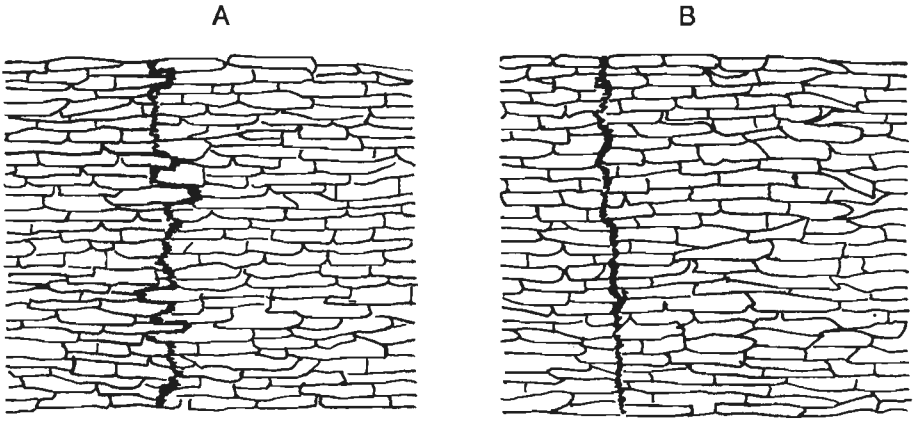


**Figure 4.19** Crack formation in a cooled (A) and a non-cooled (B) $ZrO_2$ coating, caused by tensile stresses. The cracks in the cooled coating ran mainly along the particle boudaries. In the case of the non cooled coating, the crack traverses through the particles.

The macro cracks in a cooled coating ran from the top of the coating down to the bondcoat. The crack path partly followed the particle boundaries and partly proceeded through the individual particles. Cracks in the non-cooled coatings predominantly traversed through the particles and followed seldomly the particle boundaries. This phenomena was also observed by Watson and Levine [27] who investigated crack formation in TBC's, sprayed on cooled and non-cooled substrates, after thermal shock tests, and by Lapierre and

Herman [28] who studied the formation of cracks in sintered and as-sprayed ceramic coatings. Figure 4.19 shows the cracks which were formed in a cooled and a non-cooled coating.

A second phenomenon played a role in the different failure behaviour of cooled and non-cooled coatings. As was stated in chapter 3, the cooled coatings possessed residual tensile stresses. The non-cooled coatings possessed lower tensile stresses or even compressive residual stresses. Because of this, the cooled coatings will develop macrocracks at a lower strain than the non-cooled coatings will do.
But if this difference in residual stress state would mainly have determined the failure behaviour, the hits versus displacement graphs of the cooled and non-cooled coatings had to be the same. Only the point where the abrupt increase of the AE hits started would have shifted to a lower displacement in the case of the cooled coating.

The sources causing the AE hits were in both cases, non-cooled and cooled the same. Macrocracks were formed by the growth of microcracks or the development and growth of microcracks. Because of this, the hits produced by the different types of coatings are of the same type and only differ in strength. The formation of a crack in a non-cooled coating causes stronger hits than a crack which is developed in a cooled coating.
The formation of macro cracks in the cooled coating was facilitated by the presence of the dense microcrack network. The microcracks had to grow over only little distance before interconnection with other microcracks occurred. This in contrary to the non-cooled coating where the number of microcracks is much less. The micro cracks had to bridge larger distances before interconnection took place. The
energy release during the macrocrack formation in non-cooled coatings was greater than in the cooled coatings. Because of this, the non-cooled coatings produce AE hits with a larger energy, duration and amplitude.

The TBC's, subjected to compressive stresses, showed a hits versus displacement relationship, which was totally different from the ones observed during tensile loading. The number of hits was much less and no distinct difference between the cooled and non-cooled specimens was observed.
The low number of hits was caused by the fact that the coatings, loaded to

compressive stress showed almost no crack formation. The cracks which could be observed were very short horizontal cracks which only appeared in the cooled coatings sprayed with an extended anode channel. These cracks grew from the already existing short vertical cracks which were present in these types of coatings after spraying. The cracks which developed in these coatings are shown in figure 4.20.

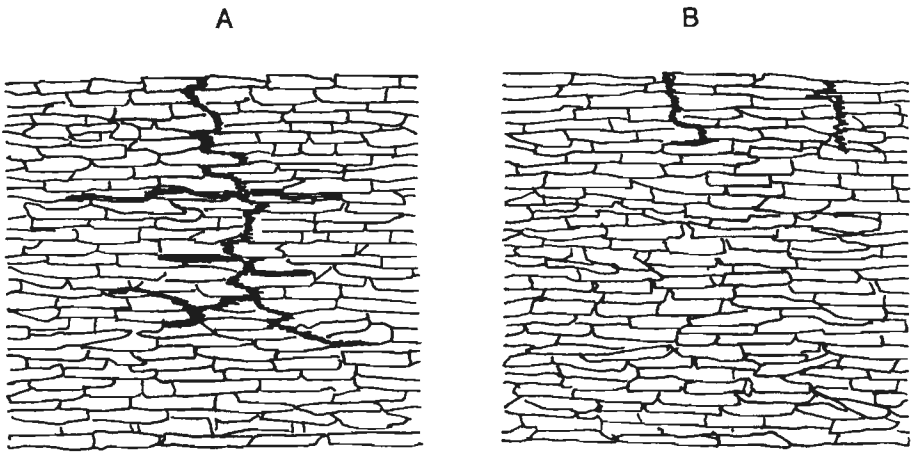


**Figure 4.20** Development of cracks in a cooled (A) and a non-cooled (B) $ZrO_2$ coating, subjected to compressive stresses. Both the cooled and the non-cooled coating show vertical cracks. The cracks in the cooled coating have branches, parallel to the substrate.

The difference in AE production between the cooled and non-cooled bondcoats could not be explained by a difference in microstructure. Microscopical investigation did not show differences in microstructure. The difference probably can be explained by the oxide content of both layers. The oxygen content was measured at Philip's Centre for materials technology, using a reduction method with carbon at 2950 K. The oxygen content of the non-cooled bondcoats was about wt. 50 % higher than the oxygen content of the cooled one. This higher content could be explained by oxidation of the bondcoat after it was sprayed and cooled down to room temperature.

The higher content of oxides made the non-cooled coating more brittle than the cooled one. The cracking of the oxides caused a high amount of AE. Microscopical investigation showed that the cooled coating could be strained further than the non-cooled one before cracking occurred. Figure 4.21 shows

the oxide content of the cooled and non-cooled bondcoats and the FeCrAlY powder, the coatings were sprayed with.

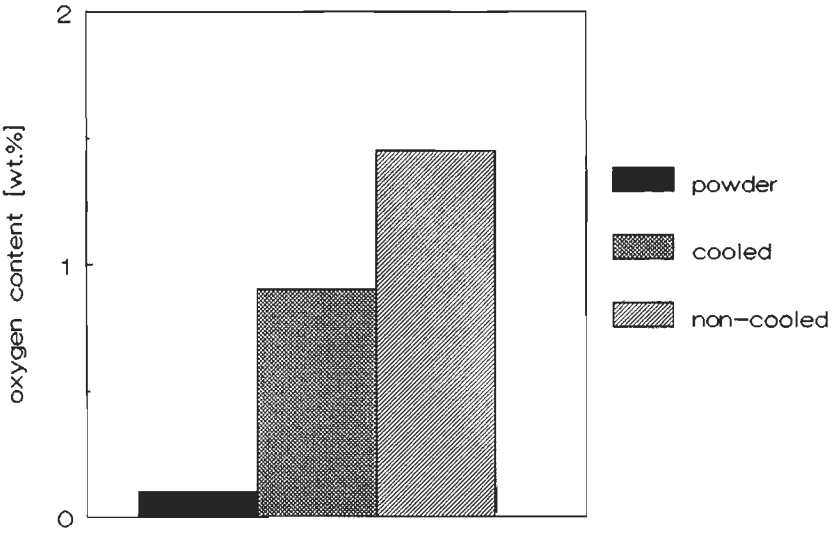


**Figure 4.21** Oxygen content of the cooled and the non-cooled air plasma sprayed FeCrAlY bondcoats. The oxygen content of the FeCrAlY powder is also given.

As could be read in the foregoing section, the bondcoats, sprayed on a non-cooled substrate, did show an abrupt increase in the production of AE hits beyond a certain strain. This phenomenon was almost the same as could be observed during the AE testing of the specimens consisting of a non-cooled bondcoat and a non-cooled topcoat. The assumption may arise that the high amount of hits emitted by the specimens with a non-cooled bondcoat and topcoat, was not or not only caused by the ceramic topcoat, but by the non-cooled bondcoat. To investigate this, specimens consisting of a cooled bondcoat and a non-cooled topcoat were tested. These specimens showed hits versus displacement graphs, which were the same as produced by the specimens with both a non-cooled bond and topcoat.
Secondly, the NCEP 70/15 specimens, which also contained a non-cooled bondcoat, did not show the AE graphs which were observed during testing of the other non-cooled coatings. The ceramic topcoat of the NCEP70/15 specimens showed already some macrocracks after spraying. That is why the sharp increase in AE hits was not observed during the AE experiments.

When however the non-cooled bondcoat should have produced the high amount of AE hits during the bending tests of the non-cooled coatings, it should have been observed also during the experiments with these specimens. This abrupt increase however, was not observed during these test. From this and from the foregoing experiment it may be concluded that the AE signals are mainly produced by the ceramic topcoat and not by the metallic bondcoat.

**2.8 Conclusions**

Acoustic emission evaluation has proven to be a suitable tool to investigate the failure behaviour of plasma sprayed thermal barrier coatings. Especially the formation of macrocracks in coatings, sprayed onto non-cooled substrates, could be determined, long before they could be observed visibly.

The failure behaviour of coatings, sprayed on cooled and non-cooled substrates, showed great differences. These differences were mainly determined by the difference in microstructure between the cooled and non-cooled ceramic coatings. Due to the dense network of microcracks in the cooled coatings, the macrocracks in these coatings had a more craggy appearance than the cracks which were formed in the non-cooled coatings.

The residual stress state in the cooled and non-cooled coatings also played a role in the difference of the failure mode. The cooled coatings have higher residual tensile stresses than the non-cooled coatings (See chapter 3). Because of that, the growth of cracks in the cooled coatings will start at a lower strain than in the non-cooled coatings.

## 3 References chapter 4


[1] Kaiser J.,Erkentnisse und Folgerungen aus der Messung von Gerauschen bei Zugbeanspruchungen von Metallische Werkstoffe Archiv Eisenhuettenwesen 24(1953) 43-45

[2] Scruby C.,Quantitative Acoustic Emission Techniques, In: Research Techniques in Non Destructive Testing, Vol. 8, editor R.S. Sharpe, Academic Press, London, 1985

[3] Scruby C., Wadley H., Sinclair J.E., The Origin of Acoustic Emission during Deformation of Aluminium and Aluminium-Magnesium Alloys Phil. Mag. A. vol. 44(1981) no. 2, pp. 249-274.

[4] Wadley H.N.G., Scruby C., Elastic Wave Radiation from Cleavage Crack Extension, Internat. J Fracture 23(1983)

[5] Wadley H.N.G. Acoustic Emission, A Quantitative NDE Technique for the Study of Fracture. In: Solid Mechanics Research for Quantitative Non Destructive Evaluation, Editor J.D. Achenbach, Martinus Nijhoff Publishers, Dordrecht, the Netherlands 1987.

[6] Green R.E. Basic Wave Analysis of Acoustic Emission Testing. In: Mechanisms of Non Destructive Testing Editor W.W. Stinchecomb, Plenum Press, New York, 1980.

[7] Ohira t., Pao Y-H.,Acoustic Emission Source Characterization of Microcracking in A533B Steel.

[8] Rustidge A.B., Een studie naar het Breukgedrag van Koolstof en Polyetheen Hybride Composieten met behulp van de Akoestische Emissie Techniek, Master's Thesis, Eindhoven University of Technology, 1990

[9] Waschkies E., Fraunhofer Institut Saarbrücken,
Private Communication, March 1990

[10] Boehm P., Crostack H.A., Dvorak M., Steffens H.D. Monitoring of the Thermal Coating Process by Means of Acoustic Emission Analysis. In: Non Destructive Testing, Editor J. Bogaard and G.M van Dijk , Elseviers Science Publishers, Amsterdam 1989.

[11] Berndt C.C., Miller R.A., Failure Analysis of Plasma Sprayed Thermal Barrier Coatings. Thi. Sol. Fi., 119(1984) 427-437.

[12] Berndt C.C., Herman H., Failure during Thermal Cycling of Plasma Sprayed Thermal Barrier Coatings, Thi. Sol. Fi. 108 (1983)

[13] Pantucek P., Evaluation of Ceramic Thermal Barrier Coatings under Combined Thermal and Mechanical Loads. COST 501, Final Report, Darmstadt, 1987.

[14] Verbeek A.T.J., Klostermann J.A., Houben J.M. Adhesion and Ductility of Plasma Sprayed Thermal Barrier Coatings. In: Euro Ceramics, Vol3. Engineering Ceramics, Editors de With, Terpstra, Metselaar. Elseviers Applied Science, London, New York, 1989.

[15] Verbeek A.T.J., Houben J.M., Klostermann J.A., Acoustic Emission Evaluation of Thermal Barrier Coatings Using the Three Point Bending Test. ASME Paper 91-GT-279, 1991.

[16] Crostack. H.A., Steffens H.D., Krueger A., Pohl K.J. Non Destructive Testing of Plasma Sprayed Ceramic and Metallic Coatings. In: Advanced Materials Research and Development for Transport, Ceramic Coatings for Heat Engines, Strasbourg, 1985, Les Editions de Physique, Les Ulis France, 1985.

[17] Almond D., Moghishi M., Reiter H., The Acoustic Emission Testing of Plasma Sprayed Coatings Thin Sol. Fi.108(1983) 439-447.

[18] Wen L.S., Zhang H.T., Zhou X.K., Acoustic Emission Research in the Fracture behaviour of Plasma Sprayed NiAl Coatings during Bend Testing, Surf. Coat. Techn. 30(1987) 115-123.

[19] Mora-Marquez J.G., Lira-Olivares J. A Study of Crack Initiation and Propagation in NiCR Thermally Sprayed Coatings using AE Techniques. Thi. Sol. Fi. 153(1987)

[20] Cohrt H. Thuemmler F. Degradation Mechanisms of Thermal Barrier Coatings in Bending Tests. Surf Coat. Techn. 32(1987)

[21] Shankar N.R., Berndt C.C., Herman H., Failure and AE Response of Plasma Sprayed $ZrO_2$ 8 wt% $Y_2O_3$ Coatings. Ceram. Eng. Sci. Proc., 3(1982) 9/10

[22] Chulya A., Baaklini G.Y., Vary A. In Situ Monitoring of Failure Mechanisms in Brittle Matrix Composites, Using AE. Japanese Non Destructive Testing Society Seminar, Summer 1991, Japan.

[23] Scruby C., Baldwin G.R., Stacey K.A., Characterization of Fatigue Cracks Extension by Acoustic Emission. Int. Journ. of Fract. 28 (1985) 201-222.

[24] Felsen L.B.Propagation and Scattering of High Frequency and Pulsed Signals in the Presence of a Concave Boundary. In: New Procedures in Non Destructive Testing, editor P. Höller, Springer Verlag, 1983

[25] Steffens H.D., Fischer U., Correlation between Microstructure and Physical Properties of Plasma Sprayed $ZrO_2$ Coatings. In: Thermal Spray Technology, editor D.L. Houck, ASM, Ohio, USA, 1989.

[26] Berndt C.C., Material Property Measurements on Thermal Barrier Coatings. ASME paper 88-GT-277, 1988.

[27] Watson J.W., Levine S.R. Deposition Stress Effects on the Life of Thermal Barrier Coatings on Burner Rigs.
Thi. Sol. Fi. 119(1984) 185-193

[28] Lapierre K., Herman H., Tobin A.G., The Microstructure and Properties of Plasma Sprayed Ceramic Composites. Ceram. Eng. Sci. Proc. 12 (1991)

[29] Ugural A.C., Fenster S.K., Advanced Strenght of Materials, Elseviers Science Publishing, New York, 1987

[30] Roark R.J., Young W.C., Formulas for Stress and Strain, Mac Graw Hill, 1985

## CHAPTER V TESTING OF THERMAL BARRIER COATINGS

### 1 Introduction

This chapter describes the methods and results of tests of plasma sprayed thermal barrier coatings. The coatings were sprayed according to the methods described in chapter III.

The thermal shock and the erosion resistance were determined.

The influence of the bondcoat on the performance of the ceramic topcoat was studied. Furthermore, the long term behaviour of $ZrO_2$ 7.6 wt.% $Y_2O_3$ at elevated temperatures was investigated, using X-ray diffraction for phase determination.

The bond strength of the different thermal barrier coatings was measured, using a tensile adhesion test.

### 2 Thermal shock resistance

One of the most important characteristics of thermal barrier coatings is the ability to undergo fast temperature changes without failing; the so called thermal shock resistance.

The thermal shock resistance is defined as the number of thermal shocks a thermal barrier coating withstands without failing.

Mainly all thermal shock tests are carried out, using burner rigs. The coated specimen are heated up to a certain temperature by a burner and subsequently they are cooled by an air jet.

Since thermal shock tests are not standardized, it is very difficult to compare results, reported in literature. Each manufacturer or laboratory uses its own test method. As well the temperatures as heating and cooling times differ strongly. However, temperature cycles between 300 and 900 °C and 400 and 1100 °C are often reported. The heating times vary from several seconds to 1 hour.

It has to be remarked that these long heating times are more suitable for the investigation of the oxidation behaviour of the bondcoat than of the thermal shock resistance of the thermal barrier coating.

Berndt [1] compared the results of different thermal shock tests, applied to the same thermal barrier coatings. He concluded that the thermal shock resistance of the coatings strongly increased with decreasing testing temperature. The thermal shock resistance of an $Y_2O_3$ stabilized $ZrO_2$ coating with a NiCrAlY bondcoat increased by ten times when the

temperature during a cyclic furnace test was lowered from 1100 to 1000 °C.

### 2.1 Thermal shock testing

During the research project, two types of thermal shock tests were carried out: the burner rig test and the furnace test. These tests and the obtained results will be described in the next paragraphs. The number of thermal cycles the coatings withstood before delamination or severe damage of the specimen's edge occurred, was taken as the failure criterion.

#### 2.1.1 Burner rig testing

The burner rig which was developed at Eindhoven University. It consisted of an acetylene-compressed-air burner and two air jets. Due to its special construction, the burner produces a completely flat flame front, thus avoiding point loading of the coating. The burner was developed Hoek [2] on the basis of an initial construction produced by Schumacher of the Linde Company.

The air jets are placed at both sides of the burner. Burner and air jets are mounted on a moveable carriage. The carriage is moved by a pneumatic cylinder. This cylinder is controlled by an electronic circuit with adjustable heating and cooling times.

The strip shaped specimen were clamped in a water cooled specimen holder, which could contain two specimen.

The temperature of the specimen was measured by thermo-couples which were spot-welded to the back side of the specimen. The signals of these thermo couples were registered by a T,t recorder.

The choice to move the burner and air jets and keep the specimen at a fixed place was made to make it possible to apply acoustic emission evaluation during thermal shock testing. Moving and suddenly stopping of the specimen holder might have produced too much acoustic emission, veiling the acoustic emission produced by the specimen.

Figure 5.1 shows the set up of the thermal shock test.

The temperature cycle during burner rig testing changed between 380 and 1100 °C. After the coating had failed, the test was stopped and a cross section of the specimen was prepared for microscopical examination in order to determine the cause of failure. When the coating did not fail after 1000 cycles, the test was also stopped. Subsequently a cross section of the specimen was polished and examined. The amount and the dimensions of the

cracks in the coatings were determined.

**Figure 5.1** Set up of the burner rig for thermal shock testing.
The system consists of an acetylene-compressed air burner and two air jets. The rig may contain two strip shaped specimens which are clamped in a water cooled holder.

When the coating did not fail after 1000 cycles in the burner rig test, the specimen was loaded in the furnace test.

### 2.1.2 Furnace testing

The specimen were heated up for three minutes in rapid heating furnace which was at a constant temperature of 1100 °C. Subsequently they were taken out of the furnace and quenched to room temperature in a vessel, containing water at room temperature. During cooling down in the water the specimen were rapidly moved in order to remove steam from the specimen's surface. This cycle was repeated for 50 times. Afterward the specimen were prepared and the damage in the coatings was determined.

### 2.1.3 Specimen

The specimen consisted of a 3.2 mm Hastelloy X substrate covered with a 0.1 mm MCrAlY bondcoat and a $ZrO_2$ 7.6 wt.% $Y_2O_3$ topcoat. The bondcoats were low-pressure plasma sprayed FeCrAlY and air plasma sprayed FeCrAlY or NiCrAlY. They were sprayed as described in chapter III. The ceramic topcoats were also sprayed as described in chapter III. All

together 8 different topcoats and 3 different bondcoats were tested.
Besides these coatings, conventional thermal barrier coatings as described in chapter III, were tested. The results of the thermal shock tests are described in the next paragraphs.

### 2.2 Results of the thermal shock tests

It appeared that the type of FeCrAlY bondcoat (LPPS or APS) had a strong influence on the thermal shock behaviour of the thermal barrier coatings. Hence, the results will be discussed in separate paragraphs.

#### 2.2.1 Specimen with an APS FeCrAlY bondcoat

These specimen showed a low thermal shock resistance in the burner rig test. Failure already occurred after 5 to 50 thermal shocks. Figure 5.2 shows the results of this test.

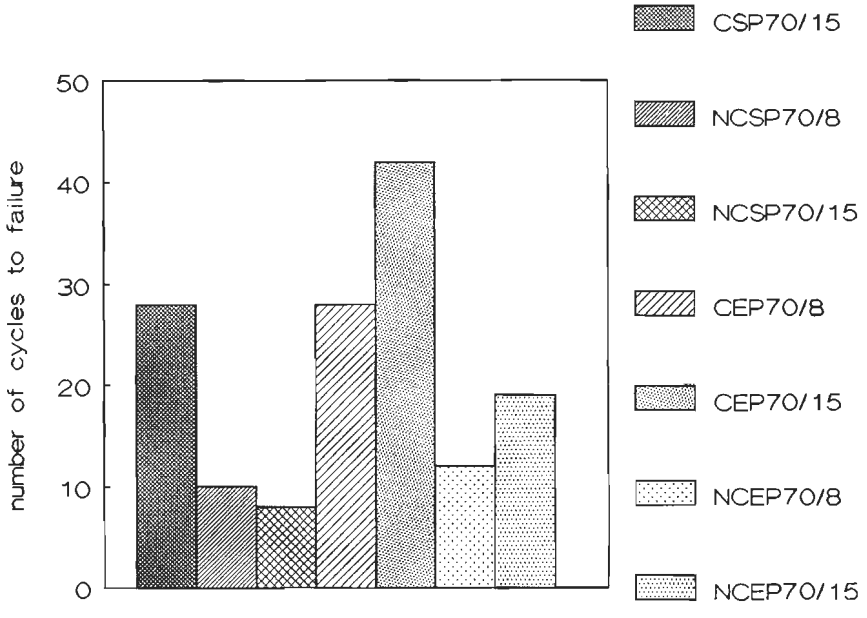


**Figure 5.2** Results of the thermal shock tests on thermal barrier coatings with an APS (air plasma sprayed ) FeCrAlY bondcoat.

During thermal cycling, a 20-30 $\mu$m oxide layer was formed at the interface bondcoat-topcoat. Crack formation in this oxide layer led to delamination of the $ZrO_2$ topcoat. Figure 5.3 shows a cross section of the interface of an APS

FeCrAlY bondcoat and a $ZrO_2$ topcoat. The crack in the oxide layer can be observed clearly.

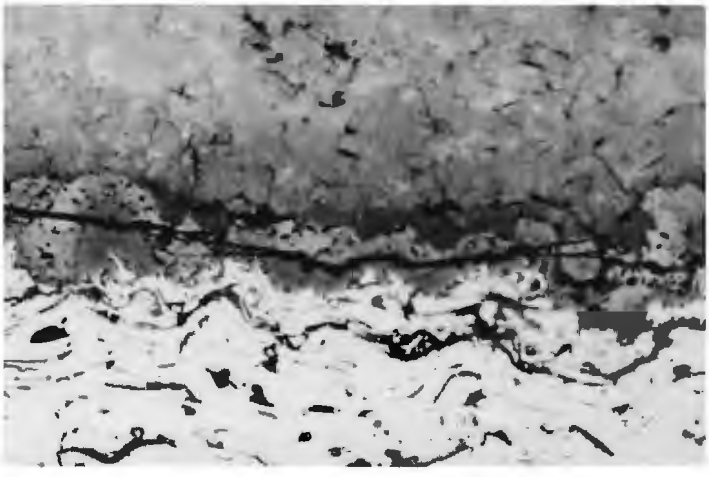


**Figure 5.3** Cross section of a failed thermal barrier coating. The photograph shows a 20 µm oxide film which developed at the interface bondcoat-topcoat. Cracking of these oxidefilm resulted in delamination of the $ZrO_2$ topcoat.

Figure 5.2 indicates that the coatings, sprayed on a cooled substrate had a higher thermal shock resistance than coatings sprayed on a non-cooled substrate.

Failure always occurred during heating up of the coating. This implies that delamination is caused by compressive stresses in the ceramic topcoat during the first stage of heating. The better performance of the cooled coatings can be explained for two reasons. The cooled coatings possess higher residual tensile stresses than the non-cooled coatings. Due to this fact, the compressive stress, occurring during the first stage of heating, is compensated. Furthermore, the cooled coatings possess a dense network of cracks, giving them a greater flexibility than the non-cooled coatings.

Nevertheless, the thermal shock resistance of the thermal barrier coating with the APS FeCrAlY bondcoats is low and their use is limited by the bondcoat.

### 2.2.2 Specimen with a LPPS FeCrAlY bondcoat.

The specimen with a LPPS FeCrAlY bondcoat showed a remarkably higher thermal shock resistance than the ones with an APS FeCrAlY bondcoat. The

results are shown in figure 5.4.

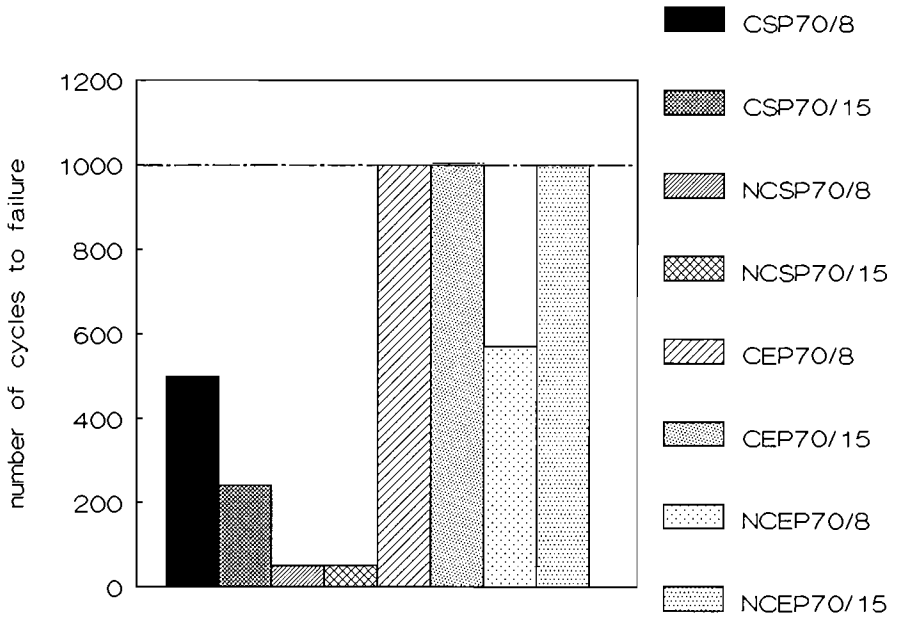


**Figure 5.4** Results of thermal shock tests on thermal barrier coatings with a LPPS (Low Pressure Plasma Sprayed) FeCrAlY bondcoat. The types of coatings, which reached the 1000 cyle line, indicated by the dashed, horizontal line, did not fail after 1000 cycles and were subsequently tested in the furnace test.

The NCEP70/15, the CEP70/8 and the CEP70/15 coatings did not fail after 1000 thermal shocks. The CSP 70/8 specimen, showed some damage at the edges of the $ZrO_2$ topcoat after 500 shocks, but no delamination occurred.

The NCSP70/8, NCSP70/15, NCEP70/8 and the CSP70/15 specimen failed by delamination, appearing in the ceramic topcoat, just above the interface bondcoat-topcoat. Delamination was caused by the formation of macrocracks, parallel to the substrate.
Microscopical examination of cross sections of specimen during the test (The coatings were still intact), proved that these parallel cracks grew during the course of the test. When they became too large, delamination arose during heating up of the coating.

After 1000 cycles, the NCEP70/15 coating showed some parallel cracks. Failure at short term, however, was not to be expected, taking into account the length (0.5 to 2 mm) of the parallel cracks and the fact that the cracks were not interconnected.

After 1000 cycles the CEP 70/8 and CEP70/15 topcoats did not show parallel cracks just above the interface bondcoat- topcoat. These coatings showed some small vertical and horizontal cracks.

**2.2.3 Specimen with an APS NiCrAlY bondcoat.**

Specimen consisting of a NiCrAlY bondcoat and a CEP70/15 $ZrO_2$ topcoat were tested for 1000 cycles. No failure of the ceramic topcoat was observed. Cross sections showed that a 2 to 3 $\mu$m $Al_2O_3$ oxide film developed at the interface bondcoat-topcoat.

**2.2.4 Conventional thermal barrier coatings**

The conventional TBC did not fail after 1000 cycles in the burner rig test. Microscopical observation of a cross section of the specimen showed that there existed small horizontal cracks, about 50 to 100 $\mu$m under the surface of the coating.

The maximum length of these cracks was 500 $\mu$m. The cracks were not interconnected, so failure due to delamination of parts of the coating was not to be expected.

During thermal shock testing, particles were swept away from the surface of the $ZrO_2$ coating. This phenomena could be observed during the heating cycle: lightened particles were blown away by the flame of the burner.

Figure 5.5 shows a cross section of the shocked coating. The horizontal cracks as well as the loose particles can be observed.

**2.4 Discussion**

**2.4.1 Behaviour of the ceramic topcoat**

Figure 5.4 reveals that substrate cooling has a positive influence on the thermal shock resistance of thermal barrier coatings. Especially in the case of coatings, sprayed with a standard anode channel this is evident. The non-cooled specimen failed after 50 to 80 cycles, whereas the cooled specimen resisted at least 260 cycles.

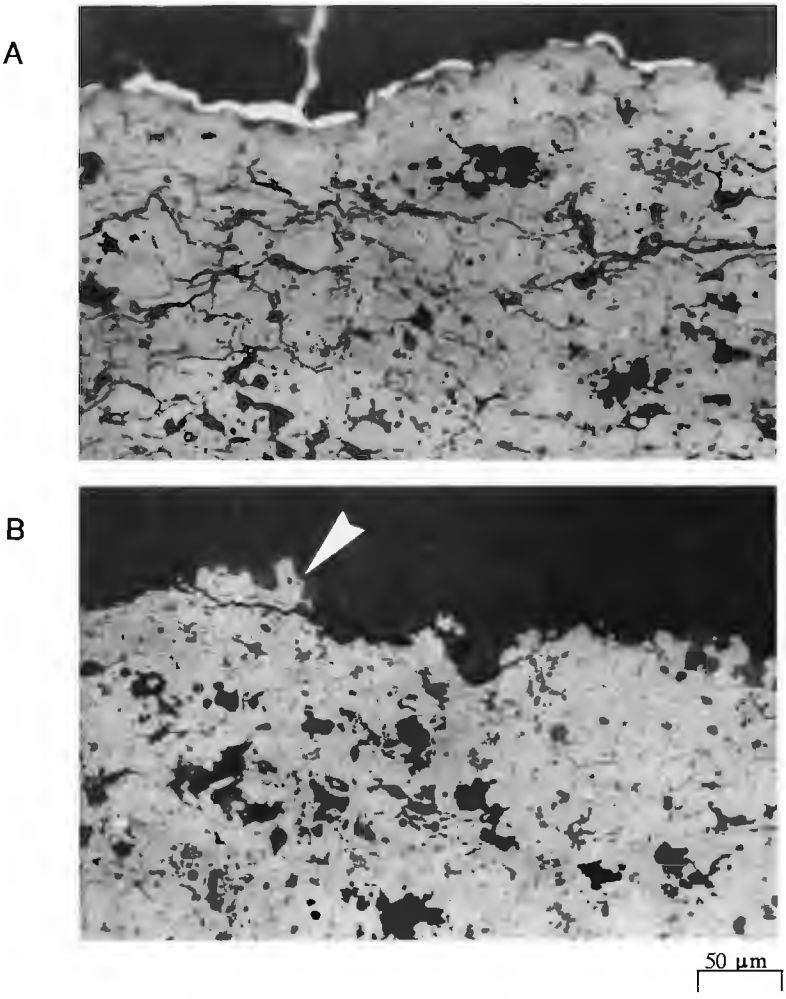


**Figure 5.5** Cross section of a conventional thermal barrier coating after 1000 cycles in the burner rig test. The coating shows some minor horizontal cracks. The arrow indicates a loose particle at the surface of the coating.

The improved thermal shock resistance is caused by the presence of a dense micro crack network, which gave the coating a certain flexibility. Since the cooled coatings possessed residual tensile stresses, the compressive stresses arising, during heating up of the coating, are compensated and buckling is avoided. The non-cooled coatings do not have the dense micro crack network. Furthermore, they hold lower tensile stresses than the cooled coatings. In some cases, they even may possess compressive residual stresses (See chapter III).

The fact that failure of the CSP70/15 coatings occurred after 260 cycles (mean value) whereas the CSP70/8 coatings were still intact after 500 cycles (they showed only some damage on the edges), is not well understood. A possible reason may be that the coating is less flexible than the 70/8 coating. The amount of horizontal micro cracks is higher in the CSP70/8 coating than in the CSP70/15 coating.

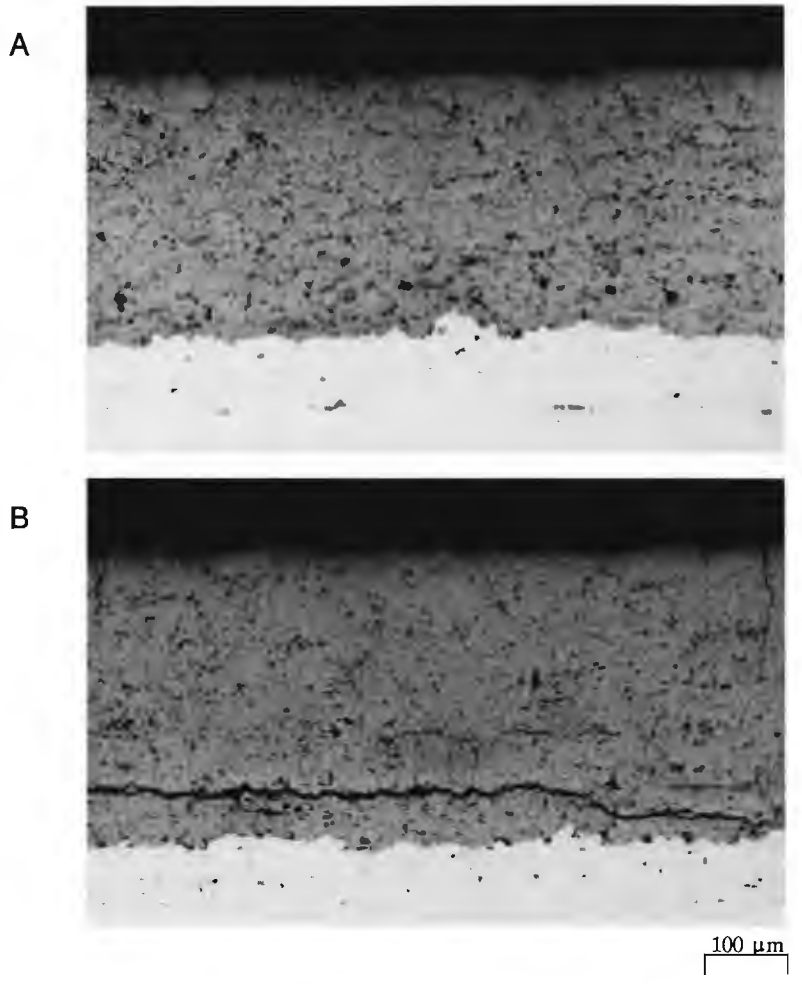


**Figure 5.6** Cross sections of $ZrO_2$ topcoats sprayed with a standard anode channel, using an $Ar/H_2$ flow of 70/8. A) was sprayed on a cooled substrate (CSP 70.8), whereas B) was sprayed on a non-cooled substrate (NCSP 70.8). A) was cycled for 280 times and showed no damage. B) showed severe horizontal cracking after 44 cycles.

Figures 5.6 A and 5.6 B show a CSP 70/8 coating after 280 cycles and a

NCSP 70/8 coating after 44 cycles. The non-cooled coating possessed large macrocracks, whereas the cooled coating was still undamaged.
The use of an extended anode channel had a positive influence on the thermal shock resistance of the ceramic topcoats. The thermal shock resistance of the cooled coatings as well of the non-cooled coatings increased. The use of an extended anode channel resulted in an increased intrinsic strength of the $ZrO_2$ topcoat. Since the particles, sprayed with an extended anode channel, are overheated (See Chapter II, paragraph 4.3.3), they spread out well and adhere well.
That the coatings sprayed with and extended anode have a higher intrinsic strength may be concluded also from the tensile adhesion tests, which will be described further on in this chapter (paragraph 4.3). Due to this higher intrinsic strength, the formation of horizontal cracks was less easy in coatings sprayed with an extended anode channel than in coatings sprayed with a standard anode channel.

The non-cooled $ZrO_2$ coatings, sprayed with an extended anode channel possessed horizontal cracks, just above the interface bondcoat topcoat. These cracks were not observed in the cooled coatings. The cooled coatings (CEP70/8 and CEP70/15) contained small vertical and horizontal cracks after 1000 cycles. Between the two cooled coatings, no distinct differences in crack formation were observed. Figures 5.7 A and 5.7 B show polished cross sections of the NCEP70/15 coating and the CEP70/15 coating.
No horizontal cracks were formed in the cooled coatings which may be caused by two reasons. First, these coatings possess more microcracks than the non-cooled coatings. As a result, the coatings are more flexible. The density of the micro crack network, however, is less than in the cooled, standard plasma coatings (CSP70/8 and CSP 70/15).
Secondly, the cooled coatings possessed a higher residual tensile stress than the non-cooled coatings. For this reason, compressive stresses, occurring during heating of the coatings are compensated.

The conventional thermal barrier coating, showed hardly any damage after 1000 cycles. Only some small cracks could be observed. The conventional coating possessed a high porosity (15 volume %) and hence a high flexibility. This gave the coating a good thermal shock resistance. Although the coatings did not fail due to crack formation or delamination, the coating thickness

decreased during the course of the test. Single $ZrO_2$ particles were swept

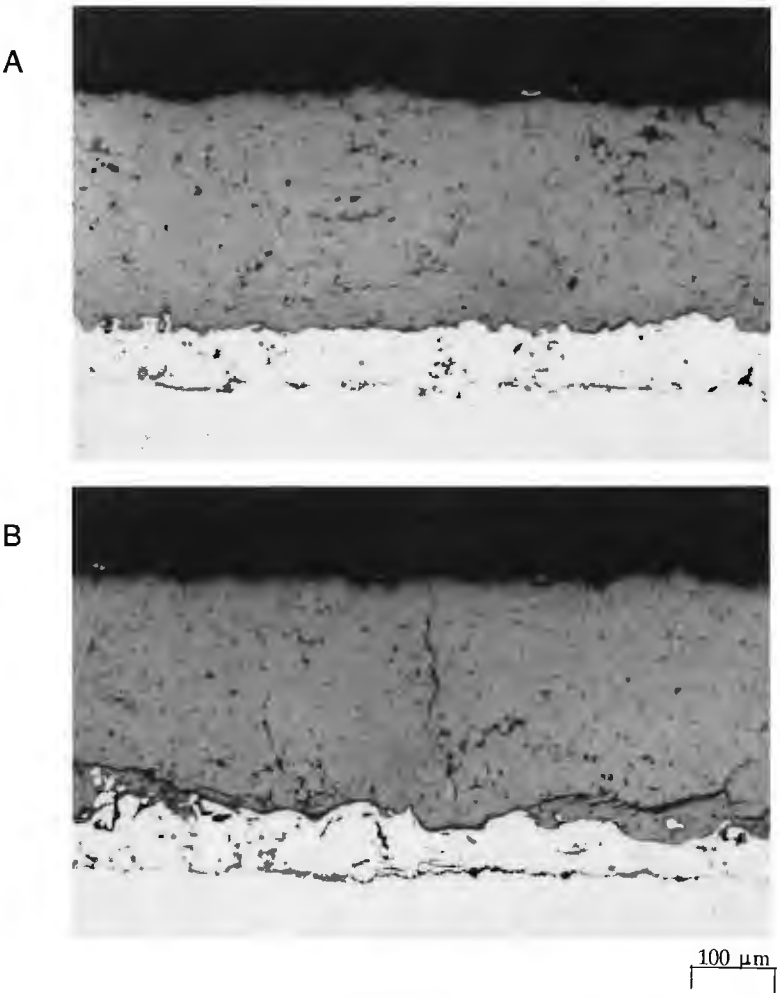


**Figure 5.7** Cross sections of coatings after 1000 cycles in the burner rig test. A) shows a cross section of a coating, sprayed on a cooled substrate, using an extended anode channel and a plasma gas flow of $Ar/H_2$ of 70/15 (CEP 70.15). B shows a coating, sprayed to the same conditions as A), but without substrate cooling (NCEP 70.15). A shows some little cracks, whereas B shows horizontal cracks above the interface bondcoat-topcoat

away from the coating's surface. At long term, this may lead to a decreased performance of the thermal barrier coating.

### 2.4.2 Behaviour of the APS and the LPPS FeCrAlY bondcoat

The thermal barrier coatings with the APS FeCrAlY bondcoat failed due to

bondcoat oxidation, whereas the coatings with a LPPS FeCrAlY bondcoat failed by crack formation in the $ZrO_2$ topcoat.

Electron micro probe analysis (EPMA) proved that the oxide film at the APS bondcoat mainly contained Fe and Cr. Figure 5.8 shows the results of this analysis. It appears that a high concentration of Fe is present just at the interface with the topcoat.

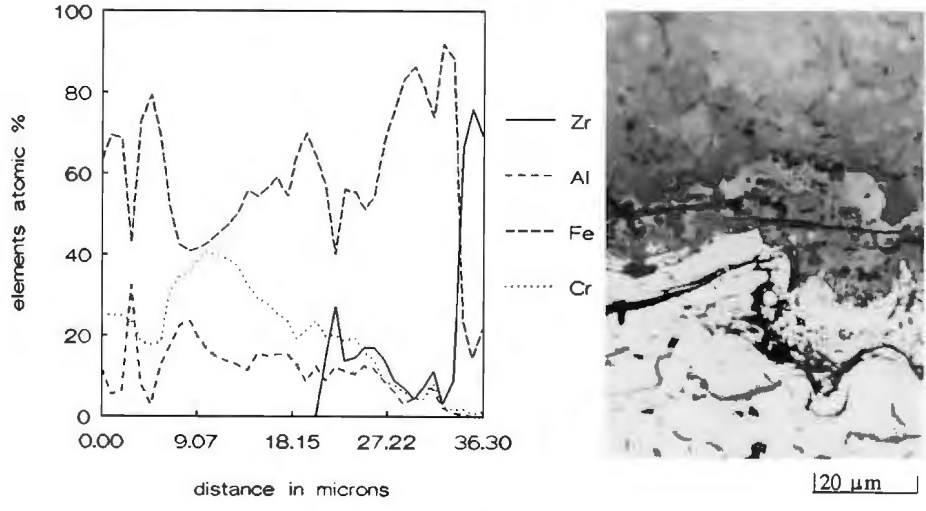


**Figure 5.8** Micro-analysis of cross section of the oxide film at the interface bondcoat topcoat of a thermal barrier coating with an APS FeCrAlY bondcoat. The analysis was made over the thickness of the oxidefilm. The "0" position in the graph indicates the interface bondcoat-oxide film. The graph reveals that the Fe concentration is high at the interface oxidefilm-$ZrO_2$ coating.

Further it can be seen that the amount of Cr in the oxide film is high at the substrate side of the oxide film. This tendency was observed during all measurements carried out on these oxide films.

X-ray diffraction at the plane of fracture in the oxide film proved that the oxide layer consisted mainly of $Fe_2O_3$. A protective $Al_2O_3$ scale, as was expected to be formed during service of the coating, was not found.

The LPPS bondcoat on the contrary showed a 2-3 $\mu$m oxide film at the interface bondcoat-topcoat. This film had a uniform thickness and did not show any cracks.(figure 5.9) Adhesion between the film and the $ZrO_2$ topcoat was good. No signs of delamination could be observed. X-ray micro analysis proved that the oxide film mainly contained Al. (Oxygen could not be determined).

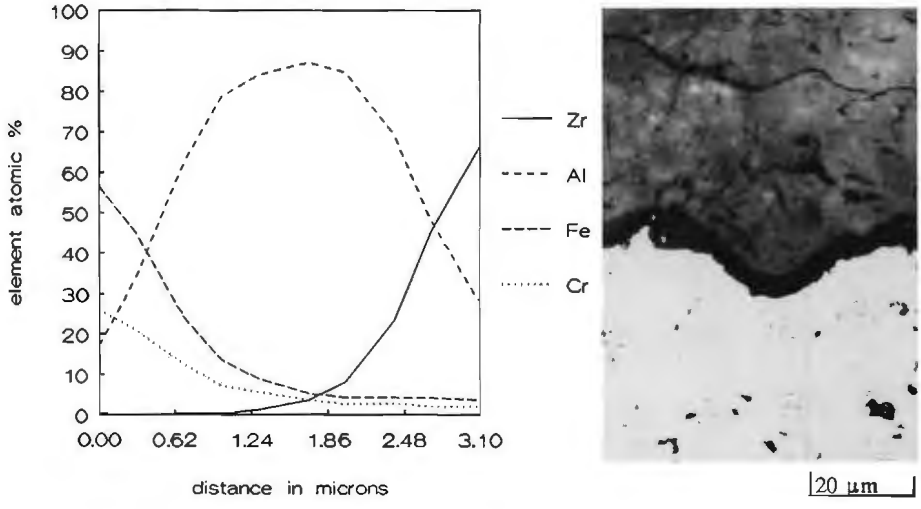


**Figure 5.9** Micro-analysis of the oxide film at the interface bondcoat-topcoat of a thermal barrier coating with a LPPS FeCrAlY bondcoat. A 2 µm oxidefilm, containing mainly $Al_2O_3$ was formed on this interface. The analysis started at the interface bondcoat-oxidefilm.

From the foregoing it may be concluded that the LPPS FeCrAlY bondcoat developed a protective alumina scale, whereas the APS FeCrAlY bondcoat showed severe oxidation of the bondcoat, causing spalling of the ceramic topcoat.

The compositions of both the APS and LPPS FeCrAlY in as sprayed state were studied, using EPMA. The maps of the different elements of the bondcoat: Fe, Cr, Al and O, are shown in figure 5.10.
It can be seen that the LPPS bondcoat has a rather uniform distribution of the elements throughout the coating. The APS coating on the contrary presented a high concentration of Al and O at the border of each individual particle. This means that a part of the Al in the FeCrAlY particles is already oxidized during air plasma spraying. This was confirmed by quantitative determination of the concentration of free Al in the splashed particles.
The concentration of free Al in the APS and LPPS bondcoats
was 4.5-5.5 and 9.5-10.5 wt.% respectively.
Due to the low amount of free Al in the APS bondcoat, a protective $Al_2O_3$ film was not formed.

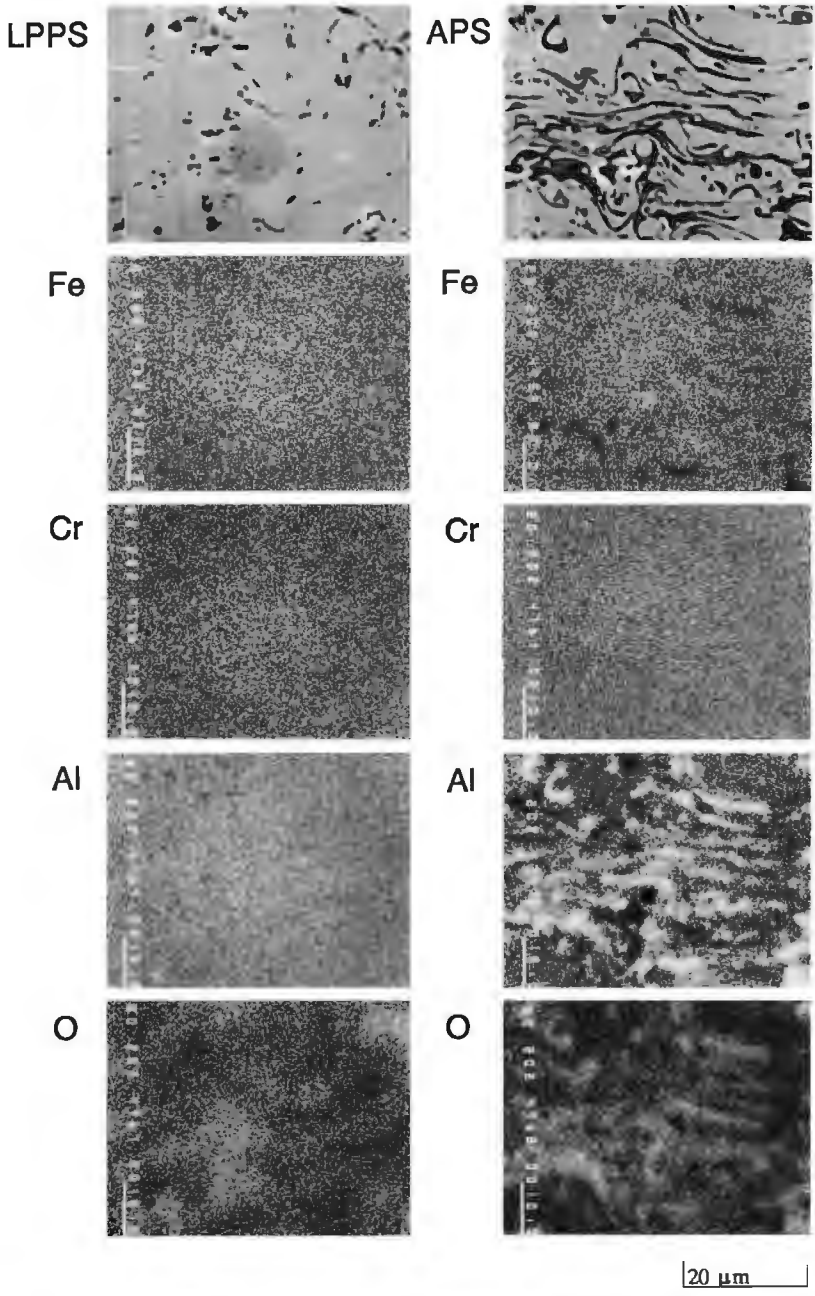


**Figure 5.10** Mappings of the elements in a LPPS and an APS FeCrAlY bondcoat. It is shown that the concentration of Al and O is high at the particle boundaries in the APS bondcoat. In the LPPS bondcoat, the elements are distributed uniformly.

Analysis of the NiCrAlY bondcoat, after 1000 cycles revealed that there existed a 3 $\mu$m $Al_2O_3$ scale at the interface bondcoat-topcoat. Analysis showed further, that the amount of free Al in the as sprayed coating was 1 to 1.5 wt% less than the amount of free Al in the NiCrAlY powder material before spraying. This means that The NiCrAlY powder oxidized less than the FeCrAlY powder during the flight from the plasma torch to the substrate. The coarse grain size of the NiCrAlY particles (45 to 90 $\mu$m) might have played an important positive role in this. The grain size of the FeCrAlY particles, on the contrary, ranged from 22.5 to 45 $\mu$m.

**2.5 Results of furnace testing**

The coatings which did not fail after 1000 burner rig cycles, were subsequently loaded in the furnace test. After 50 cycles, the specimen were prepared for microscopical observation.

The conventional TBC had large parallel cracks of several mm length. Large parts of the coating disappeared. Delamination at the interface bondcoat-topcoat, however, was not observed. Figure 5.11 gives a cross section of the ceramic topcoat after 50 furnace cycles.

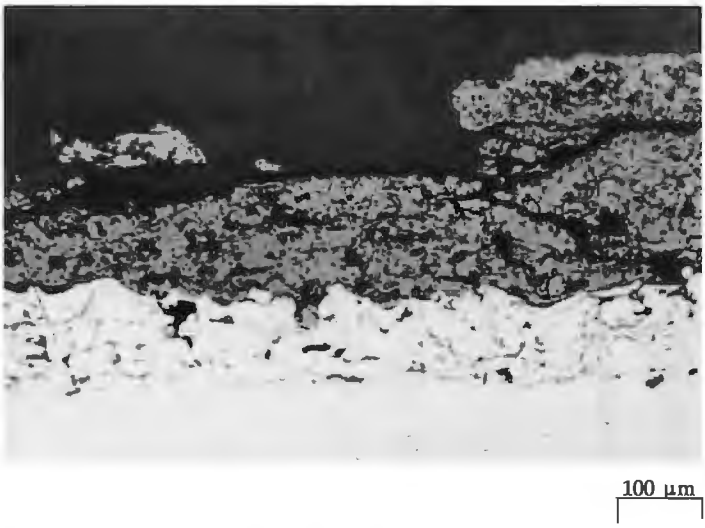


**Figure 5.11** Cross section of a conventional thermal barrier coating after 50 cycles in the furnace test. It can be seen that large parts of the coating disappeared.

The NCEP70/15 coating exhibited coarse parallel cracks just above the interface bondcoat-topcoat. The parallel cracks which were present after burner rig testing grew to coarse cracks. Due to this, the edges of the coating were damaged. Next to the parallel cracks, also vertical cracks came into being. Figure 5.12 gives the cross section of this coating.

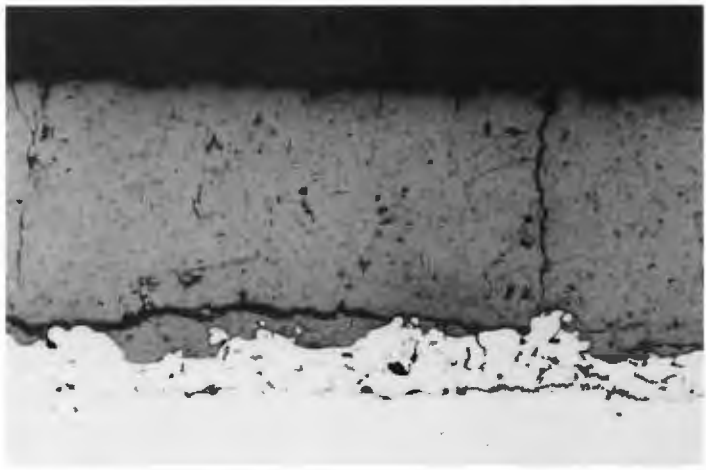


**Figure 5.12** Cross section of a thermal barrier coating, sprayed with an extended anode channel on a non cooled substrate (NCEP70/15) after 50 cycles in the furnace test. The ceramic topcoat showed coarse horizontal cracks just above the interface bondcoat-topcoat. Besisdes the horizontal cracks, vertical ones can be observed.

The CEP70/15 and the CEP70/8 coatings showed coarse vertical cracks after the furnace test. These cracks had small horizontal branches which can be seen in figure 5.13. The coarse parallel cracks, above the interface bondcoat-topcoat as were observed in the non-cooled coating, were not present. Because of this, delamination of the cooled specimen is not to be expected.

**2.6 Conclusions.**

Substrate cooling has a positive influence on the thermal shock resistance of thermal barrier coatings. The application of an extended anode channel results also in a $ZrO_2$ topcoat, with an increased erosion resistance.

Coarse horizontal cracks, resulting in delamination of the ceramic topcoat were not observed in the topcoats, sprayed on cooled substrates, using an extended anode channel.

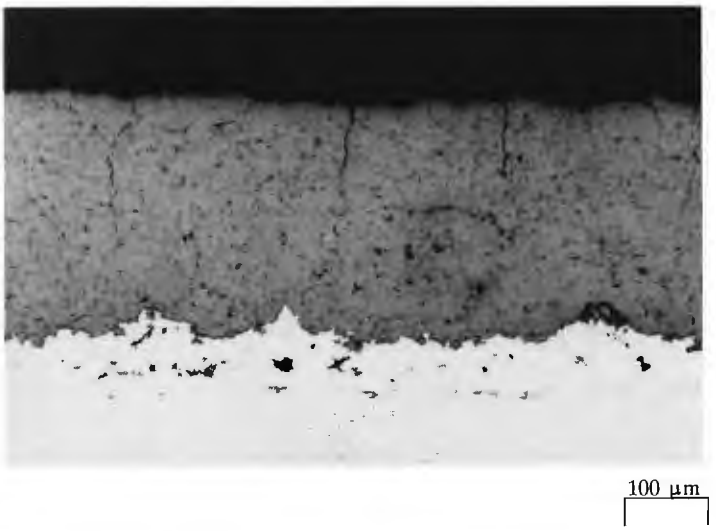


**Figure 5.13** Cross section of a thermal barrier coating after 50 cycles in the furnace test. The coating was sprayed on a cooled substrate, using an extended anode channel (CEP70/15). The coating shows vertical cracks with short horizontal branches.

The APS FeCrAlY coating showed severe oxidation. A protective $Al_2O_3$ film was not formed. On the contrary the LPPS FeCrAlY coating did form this protective $Al_2O_3$ film.

Thermal barrier coatings with an APS NiCrAlY bondcoat, did not show any failure due to bondcoat oxidation. At the interface bondcoat-topcoat a 2-3 $\mu$m $Al_2O_3$ film was formed.

The conventional thermal barrier coating showed a good thermal shock resistance in the burner rig test although the $ZrO_2$ topcoat lost thickness during the test. In the furnace test, the coating was severely damaged.

**3 Erosion**

Generally, the erosion resistance of a thermal barrier coating is low. Especially when the coating is applied in a combustion chamber, erosion is not a main problem. If thermal barrier coatings are used on the first stage vanes, erosion may play an important role. Because of this, erosion tests were carried out on a conventional thermal barrier coating and on the coatings which showed the best thermal shock resistance.

### 3.1 Mechanisms of erosion

Eaton and Novak [3] distinguish three different types of erosion of plasma sprayed coatings which are described below.

1) Low erosion velocity
The surface of the coating is slightly damaged by erosive particles which plow little grooves in the surface. The material loss due to this mode of erosion is low.

2) Moderate erosion velocity
The impacting erosive particles cause crack formation in the coating in their areas of impact. These cracks run along and through single particles. The surface of a coating subjected to this form of erosion has a craggy appearance.

3) High erosion velocity
At this form of erosion, pieces of coating material are removed out of the coating's surface. The impacting particles cause cracks that are directed along the trajectory of the impacting particles. These cracks inter-connect the pores in and just under the surface of the coating. Because of this, pieces of the coating loose their bonding with the surrounding and will be removed by impacting particles. This form of erosion is also called tunneling.

Several authors report results of erosion tests carried out on thermal barrier coatings. Because all these tests were different, the results can not be compared. Although, some tendencies may be observed:
Dense coatings possess the highest erosion resistance.
Erosion under an angle of 90 ° causes the highest material loss. When the angle of impact is increased from 15 to 90 °, the erosion velocity is increased by a factor 2.5.
There is a direct relationship between the 4-point bending strength and the erosion resistance. A high bending strength is accompanied by a high erosion resistance. When the 4 point bending stress of the tested coating was lower than 15 MPa, fatal erosion occurred. At higher strengths, material loss due to erosion decreased and only some plowing was observed. (Low erosion velocity).

### 3.2 Erosion testing

The erosion tests were carried out at IPL-TNO on three types of coatings: NCEP70/15, CEP70/15 and a conventional thermal barrier coating, sprayed according to the specifications, prescribed by a turbine manufacturer.
The next parameters were used for the erosion tests.

| | |
|---|---|
| Abrasive particles: | $Al_2O_3$ |
| Grain size: | 0.2 to 0.5 mm |
| Feed rate: | 200 grams/minute |
| Velocity: | 20 m/s |
| Angle: | 90 ° |
| Temperature: | 20 °C |

#### 3.2.1 Results of the erosion tests.

The coatings were tested during 15 minutes. Each 5 minutes, the weight loss and mean decrease of thickness of the $ZrO_2$ coatings were determined. Figure 5.14 shows the results of the tests.

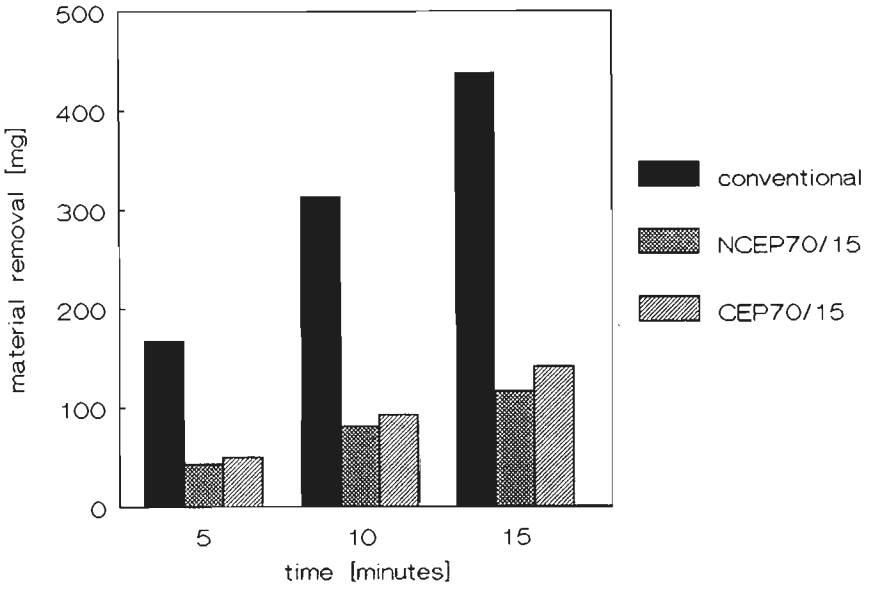


**Figure 5.14** Results of the erosion tests. The figure shows the weight loss due to erosion for a conventional coating and a CEP70/15 and NCEP70/15 coating, sprayed at Eindhoven University.

It can be seen that the conventional coating possessed the lowest erosion resistance. There was a minor difference between the cooled and non-cooled coatings, sprayed at Eindhoven University. The cooled coating showed a 10 % higher weight loss than the non-cooled one. This may be explained by the fact that the cooled coating possessed a dense crack network which lowered the cohesion between the individual particles of the coating.

### 3.2.2 Failure mechanisms

Cross sections of the eroded specimen were examined by light microscopy. It appeared that the conventional thermal barrier coating failed due to the mechanisms 2 and 3, described in paragraph 3.1 (Moderate and high erosion velocity). Figure 5.15 shows the damage due to erosion in a conventional thermal barrier coating.

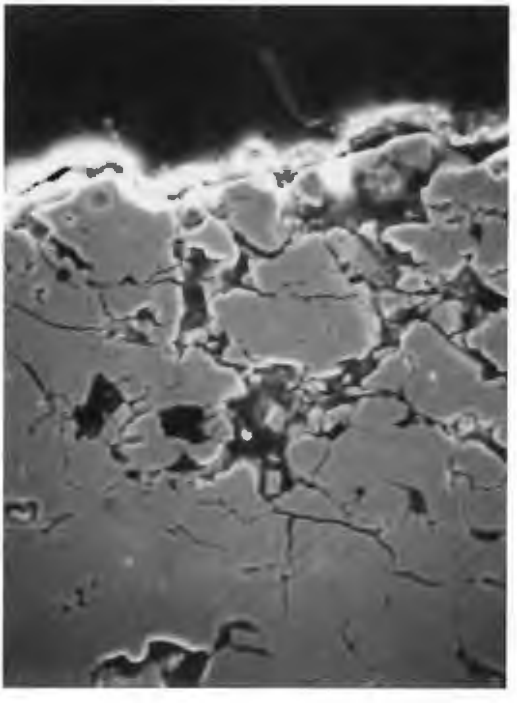


**Figure 5.15** Cross section of a conventional thermal barrier coating after erosion testing. The micrograph shows that the particles at the coatings surface are totally fractured. Furthermore, large cracks developed in the coating.

The individual particles of the coating were fractured by the impacting erosive particles. Next to this, large cracks, running along the particle

boundaries and interconnected by pores, could be observed. Due to these cracks, complete particles were swept away from the coating's surface. The surface zone, attacked by the erosive particles could be well distinguished. This zone showed small cracks in the individual particles right at the surface and had coarse cracks along the particle boundaries. The mean depth of the attacked zone was 50 to 55 $\mu$m.

Failure due to erosion in the NCEP70/15 and CEP70/15 coatings was mainly caused by erosion mechanism 2. (Moderate erosion velocity)

The particles at the surface of the coating were fractured by the impacting erosive particles. Subsequently, parts of the fractured particles are swept away by other impacting particles. The cooled coating (CEP70/15) did also show some coarser cracks along the particle boundaries. The maximum depth of the damaged zone was 15 $\mu$m. Because of the low porosity of the coating, the cracks were not interconnected by the pores. Due to this, damage caused by mechanism 3 was limited. Figure 5.16 shows the cross section of an eroded CEP70/15 $ZrO_2$ coating.

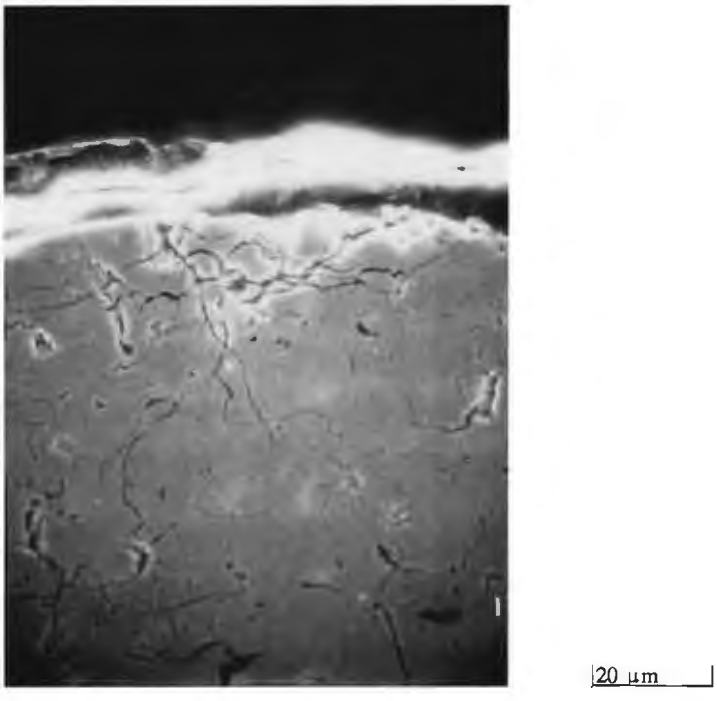


**Figure 5.16** Cross section of a CEP 70/15 thermal barrier coating after erosion testing. It can be seen that the particles at the surface are fractured. Large cracks in the coating can hardly be observed.

The erosion resistance of the CEP70/15 and NCEP70/15 coatings was 3 to 4 times as high as that of the conventional coating. This difference is mainly caused by the low cohesive strength and porous structure of the conventional coating. Erosion due to tunneling (Mechanism 3) is favoured by this microstructure. The coatings sprayed on Eindhoven University on the contrary possessed a low porosity and good adhesion between the particles. Because of this, erosion due to tunneling was limited.

## 4 Tensile adhesion testing

### 4.1 Introduction

The bond strength of a plasma sprayed coating is often used as a criterium to evaluate the quality of these coatings. Generally, the bond strength is determined by tensile adhesion tests. These tests are standardized in both a DIN standard (DIN 50160) and an ASTM standard (ASTM C 633 or ASTM F1147). The principles and realisations of these tests are similar, only the size of the specimen differs slightly. The tests are based on the next principle. A cylindrical specimen with a prescribed size is coated on its crosscut side. Subsequently, an identical metallic body is glued to the coating, using a high strength adhesive. This construction is mounted in a tensile testing machine which is equipped with universal joints in order to avoid the introduction of bending forces or couples on the coating. The coating is loaded until failure occurs. The tensile adhesion strength is now defined as the maximum force to failure, divided by the surface area of the coating.

$$\sigma = \frac{F}{A}$$

$\sigma$: tensile adhesion strength [MPa]
F: maximum force [N]
A: surface area of the coating [$mm^2$]

Since the ASTM and DIN specimen are being rotated during spraying, the tangential velocity of the centre of the specimen is zero. At the boundary the velocity is maximal. Because of this, the deposition circumstances at the centre differ from those at the specimen's boundary. This results in a coating with varying characteristics. This may be one of the reasons why the reproducibilities of the ASTM and DIN tests are moderate [4].

To meet with the varying tangential speed, new tensile adhesion tests were developed; the TNO test (Developed and generally used in the Netherlands) and the TUE test, developed at Eindhoven University of Technology [5]. These tests are described in reference [6]. Next to this, a new adhesion test was developed by Verbeek and Houben [6,7]. This test does not use any adhesive, but introduces tensile stresses by elastic deformation of a thin walled metallic cylinder covered with a plasma sprayed coating. This test is now further developed by the Netherlands Institute for Welding Technology (NIL).
Because of the fact that all newly developed tests are not standardized, they can not be used for commercial purposes.

Next to the tensile adhesion strength the shear strength of a plasma sprayed coating can be measured. This type of test which is standardized in DIN (DIN 50161) and ASTM standard (F1044) is less common than the tensile adhesion test.

During this research programme a tensile adhesion test, which was based on an adhesive test, was used.

**4.2 Specimen and test set up**

The specimen for the tensile adhesion tests consisted of a 1.6 mm Hastelloy X substrate with a 0.1 mm FeCrAlY bondcoat and a 0.3 mm $ZrO_2$ topcoat. The bondcoats and topcoats were sprayed as described in chapter III (Specimen for the three point bending test). The specimen had a size of 18*18 $mm^2$ and were cut out of the bending specimen by a diamond wire saw. In order to make it possible to apply a force to these thin specimen, they were glued to square metallic bars, using a high strength adhesive (3M 2214 HT). All together, eight different topcoats were tested.

To avoid the penetration of the adhesive into the porous ceramic coating, the pores and cracks of the coating were sealed with a sealer. (Metco AP). When no sealer was used, the glue penetrated into the coating and reinforced it. This resulted to the measurement of an increased bond strength. Previous investigations [8] showed that the measured bond strength of a plasma sprayed $ZrO_2$ coatings on steel substrates was as twice as high when no sealer was used. (80 MPa instead of 40 MPa). This strength was

equal to the bond strength of the adhesive (80 MPa).

Glueing of the specimen was carried out in special moulds in order to assure a perfect alignment of the metallic bars.
Figure 5.17 shows a tensile adhesion test specimen and the way it is mounted in the tensile testing machine.

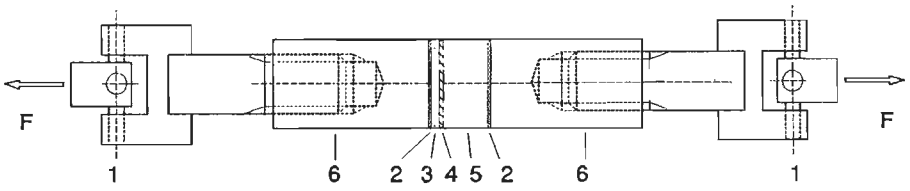


**Figure 5.17** Tensile adhesion test-rig. The specimen is screwed to two special mountings wich are attached to the crossheads of the tensile testing machine by universal joints. The numbers in the sketch indicate the next parts: 1) universal joints, 2) Adhesive, 3) $ZrO_2$ topcoat, 4) bondcoat, 5) Hastelloy X substrate, 6) square steel bars (18*18 mm)

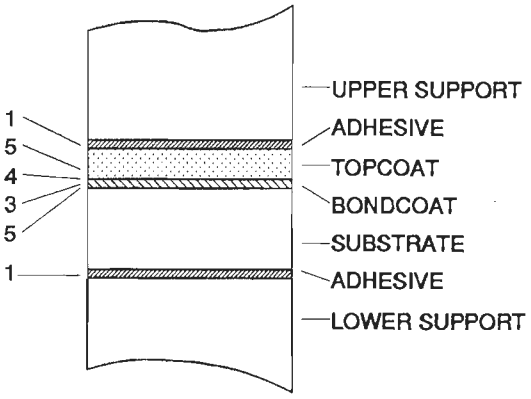


**Figure 5.18** Failure modes of a thermal barrier coating during the tensile adhesion test. The numbers indicate the possible failure sites.

The 100 kN tensile testing machine used for the tensile adhesion tests was equipped with special attachments, avoiding the introduction of bending forces and bending couples.

### 4.3 Results and discussion

Failure of the thermal barrier coatings during tensile adhesion testing may occur in 5 different modes. These modes are indicated in figure 5.18.

The next table shows the results of the tensile adhesion tests. Next to the mean stress of failure, the maximum and minimum bond strength of each type of coating are given.

Table 1
Bond strength of different types of thermal barrier coatings

| topcoat | mean stress [MPa] | maximum stress [MPa] | minimum stress [MPa] | failure mode |
|---|---|---|---|---|
| NCEP70/15 | 58.8 | 64.8 | 53.1 | 2 |
| NCEP70/8 | 65.1 | 69.1 | 61.2 | 2 |
| CEP70/15 | 53 | 58.2 | 43.7 | 2 |
| CEP70/8 | 45.9 | 52.2 | 32.8 | 2; 2,3 |
| NCSP70/15 | 37.9 | 41.4 | 36.4 | 4 |
| NCSP70/8 | 48.2 | 60.4 | 41.7 | 4 |
| CSP70/15 | 30.3 | 36.9 | 20.2 | 5 |
| CSP70/8 | 31.9 | 42.2 | 25.1 | 5 |

Table 1 shows that failure of the coatings, sprayed with an extended anode channel, generally occurred at the interface substrate-bondcoat (Failure mode 2). This indicates that the bond-strength of $ZrO_2$ to FeCrAlY exceeds the bond-strength of FeCrAlY to Hastelloy X. The good adherence of $ZrO_2$ , sprayed with an extended nozzle, agrees with the observations, described in chapter II, paragraph 5.3.3. It was found that single $ZrO_2$ particles, sprayed with an extended anode channel showed a better adherence than the ones sprayed with a standard anode.
From the above, it may be concluded that the bond-strength of the bondcoats, sprayed on a cooled substrate, is lower than the bond-strength of the same bondcoats, sprayed on a non-cooled substrate. The fact that

substrate cooling during spraying results in a lower bond strength was reported by Steffens c.s. [9]

The cooled specimen, sprayed with a standard anode, failed due to fracture in the ceramic topcoat. Since these coatings possess a very dense network of both vertical and horizontal cracks, the formation of horizontal macro cracks resulting in delamination of the ceramic topcoat, is facilitated.
The non-cooled specimen, sprayed with a standard anode channel, failed due to fracture at the interface bondcoat topcoat. Due to the absence of the horizontal micro cracks, no horizontal cracks in the ceramic were formed.

Figure 5.19 shows the results of the tensile adhesion tests. The difference between the bond-strengths of the various coatings is evident. (The figure shows the mean bond-strength)

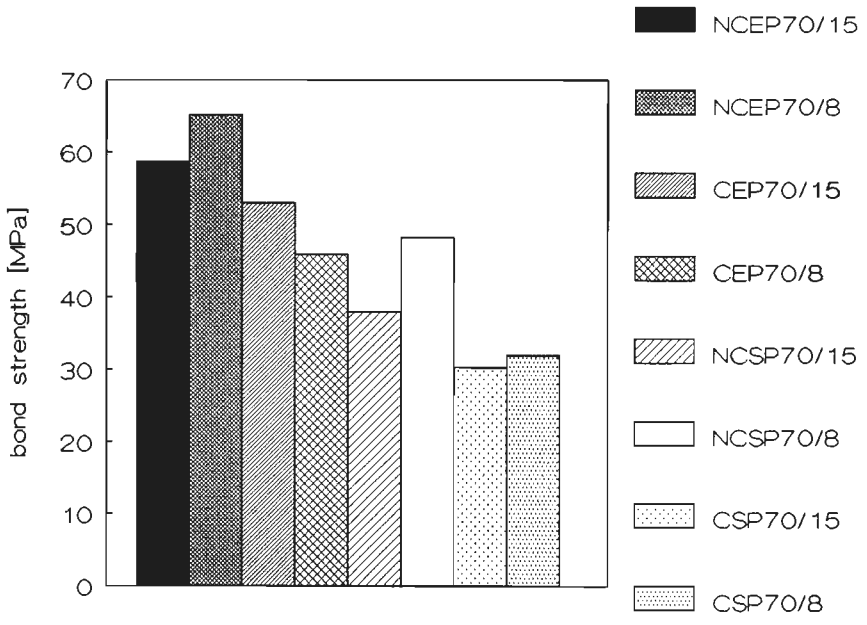


**Figure 5.19** Results of the tensile adhesion tests on the different types of thermal barrier coatings.

## 5 Phase stability of $ZrO_2$ 7.6 wt % $Y_2O_3$ at elevated temperatures

### 5.1 Introduction

As stated in paragraph 2.3.1., chapter I, pure $ZrO_2$ has three crystal structures: monoclinic at room temperature, tetragonal above 1220 K and cubic (fluorite type structure) above 2640 K.
To avoid the phase transformation tetragonal to monoclinic, $ZrO_2$ has to be stabilized. (See chapter I)
The next paragraphs describe the results of annealing tests of $ZrO_2$ 7.6 wt.% $Y_2O_3$: the material used for the ceramic topcoats, described in this thesis. From now on this material will be abbreviated to $ZrO_2$.

### 5.2 Theory

Figure 5.20 shows the phase diagram of $ZrO_2$-$Y_2O_3$ according to Scott. From this diagram it appears that $ZrO_2$ with 7.6 wt.% $Y_2O_3$ would be unstable at room temperature and decompose in a mixture of a monoclinic and cubic crystal structure (M and F). This is true if the alloy is in equilibrium. During plasma spraying, however, the $ZrO_2$ particles solidify and cool down very rapidly (See chapter II, paragraphs 5.2.1 and further). Due to these quench effects a meta-stable tetragonal phase comes into being. In literature this phase is called the T'-phase. According to Miller [16], this is a non-transformable tetragonal phase which will not transform to the monoclinic phase under mechanical loading. As a result, transformation toughening in plasma sprayed $ZrO_2$ coatings is not likely.

When the T'-phase is annealed above 1200 °C, diffusion processes start. The T'-phase disappears and a tetragonal phase with a low yttria content, and a cubic phase with a high yttria content are formed. On cooling down to room temperature, the tetragonal phase transforms to monoclinic, whereas the cubic phase is retained at room temperature. The formation of the monoclinic phase may cause failure of the $ZrO_2$ coating. Due to the volume increase of 5%, high compressive stresses arise. These may cause cracking of the coating.

The rate of formation of the tetragonal and cubic phase out of the T' phase at temperatures below 1200 °C is very low. Failure of thermal barrier coatings exposed to temperatures of 1200 °C, due to the mechanism

described above is therefore not likely to happen and is also not reported in literature.[16]

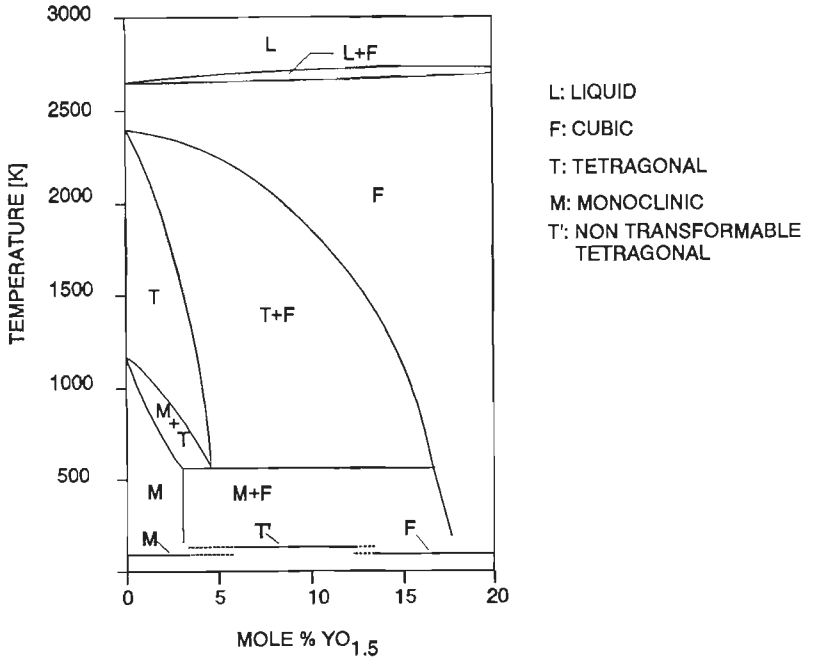


**Figure 5.20** Low yttria region of the phase diagram of $ZrO_2$-$Y_2O_3$. The non transformable T'phase comes into being when $ZrO_2$ with a $Y_2O_3$ content between 5 and 12 mole% is quenched from liquid to solid. The equilibrium phases of cubic and monoclinic will only be formed after annealing at high temperatures.(Redrawn from [17])

### 5.3 Quantitative determination of the phases

Several authors present methods for the determination of the quantitative phase composition of partially stabilized $ZrO_2$.

Two principal methods can be distinguished: The calibration curve method [12,13,14,15] and the polymorph method [10,11,14,16]

For the calibration curve method, the intensities of the characteristic diffraction peaks of the different phases (monoclinic, tetragonal and cubic) of $ZrO_2$ with a well known phase composition have to be registered. This procedure is repeated for several phase compositions. Together these values form the calibration curve.

When the diffraction peaks of $ZrO_2$ with an unknown phase composition are measured, it is possible to determine the phase composition by comparing the peak intensities with the calibration curves.

Generally these calibration curves are not available and an other method has to be used, the polymorph method. This method is based on the assumption that the next equation is valid:

$$I_m(111)+I_m(11\bar{1})=I_c(111) \tag{2}$$

$I_m$: Intensity of the diffraction peak of monoclinic $ZrO_2$
$I_c$: Intensity of the diffraction peak of cubic $ZrO_2$.

The amount of the monoclinic phase may now be calculated by equation 3:

$$X_m=\frac{I_m(111)+I_m(11\bar{1})}{I_m(111)+I_m(11\bar{1})+I_c(111)} \tag{3}$$

$X_m$: relative amount of monoclinic phase.

Equation 3 has been corrected for the structure and multiplicity factor. Furthermore it is rewritten to mole fractions and adapted to a three phase system. The mole fractions of the monoclinic, tetragonal and cubic phase can now be calculated by using the next equations [10].
Equation (3) now turns into:

$$\frac{M_m}{M_{c,t}}=0.82*\frac{I_m(111)+I_m(11\bar{1})}{I_{c,t}(111)} \tag{4}$$

$$\frac{M_c}{M_t}=0.88*\frac{I_c(400)}{I_t(400)+I_t(004)} \tag{5}$$

$$M_c+M_t+M_m=1 \tag{6}$$

$I_{c,t,m}$: Intensity of diffraction peaks of cubic, tetragonal and monoclinic respectively.
$M_{c,t,m}$: Mole fractions of cubic, tetragonal and monoclinic.

**5.4 Specimen and test set up**

Since the ceramic coatings were annealed at temperatures including and

exceeding 1300 °C, the metallic substrates and bondcoats had to be removed. This was done by etching of the specimen in concentrated HCl. The bondcoat partly dissoluted and the $ZrO_2$ coating could be removed from the Hastelloy X substrate.

Annealing of the coatings was done under atmospheric conditions in a rapid heating furnace. The annealing temperatures were 1300, 1400 and 1500 °C. The coatings were annealed for 25, 50 and 100 hours at each temperature.

The phase structure of the coatings after annealing was determined by X-ray diffraction (XRD). The XRD measurements were carried out at the faculty of chemistry of Eindhoven University of Technology, using a Rigaku XRD apparatus. The radiation used was $Cu_{k\alpha}$. The results of the measurements are compared to the phases which were present in the coating powder and in the coating in the as sprayed state.

### 5.5 Results of the measurements

Figure 5.21 shows the diffraction pattern of the $ZrO_2$ powder. This powder existed mainly of the T'- and cubic (F)-phase. Besides these phases, a little amount of monoclinic phase can be observed. The characteristic monoclinic peaks at both sides of the (111) tetragonal and cubic peak are indicated by the arrows.

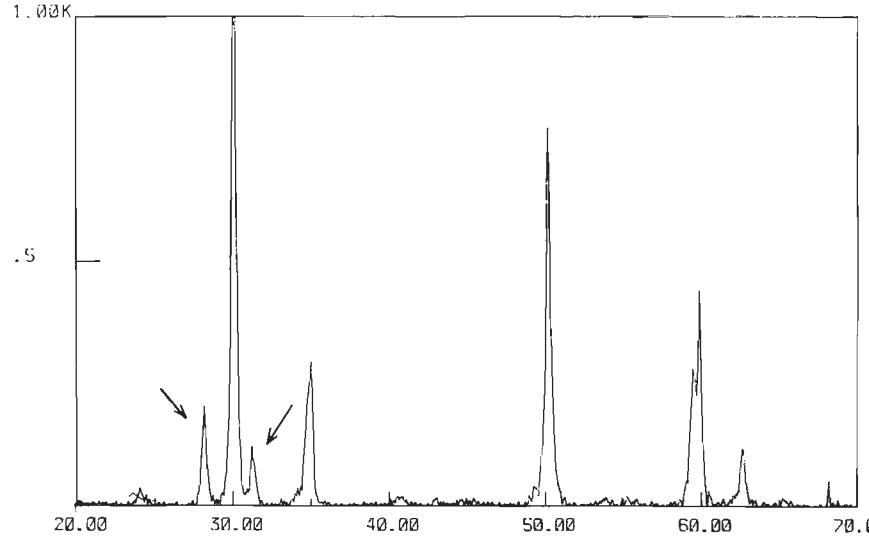


**Figure 5.21** Diffraction pattern of $ZrO_2$ 7.6 wt% $Y_2O_3$ powder, used during this research project. This powder contains about 10 % monoclinic phase, which dissappears during spraying. The arrows indicate the monoclinic peaks

The coating in the as-sprayed state shows the T'-phase. The monoclinic phase present in the powder disappeared during the spraying process.
When the coatings were annealed for 25, 50 and 100 hours at 1300 °C, a shift from the tetragonal phase (T') to the cubic phase (F) occurred. The monoclinic phase did not develop. This implies that the amount of $Y_2O_3$ in the T'-phase is still sufficient to maintain this phase at room temperature.

After annealing at 1400 °C, the monoclinic phase was found. After annealing during 100 hours, the total amount of monoclinic phase was about 22 mole %. A strong shift from T' to cubic could be observed. See table 2

During annealing at 1500 °C, the amount of the monoclinic phase rapidly increased. After annealing for 25 hours, already 21 mole % monoclinic could be observed, increasing to 26 mole % at 100 hours. The amount of the T'-phase decreased to 25 %. See table 2 and also appendix D

In figure 5.22, the results of the annealing experiments at different temperatures, for 100 hours, are compared. It can be seen that during annealing at 1300 °C no monoclinic phase developed. At 1400 °C, the amounts of cubic and T' were 43 and 35 mole % and about 22 mole % monoclinic phase was formed. See also table 2 and appendix D

During annealing at 1500 °C, the amount of the T'-phase strongly decreased to about 25 %. The amount of monoclinic was high at 26 %.
During annealing at 1400 and 1500 °C, a tetragonal phase with a low $Y_2O_3$ content is formed. On cooling down to room temperature, this phase transforms to the monoclinic phase. On the other hand, a cubic phase with a higher $Y_2O_3$ content is formed. This phase maintains its cubic crystal structure at room temperature.

**5.6 Conclusions**

From the foregoing results, it may be concluded that plasma sprayed $ZrO_2$ 7.6 wt% $Y_2O_3$ mainly contains the non-transformable tetragonal phase (T' phase). When the coatings are annealed for long periods of time at temperatures above 1300 °C, the T'-phase decomposes in a cubic phase with a high $Y_2O_3$ content and a tetragonal phase with a low $Y_2O_3$ content. On cooling down to room temperature, this tetragonal phase will transform to

the monoclinic phase. The formation of this phase may result in failure of the $ZrO_2$ topcoat, caused by the introduction of compressive stresses, resulting in cracking of the coating.The cubic phase retains its cubic crystal structure at room temperature.

table 2
Amounts of phases after annealing (mole %)

| Tem | 1300 °C | | | 1400 °C | | | 1500 °C | | |
|---|---|---|---|---|---|---|---|---|---|
| time | M | T' | F | M | T' | F | M | T' | F |
| 25 | 0 | 100 | 0 | 1 | 69 | 30 | 21 | 51 | 28 |
| 50 | 0 | 66 | 34 | 3.5 | 59 | 37.5 | 22 | 45 | 35 |
| 100 | 0 | 62 | 38 | 22 | 35 | 43 | 26 | 25 | 49 |

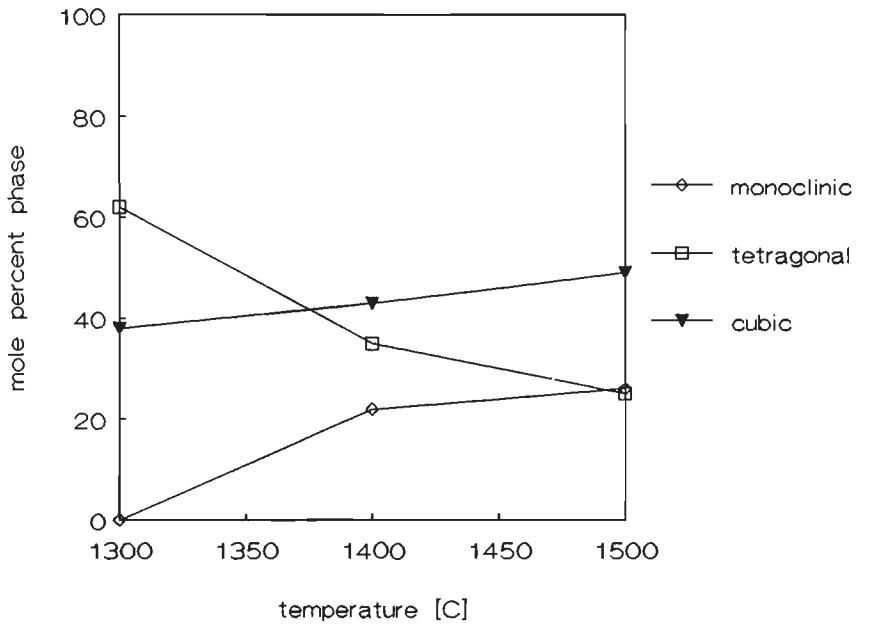


**Figure 5.22** Phase composition after annealing at different temperatures. It can be seen that no monoclinic phase is formed during annealing at 1300 °C. At 1500 °C, the amount of the tetragonal T'-phase becomes very low.

From the experiments, it appeared that no monoclinic phase was formed at temperatures unto 1300 °C when the coating was annealed for 100 hours. Because of this, it may be concluded that the $ZrO_2$ 7.6 wt% $Y_2O_3$ coatings can be used at temperatures up to 1300 °C for at least 100 hours. The composition of the coating for significantly longer periods of time; e.g. 1000 hours at this temperature, has to be studied.

**6 General conclusions chapter V**

Thermal barrier coatings, sprayed with overheated $ZrO_2$ particles on cooled substrates showed the highest thermal shock resistance. The high thermal shock resistance is caused by the presence of a micro crack network, which gives the coating a certain flexibility and by the fact that the coatings, sprayed on cooled substrates, possessed residual tensile stresses. These stresses compensate the compressive stresses arising in the $ZrO_2$ topcoat during the first stage of heating up of the coating.

The erosion resistance of the $ZrO_2$ topcoats, sprayed with overheated $ZrO_2$ particles, both on a cooled and on a non cooled substrate, appeared to be three to four times higher than the erosion resistance of conventional thermal barrier coatings. This was caused by the fact that in the conventional coating, due to its low intrinsic strength, another, more severe, erosion mechanism operated than in the coatings sprayed at Eindhoven University.

The bond-strength and the way the thermal barrier coatings failed during tensile adhesion tests, were strongly determined by the way the coatings were sprayed. Substrate cooling and the use of an extended anode channel had a distinct influence on the bond strength and the failure mode. The bond-strength between the FeCrAlY bondcoat and the $ZrO_2$ topcoat, increased when an extended anode channel was used.

The plasma sprayed $ZrO_2$ 7.6 wt.% $Y_2O_3$ coating consisted mainly of the non-transformable tetragonal phase. (T' phase). After annealing for long periods of time at temperatures above 1300 °C, the T'-phase decomposed into a cubic phase and a tetragonal phase. On cooling down to room temperature, the tetragonal phase transformed to the monoclinic phase, whereas the cubic phase was retained at room temperature.

## 7 References Chapter V


[1] Berndt C.C. Material Property Measurement on Thermal Barrier Coatings ASME-paper 88-GT-277, 1988

[2] Hoek M.J.W, Thermal Shock Resistance van $ZrO_2$ Thermal Barrier Coatings met een FeCrAlY Hechtlaag. (In Dutch) Internal Report, Eindhoven University of Technology, Faculty of Mechanical Engineering, Thermal Spraying Group, 1992

[3] Eaton H.E, Novak R.C., Particulate Erosion of Plasma Sprayed Porous Ceramics, Surf. Coat. Techn. 30(1987) 41-50

[4] Strompen N., Plasmagespritzte Metalloxid und Oxid Schichten. Doctor's Thesis, Aachen University, 1986

[5] Houben J.M., Synopsis, Eindhoven University of Technology, Thermal Spraying Group, Faculty of Mechanical Engineering, 1986

[6] Verbeek A.T.J., Ontwikkeling van een Nieuwe Methode voor het Beproeven van de Hechtsterkte van Plasmagespoten Coatings. Master's Thesis, Eindhoven University of Technology, 1988

[7] Verbeek A.T.J., Houben J.M., Klostermann J.A., Adhesion and Ductility of Plasma Sprayed Thermal Barrier Coatings. In: Euro Ceramics, Vol. 3 Engineering Ceramics. Editors: G. de Wit, Elsevier Applied Science, London, 1989

[8] Verbeek A.T.J., Problemen bij het Bepalen van de Hechtsterkte van Plasmagespoten Thermal Barrier Coatings. Internal Report, Eindhoven University of Technology, Faculty of Mechanical Engineering, Thermal Spraying Group, 1990

[9] Steffens H.D., Höhle H.M., Ertürk E., Untersuchung zum Kühlen mit Kohlendioxid beim Plasmaspritzen, Schweissen und Schneiden, 33(1981), No 4, 159-164.

[10] Miller R.A., Smialek J.L., Garlick R.G., Phase Stability on Plasma Sprayed partially Stabilized Zirconia-Yttria. In: Advances in Ceramics, Vol 3 Science and Technology of Zirconia. Editors: A.H. Heuer and L.W. Hobbs. American Ceramic Society, Ohio, 1981

[11] Porter D.L. Heuer A.H., Microstructural Development in MgO Partially Stabilized Zirconia (Mg-PSZ) J. Am. Ceram. Soc. 62(1979) No 5-6, 298-304

[12] Toraya H., Yoshimura M., Somiya S., Calibration Curve for Quantitative Analysis of the Monoclinic-Tetragonal $ZrO_2$ system by X-ray Diffraction, Communications of the American Ceramic Society, june 1984, C119-121

[13] Schmid H.K., Quantitative Analysis of Polymorphic Mixes of Zirconia by X-ray Diffraction, J. Am. Ceram. Soc., 70(1987), No5, 367-376

[14] Evans P.A., Stevens R., Binner J.G., Quantitative X-ray Diffraction Analysis of Polymorphic Mixes of Pure $ZrO_2$. Br. Ceram. Trans. J. 83(1984) 39-43

[15] Garvie R.C., Nicholson P.S., Phase Analysis in Zirconia Systems. J. Am. Ceram. Soc. 55(1972), No 6, 303-305

[16] Miller R.A., Garlick R.G., Smialek J.L., Phase Distributions in Plasma Sprayed Zirconia Yttria, J. Am. Ceram. Soc. 62(1983), No 12, 1355-1358

[17] Scott H.G, Phase Relationships in the Zirconia-Yttria System, J. Mater. Sc. 10(1975), 1527-1535

## CHAPTER VI CONCLUSIONS AND RECOMMENDATIONS

This chapter indicates the main results described in the foregoing chapters. Although for several problems related with the spraying of thermal barrier coatings, solutions were indicated, there still exist many questions. In recommendations for further research some of them are mentioned.

### 1 RESULTS

#### 1.1 The behaviour of single $ZrO_2$ particles

The morphologies of the splashed $ZrO_2$ particles depend mainly on the velocities and the heat contents of the $ZrO_2$ particles during the plasma spray process. The substrate material plays a minor role in the morphology of the splashed particles.

The adhesion of plasma sprayed $ZrO_2$ particles appeared to depend mainly on the substrate material. Whether adhesion would exist or not did not only depend on the contact temperature during solidification of the $ZrO_2$ particles. Generally it could be stated that an increased impact velocity of the particles resulted in an improved adhesion to the substrate material. A high particle velocity and a high heat content of the particles were required for adhesion of $ZrO_2$ to W and Mo.

#### 1.2. The use of extended anode channels

To obtain overheated $ZrO_2$ particles, the dwell time of the particles has to be increased. This can be achieved by the use of an extended anode channel. The heat content of the particles is further increased when the plasma gas mixture contains a high amount of $H_2$. A too high $H_2$ content may result in severe erosion of the anode channel.

The use of an extended anode channel resulted in both an increased particle velocity and an increased heat content of the particles.

#### 1.3. The influence of substrate cooling

Substrate cooling during the plasma spray process resulted in a $ZrO_2$ coating with residual tensile stresses. Furthermore, substrate cooling resulted in a dense micro crack network all over the $ZrO_2$ coating.

### 1.4. Fracture behaviour of cooled and non-cooled $ZrO_2$ coatings.

When subjected to mechanical stresses, the coatings sprayed on cooled substrates showed a fracture behaviour that differed from that of the coatings sprayed on non-cooled substrates. Cooled coatings showed cracks which mainly proceeded along the particle boundaries. In the non-cooled coatings, on the contrary, the cracks mainly proceeded across the particles. A difference in fracture behaviour also could be observed using acoustic emission evaluation. Fracture due to tensile stress in the cooled coatings occurred by the formation of several minor macro cracks in the $ZrO_2$ topcoat. These cracks were formed right from the start of the three point bending test.

Fracture due to tensile stresses in the non-cooled coatings occurred by the formation of large macro cracks after exceeding a certain strain.

### 1.5. Conclusions concerning the thermal shock behaviour of thermal barrier coatings

#### 1.5.1. The influence of substrate cooling

The use of substrate cooling during spraying resulted in an increased thermal shock resistance of the thermal barrier coatings. The improved thermal shock resistance is supposed to be caused by two factors. Firstly, the cooled coatings have a dense micro-crack network, resulting in a more flexible coating. Secondly, the cooled coatings have residual tensile stresses compensating the compressive stresses arising during heating up of the coating.

#### 1.5.2. The influence of overheated $ZrO_2$ particles on the thermal shock behaviour of thermal barrier coatings.

Especially the coatings, sprayed with an extended anode channel had a high thermal shock resistance. The use of an extended anode channel resulted in overheated $ZrO_2$ particles. Therefore the $ZrO_2$ coatings, produced using an extended anode channel, showed an improved intrinsic strength due to the improved adhesion between the $ZrO_2$ particles.

#### 1.5.3. Failure modes in the cooled and non-cooled $ZrO_2$ topcoats.

Failure in the non-cooled coatings, sprayed with an extended anode channel, occurred by the formation of horizontal cracks, just above the interface

bondcoat-topcoat. These horizontal cracks were not formed in the cooled coating, sprayed with an extended anode channel.

**1.5.4. The influence of the type of bondcoat on the thermal shock behaviour of thermal barrier coatings.**

Thermal barrier coatings with an APS FeCrAlY bondcoat failed due to bondcoat oxidation. Oxidation of the FeCrAlY particles during the plasma spray process, resulted in a content of free Al in the FeCrAlY bondcoat, which was too low to form a protective $Al_2O_3$ scale at the interface bondcoat-topcoat. Instead of an $Al_2O_3$ film, a $Fe_2O_3$ film was formed. Crack formation in this film resulted in delamination of the ceramic topcoat.

When the FeCrAlY bondcoat was applied, according to the low pressure plasma spraying process, the protective $Al_2O_3$ scale was formed and no delamination occurred at the interface bondcoat-topcoat.
The NiCrAlY bondcoats, sprayed with the air plasma spraying process did form also this protective alumina scale.

**1.6. Erosion resistance.**

The $ZrO_2$ coatings sprayed with an extended anode channel had a high erosion resistance due to their high intrinsic strength. The high intrinsic strength played also an important role during tensile adhesion testing. The coatings sprayed with an extended anode channel did not form any cracks in the ceramic topcoat.
The erosion resistance of these coatings was three to four times as high as that of the conventional coatings.

**1.7. Erosion resistance and thermal shock resistance**

With regard to erosion resistance and thermal shock resistance, it can be concluded that $ZrO_2$ topcoats, produced by depositing overheated $ZrO_2$ particles (which can be obtained by the use of an extended anode channel) on a cooled substrate, appeared to have both a high thermal shock resistance and a high erosion resistance.

**1.8 The stability of plasma sprayed $ZrO_2$ 7.6 wt.% $Y_2O_3$ at elevated temperatures.**

The plasma sprayed $ZrO_2$ 7.6 wt% $Y_2O_3$ coating mainly consisted of the non-

transformable tetragonal phase, the so called T'-phase. During long term annealing at temperatures above 1300 °C, this phase decomposed in a cubic phase and a tetragonal phase. The tetragonal phase transformed to the monoclinic phase on cooling down to room temperature. The cubic phase was maintained at room temperature.

## 2 RECOMMENDATIONS FOR FURTHER RESEARCH.

### 2.1. The influence of the velocity and heat content of $ZrO_2$ particles on the morphologies of the splashed particles.

The influence of the heat content and the velocity on the morphologies of splashed $ZrO_2$ particles has to be studied more thoroughly. Since the spraying process couples these two parameters, it is necessary to study the influence of each parameter separately. This can be done when the time of flight method for the determination of particle velocity will be available. This method, together with the rotating substrate holder gives the possibility to investigate the influence of both the heat content and the velocity of $ZrO_2$ particles on their splash morphologies.

### 2.2 Formation of cracks during thermal shock testing

It has to be studied why the horizontal cracks, formed during thermal shock testing of non-cooled coatings develop just above the interface bondcoat-topcoat. This is a phenomenon which is generally reported in literature, but not well understood at this moment.

### 2.3. Penetration of corrosive products in the micro cracked $ZrO_2$ topcoats.

The ceramic topcoats, sprayed on the cooled substrates displayed a dense micro crack network. Experiments proved that penetration of liquids occurred along the vertical microcracks and the horizontal fissures. It has to be studied whether corrosive liquids penetrate in this way in the ceramic coating and may harm both the $ZrO_2$ topcoat and the metallic bondcoat.
The application of a thin coating deposited on the ceramic topcoat and acting as a non-wetting agent may be studied.

### 2.4. The application of APS FeCrAlY bondcoats

The use of a coarse FeCrAlY powder (with the same chemical composition as the FeCrAlY powder used during this research programme) for the

production of APS bondcoats has to be studied. The influence of the grain size on the oxidation of Al during the flight from the plasma torch to the substrate has to be investigated. The influences on the oxidation behaviour of laser melting of the bondcoat's surface and the use of a transferred-arc during spraying of the bondcoat have to be studied.

**2.5. Measurement of the thermal conductivity of $ZrO_2$ topcoats.**
The thermal conductivities of the different $ZrO_2$ topcoats, sprayed during the research programme, have to be determined.

**2.6. Application of the new developed thermal barrier coating in a gas turbine.**
The thermal barrier coatings which were developed during this research programme have been tested in laboratory set ups and not in real gas turbines. For this reason it may be interesting to apply the new coatings to some parts of a gas turbine (combustion chamber and especially the first stage of the vanes) and compare their performance with that of the conventional thermal barrier coatings.

**2.7. Application of acoustic emission evaluation during thermal shock testing**
The application of acoustic emission evaluation during thermal shock testing of the thermal barriers coatings may give insight in the development and growth of the cracks which cause delamination of the $ZrO_2$ topcoat.

**2.8. The spraying of $ZrO_2$ coatings with increased deposition rates.**
Preliminary experiments proved that deposition rates, exceeding 100 grams $ZrO_2$ powder per minute, can be obtained, using an extended anode channel. The characteristics of the coatings, sprayed with these high deposition rates, have to be investigated.

**2.9. Spraying of $ZrO_2$ topcoats with increased thickness.**
The developed techniques of spraying overheated $ZrO_2$ particles on a cooled substrate to obtain coatings with both a high erosion and a high thermal shock resistance can be applied to produce thermal barrier coatings with thicknesses of 1 mm and more. These coatings have to be tested in thermal shock tests.

## SAMENVATTING

Het thermodynamisch rendement van gasturbines en dieselmotoren kan verhoogd worden door de toepassing van een hogere verbrandings-temperatuur. Om de metalen delen van een gasturbine te beschermen tegen deze verhoogde temperatuur worden warmteremmende lagen toegepast, zogenaamde "thermal barrier coatings". "Thermal barrier coatings" worden toegepast in de verbrandingskamers en leidkanalen en op de leidschoepen van gasturbines. In dieselmotoren worden "thermal barrier coatings" aangebracht op de zuigerkop en op de kleppen.
"Thermal barrier coatings" bestaan in het algemeen uit een metallische hechtlaag (Bondcoat) van het MCrAlY-type (waarbij M staat voor Fe, Ni, Co, CoNi) en een keramische toplaag (topcoat) van (partieel) gestabiliseerd zirkoonoxide ($ZrO_2$). Zowel de hechtlaag als de keramische toplaag worden door middel van poederplasmaspuiten aangebracht. De dikte van de hechtlaag is meestal 0.1 mm, terwijl de dikte van de toplaag varieert van 0.3 mm voor een gasturbine, tot enkele mm voor een dieselmotor.
De "thermal barrier coatings" die tijdens dit onderzoek gespoten zijn bestonden uit een 0.1 mm FeCrAlY of NiCrAlY hechtlaag en een 0.3 mm $ZrO_2$-7.6 wt.% $Y_2O_3$ topcoat. De FeCrAlY lagen werden door middel van atmosferisch plasmaspuiten (APS) en lage druk plasma spuiten (LPPS) aangebracht. De keramische hechtlaag werd altijd door middel van atmosferisch plasmaspuiten aangebracht.
De $ZrO_2$ lagen die momenteel worden toegepast in gasturbines bezitten een grote porositeit. Door deze porositeit worden de coatings flexibeler, waardoor de thermische wisselbelastings-weerstand toeneemt. Door de hoge porositeit (10-25 %), neemt de erosieweerstand echter af.
In dit onderzoek is er naar gestreefd een coating te ontwerpen en produceren die zowel een hoge thermische wisselbelastingsweerstand heeft, als een hoge erosieweerstand. Om dit doel te bereiken zijn de productie-factoren en de daaraan gerelateerde eigenschappen van "thermal barrier coatings" bestudeerd. De invloed die de variatie van de plasmaspuit-parameters heeft op de snelheid, de warmte-inhoud en het depositiegedrag van enkelvoudige $ZrO_2$ deeltjes is onderzocht.
Naast het variëren van de plasmaspuitparameters, werden verlengde anodekanalen toegepast, die leidden tot een verhoogde warmte-inhoud en een verhoogde snelheid van de deeltjes. Voor het bepalen van de warmte-

inhoud en de snelheid van de $ZrO_2$ deeltjes werden experimentele technieken ontwikkeld. De invloed die snelheid en warmte-inhoud hebben op de hechting van $ZrO_2$ deeltjes op verschillende metallische substraten werd onderzocht. Het blijkt dat $ZrO_2$ op Mo en W pas tot hechting komt als de deeltjes sterk oververhit zijn en een hoge snelheid bezitten.
De resultaten van het onderzoek naar het gedrag van enkelvoudige $ZrO_2$ deeltjes werden gebruikt bij de productie van de $ZrO_2$ toplagen. De opbouw van spanningen tijdens het plasma spuitproces werd voorspeld met een rekenmodel. Dit model werd experimenteel geverifieerd. Bij het spuiten van $ZrO_2$ lagen werd, naast de variatie van de plasmaspuitparameters en de toepassing van verschillende anodekanalen, ook gebruik gemaakt van substraatkoeling. Substraatkoeling bleek zowel de microstructuur als de eigenspanningstoestand van de coating sterk te beïnvloeden. Substraatkoeling leidde tot $ZrO_2$ lagen met een dicht netwerk van microscheuren, dat de coating een zekere flexibiliteit verschaft.
De vorming van macroscheuren in de verschillende typen "thermal barrier coatings" is onderzocht door middel van akoestische emissie in combinatie met de drie-punts buigproef. Het bleek dat substraatkoeling een grote invloed had op de wijze van scheurvorming in de $ZrO_2$ coating.
De erosieweerstand en de thermische wisselbelastingsweerstand van de coatings zijn bepaald in erosieproeven en thermoshock proeven. Hierbij bleek dat coatings, die gespoten zijn met sterk oververhitte $ZrO_2$ deeltjes, op gekoelde substraten, zowel een hoge erosieweerstand als een hoge thermoshockweerstand bezitten. Tevens werden conventionele "thermal barrier coatings" getest. Het bleek dat de erosieweerstand van de nieuw ontwikkelde coatings met minimaal een factor 3 was toegenomen, terwijl de thermische wisselbelastingsweerstand ook was toegenomen.
Bij onderzoek naar de invloed die de metallische hechtlaag heeft op de thermische wisselbelastingsweerstand bleek dat de LPPS FeCrAlY hechtlaag en de APS NiCrAlY hechtlaag een beschermde $Al_2O_3$ film vormen op het grensvlak tussen hechtlaag en toplaag.
Bij de APS-FeCrAlY hechtlagen werd deze $Al_2O_3$ film niet gevormd. Ten gevolge van oxydatie van de FeCrAlY deeltjes tijdens het spuitproces bevatte de FeCrAlY hechtlaag te weinig vrij Al om een beschermende $Al_2O_3$ film te vormen. Falen van de "thermal barrier coating" in de thermoshockproef werd veroorzaakt door hevige oxydatie op het grensvlak hechtlaag-toplaag. Scheurvorming in deze oxydefilm, die hoofdzakelijk Fe bevatte leidde tot

delaminatie van de keramische toplaag.
De invloed die substraatkoeling, variatie van de plasmaspuitparameters en de toepassing van verschillende anodekanalen hebben op de hechtsterkte van de "thermal barrier coatings" werd bepaald. Hierbij bleek dat de methode van opspuiten een grote invloed heeft op de hechtsterkte en de faalvorm. Bij het spuiten met oververhitte deeltjes neemt de hechtsterkte toe en faalt de coating op de verbinding tussen substraat en hechtlaag in plaats van door scheurvorming in de keramische laag.
Door middel van gloeiproeven werd de stabiliteit van $ZrO_2$-7.6 wt%$Y_2O_3$ onderzocht. Bij fase-analyse door middel van Röntgen-diffractie bleek dat de plasma gespoten $ZrO_2$ laag, die in gespoten toestand hoofdzakelijk uit de niet-transformeerbare tetragonale fase bestaat, bij langdurig gloeien op temperaturen boven 1300 °C, uit elkaar viel in een kubische fase en een tetragonale fase. Bij afkoeling naar kamertemperatuur transformeert de tetragonale fase naar de monokliene fase. Deze fase-transformatie kan grote invloed hebben op de levensduur van de coating.

**Nawoord**

Het onderzoek dat in dit proefschrift is beschreven was slechts mogelijk door de hulp van velen. Met name de promotoren prof. dr. ir. J.A. Klostermann, prof. dr. R. Metselaar en dr.ir. Jos Houben, en de leden van de groep thermisch spuiten, Gijs van Liempd en Piet de Waal wil ik bij deze hartelijk danken. Daarnaast wil ik de eindstudenten ir. Maarten Spanjers en ir. Bas Mathijsen en de vele stagiaires danken voor hun bijdragen aan het onderzoek. Mijn dank gaat verder uit naar alle medewerkers van de faculteiten werktuigbouwkunde en scheikundige technologie van de TUE die mij bij mijn onderzoek geholpen hebben.
Ing. J. van der Goes van de "Royal Schelde Group", Ir. R. Zaalberg van "Thomassen International" en de leden van de programmacommissie van het IOP technische keramiek wil ik danken voor de prettige samenwerking gedurende de onderzoeksperiode.

**Curriculum Vitae**

Ad Verbeek werd geboren op 23 februari 1964 te Heythuysen. Na het behalen van het atheneum-B diploma aan het bisschoppelijke college Broekhin te Roermond startte hij in september 1982 met de studie werktuigbouwkunde aan de Technische Universiteit Eindhoven. In januari 1988 werd het doctoraal examen afgelegd na een eindstudie binnen de groep thermisch spuiten onder leiding van prof. Klostermann en dr.ir. J.M. Houben. In februari 1988 startte hij met een promotie-onderzoek binnen dezelfde groep.

## Appendix A
## DERIVATION OF THE EQUATIONS FOR THE CALCULATIONS OF THE CONTACT TEMPERATURES AND SOLIDIFICATION TIMES OF PLASMA SPRAYED PARTICLES

Figure A1 shows the system to be considered; a solid substrate and a deposit, which is partly liquid. The location of the solidification front at the time t, is equal to x=X(t).

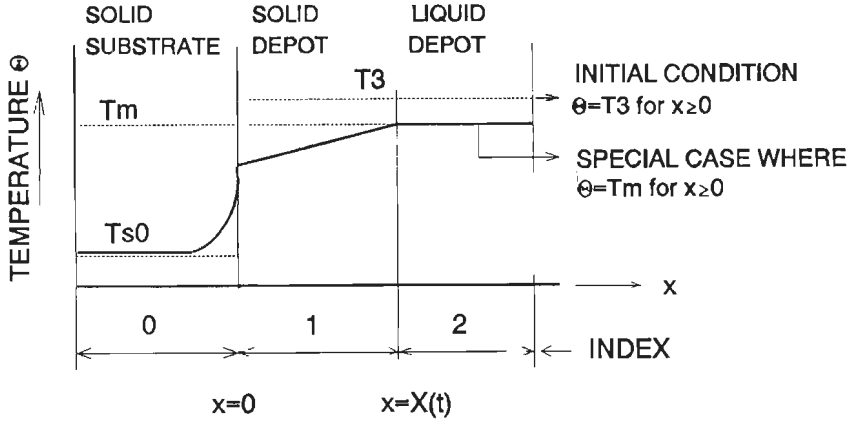


**Figure A-1** System to be considered for the calculation of the solidification of a molten particle on a solid substrate (Redrawn from [A1])

### Initial conditions

For t=0, the region x>0 is supposed to be liquid. This region has an uniform temperature $T_3$. The region x<0 is solid and has a uniform temperature $T_{s0}$. This situation is described by the next conditions.

$x<0$: $\theta_0=T_{s0}$ *for* $t=0$

$x<0$: $\theta_2=T_3$ *for* $t=0$

In this appendix we will consider the simplified case were

$\Theta_2 = T_3 = T_m$ for x>0

$T_m$ is the melting temperature of the deposit

The equations for heat conduction in the different sections, indicated in figure A1, are give below.

$$for\ x \le 0: \quad \frac{\partial^2 \theta_0}{\partial x^2} - \frac{1}{a_0}\frac{\partial \theta_0}{\partial t} = 0 \tag{1}$$

$$for\ 0 \le x \le X(t): \quad \frac{\partial^2 \theta_1}{\partial x^2} - \frac{1}{a_1}\frac{\partial \theta_1}{\partial t} = 0 \tag{2}$$

$$for\ x \ge X(t) \quad \frac{\partial^2 \theta_2}{\partial x^2} - \frac{1}{a_2}\frac{\partial \theta_2}{\partial t} = 0 \tag{3}$$

**Boundary conditions**

The situation is described by the next boundary conditions:

$$\theta_0 = T_{s0} \quad as\ x \to -\infty \tag{4}$$

$$\theta_0 = \theta_1 \quad as\ x = 0 \tag{5}$$

$$\lambda_0 \frac{\partial \theta_0}{\partial x} = \lambda_1 \frac{\partial \theta_1}{\partial x} \quad as\ x = 0 \tag{6}$$

$$\lambda_1 \frac{\partial \theta_1}{\partial x} - \lambda_2 \frac{\partial \theta_2}{\partial x} = L\rho \frac{dX}{dt} \quad as\ x = X(t) \tag{7}$$

$$\theta_1 = \theta_2 \quad as\ x = X(t) \tag{8}$$

When $\theta_2 = T_3 = T_m$, equation (7) becomes:

$$\lambda_1 \frac{\partial \theta_1}{\partial x} = L\rho \frac{dX}{dt} \quad as\ x = X(t) \tag{7a}$$

and equation (8) changes into

$$\theta_1 = \theta_2 = T_m \quad as\ x \ge X(t) \tag{8a}$$

The next general solutions are assumed for the above equations:

**For the substrate:**

$$\theta_0 = T_{s0} + \alpha\left(1 + erf\frac{x}{\sqrt{4a_0 t}}\right) \tag{9}$$

$\alpha$ is a constant which has to be determined from the boundary conditions. (9) satisfies equation (1) and condition (4)

**For the deposit:**

$$\theta_1 = T_{s0} + \beta + \gamma erf\frac{x}{\sqrt{4a_1 t}} \tag{10}$$

$\beta$ and $\gamma$ are constants to be determined from the boundary conditions. (10) satisfies equation (2) and condition (5) if $\alpha = \beta$
At x=0, the following condition is valuable:

$$\theta_0 = \theta_1 \quad \Rightarrow \quad \beta = \alpha$$

$\Theta_1$ can now be written as:

$$\theta_1 = T_{s0} + \alpha + \gamma erf\frac{x}{\sqrt{4a_1 t}} \tag{10a}$$

The relationship between $\alpha$ and $\beta$ can be determined by the differentiation of equations (9) and (10) and subsequently by substituting the results in condition (6)

$$\frac{\partial\theta_0}{\partial x} = \alpha\frac{\partial}{\partial x}erf\frac{x}{\sqrt{4a_0 t}} = \alpha\frac{2}{\sqrt{\pi}}e^{-x^2/4a_0 t}\frac{1}{\sqrt{4a_0 t}} = \frac{\alpha}{\sqrt{\pi a_0 t}}e^{-x^2/4a_0 t} \tag{11}$$

For x=0 this can be written as:

$$\left(\frac{\partial\theta_0}{\partial x}\right)_{x=0} = \frac{\alpha}{\sqrt{\pi a_0 t}} \tag{12}$$

For the deposit:

$$\frac{\partial\theta_1}{\partial x} = \gamma\frac{\partial}{\partial x}erf\frac{x}{\sqrt{4a_1 t}} = \frac{\gamma}{\sqrt{\pi a_1 t}}e^{-x^2/4a_1 t} \tag{13}$$

For x=0, this turns into:

**APPENDIX-A 3**

$$(\frac{\partial\theta_1}{\partial x})_{x=0}=\frac{\gamma}{\sqrt{\pi a_1 t}} \tag{14}$$

substitution of equation (12 and (14) into (6) gives:

$$\lambda_0\frac{\alpha}{\sqrt{\pi a_0 t}}=\lambda_1\frac{\gamma}{\sqrt{\pi a_1 t}}$$

Now a new term is introduced: B = $\alpha/\gamma$. B can now be written as:

$$B=\frac{\alpha}{\gamma}=\frac{\sqrt{\lambda_1\rho_1 c_1}}{\sqrt{\lambda_0\rho_0 c_0}}, \quad a \text{ was rewritten as } \frac{\lambda}{\rho c} \tag{15}$$

With this choice of B, condition (6) is satisfied.

The equation, describing the temperature in the substrate may now be written as:

$$\theta_1=T_{s0}+\gamma(\frac{\alpha}{\gamma}+erf\frac{x}{\sqrt{4a_1 t}}) = T_{s0}+\gamma(B+erf\frac{x}{\sqrt{4a_1 t}}) \tag{10b}$$

Solutions (9) and (10) are appropriate for the equations (1) and (2). Furthermore, the conditions (4),(5) and (6) are satisfied. In our case $\Theta_2=T_3=T_m$. The remaining boundary conditions are therefore (7a) and (8a). Condition (8a) requires $\Theta_1=\Theta_2=T_m$ as $x \geq X(t)$. Using equation (10b) at x=X(t), condition (10b) turns into:

$$\gamma(B+erf\frac{X}{\sqrt{4a_1 t}})=T_m-T_{s0} \tag{16}$$

This equation has to be valid for all values of the time t. For this reason X must be proportional to $\sqrt{t}$. This is the Neumann's assumption, and is stated below

$$X=p\sqrt{4a_1 t} \tag{17}$$

p is a constant which has to be determined from condition (7a).

Using (13) for x=X(t), we can write condition (7a) as:

$$\lambda_1 \frac{\gamma}{\sqrt{\pi a_1 t}} e^{-X^2/4a_1 t} = L\rho \frac{dX}{dt} \tag{18}$$

This equation represents the energy balance at the solidification front. Differentiating the Neumann's assumption gives:

$$\frac{dX}{dt} = p\sqrt{\frac{a_1}{t}} \tag{19}$$

Substitution of the above equation in equation 18 gives:

$$\lambda_1 \frac{\gamma}{\sqrt{4a_1 t}} e^{-X^2/4a_1 t} = L\rho p\sqrt{\frac{a_1}{t}} \tag{20}$$

Equations (16) and (17) can be put together to:

$$\gamma = \frac{T_m - T_{s0}}{B + erf \dfrac{X}{\sqrt{4a_1 t}}} = \frac{T_m - T_{s0}}{B + erf\ p} \tag{21}$$

When we insert the above equation and equation (17) into (20) we get:

$$\lambda_1 \frac{T_m - T_{s0}}{B + erf\ p} \frac{1}{\sqrt{\pi a_1 t}} e^{-p^2} = L\rho p\sqrt{\frac{a_1}{t}}$$

When is supposed that the density of the liquid equals the density of the solidified material: $\rho = \rho_1$, the above equation may be rewritten as:

$$\lambda_1 \frac{T_m - T_{s0}}{B + erf\ p} \frac{1}{\sqrt{\pi a_1 t}} \frac{1}{\sqrt{\dfrac{a_1}{t}}} = L\rho_1 p e^{p^2}$$

This can be rewritten to:

$$(B + erf\ p)\ p\ e^{p^2} = \frac{c_1(T_m - T_{s0})}{L\sqrt{\pi}} \tag{22}$$

**APPENDIX-A 5**

p and erf p can now be calculated by numerically solving this equation.

The most important equations are now recapitulated

**Temperature profile in the substrate**

$$\theta_0 = T_{s0} + \alpha\left(1 + erf\frac{x}{\sqrt{4a_0 t}}\right)$$

**Temperature in the solid deposit**

$$\theta_1 = T_{s0} + \gamma\left(B + erf\frac{x}{\sqrt{4a_1 t}}\right)$$

**The constant B is written as**

$$B = \frac{\alpha}{\gamma} = \frac{\sqrt{\lambda_1 \rho_1 c_1}}{\sqrt{\lambda_0 \rho_0 c_0}}$$

**The Neumann's assumption**

$$X = p\sqrt{4a_1 t}$$

X gives the location of the solidification front in the deposit.
**$\gamma$ is written as:**

$$\gamma = \frac{T_m - T_{s0}}{B + erf\ p} = constant$$

**p and erf p can be calculated from the next equation:**

$$(B + erf\ p)\ p\ e^{p^2} = \frac{c_1(T_m - T_{s0})}{L\sqrt{\pi}}$$

**Since $\alpha = \gamma B$, $\alpha$ can be written as:**

$$\alpha = \frac{B(T_m - T_{s0})}{B + erf\ p} \qquad (23)$$

**The substrate temperature profile can now be written as:**

$$\theta_0 = T_{s0} + \frac{B(T_m - T_{s0})}{B + erf\ p}\left(1 + erf\frac{x}{\sqrt{4a_0 t}}\right) \tag{24}$$

**And the temperature profile in the solid deposit is given by:**

$$\theta_1 = T_{s0} + \frac{T_m - T_{s0}}{B + erf\ p}\left(B + erf\frac{x}{\sqrt{4a_1 t}}\right) \tag{25}$$

**These equations can be rewritten to the next temperature profiles for the substrate and the solid deposit**

$$\frac{\theta_0 - T_{s0}}{T_m - T_{s0}} = \frac{B}{B + erf\ p}\left(1 + erf\frac{X}{\sqrt{4a_0 t}}\right) \tag{24a}$$

$$\frac{\theta_1 - T_{s0}}{T_m - T_{s0}} = \frac{1}{B + erf\ p}\left(B + erf\frac{x}{\sqrt{4a_1 t}}\right) \tag{25a}$$

These equations strictly hold for two semi-infinite bodies. They describe the exact temperature-time history of a disk shaped deposit of limited thickness and of the substrate during solidification of the deposit. For this reason, the equations are valid under the assumption that $t \leq t_{sol}$.
Equation (17) may be written as:

$$t = \frac{X^2}{4a_1 p^2} \tag{17a}$$

Because of the fact that X gives the position of the solidification front this equation may be written as:

$$t_{sol} = \frac{X^2}{4a_1 p^2} \tag{17b}$$

[A1] Houben J.M., Doctor's thesis, Eindhoven University of Technology, 1988

**APPENDIX-A 7**

**Appendix B-I**
**CALCULATION OF THE RESIDUAL STRESS IN A PLASMA SPRAYED COATING.**

Consider the situation which is given in figure B1.

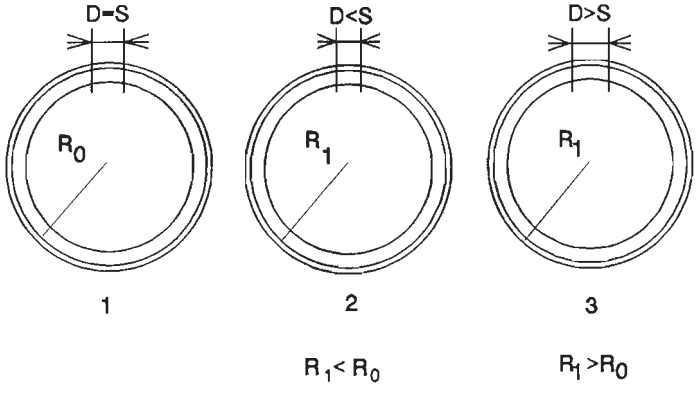


**Figure B-1** Cross sections of thin metallic rings with a plasma sprayed coating. The rings are sectioned by a saw-cut with width "S". If the specimen is stress free, the opening "D" is equal to "S". If the coating possess residual tensile stresses than "D"<"S". In the case of residual tensile stress "D">"S"

A closed ring with thickness $t_2$ is covered with a plasma sprayed coating with thickness $t_1$. Due to the coating process residual stresses exist in the coating-substrate system.
The ring has an original radius $R_0$
When a saw-cut with width "s" is made in the ring the slit will be opened or closed due to the residual stresses. The change of the slit width, "d" can be positive (wider opening) or negative (closure of the slit).

The stresses causing these opening or closure can be calculated by models, presented by 't Hart [B1] and Kouyumdjiev [B2]. These models relate the change of the initial radius $R_0$ and the new radius $R_1$ to the residual stresses. However, this is not the stress distribution as was present in the closed ring. To obtain the stress distribution in the closed ring, the slit in the ring has to be closed or opened to the width of the saw cut, by bending couples applied to the ends of the separated ring. The stress distribution, caused by these bending couples has to be added to the stress distribution calculated using the models of 't Hart and Kouyumdjiev.

The principle of the calculation of the stresses is shown in figure B-2.

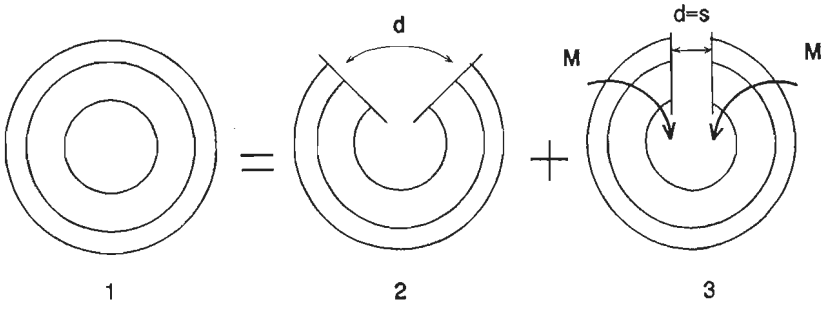


**Figure B-2** Method for the calculation of residual stresses in plasma sprayed coatings. (1) gives a closed ring with coating, containing residual stresses. After the ring is cut, the width of the slit can be measured (2) and the stresses can be calculated using the models of 't Hart and Kouyumdjiev. Adding to these stresses the stresses, caused by the moments M (3), the stress state in the coating on the closed ring can be calculated.

## 1 stress distribution calculated by models of 't Hart and Kouyumdjiev.

The change of the radius $R_0$ to the new radius $R_1$ of the ring with the sawcut can be calculated by the change of the opening "d".
The stresses in the coating can now be calculated by the following equation of 't Hart

$$\sigma_{1,2}=\frac{2}{(t_1+t_2)t_1}\frac{E_1I_1+E_2I_2}{R}\mp\frac{E_1*0.5t_1}{R} \qquad (1)$$

$t_{1,2}$: thickness of the coating and substrate respectively

$E_{1,2}$: Young's moduli of the coating and substrate respectively

$I_{1,2}$: Moments of inertia of the coating and the substrate respectively.

R: Change of curvature of the deformed ring.

Kouyumdjiev derives the next equation for the stress in the coating:

$$\sigma_{1,2}=\frac{\tilde{E}_1t_1}{6R\theta}\left(\frac{1+\gamma\theta^3}{1+\theta}\mp 3\gamma\theta^2\right) \qquad (2)$$

$$\theta=\frac{t_1}{t_2} \qquad \gamma=\frac{\tilde{E}_2}{\tilde{E}_1} \qquad \tilde{E}_1=\frac{E_1}{1-\nu_1} \qquad \tilde{E}_2=\frac{E_1}{1-\nu_2}$$

$\nu_{1,2}$: poisson modulus coating and substrate

When the Young's moduli in equation 1 ('t Hart ) are replaced by the modified Young's modulus as done by Kouyumdjiev, the results of the calculations made using both models will be almost similar.

Figure B3 shows the sites of the stresses in the coating, calculated by the foregoing mentioned equations. The stress distribution may assumed to be linear over the specimen's thickness, takin into account the high $R_1(t_1+t_2)$ ratio.

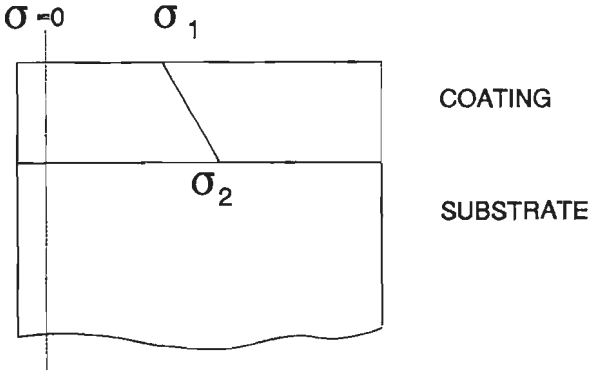


**Figure B-3** Stress distribution in the coating as calculated by the models of 't Hart and Kouyumdjiev.

**2 stress caused by the bending moments**

The bending moment which must be applied to the ends of the ring with the saw-cut to regain the original width of the saw-cut can be calculated using next equation which was derived by Hartog [B3] :

$$M=\frac{2*(R_1-R_0)*(EI)'}{2R_0^2} \qquad (3)$$

(EI)' is the combined young's modulus and moment of inertia for a layered beam and is given by Roark and Young [B4]

$$(EI)' = \frac{bt_1 t_2^3 E_1 E_2}{12(t_1 E_1 + t_2 E_2)} * (4 + 6\frac{t_1}{t_2} + 4(\frac{t_1}{t_2})^2 + \frac{E_1}{E_2}(\frac{t_1}{t_2})^3 + \frac{E_2}{E_1}\frac{t_2}{t_1}) \quad (4)$$

The stresses, caused by the bending moment can now be calculated using the equations given by Ugural [B5]

$$\sigma = \frac{M * y}{I_t} \quad (5)$$

y: distance from the place in the coating to the neutral axis of the coating-substrate combination

$I_t$: Moment of inertia of the coating substrate system.

$$I_t = \frac{1}{12} bt_1^3 + bt_1(t_n - 0.5t_1)^2 + \frac{1}{12} bt_2^3 + bt_2(t_n - 0.5t_2)^2 \quad (6)$$

b: width of the ring

$t_n$: position of the neutral axis, measured from the coatings surface.

$$t_n = \frac{bt_1 0.5t_1 + \frac{E_2}{E_1} bt_2(t_1 + 0.5t_2)}{bt_1 + \frac{E_2}{E_1} bt_2} \quad (7)$$

By adding the stresses of the models of 't Hart and Kouyumdjiev to the stress calculated by the bending moments, the stress in the coating on the closed ring is obtained.

References


[B1] Hart 't W. Master's Thesis, Einhoven University of Technology, 1972.

[B2] Kouyumdjiev C.N., Surf. Techn. 26(1985) 35-43

[B3] Hartog J.P. den, Strength of Materials, Dover Publications, New York, 1961

[B4] Roark R.J., Young W.C.,Formulas for Stress and Strain, Mc Graw Hill, 1975

[B5] Ugural A.C., Fenster S.K., Advanced Strength of Materials, Elsevier's Science Publishing, New York, 1987

## Appendix B-II
## PREPARATION OF THE SPECIMENS FOR MICROSCOPICAL EXAMINATION

The following procedure was used to prepare samples of plasma sprayed $ZrO_2$ coatings for microscopical examination.

### 1 Cutting of the samples

Samples were cut out from the strip shaped specimens by diamond wire sawing. This way of sectioning causes no crack formation in the ceramic topcoat. The use of an grinding machine to cut out the samples is not to be advised since this method may cause severe cracking of the $ZrO_2$ topcoat; both horizontal and vertical cracks may be formed. Diamond wire sawing with a 0.5 mm diamond wire did not cause any crack formation in the ceramic coating. Grain size of the diamond: 46 $\mu$m

### 2 Embedding of the samples

The hot embedding took place by a pressure of 2 bars, using Struers Resin-6 HQ. Cold embedding was done using Technovit 4071.

### 3 Grinding and polishing

Wet grinding of the sample until a plane surface is obtained, using SiC paper 220.

**Polishing** is preferably done on an automatic or semi-automatic polishing machine.

**First** the sample is polished on a Petrodisk for 15 minutes, using a 6 $\mu$m diamond spray (Struers, Buehler, Engis) and Lubricant Blue (Struers). Force on the sample: 15 N

**Secondly,** polishing for 5 minutes on a DP Plan cloth (Struers), using 6 $\mu$m diamond spray and Lubricant Blue. Force on the sample during polishing 15 N.

**Third,** polishing for 5 minutes on a Pan W cloth (Struers), using 3 $\mu$m diamond spray and Lubricant Blue. Force 15 N.

**Fourth,** polishing for 3 minutes on a DP Dur cloth (Struers), using 1 $\mu$m diamond spray and Lubricant Blue. Force 15 N.

**Fifth**, final polishing for 30 seconds on an OP Chem cloth (Struers), using OP-S $SiO_2$ (Struers). Force 10 N.

This method delivers plane samples (almost no round off of the edges of the coating) and a well visible microstructure.

The columnar grain structure, however, is hardly visible. To make this structure visible, ion etching is needed.

Ion etching was done, using a Balzers ion etching device, applying a tension of 20 kV and a current of 0.62 mA, using Argon as the etching medium. Minimum time required; 30 minutes. Angle of etching: 20 °with the normal to the plane.

**Appendix C-I**
**SEISMIC MOMENT TENSORS**

Acoustic emission sources can be represented by pairs of forces, working on a point. The forces, acting in pairs of two equal, opposite forces, are called force dipoles.
These forces work for very short times and have a dirac or $\delta$-function time dependency.

The stress and strain fields, caused by the force dipoles, in the material, are coupled via Hooke's law:

$$\tau_{ij}=C_{ijkl}\varepsilon_{kl} \tag{1}$$

Where $\tau_{ij}$ and $\epsilon_{kl}$ are the stress and the strain tensor respectively and $C_{ijkl}$ the general form of the elastic constant.
In the case of elastic isotropy $C_{ijkl}$ can be written as:

$$C_{ijkl}=\lambda\delta_{ij}\delta_{kl}+\mu(\delta_{ik}\delta_{jl}+\delta_{il}\delta_{jk}) \tag{2}$$

$\lambda$ and $\mu$ are the Lamé elastic constants.

$$\lambda=\frac{E\nu}{(1+\nu)(1-2\nu)} \qquad \mu=\frac{E}{2(1+\nu)} \tag{3}$$

$\delta_{xy}$ is the Kronecker delta function. $\delta_{xy}$ = 1 if and if only as x=y, all other cases $\delta_{xy}$ = 0.
With the help of (2), the stress tensor becomes:

$$\tau_{ij}=\lambda\varepsilon_{kk}\delta_{ij}+2\mu\varepsilon_{ij} \tag{4}$$

Any source can be represented either by a set of stresses or a set of strains, acting within a volume V, where V>0 for a point source.
The strength of an AE source is described by the seismic moment tensor $D_{ij}$:

$$D_{ij}=\int_V C_{ijkl}\varepsilon_{kl}^{T}d^3x \tag{5}$$

In general, this volume integral will give the source strength as a force dipole tensor:

$$D_{ij}=F_i dx_j \tag{6}$$

Scruby distinghuishes two types of basic AE sources; the dilatation source and the simple shear source. The microcrack source will be considered as a special case of the two basic sources and will be derived finally.

The dilatation source

The dilatation source can be regarded as a point expansion of volume dV which is equal in all directions. This is shown in the figure below. the forces dipoles, representing this source are working along the main axis $x_1$, $x_2$ and $x_3$ and are also shown in the figure.

$$\varepsilon_{11}=\varepsilon_{22}=\varepsilon_{33}=\frac{dV}{3V} \tag{7}$$

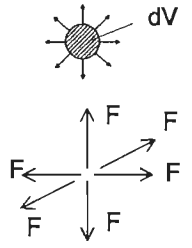


**Figure CI-1** Dilatation source, represented by force dipoles

The strain is equal in all directions:
And the stresses are thus represented by:

$$\tau_{11}=\tau_{22}=\tau_{33}=B\frac{dV}{V} \tag{8}$$

Where B is the bulk modulus:

$$B=\lambda+\frac{2\mu}{3} \tag{9}$$

The source strength is now:

$$D_{11}=D_{22}=D_{33}=BdV \tag{10}$$

The D tensor for the dilatation is shown below

$$\begin{bmatrix} BdV & 0 & 0 \\ 0 & BdV & 0 \\ 0 & 0 & BdV \end{bmatrix} \qquad (11)$$

The simple shear source

This source can be regarded as a dislocation loop represented by the burgers vector b and an area dA. Figure 2 shows this.

Scruby presents a solution for slip in a plane at 45° to the $x_3$ axis. The slip is represented by a dislocation loop of an area $dA/\sqrt{2}(1,0,-1) = \mathbf{dA}$ and the Burgers vector $\mathbf{b} = b/\sqrt{2}(1,0,-1)$.

The seismic moment tensor for simple shear is derived by Burridge and Knopoff and has the form:

$$D_{ij} = C_{ijkl} b_k dA_l \qquad (12)$$

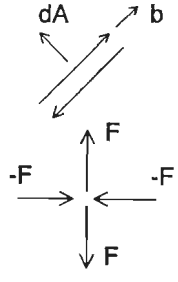


**Figure CI-2** Simple shear source, represented by force dipoles

On substituting the correct values it turns out that only $D_{11}$ and $D_{33}$ are not equal to zero. The seismic moment tensor for
this simple shear source can therefore represented by:

$$\begin{bmatrix} -\mu bdA & 0 & 0 \\ 0 & 0 & 0 \\ 0 & 0 & \mu bdA \end{bmatrix} \qquad (13)$$

The microcrack source

A microcrack source, parallel to the $x_1$ and the $x_2$ axis is represented by the vector dA3 in $x_3$ direction. The crack is supposed to be pennyshaped and can be described by an edge dislocation loop with a volume $b_3 dA_3$, which is

equivalent to the volume of the microcrack. The strength of this source is now given by :

$$D_{ij}=C_{ij33}b_3dA_3=(\lambda\delta_{ij}+\mu\delta_{i3}+\mu\delta_{j3})b_3dA_3 \tag{14}$$

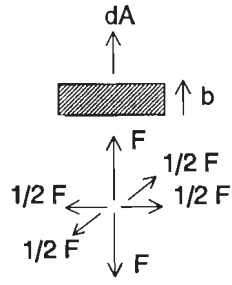


**Figure CI-3** The micro-crack source, represented by force dipoles

$$D_{11}=D_{22}=\lambda b_3dA_3 \qquad D_{33}=(\lambda+2\mu)b_3dA_3 \tag{15}$$

and the seismic moment tensor is represented by:

$$\begin{bmatrix} \lambda bdA & 0 & 0 \\ 0 & \lambda bdA & 0 \\ 0 & 0 & (\lambda+2\mu)bdA \end{bmatrix} \tag{16}$$

## Appendix C-II
## WAVE PROPAGATION IN A SOLID

The general displacement equation of motion by absence of body forces is formulated as:

$$\mu\nabla^2\boldsymbol{u}+(\lambda+\mu)\nabla\nabla\cdot\boldsymbol{u}=\rho\frac{\partial^2\boldsymbol{u}}{\partial t^2} \tag{1}$$

$$\langle \nabla^2 u \rangle_i = \frac{\partial^2 u_i}{\partial x_j \partial x_j} \tag{2}$$

$$\langle \nabla\nabla \cdot u \rangle_i = \frac{\partial}{\partial x_i}\left(\frac{\partial u_j}{\partial x_j}\right) \tag{3}$$

Above equation can be solved by expressing the displacement u in terms of 2 potentials, a scalar potential $\phi$ and a vector potential $\Phi$. Formula (1) can now be represented as stated below.

$$u = \nabla\phi + \nabla \times \psi \tag{4}$$

Formula (1) can now be divided into equations for each of the potentials

$$\nabla^2\phi = \left(\frac{1}{c_1^2}\right)\left(\frac{\partial^2\phi}{\partial t^2}\right) \qquad c_1^2 = \frac{(\lambda + 2\mu)}{\rho} \tag{5}$$

$$\nabla^2\psi = \left(\frac{1}{c_2^2}\right)\left(\frac{\partial^2\psi}{\partial^2 t}\right) \qquad c_2^2 = \frac{\mu}{\rho} \tag{6}$$

As showed above, the propagation of compression and shear waves is uncoupled now. This is valid in an infinite medium. As soon as the waves reach a surface of a body, the displacements may be coupled by the boundary conditions.
When we describe the compression or longitudinal wave in one D form we get:

$$\frac{\partial^2\phi}{\partial x_1^2} - \frac{\rho}{(\lambda + 2\mu)}\frac{\partial^2\phi}{\partial t^2} = 0 \tag{7}$$

The solution for this equation is :

$$\phi = f[t - \frac{x_1}{c_1}] + g[t + \frac{x_1}{c_1}] \tag{8}$$

f and g are any functions, representing respectively positive and negative going waves, propagating at a speed $c_1$. When we derive formula (7) for spherical coordinates, we obtain:

$$(\frac{\partial^2}{\partial r^2}) - (\frac{1}{c_1^2})(\frac{\partial^2}{\partial t^2})(r\phi) = 0 \tag{9}$$

This solution predicts ingoing and outgoing waves, but for radiation from a point source, we only need the outgoing wave solution:

$$\phi = (\frac{1}{r}) f[t - \frac{r}{c_1}] \tag{10}$$

The Green's function for a single point force acting in the direction $x_3$ is represented by equation:

$$G(r,t') = \frac{\cos\theta}{4\pi(\lambda + 2\mu)r} \delta(t - \frac{r}{c_1}) \tag{11}$$

The displacement due to the compressive wave caused by a force dipole, whose pair of forces are separated over the small distance $dx_3$, acting in the $x_3$ direction is now

$$u_r^l = \int \langle G(r,t') F_3(t-t') - G(r + dx_3, t') F_3(t-t') \rangle dt' \tag{12}$$

$$= \int \langle G(r,t') F_3(t-t') - [G(r,t') + \frac{\partial G}{\partial r}(r,t') dr] F_3(t-t') dt' \tag{13}$$

$$= -\int \frac{\partial G}{\partial r}(r,t') \frac{dr}{dx_3} F_3(t-t') dx_3 dt' \tag{14}$$

$$= -\int \frac{\partial G}{\partial r} \cos\theta D_{33}(t-t')dt' \tag{15}$$

$$\frac{\partial G}{\partial r}(r,t') = -\frac{\cos\theta}{4\pi(\lambda+2\mu)}\left[\frac{\delta'(t-\frac{r}{c_1})}{rc_1} + \frac{\delta(t-\frac{r}{c_1})}{r^2}\right] \tag{16}$$

$$\frac{\cos^2\theta}{4\pi(\lambda+2\mu)}\int\left(\frac{\delta'(t-\frac{r}{c_1})D_{33}(t-t')}{rc_1} + \frac{\delta(t-\frac{r}{c_1})D_{33}(t-t')}{r^2}\right)dt' \tag{17}$$

this results in:

$$\frac{\cos^2\theta}{4\pi(\lambda+2\mu)}\left[\frac{D_{33}(t-t')}{r^2} + \delta(t-\frac{r}{c_1})D_{33}(t-t') + \int \delta(t-\frac{r}{c_1})\frac{\dot{D}_{33}(t-t')}{rc_1}dt'\right] \tag{18}$$

the final result is :

$$U_r^I = \frac{\cos^2\theta}{4\pi(\lambda+2\mu)}\left[\frac{D_{33}(t-t')}{r^2} + \frac{\dot{D}_{33}(t-t')}{rc_1}\right] \tag{19}$$

Since we only use the far field approximation, the terms with $r^2$ disappear so that the formula for the radial displacement due to a compressive wave becomes:

$$u_r^I = \frac{\cos^2\theta}{4\pi(\lambda+2\mu)}\left[\frac{\dot{D}_{33}(t-t')}{rc_1}\right] \tag{20}$$

The displacement due to the shear wave has the form:

In the same way it is possible to derive the equations for wave propagations caused by $D_{22}$ and $D_{11}$

$$u_\theta^t = \frac{\cos^2\theta}{4\pi\mu}\left[\frac{\dot{D}_{33}(t-\frac{r}{c_2})}{rc_2}\right] \qquad (21)$$

## APPENDIX C-III
## WAVE DEFLECTIONS AND PHASE CHANGES

When a compressive wave reaches the boundary of a body, the wave will be reflected partly as a compressive wave and partly as a transversal or shear wave.
A compressive wave with an incident angle $\Theta_0$ will be reflected with an angle $\Theta_1$, where $\Theta_0 = \Theta_1$. In addition to this reflected compressive wave, a shear wave will be generated with an angle $\Theta_2$. This is shown in figure CIII-1.

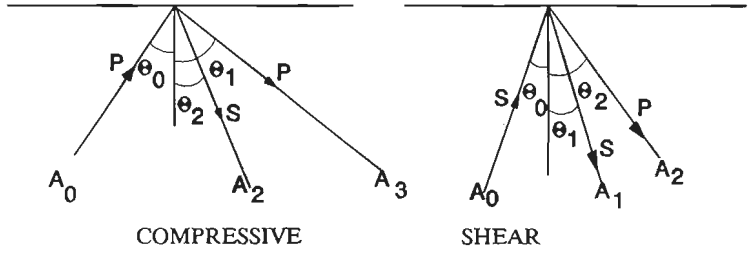


**Figure CIII-1** Deflection of compressive and shear waves

The relationship between $\Theta_1$ and $\Theta_2$ can be written as:

$$\frac{\sin\theta_2}{\sin\theta_0}=\frac{c_2}{c_1}=\frac{1}{k} \tag{1}$$

where $c_1$ is the compressive wave speed and $c_2$ the shear wave speed.
The relationship between the amplitudes $A_0$, $A_1$ and $A_2$ is given by Achenbach:

$$A_1=A_0\frac{\sin2\theta_0\sin2\theta_2-k^2\cos^2 2\theta_2}{\sin2\theta_0\sin2\theta_2+k^2\cos^2 2\theta_2} \tag{2}$$

$$A_2=A_0\frac{2k\sin2\theta_0\cos2\theta_2}{\sin2\theta_0\sin2\theta_2+K^2\cos^2 2\theta_2} \tag{3}$$

An shear wave with an incident angle $\Theta_0$ is reflected at a shear wave at angle $\Theta_2$ and a compressive wave at angle $\Theta_1$, where

$$\frac{\sin\theta_1}{\sin\theta_0}=\frac{c_1}{c_2}>1 \tag{4}$$

When the angle of incidence of the shear wave, $\Theta_0$, exceeds the value:

$$\theta_0>\sin^{-1}\left(\frac{c_2}{c_1}\right) \tag{5}$$

the situation occurs that $\sin\Theta_1 > 1$, to meet equation 4. Due to the fact that this is impossible, the problem can only be met by the additional generation of a surface wave, a so called Rayleigh wave. Rayleigh waves have a velocity, which is slight leess then the velocity of shear waves. They attenuate with distance as $R^{-0.5}$ whereas bulk waves attenuate with $R^{-1}$.
As a result the waves which are measured at great distances of the source are predominantly of the Rayleigh type.
Rayleigh waves consist of a perpendicular motion of the surface with a small parallel component.

## Appendix D
## DIFFRACTION PATTERNS OF ANNEALED $ZrO_2$ COATINGS

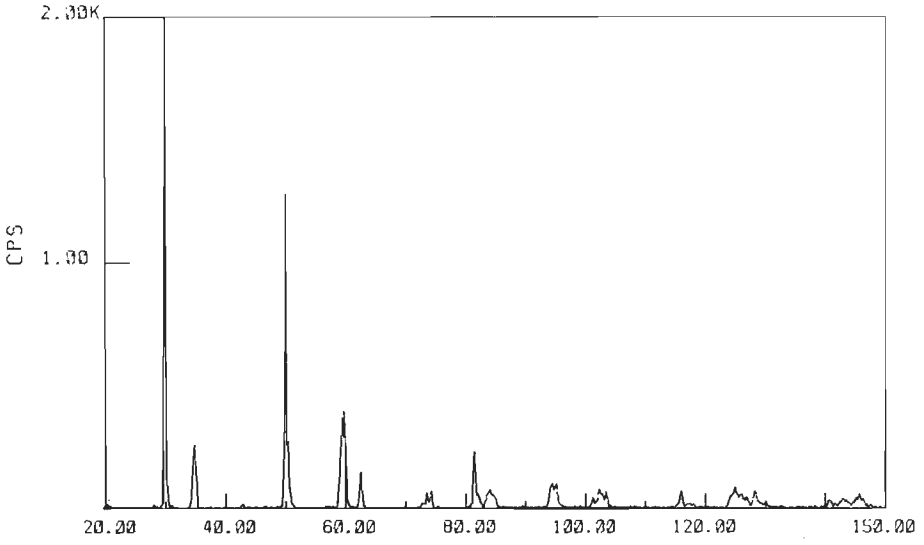


**Figure D-1** Diffraction pattern of $ZrO_2$ -7.6 wt $Y_2O_3$ in as-sprayed state. no monoclinic phase is observed.

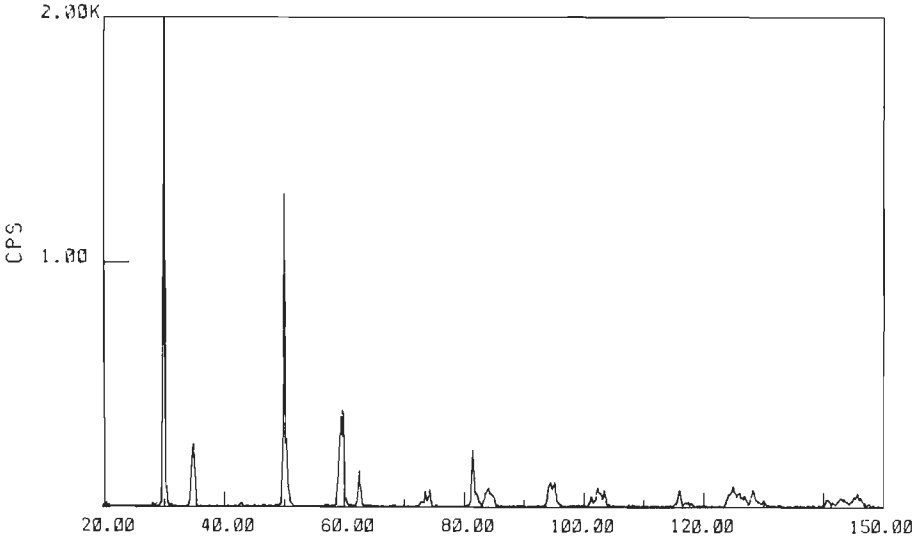


**Figure D-2** Diffraction pattern of $ZrO_2$ 7.6 wt% $Y_2O_3$ after annealing for 100 hours at 1300 °C. No monoclinic phase did develop.

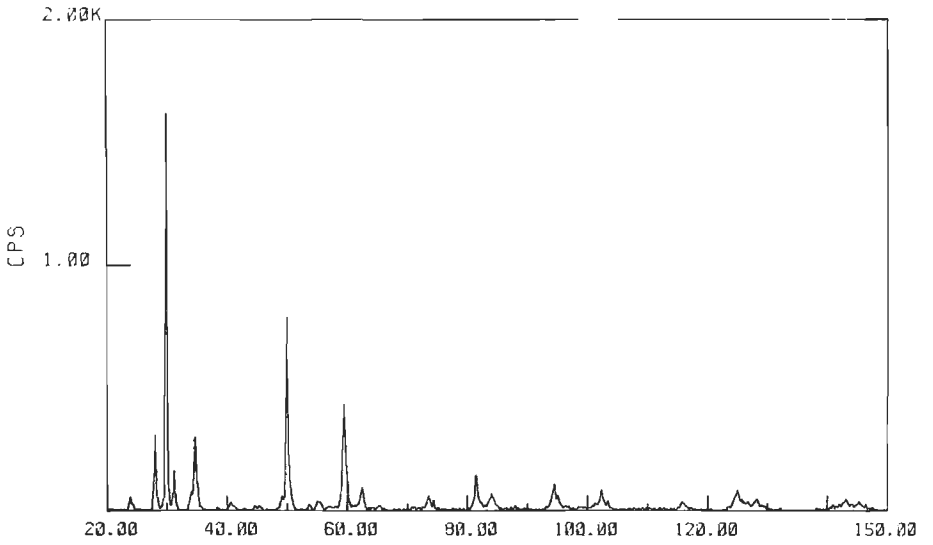


**Figure D-3** Diffraction pattern of $ZrO_2$ 7.6 wt% $Y_2O_3$ after annealing for 100 hours at 1400 °C. It can be seen that the monoclinic phase came into being.

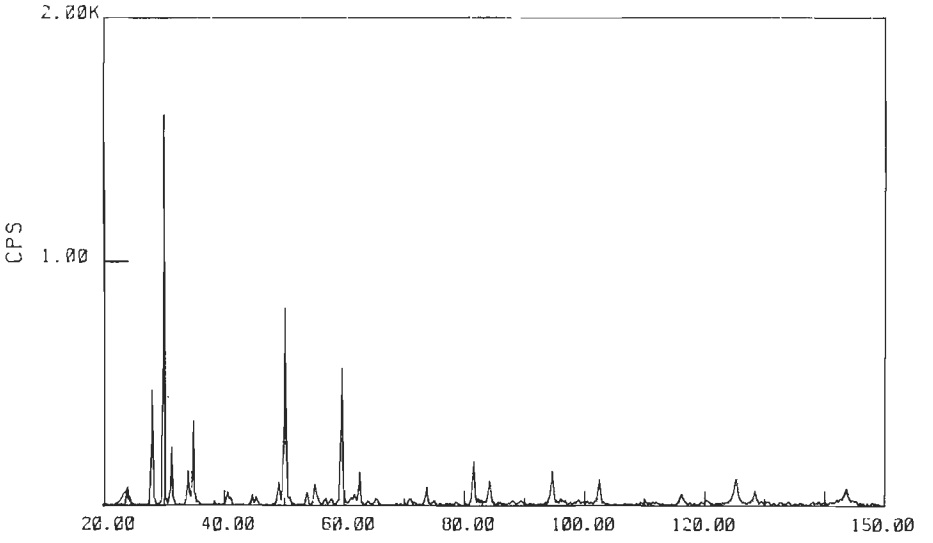


**Figure D-4** Diffraction pattern of $ZrO_2$ 7.6 wt% $Y_2O_3$ after annealing for 100 hours at 1500 °C. About 20 mole % monoclinic phase developed.

## APPENDIX-D 2

STELLINGEN

Behorende bij het proefschrift "Plasma Sprayed Thermal Barrier Coatings: Production, Characterization and Testing" van A.T.J. Verbeek.

1
Het ontbreken van normen voor het uitvoeren van thermische wisselbelastings- en erosieproeven maakt het bijna onmogelijk om meetresultaten, gerapporteerd door diverse auteurs, te vergelijken.

2
De spanningstoestand in een plasmagespoten deeltje veroorzaakt door primaire koeling, is een functie van de kontaktvlaktemperatuur tussen deeltje en substraat en niet van de substraattemperatuur.
(dit proefschrift, hoofdstuk II, paragraaf 5.4.3)

3
De veronderstelde wetmatigheid dat de verhoging van de erosieweerstand van een plasmagespoten "thermal barrier coating" leidt tot een verlaging van de thermische wisselbelastings-weerstand, blijkt niet geldig.
(dit proefschrift, hoofdstuk V, paragrafen 2 t/m 2.6)

4
Het feit dat partieel gestabiliseerde, **plasmagespoten**, $ZrO_2$ coatings (met 7-8 wt% $Y_2O_3$) de hoogste thermoshock weerstand bezitten, kan niet toegeschreven worden aan het optreden van "transformation toughening", aangezien deze coatings bestaan uit de niet-transformeerbare tetragonale fase.
(Miller R.A., Garlick R.G., Smialek J.L., Phase Distributions in Plasma Sprayed Zirconia Yttria, J. Am. Ceram. Soc. 62(1983), No 12, 1355-1358)

5
Het niet, of niet in voldoende mate, beschikbaar zijn van gegevens aangaande mechanische en fysische eigenschappen bij hoge temperatuur, van keramische materialen vormt een belemmerende factor in de ontwikkeling van toepassingen van deze materialen.

6
Het feit dat "kleine criminaliteit" welig tiert, is niet alleen te wijten aan politie en politici, maar ook aan het teloorgaan van het collectief verantwoordelijkheidsgevoel. De steeds individueler wordende maatschappij, die onbetamelijk gedrag niet corrigeert, maar er of angstig of schouderophalend aan voorbij gaat, is hier mede de oorzaak van.

7
Aan het, in bepaalde kringen bejubelde, "just-in-time" systeem, kleeft een belangrijk nadeel, namelijk het feit dat de toch al overvolle openbare weg als magazijn wordt gebruikt.

8
Een regio dient in de produktie van zijn eigen voedselbehoefte te kunnen voorzien. Dit beperkt de afhankelijkheid van een kwetsbaar (en milieubelastend) distributiesysteem.

9
Het instellen van een eerstejaars-college "eten met mes en vork" zal niet alleen de kantine een betere aanblik geven, maar heeft bovenal een grote meerwaarde voor de Nederlandse economie.

10
De huidige tendens tot het instellen van studierichtingen vanwege vermeend economisch- en maatschappelijk belang, doch niet gebaseerd op samenhangende, goed gefundeerde kennis, kan leiden tot het instellen van een "Faculteit der Fritologie".

Eindhoven, juli 1992, Ad Verbeek